The plasma treatment of inorganic waste streams for the production of monolithic glass-ceramic tiles

Deegan, David

Award date:
2002

Awarding institution:
University of Bath

THE PLASMA TREATMENT OF INORGANIC WASTE STREAMS FOR THE PRODUCTION OF MONOLITHIC GLASS-CERAMIC TILES

submitted by David Deegan

for the degree of PhD

of the University of Bath

2002

ProQuest LLC
789 East Eisenhower Parkway
P.O. Box 1346
Ann Arbor, MI 48106-1346

1 Abstract

In the UK, 21 mega-tonnes per annum of household waste requires disposal at a cost of £15 per tonne. The objective of this research was to process waste materials into economically viable, glass-ceramic tiles with mechanical and ecological properties equivalent to those of commercial granite products. The commercial and technical issues associated with the acceptance of processed wastes, namely ecological compatibility, the physio-mechanical properties of the product and whether the technology is scalable to meet the requirements of the waste industry were addressed. The process was also proven to be tolerant of the inherent variability of the waste materials.

Initially, four silicate mineral wastes were thermally processed in a muffle furnace to select which was most appropriate, both in terms of ease of production and physical, mechanical and chemical properties. The crystallisation behaviour of the selected material was systematically quantified.

The work was repeated using a twin electrode, cold skull DC plasma reactor to process the selected wastes. The reactor produced a homogeneous and de-gassed melt over a skull of the same composition within a single chamber at temperatures above 1600 °C. The melt was cast periodically into tiles, which were cooled at a sufficient rate to form a glassy microstructure. The tiles were subsequently heat treated to develop a uniform crystalline microstructure. The process was operated on a semi-continuous basis and dynamic process control was used to compensate for the variable waste characteristics.

The glass-ceramic tiles produced by optimisation of the production process (130 x 130 x 10 mm), had flexural strengths of > 60 MPa, Young's moduli of 80 GPa, a Weibull modulus of 12.9 and cost £11.8 m^{-2} to produce. They had an albite - anorthite based microstructure and the retained heavy metal species displayed low leachability, of the order of $\mu g\ l^{-1}$, meeting the Water Supply Regulations requirements. This confirmed the economic and technological viability of the process and product.

Contents

Figures

List of Symbols

T	is the absolute temperature (K).
T_m	is the solidification temperature (K).
T_g	is the glass transition temperature (K).
T_{DSP}	is the dilatometric softening point (K).
ΔG	is the free-energy change, per unit volume or per mole, for the crystal – liquid phase transformation (J m^{-3}).
ΔG_r	is the free-energy change associated with the formation of a singular spherical nucleus (J).
r	is the radius of the spherical nucleus (m).
r^*	is the critical radius of the spherical nucleus (m).
σ	is the interfacial surface free energy of a homogeneously nucleated liquid – crystal interface (J m^{-2}).
π	is the mathematical constant pie.
ΔG^*_{hom}	is the free energy barrier to the homogeneous nucleation of a single spherical nucleus (J), often referred to as the *thermodynamic barrier to nucleation.*

v	is the individual atomic volume of the atoms making up a nucleus (m^3).
n	is the number of atoms in a nucleus
n^*	is the number of atoms in a critically sized nucleus
ΔG_n	is the free-energy change associated with the formation of a number 'n' of singular spherical nucleus, assuming the properties of an ideal solution (J).
N_r	is the number of nuclei formed of radius, 'r'.
N	is the number of atoms per unit volume of crystal.
k	is Boltzman's constant ($J K^{-1}$).
N_{r^*}	is the number of critically size nuclei formed of radius, 'r*'.
h	is Planck's constant (J s).
P	is the probability with which an atom attempts to cross the embryo/parent phase interface.
N_s	is the number of atoms adjacent to a crystal growth interface.
I	is the rate of nucleation ($m s^{-1}$).
ΔG_a	is the free energy barrier for the assimilation of a single atom across a crystal growth interface (J), often referred to as the *kinetic barrier to nucleation.*
ΔS_f	is the entropy of fusion ($J K^{-1}$).
v_c	is the volume of the heterogeneously nucleated cluster (m^3).
v_m	is the molar volume of the crystalline phase ($m^3 mol^{-1}$).
S_{lc}	is the surface areas of the liquid-crystal interfaces (m^2).
S_{cs}	is the surface areas of the crystal-substrate interfaces (m^2).
σ_{lc},	is the liquid-crystal interfacial energies ($J m^{-2}$).
σ_{cs}	is the substrate-crystal interfacial energies ($J m^{-2}$).
σ_{ls}	is the liquid-substrate interfacial energies, ($J m^{-2}$).
θ	is the wetting angle of the substrate crystal interface (°).
$f(\theta)$	is a mathematical function of the wetting/contact angle, 'θ'.
ΔG^*_{het}	is the free energy barrier to the heterogeneous nucleation of a single spherical nucleus (J), often referred to as the *thermodynamic barrier to nucleation.*
u	is the crystal growth rate ($m s^{-1}$).
δ	is the disregistry between two materials' crystal structure.
a	is the inter-atomic spacing of a material (m).
s	is the number of atoms of a glassy material adjacent to a crystalline phase.

v_0	is the vibration frequency of an atom due to thermal energy (s^{-1}).
λ	is the crystal growth increment of a mono-layer addition of atoms (m).
R	is the ideal gas constant ($J^{-1} K^{-1} mol^{-1}$).
D	is the atomic diffusion coefficient ($m^2 s^{-1}$).
ΔG_m	is the free energy change of mixing of two liquids ($J mol^{-1}$).
ΔH_m	is the enthalpy change of mixing of two liquids ($J mol^{-1}$).
ΔS_m	is the entropy change of mixing of two liquids, ($J mol^{-1}$).
x_t	is the volume fraction transformed ($v_{crystal}/v_{glass}$).
t	is the lapsed time (s).
m_x	is the mass of a plasma particle (kg).
v_x	is the velocity of a plasma particle ($m s^{-1}$).
T_x	is the absolute temperature of a plasma particle (K).
ϕ_c	is the plasma electrode material work function (eV).
ε	is the electronic charge (C).
j_s	is the saturated 'zero potential' surface flux of electrons ($A m^{-2}$).
α	is the linear thermal coefficient ($°C^{-1}$).
K	is the bulk modulus (Pa).
F	is the weight fraction of a component.
ρ	is the phase apparent density ($kg m^{-3}$).
$2c$	is the indentation radial crack characteristic dimension (m).
$2a$	is the hardness impression characteristic dimension (m).
K_{1C}	is the critical stress intensity factor ($Pa m^{0.5}$), fracture toughness.
E	is the elastic modulus (Pa).
HV	is the Vickers hardness (Pa).
P'	is the peak force (N)
c_0	is the equilibrium crack dimension (when $K_r = K_c$) (m)
δ_v^R	is the calibration constant = 0.016±0.004.
χ_r	is the constant associated with material constants and loading geometry.
D_l	is the true density of the immersion fluid ($kg m^{-3}$).
W_a	is the sample's dry weight (kg).
W_b	is the sample's immersed weight (kg).
W_c	is the sample's soaked weight (kg).
ν	is the Poission's ratio.

c_l	is the pulse velocity of an ultrasonic signal (ms^{-1}).
f	is the frequency of an ultrasonic pulse vibration (s^{-1})
λ'	is the wavelength of an ultrasonic pulse vibration (m).
E_r	is the radiant energy emitted by unit surface in unit time ($J\ m^{-2}\ s^{-1}$).
σ	is the Stefan – Boltzmann constant ($J\ m^{-2}\ s^{-1}\ K^{-4}$).
ε	is the hemispherical emissivity.
n'	is the order of reflection (indices).
λ''	is the wavelength of the incident radiation (m).
d	is the inter-crystallographic plane spacing (m).
θ	is the Bragg angle (°).
N'	is the molar fraction.
N_a	is the silica equivalence of Al_2O_3.
η	is the viscosity of a material ($kgm^{-1}s^{-1}$).
L	is the specimen length (m).
$T_{annealing}$	is the glass annealing temperature (K).
T^{max}	is the maximum radial solidification temperature differential (K).
q_k	is the heat loss through thermal conduction (W).
A	is the area normal to the direction of heat transfer (m^2).
k'	is the material's thermal conductivity ($W\ m^{-1}\ K^{-1}$).
P''	is the material pouring rate from the plasma furnace ($kg\ s^{-1}$).
C_p	is the material's specific heat capacity under constant pressure ($J\ kg^{-1}\ K^{-1}$).
ΔT_{lost}	is the degrees of superheat lost (K).
Q_{loss}	is the thermal loss of a process (kW).
F_R	is the water flow rate through a water-cooled component ($l\ m^{-1}$).
T_{rtn}	is the return water temperature of a water-cooled component (°C).
T_{flw}	is the flow water temperature of a water-cooled component (°C).
D_{grain}	is the average grain size (m).
C	is the length of the test line (m).
M	is the magnification of the electron micrograph.
N''	is the number of intercepts.
N_{eff}	is the effective number of intercepts.
N_{aa}	is the intercept boundaries of continuous grains of the primary phase.
N_{ab}	is the intercept boundaries between primary and secondary phases.

N_r is the number of growth centres per unit volume (m^{-3}).

E^*_i is the leaching test measured leaching of a component in fraction i (mg m^{-2}).

c_i is the leaching test concentration of component in fraction i (μg l^{-1}).

V is the volume of the eluate in litres.

A' is the surface area of the test piece (m^2).

f' is a dimensionless factor; 1000 μg mg^{-1}.

ε^*_n is the leaching test measured cumulative leaching of a component for period 'n' comprising fractions i = 1 to n (mg m^{-2}).

N^* is the leaching test number of fractions which is equal to the number of specified replenishment times.

ε_n is the leaching test arithmetical cumulative leaching of a component for period i = 1 to n (mg m^{-2}).

t_i is the leaching test replenishment time of fraction i (s).

t_{i-1} is the leaching test replenishment time of fraction i-1 (s).

b is the flexural test specimen width (m).

L' is the flexural test specimen inner span (m).

d' is the flexural test specimen thickness (m).

j is the Weibull ranking number.

N_o is the total number of flexural test samples.

σ^* is the externally applied engineering stress (Pa).

σ_u is the stress below which fracture is assumed to have zero probability of occurrence for ceramics (Pa).

σ_o is a material constant, the characteristic strength (Pa).

m is a material constant, the Weibull modulus.

n'' is the number of measurements in a data set.

s^d is the sample standard deviation of a data set (using Bessel's correction).

$\bar{x}$ is the sample mean of a data set.

Acknowledgements

I would like to thank all of the academic and technical staff in the Department of Engineering and Applied Science and Electron Optics at the University of Bath. They provided an interactive and stimulating environment and helped with all of the practical laboratory requirements needed to carry out the analytical components of this work. My work colleagues at Tetronics have been generous in discussion, criticism and constructive suggestion and have supported and helped me in the design, installation and operation of the plasma reactor. I would like to particularly thank Dr Mike Wise and Dr Chris Bowen who have read the entire text of this thesis and made numerous astute suggestions. A large number of people have contributed to discussion in the preparation of this thesis, including:

Dr. C. Bowen (Dept. of Engineering and Applied Science, University of Bath)
Dr Mike Wise (Process Engineer, Tetronics Limited, Oxfordshire)
Prof. R Stevens (Dept. of Engineering and Applied Science, University of Bath)
Mr C Chapman (Senior Process Engineer, Tetronics Limited, Oxfordshire)
Dr T Johnson (Process Engineer, Tetronics Limited, Oxfordshire)
Mr Peter Taylor (Dept. of Engineering and Applied Science, University of Bath)
Dr Barry Chapman (Dept. of Engineering and Applied Science, University of Bath)
Mrs Rachel Deegan (Chief Mentor to the author of this text)

2 Introduction

2.1 Background

Waste management is a growing problem, and the crude disposal of waste materials in landfill sites is obtaining increasing opposition, from both political and environmental standpoints. The vitrification of waste materials provides an alternative route to disposal by dumping at sea or land filling. Land filling is currently the most widely used disposal method within Europe however new legislation is increasing the requirement for technological change, [1, 2, 3]. The lack of landfill sites and increasing landfill costs are driving the need for the development of alternative technologies for the environmentally efficient disposal of wastes. These features are exaggerated by the increasing amount of waste being generated [4, 5].

Vitrification technology is considered to be one of the most promising solutions to the waste problem, however little attention is given to the materials engineering associated with the approach, hence it is predominantly considered as a pre-treatment for ultimate disposal and is seen as a solution for incinerator waste, where secondary ashes account for 15 – 20 wt% of the incinerator feed material. There are commercial vitrification units in operation that process municipal incinerator ashes and asbestos containing wastes where the aim is to immobilise toxins and consolidate the wastes. Additionally, pyro-metallurgical wastes and industrial wastes are vitrified to obtain similar final results but also to reclaim the intrinsic metal from the wastes, and in this sense it is similar to a smelting operation. These processes produce quenched and partially annealed glassy products in which little consideration, beyond compositional issues, has been given to the material properties. The products are commonly marketed as coarse and fine aggregates, but the mechanical property consistency of these materials limits their commercial utilisation and exploitation has been limited [6].

The research in this area is predominantly laboratory based and examines the melting processes, crystallisation characteristics and product's properties. The outcome of the research is examined in isolation to any commercial requirements or processing scale and the relationship between material structure and properties is not assessed comprehensively. The larger scale research tends to concentrate on the processing equipment/devices and

their performance, and work that bridges these two approaches is required. The material outcome of the work is commonly superficial and questionable, especially in relation to plasma technology. If all of the research is consolidated the scope of understanding will increase, but unfortunately there is minimal material consistency. No work combines a scientific interpretation of the processed waste materials properties with an industrial scale simulation, and product analysis tends to be application based and not comprehensive.

It is possible to improve and extend the vitrification-processing route by production of shaped semi-crystalline materials from vitrified wastes, which can be used in building material applications. This offers the potential to add value to the processed waste. Value addition is considered to be the most important factor in shifting the economic argument in favour of vitrification technology.

2.2 Aims

This research aims to develop a plasma-based waste treatment solution that encompasses these technological features, especially the requirement to improve the quality of the evolved glass, and produce a commercially viable glass-ceramic product from wastes. The work was organised into the following stages:

(i). Undertake the specification, design and installation of a pilot scale plasma waste melting furnace, whilst simultaneously undertaking laboratory experimentation with four wastes to optimise the generic composition, melting conditions and crystallisation requirements of the vitreous material. Analyse of the physical and mechanical properties of the product for comparison with commercially available products.

(ii). The plasma melting equipment was used to repeat the most promising laboratory research, to demonstrate larger scale replication of the laboratory work and the production of cast near-to-net shape tiles. This work was monitored to give an empirical basis to the economic analysis of the process and product. Simultaneously, laboratory experimentation was used to quantify the crystallisation process, ensuring that the desired crystalline phase identity and microstructure were produced upon heat treatment.

(iii). The mechanical properties of the crystallised plasma furnace product and the glassy precursor were analysed to statistically define the variations and

improvements in properties. This was accompanied by the assessment of ecological compatibility using a leaching test to determine the environmental impact of the monolithic products.

2.3 Summary of the Research Activity

The DC thermal plasma technology immobilised the heavy metal species, such as chromium and lead and other chemical species arising from the destruction of organic compounds. The high-temperature processing environment, with independent control of process chemistry, aided success, i.e. combustion of fuel was not required to liberate energy. The plasma was used to vitrify, condition and de-gas melts produced from Municipal Solid Waste (MSW) incinerator grate and fly ashes, British China Clay Waste (BCC) and Contaminated German Harbour Sediment (GHS). Real wastes were employed and not surrogates. These wastes were selected because they contained a large proportion of glass forming oxides, which reduced the requirement for the addition of a host glass [7, 8]. Manipulation of the proportions of glass forming oxides in the waste, prior to melting, was used to improve the stability of the glassy phase. The melts were cast and controlled de-vitrification was possible for certain glass compositions and involved a two-stage heat treatment, namely nucleation and crystallisation. This enabled the production of semi-crystalline tile products.

The material produced arose from the combination of a glass making technology and controlled de-vitrification, and in this sense belongs to the general class of materials referred to as 'glass-ceramics'. It differed from industrially known glass-ceramics as it was aimed at a tonnage market rather than a relatively small and specialised market arising from high purity materials. This type of material has already been successfully generated from predicatable industrial waste streams [9], but never from municipal wastes or in the context of transferred arc plasma processing.

The controlled de-vitrification of the waste materials, and their physio-mechanical properties, were quantitatively examined to determine the level of property enhancement that could be obtained through a glass ceramic processing route. This gave an assessment of the feasibility of producing glass-ceramic tiles from low-grade wastes. The most promising material was selected and its nucleation and crystallisation were examined in

detail. Observed variations in micro-structural features, e.g. grain size, number density and volume fraction, were correlated so that optimum conditions could be identified and exploited. Materials engineering was used to control and maximise desirable properties through the selection of crystal type, shape and size.

The glass-ceramic route required uniform crystal growth throughout the bulk of the material. This was achieved by the development of a uniform dispersion of nuclei, which were assessed indirectly. The evolved process comprised the melting of an appropriate composition, cooling to form a shaped glass article, reheating to develop a uniform distribution of nuclei, and heating to allow the growth of crystals upon the nuclei until only a small proportion of the initial glassy phase was retained.

The heterogeneities within a waste material, such as partially combusted organics, refractory oxides and metallic inclusions, hindered the work. However, the complexity and variability of the wastes were approached as a challenge and dictated where the application of pure scientific principles started and ended, and where process control was used to compensate for uncertainty. A practical evaluation of temperature profiles within a solidifying tile was used to determine the limiting dimensions of the product and elastic properties were used to assess the thermal stress produced in a tile of defined geometry.

Upon identification of the desirable processing environment several duplicated samples of the semi-crystalline ceramics were prepared from the plasma furnace product. Weibull statistics and a leaching test were used to assess the improvement in the mechanical properties and environmental impact respectively of the ceramic product.

2.4 Layout of the Thesis

This thesis is structured to firstly review the current volume of published literature within the subject areas of plasma technology and inorganic waste processing (Section 3). It is segmented in material categories to aid interpretation within context. This is followed by a full description of the fundamental scientific principles employed in controlling and manipulating the processing route of the waste materials (Section 4), to achieve both a stable glass using plasma heating and subsequently a stable glass-ceramic material with enhanced properties, through thermal transformation.

Work is firstly described on a laboratory scale (Section 5) where the experimental characterisation of the raw wastes and the thermal, physical, chemical and mechanical properties of the evolved glasses were undertaken. This work defined the processing regime employed in the prototype scale plasma furnace experiments and the secondary crystallising heat treatments. This is followed by a full description of the characterising technological and physical features of the plasma equipment and its fundamental operating and design basis (Section 6).

Subsequent to the laboratory work, the plasma furnace experimentation is described (Section 7). Here the key processing stages and historical trends are present and explained. This allows the quantitative definition of processing costs and energy efficiencies to be provided for each waste material processed. All of which gives rise to a production cost for the glassy material product.

The thesis goes on to describes the experimental investigation of the crystallisation behaviour of a selected glassy material product from the plasma furnace (Section 8), and how the heat treatment schedule was optimised to improve both ecological (Section 9) and mechanical (Section 10) material performance.

3 Literature Review

3.1 Introduction

Vitrification of both hazardous and non-hazardous wastes for the production of commercial glasses or glass ceramics provides an alternative to waste treatment, such as disposal at sea and land filling. However, alternative solutions that require costly classification and selection are not acceptable [10]. Although land filling is currently the most widely used disposal method, it is becoming environmentally unacceptable, and a better strategy is being sought. Legislation is accelerating the requirement for technological change, as waste treatment is acquiring greater financial and political importance [1, 2, 3]. Prior to this research, limited emphasis has been given to the production of semi-crystalline products from natural or municipal waste materials. The bulk of the literature available focuses on vitrification technology for the production of leach resistant glasses that encapsulate radionuclides for disposal, [11, 12, 13]. However this is a treatment method used to generate material for ultimate disposal and is of limited relevance in this work, where the aim is to further utilise the products.

The utilisation of waste materials to produce commercially viable glass-ceramic products has significant economical and environmental benefits, primarily because the wastes contain large proportions of glass forming oxides which reduces the requirement for the provision of a host glass [7, 8]. This approach is a logical development of the waste management hierarchy adopted in industrialised nations: i.e. prevention, minimisation, material recovery, incineration and finally landfill. Increasing lack of sites and landfill costs are the economic drivers presently pushing the development of alternative technologies for the efficient and environmentally safe disposal of hazardous wastes. These features are also exaggerated by the increasing amount of waste being generated [4, 5]. The application of incineration technologies with energy recovery, that produce either electricity or steam, is not without difficulties, and incineration itself has many problems, including questionable effective treatment, emissions and a high volume of by-product waste ash. Solid residues such as fly ash, bag-house dusts, water treatment sludge, bottom ash and slags, account for approximately 25 wt% of the original feed materials in a voluminous form. The high surface area of the individual particulates and organic/inorganic chemical toxicity of these materials, leads to its classification as a

harzardous or special waste in European countries through the Landfill Directive [10]. Hence segregation and diposal methods are becoming increasingly costly.

Thermal plasma technology is an effective tool for the immobilisation of heavy metallic species and other chemical species arising from the destruction of organic compounds, in 'non-leachable' inorganic slags that act as repositories for regulated chemical species. The process involves subjecting the waste materials, which have similar chemical compositions, to high temperatures (1500 – 1800 °C) such that non-volatile species become chemically bonded in the resulting inorganic matrix, i.e. the slag. This is achieved by manipulation of the intrinsic glass forming oxide materials of the waste, prior to melting, so that the stability of the glassy phase, a precursor to the glass-ceramic materials, is improved.

The aim of this research was to produce a glass-ceramic product, prepared by controlled de-vitrification of glasses. The intention was to develop a new marketable waste product, by developing the microstructure of the slag, [14]. Controlled de-vitrification is possible for certain glass compositions and involves a two-stage heat treatment, namely nucleation and crystallisation. The nucleation stage produces crystal growth centres (nuclei) within the parent glass matrix. Subsequent crystallisation proceeds by the growth of a new crystalline phase in close association with these nucleating phase(s).

Current industrial waste processing systems produce quenched, or partially annealed, glassy products, in which little consideration, beyond compositional issues has been given to the material transformations that occur. The most stringent processing criteria are those that ensure good feeding characteristics and ease of removal of the product from the vitrification furnace. In addition, there may be requirement to maintain the feed material's calorific value for effective treatment to occur. Because these materials are generally glassy, or heterogeneously crystallised, the quality requirement for their commercial utilisation and exploitation have yet to be achieved [6].

3.2 Glass-Ceramics

A glass ceramic is a glass that has been de-vitrified in a controlled manner, so that it consists of evenly distributed small crystals in a glassy matrix. Commonly, the largest dimensions of the crystallites present are only a fraction of a micrometre, and there may be present some 10^{10} –10^{12} crystals mm^{-3}. The parent glass, which is brittle in nature (linearly elastic), is transformed into a semi-crystalline material by a tailored thermal heat treatment. The aim is to produce a product that has superior mechanical and physical properties to those of the parent glass. Such property enhancements may include higher mechanical strength, impact strength, refractory behaviour and/or a lower thermal expansion coefficient.

Glasses suitable for controlled devitrification must be relatively resistant to crystallisation, otherwise instantaneous transformations and failure may occur on cooling. Once a stable glassy body has been formed a nucleation mechanism must be provided so that centres for crystal growth are created, with these nuclei evenly distributed throughout the glass [15]. Conveniently, heterogeneous nuclei can be provided by the controlled precipitation of sparingly soluble phases from the melt phase, which act as nuclei for the main de-vitrification products of the glass, [15].

This description is a traditional explanation of the glass-ceramic formation process. However, it has been recognised that many glasses are not homogeneous, but are emulsions of two finely divided immiscible glasses. Here, as the temperature is raised, a point is reached where the system homogenises as a single phase. On cooling, nuclei are precipitated in one of the phases and are prevented from coarsening because the phase boundaries between the two glasses act as a diffusion barrier [15].

3.3 The Production of Glass Ceramics from Various Waste Materials

3.3.1 Fused Metallurgical Furnace Wastes

Locsei *et al,* (1950's) in Budapest examined the Na_2O-CaO-MgO-Al_2O_3-SiO_2 system and employed mixtures of blast furnace slag and used sulphide compounds as nucleating compound catalysts. The chosen synthesis method involved a combination of glass melting at 1430 °C in a reducing atmosphere, followed by casting and subsequent

crystallisation thermal heat treatment. A two stage heat treatment was used which included a nucleation hold at 800 °C for one hour followed by alternative crystal growth stages at 800 – 1000 °C for 1 – 5 hours. The furnace charge contained only 56 wt% of blast furnace slag and the final product was called 'Minelbite'. The total amount of nucleating agent used was 4 – 5 wt% and the primary crystalline phase evolved was diopside at crystallite sizes of less than 1 μm. The extent of crystallisation was monitored through observation of changes in the apparent density and coefficient of linear expansion. The material properties reported are shown in Table 1.

Material	Density (g/cm^3)	Coefficient of linear Expansion α ($°C^{-1}$)	Flexural Strength σ_f (MPa)
Parent Glass	2.70	$96x10^{-7}$	-
Minelbite	3.10	$72x10^{-7}$	46

Table 1: The properties of minelbite, [15]

It was claimed that the best mechanical properties were generated if the compositions were located on the eutectic point of the albite-anorthite-diopside phase boundaries, because of the improved melting and diffusion characteristics at the relatively low melting temperature employed. The exact form of the heat treatment schedule was claimed to have been a function of chemical composition and the size of the article under fabrication [15, 16].

There is a well-established cast stone industry in the former Soviet Union, known as 'petrurgy' and dates back to the 1970's. Green and amber glasses with relatively high proportions of metallurgical slag have been produced [15]. Kitaigorodskii *et al* claimed an 'economically advantaged' method for producing glass ceramics from fused metallurgical slag and waste slags, indicating that waste slags require additional outlay in preparation. The primary phases developed in the glass ceramics were anorthite $CaO\text{-}Al_2O_3\text{-}2SiO_2$, fluorite CaF_2, or sphene $CaO\text{-}TiO_2\text{-}SiO_2$, [16]. The term "sitall" is given to the products and is derived from the elements of 'steklo i khrystal' – glass and crystal – and is equivalent to the term glass-ceramic. Hence,

(i) Petrositall is rock based glass ceramic.

(ii) Zolositall is ash based glass ceramic.

(iii) Slagsitall is slag based glass ceramic.

Conveniently, heterogeneous nuclei can be provided by the controlled precipitation of sparingly soluble phases from the melt, as their solubility decreases with temperature. Heavy metal sulphides and spinels are reported to behave in this way and can be readily evolved from slag-based systems due to their 'sulphide capacity'. For example FeS-FeS_2-MnS-MnS_2 solid solution phases can be formed, however they do have a tendency to coarsen by diffusion mechanisms, producing fewer larger nuclei, [15]. The literature appears to give limited economic detail and only claims economic benefit.

Davis *et al,* (1970) conducted a laboratory scale study into the effect of a number of material and process variables on a glass-ceramic product named 'slagceram'. They found that the amount and nature of the nucleating agent, the time held in the molten state, the source of the slag, the overall composition of the material and the heat treatment schedule employed had the most significant effects on the product's characteristics, which is not surprising. The nucleating agents chosen in the study were iron ore, chromium ore and titania. Various additions were made to a slag including sand mixtures in the following composition range, i.e. 30 parts to 100 parts $^{w}/_{w}$, Table 2.

	Raw Slag	Blended Material
Species	Wt%	Wt%
SiO_2	31.3	48.0
Al_2O_3	17.9	14.0
FeO	0.64	0.5
MgO	7.1	5.6
MnO	0.59	0.5
CaO	37.9	29.7
Fe_{Total}	0.75	0.6
S_{Total}	1.60	1.3

Table 2: Overall composition of the blended batches, David *et al.*

Melting was carried out in refractory lined vessels at 1450 °C and both the size of the vessel and the depth of the melt were varied. This gave rise to the problems associated with the assimilation of the container by the melt. Optical and X-ray means were used to allow assessment of the success of nucleation, but no details were given. The conclusions were that the time of holding at the melt temperature and the size of the vessel were more important than the identity of the nucleation agent present. Generally it was observed that the effectiveness of nucleating agents decreased with increasing melt holding time, particularly in the case of refractory lined vessels.

Titania was considered to be one of the most successful nucleating agents. Fluorides were considered, however they were neglected because of gas emission problems for production scale operation. Some limited consideration was given to casting, forming and heat treatment techniques.

Reducing atmospheric conditions stimulated improved effectiveness of the nucleating agents, however, no reasoning was presented. It was postulated that redox potential and valency influence either reaction kinetics or phase identity and, hence, stability.

In the context of glass melting, argon atmospheres are reducing, due to the limitation of oxygen partial pressure. This work was taken to the pilot plant scale and found to be successful, and a 6 wt% addition of titania was accepted as the standard addition, which is very high when compared with the 1 – 2 wt% commonly employed.

Casting was carried out at 1450 °C and the subsequent crystallisation heat treatment schedule employed was 10 hours at 720 °C followed by heating at 1 °C min^{-1} to 900 °C where it was held for 3 hours. Crystallite sizes were reported to be in the region of 5 – 25 μm. Holding times between 2 to 3 hours were observed to allow crystallisation to occur with limited slumping and change in shape of the material. Crystallisation was examined using microscopy techniques; as in previous work the primary phase to crystallise was subsequently modified in the latter stages of crystallisation process, so that a secondary stage of crystallisation was observed. The two crystalline phases had distinctly different morphologies, one polygonal and the other dendritic.

Carbon additions were observed to retard the onset of the secondary crystallisation stage and allowed the evolution of finer microstructures, this effect was explained by the reducing action of the materials and the presence of multivalent ions, the potential nucleating species being $CO_{(g)}$, Fe and FeS.

One of the most significant outcomes of this work was that reducing atmospheres are extremely desirable in producing successful nucleation, as they modified the Fe^{2+}/Fe^{3+} ratio. As would be expected, the presence of the higher temperature crystalline phase was associated with a high degree of slumping. Variations in the proportions of the major

constituents were observed to have a marked effect of the whole process's melting and heat treatment characteristics.

Magnesia additions were observed to give a steeper viscosity vs temperature curve for the glass, thereby lowering the viscosity at casting and accelerating assimilation and allowing a lower melting temperature. It also increased the melt viscosity at the heat treatment temperature and reduced slumping.

Lime additions were observed to have similar higher temperature effects to magnesia but had no influence on the slumping and shortened the holding time for de-vitrification. Alumina additions reduced the rate of material assimilation and lowered the quality of the short holding time glass.

They went on to consider the effect of variations in heat treatment parameters on the product. Endothermic peaks, identified using differential thermal analysis (DTA), were identified and attributed to nucleation, which is questionable, and more pronounced exothermic peaks were attributed to crystallisation processes. The experimentation was carried out in a tank furnace of 100 kg capacity. The main outcome of the pilot plant experimentation was that the larger the furnace the more easy it was to form a product of consistent quality. Additionally small batch composition variations could be accepted.

The crystallisation stages of the process were undertaken in a furnace powered by a propane burner, and again the pilot plant experimentation was plagued by refractory corrosion problems, which had an uncontrollable effect on the constitution of the melt. The depth of the melt was limited to 75 – 100 mm by the large temperature gradient across the melt and inefficient stirring. The crystallite sizes in the pilot plant test work varied in comparison to the laboratory experimentation. The microstructure was slightly coarser when compared with the laboratory work, i.e. crystallite sizes between 40 – 50 μm were observed. The properties of the material generated in the pilot plant work are given in Table 3.

Property (Units)	Magnitude
Apparent density (g cm^{-3})	2.9 – 3.0
Specific Heat (cal $g^{-1}°C^{-1}$)	0.17
Coefficient of Linear Expansion ($°C^{-1}$ @ RT)	$5x10^{-6}$
Modulus of Rupture (MPa)	140
Total Porosity (%) by microscopy	~10
Open Porosity (%) by water intrusion	~5
Indentation Microhardness (Vickers Diamond Pyramid)	750
Young's Modulus (non – destructive) (GPa)	9 – 13

Table 3: Properties of blast furnace slagceram [9]

Significant material property scatter was observed indicating preparation inconsistency, the magnitude of this effect gave rise to 40% variations of the slagceram product, however the product did have superior wear resistance properties to those of fusion cast basalt or granite, [9].

Davis *et al,* (1970) published again in the same year, placing more emphasis on the nucleation and crystallisation process in slag based glass-ceramics containing both Fe-S and Fe-Cr. Elemental species were often present in the parent slag materials. Experimental trials were carried out on both slag based glasses and synthetic glasses of the following composition, Table 4.

	Glass Composition
Species	Wt%
SiO_2	53.0
Al_2O_3	15.0
MgO	4.0
CaO	28.0

Table 4: Composition of the base synthetic glasses, [19].

The objective of the work was to study the mechanism of nucleation prior to formation of the glass-ceramic and hence elucidate the effects of iron oxide and sulphur with those containing iron oxide and chromium oxide as nucleating agents. In the iron sulphur (Fe-FeS) system nucleation occurred in a heterogeneous manner with the appearance of iron sulphide droplets, which were identified using electron probe microanalysis. The observed

nuclei size distribution was coarse at 0.02 – 100 μm, with the bulk of the droplet formation being obtained as the glass cooled, of about 6 μm in size. The paper concluded that a two-stage heat treatment process was necessary to generate a very fine microstructure, in which the silicate species could heterogeneously nucleate and grow. In contrast, the glasses containing both iron oxide and chromium oxide showed no evidence of phase separation. The nucleation process in this case was assumed to be a homogeneous mechanism provided that the solubility limits were not exceeded. Nucleation in the Fe-S system occurred in a less rapid manner to that in the Fe-Cr glass. Quantitative observations confirmed that classical Tamman type behaviour was observed [20, 9]. The Fe-S nucleation process gave rise to the spherulitic fibrous growth and the Fe-Cr glass generated dendritic growth features. In all cases the major crystalline phase evolved was clinopyroxene. If the slag, on exiting the furnace, was allowed to cool slowly the crystalline phase was akermanite $Ca_2MgSi_2O_7$ (a solid solution of melilite $[(Na,Ca)_2(Mg,Al)(Si,Al)_2O_7)]$ with gehlenite). This observation has been made by other researchers, [19].

Silica enrichment, ≤ 30 wt%, was employed to generate a stable glass and promote the development of more desirable crystalline phases for property enhancement. The nucleating agents specified allowed subsequent heat treatment to result in controlled de-vitrification and the development of a dense hard finely crystalline glass ceramic material, namely 'slagceram'. The main phases within this material were clinopyroxene, anorthite and wollastonite.

The chosen compositional material area of the research was located within the anorthite region of the SiO_2-Al_2O_3-CaO ternary system. The experimental work was conducted on a laboratory scale using an electric resistance furnace using batches of 120 g contained in Pt/10 wt% Rh dishes. The melting temperatures employed were 1450 °C for various periods of time. The base glasses for all synthetic and slag melts were prepared by melting the required composition of oxide species then casting, crushing and remelting the oxide glass to give comparable results. Ferrous sulphide or 5 wt% Fe_2O_3 plus 1wt% Cr_2O_3 were added to these base glasses. Slag based glasses were obtained by adding 30 parts by weight silica and 1 part by weight carbon to the slag. Optical microscopy was used in a novel manner to image reflective droplets in the glasses containing Fe-S, which indicates

that they were very coarse, i.e. larger than 1 μm. The droplets were surrounded by darkened halos, indicating some level of material / property segregation, e.g. the depletion of the melt with respect to FeS. The presence of these droplets was observed to diminish with increasing holding time in the molten state, resulting in unsuccessful crystallisation. The success of the crystallisation process was postulated to be due to a balance of participation, for the nucleation process, and vapour phase losses, through oxidation reactions with increased holding time. A holding time of 3 hours was determined to be the maximum. Careful examination showed that only the large and medium sized droplets, i.e. ≥ 0.5 μm, had acted as growth centres.

Making assumptions to allow for the two dimensional nature of these images, it was concluded that the droplets were comprised of FeS as the majority phase with metallic Fe as the secondary interstitial phase. It was observed that the melt cooling rate in the high temperature region is critical in determining the distribution of the FeS in the melt with slower cooling rates allowing more droplet separation. Crystallisation experiments failed to give any more information about the mechanism by which only certain sized droplets were active as nuclei, even though there was compatibility in the registry factor between FeS and clinopyroxene. The nucleation process, nucleation rate = $1x10^3$ cm^3 min^{-1}, was only observed to be successful at temperatures below 850 °C and was weakly temperature dependent. The optimum temperature was approximately 820 °C, hence, it was claimed that it was not possible to plot a conventional Tamman type curve for the FeS nucleation process. This was not observed to be the case for glasses containing iron and chromium.

Glasses containing the highest Fe_2O_3 and Cr_2O_3 content showed the presence of Cr_2O_3 crystals greater than 10 μm in size. This observation was later related to the lack of solid solubility, as these crystals did not act as centres for crystal growth on heat treatment, in fact they had the reverse effect as they were surrounded by a vitreous layer of material in an otherwise completely crystalline material. It was suggested that nucleation may have been occurring in a homogeneous manner, but it was indicated that the techniques used were limited to resolving micro-structural features greater than 10 nm in size. The extent of nucleation was quantitatively assessed and the number of nuclei present in quenching subtracted. Hence the observed number of nuclei evolved was of the order 1×10^{11} cm^{-3}, and the Arrhenius plot gave an activation energy value of 418 kJ mol^{-1}.

Crystal growth in synthetic oxide glasses was subsequently examined, as these glasses generated a more sparse distribution of nuclei, allowing crystal growth kinetics to be followed for the Fe/S containing system. In all cases, Arrehnius plots gave linear crystal growth rates for the longest crystal dimension. Growth rates within each section of the sample approached a steady state level almost immediately, which remained constant for the duration of the process. The activation energy for the crystallisaton process, as determined from the slope of the graph, was 263 $kJ.mol^{-1}$.

Agarwal *et al*, (1991) considered crystallisation phenomenon associated with cupola furnace slag for cast iron manufacturing. The slag was quenched to form a glassy body, and then devitrification was quantitatively examined as a function of thermal processing parameters. X-ray diffraction (XRD), scanning electron microscopy (SEM), transition electron microscopy (TEM), DTA and dilatometry were used interactively, a feature common to many of the publications. The crystalline phase primarily responsible for superior mechanical properties was identified as a wollastonite solid solution that appeared at 950 °C and had a microstructure that exhibited intertwined fibrous growths. A higher temperature treatment produced diopside formation which led to a deterioration of mechanical properties. A factor of 1.5 - 2.0 increase in Vickers hardness values was achieved with optimized thermal treatments. The composition of the slag generated is shown in Table 5.

Main Species	Wt%
SiO_2	42
Al_2O_3	8
MgO	11
MnO_2	3
CaO	34

Table 5: Compositional information for cast iron cupola slag, [21]

The slag also contained a wide variety of heavy metals and other impurities, such as iron oxide, TiO_2 and sulphur oxides etc. This material was quenched after melting to form a fully amorphous material, as observed through X-ray diffraction studies. Thermal treatment was subsequently employed to increase the hardness as a result of devitrification. The work focussed on maximising the mechanical and thermal shock properties of these materials while minimising the costs associated with these processes, thus making

recycling economically more attractive. This work again occurred on a laboratory scale, the melt trial being achieved in silica crucibles located in a SiC muffle furnace. Samples were cast into preheated steel moulds and transferred immediately into a muffle furnace at 400 °C for 2 hours. Normalised furnace cooling was then allowed, prior to product removal. The glass generated exhibited the following properties: the glass transition temperature was 730 °C and the dilatometric softening point was 775 °C, additionally the DTA traces indicated two pronounced overlapping exothermic peaks associated with the crystallisation processes.

The XRD pattern associated with the lower temperature exotherm showed close correlation with the JCPDS data (Joint Committee on Powder Diffraction Standards) for bustamite $(Mn, Ca)_3Si_3O_9$. This is a Mn silicate, but MnO_2 only represented 3 wt% of the material composition, hence the identification was questioned based on the volume fraction transformed. The XRD peaks also corresponded well with wollastonite ($CaSiO_3$) in solid solution and with MnO, MgO or FeO, identified as being present in the slag. The phase was labelled 'complex wollastonite' and grew in a spherulitic fashion, forming fibrous interwoven microstructures.

The second exotherm corresponded to the formation of anorthite ($CaAl_2Si_2O_8$) that had a similar microstructural appearance.

At higher temperatures (1120 °C) diopside $CaMg(SiO_3)_2$ and wollastonite $CaSiO_3$ were present as major phases. It appears that complex wollastonite crystals first rejected oxide impurities that could not be incorporated into the structure, hence these regions became rich in rejected species and the transformation slowed as the driving force for diffusion diminished. The higher temperature phases were accounted for through the decomposition of complex wollastonite to the pure form of wollastonite and the appearance of diopside was associated with the incorporation of the rejected species into a new crystalline phase.

This phase showed a normal growth direction from the wollasonite phase, forming large columnar crystals, disrupting the fibrous structure. Phase density differences meant that the appearance of diopside was associated with an increase in sample porosity and subsequent reduction in mechanical properties as the overall flaw size increased.

TEM-Energy dispersive X-ray analysis (EDX) indicated that nuclei were uniformly distributed and approximately 10 nm in diameter. These nuclei contained significant amounts of iron, manganese and sulphur, which were previously claimed to form dispersed immiscible droplets in the melt. These droplets acted as nuclei for the spherulitic growth of silicate minerals. These droplets were commonly located at the centre of spherulitic growth features, which would indicate their inclusion in a nucleation mechanism.

The nucleation sites were claimed to pre-exist in the as-cast glassy material, which meant the temperature and time of nucleation would not have an effect on the final microstructure.

The effect of microstructure on the material properties was evaluated using hardness measurements and dilatometry. The thermal expansion coefficient and Vickers hardness values were respectively; 9.65×10^{-6} °C^{-1} and 454 HV, for the as quenched glass compared with 6.83×10^{-6} °C^{-1} and 766 HV for the fully developed fibrous microstructure (with limited diopside formation), between room temperature and 500 °C. However, compositional inhomogeneity and resulting property variations were significant, indicating that not enough attention had been given to the processing of the glassy precursor. However the overall outcome of the work was claimed to give a 'genuine economic research opportunity', [21].

Agarwal *et al*, (1992) placed emphasis on the secondary uses of de-vitrified cupola slag as abrasive products. The equivalent product also appeared in Great Britian called 'slagceram'. The product was compared with cast basalt (naturally occurring rocks with compositions similar to the slags) based on the SiO_2-Al_2O_3-CaO ternary system. The compositions employed in this extended work are as follows, Table 6:

	CaO Rich	Original Slag	SiO_2 Rich
Species	Wt%	Wt%	Wt%
SiO_2	37.6	42	47.3
Al_2O_3	40.9	8	7.3
MgO	9.9	11	10.0
MnO_2	2.7	3	2.7
CaO	40.9	34	30.9

Table 6: Composition of the cupola slags [21]

The evaluated hardness properties were used to determine micro-hardness and fracture toughness values, but no information or explanation was given for the value of elastic modulus, which are required for the calculation. From this information a grindability parameter was determined, defined as (H_v/K_{IC}) and the inverse of this parameter was used as an indicator of abrasion resistance. Chemical durability testing complemented this evaluation. Again, a bustamite fibrous microstructure was identified upon heat treatment.

The response of the slag compositional modification compared to those associated with chemically pure materials was evaluated. Overall, silica enrichment generated some segregation within the microstructure where as diopside formed in silica rich regions and Mg-wollastonite formed in silica depleted regions. Increasing the crystallisation temperature gave rise to microstructural coarsening but temperatures exceeding 1100 °C gave rise to porosity associated with $SO_{2(g)}$ formation. Generally, the most advantageous increases in mechanical properties were associated with the CaO rich modification of the original slag composition, Table 7.

	CaO Rich Slag			Silica Rich Slag			Original slag		
Heat Temp (°C)	K_{IC} (MPa√m)	Hv (GPa)	K_{IC}/ Hv x10^{-3} ($m^{-0.5}$)	K_{IC} (MPa√m)	Hv (GPa)	K_{IC}/ Hv x10^{-3} ($m^{-0.5}$)	K_{IC} (MPa√m)	Hv (GPa)	K_{IC}/ Hv x10^{-3} ($m^{-0.5}$)
Un-treated	0.97	4.85	5.00	0.90	4.78	5.30	0,88	4.45	5.06
900	1.10	5.19	4.71	0.87	5.00	5.77	0.99	6.29	6.37
950	1.52	5.99	3.94	1.71	6.87	4.01	1.67	7.51	4.50
1000	2.80	8.85	3.18	2.65	7.50	2.83	2.32	6.91	2.98
1050	2.91	7.93	2.72	1.89	7.09	3.76	2.43	6.84	2.81
1100	2.21	6.80	3.06	1.75	6.73	3.86	1.50	5.23	3.49

Table 7: Micro-indentation results for cupola slag glass ceramics [22]

The concluding remarks associated with the work hinted at a possible toughening mechanism, with crystalline fibres claimed to inhibit crack propagation by crack pinning and/or deflection at the fibre/glass interface, [22].

Shcheglova *et al,* (1995) presented a process for obtaining stone castings from blast furnace slag from the Cherepovetsk Metallurgical Plant in Russia. The intended

application for the product was the production of paving blocks and facing materials. The composition of the industrial waste was found to be uniform, Table 8, as would be expected for an industrial waste. In the work particular attention was paid to the crystallisation of slag melts, compositional corrections and the stabilisation of decomposable slag systems, i.e. those that expand on cooling. The study took laboratory testing to a semi-industrial scale and casting technology was employed to minimise cutting and polishing requirements.

Species	Wt%
SiO_2	38.5
TiO_2	1.24
Al_2O_3	9.0
FeO	0.3
MgO	10.0
MnO	0.19
CaO	41.3
Na_2O	0.35
K_2O	0.55
S	0.83

Table 8: Average bulk oxide analysis of the Cherepovetsk metallurgical slag [23]

The phase diagrams of the $SiO_2 - Al_2O_3 - CaO$ and SiO_2 - Al_2O_3 - $CaO - MgO$ systems, showed a normalised slag composition of 40 wt% SiO_2,19 wt% Al_2O_3 (combined with MgO) and 41 wt% CaO, which lay within the pseudo-ternary phase field of "wollastonite - gehlenite – anorthite" where gehlenite was predicted to crystallise first. The detrimental mineralogical phase of larnite (dicalcium silicate) was avoided, and no compositional correction was required to ensure stability of the crystallised product. The phase diagram indicates that crystallisation begins at 1360 °C and ends at 1265 °C with the decomposition of the triple phase eutectic point. On the basis of the composition information supplied, the mineralogical phases present will be 68.3 wt% akermanite $Ca_2MgSi_2O_7$ (a solid solution of melilite $[(Na,Ca)_2(Mg,Al)(Si,Al)_2O_7)]$ with gehlenite), 24.6 wt% gehlenite and 7 wt% wollastonite. If crystallisation was incomplete the material would contain a vitreous phase, the extent of which was determined by kinetic factors rather than by purely thermodynamic ones. Additionally, cooling phase decomposition mechanisms were considered and examined. Viscosity measurements were taken to indicate the level of fluidity in the melt, as an indication of castability. Laboratory experiments indicated that

there was a crystalline crust formation at low temperature (900 °C) and that complete crystallisation occurred at 1000 °C, this was generally observed in all experimentation. Compositions containing manganese and copper oxides were light brown, those with cobalt were blue, and the specimen with chromium oxide had dark green areas on a light-green surface. Generally as sand additions were increased, the samples became lighter in colour.

The principal crystal phase in the castings, based on blast furnace slag, was melilite and limiting values of 85 – 90 % were obtained. Crystallite size varied from 0.2 – 0.5 to 1.5 – 2.0 μm. The morphologies present were described as skeleton, X-shaped, envelope shaped, skeleton-prismatic and spherulitic. The size and growth of melilite crystals and formation of the structure as a whole was dependent on the temperature and time crystallisation regimes of slag melts. The tile colour was dependent on the size of melilite crystals, e.g. blue tiles mainly had a fine grain structure. The addition of 12 wt% sand led to a 65 volume percent monoclinic pyroxene of the skeleton type; of 50 – 150 μm size crystallites evolved, the interstices were filled with melilite and pseudo-wollastonite with a lowered glass content. Increasing the sand content also gave rise to a refined microstructure with 5 – 7 μm pyroxene crystallites. An overview of the product properties are presented in Table 9.

Specimen Details	Density ($kg\ m^{-3}$)	TCLE* $10^{-7}\ °C^{-1}$	Mean Compressive Strength, (MPa)
Initial slag without crystallisation cooling in a muffle furnace	2770	91	81
Initial slag, crystallisation at 1050°C for 40 mins	2910	96	153
Initial slag + 12 Wt% SiO_2, crystallisation at 1050°C for 18 mins	2950	87	124
Initial slag + 12 Wt% SiO_2, crystallisation at 1150°C for 10 mins	2940	94	122
Initial slag + 18 Wt% SiO_2, crystallisation at 950°C cooling in a muffle furnace	2970	91	296

*Thermal coefficient of linear thermal expansion

Table 9: Physico-mechanical properties of five inorganic slag castings [23]

Thermal treatment of the initial slag gave rise to large improvements in properties, claimed to be due to ordering of the structure. The specimen with the highest compressive strength

had a very fine pyroxene microstructure. The strength of the material generated was found to be a strong function of the scale of the microstructure and the extent of crystallisation transformations, [23].

Rawlings of Imperial College London, (1997) produced a glass-ceramic named 'silceram' based on compositions within the CaO – MgO – Al_2O_3 –SiO_2 system. The compositions were again located in the pyroxene, β-wollastonite and anorthite phase field. Two specific bulk oxide compositions are reported in detail, SCR25 and SCF5, Table 10.

Species	SCF5	SC19-34	SCR25-76	SCR25-75
SiO_2	56.4	52.8	48.3	48.8
TiO_2	0.2	0.3	0.6	0.5
Al_2O_3	13.2	12.5	13.3	13.5
Cr_2O_3	0.7	0.8	0.8	1.0
Fe_2O_3	2.8	4.6	4.0	2.3
MnO	-	0.1	0.4	0.5
MgO	9.7	5.9	5.7	5.9
CaO	16.3	20.1	24.7	25.3
Na_2O	0.4	2.8	1.2	1,3
K_2O	0.4	0.1	1.1	1.0

Table 10: Composition (wt%) of the Silceram glass-ceramics investigated [24]

The materials were prepared form a range of natural and waste materials using the controlled-cooling heat treatment method. The wastes included iron blast furnace slag, colliery shale, pulverized fuel ash and minestone. Experimentation was conducted in a laboratory in the case of material SCF, and using a 50 – 100 kg batch pilot plant for the other compositions. SC19 was a purer equivalent of the SCR25's, which were produced from wastes. The nucleation process involved both Cr_2O_3 and Fe_2O_3, because of the claimed synergistic effect, when the oxides were used together. They formed slightly substituted magnesio-chromite spinels, which acted as preferential sites for nucleation and crystal growth, between 850 °C and 1150 °C with a maximum rate at 950 °C. Coarsening was noted at the upper end of the nucleation temperature window. Overlap of the assessed nucleation and growth rate curves allowed a single stage heat treatment to be employed at a temperature between 900 – 950 °C for 3 hours, followed by controlled furnace cooling. The pilot plant installation was an oil-fired tilting glass tank, capable of melting 100 kg with a melt depth of 5 to 10 cm. The furnace was continuously operated at 1450 °C and

tilted for occasional pouring of the melt. Oxygen partial pressures were varied to aid melting, but this had a negative simultaneous effect on the nucleation process. Conventional casting was used for shaping and samples were transferred to a heat treatment kiln for crystallization. The kiln programme varied with sample size due to heat transfer problems and the evolved heat of crystallization. The crystalline phase was found to be a pyroxene close to diopside, $CaMgSi_2O_6$. The physical properties of the glass ceramics are given in Table 11.

Property	Value
Density (kg m^{-3})	2900
Coefficient of linear thermal expansion (K^{-1})	7.5×10^{-6}
Thermal Conductivity ($Wm^{-1}K^{-1}$)	1.76
Youngs's modulus (GPa)	120
Hardness (GPa)	7 – 8
Flexural Strength (MPa)	90 – 130
Indentation Fracture Toughness (MPa $m^{1/2}$)	0.7 – 1.2

Table 11: Typical values of physical properties of Silceram glass-ceramic [24]

The work moved form the laboratory to a pilot plant scale. It did not assess environmental performance and melting tank performance, including the quality of the glass and refractory erosion problems. Finally the material physical property data does indicate improved material properties, but does not quantify statistical scatter and these are waste materials, [24].

Marghussian *et al,* (1998) examined the use of Iranian reverberatory furnace copper slag in the production of unglazed floor tiles. They examined the phenomenon of crystallisation using simultaneous thermal analysis (STA), dilatometry and X-ray diffraction techniques. It was observed that the addition of the slag to a standard floor tile blend was limited to about 40 wt%, due to the occurrence of SO_2 emissions at higher temperatures resulting in bloating, porosity and physical deformation. The most promising tile had 40 wt% additions of slag and was fired at 1025 °C for one hour. This gave rise to a bending strength of 57 MPa, water absorption of 2 wt% and a Vickers hardness value of 750 HV. This study focused on reaction sequences, phase composition developed and the physical properties of the fired product. Table 12 gives the composition of the main materials used.

Oxide	Copper Slag Wt%	Clay A Wt%	Clay B Wt%	Sand C Wt%	Sand D Wt%
SiO_2	40.97	49.8	64.0	74.6	97.5
Al_2O_3	3.78	27.6	15.8	9.8	1.0
Fe_2O_3*	44.78	9.2	1.8	1.5	0.2
TiO_2	0.58	-	-	0.2	-
CaO	5.24	1.7	5.6	3.2	0.5
MgO	1.16	0.6	2.0	0.3	-
Na_2O	0.3	1.4	0.9	3.3	-
K_2O	2.03	1.9	1.6	2.2	-
S	1.06	-	-	-	-
LOI	-	7.8	8.2	4.7	0.5

*The slag actually contained $FeO+Fe_2O_3$ which is repesented as Fe_20_3

Table 12: Chemical composition of the raw materials employed [25]

The base mixture employed comprised 50 wt% clay A, 15 wt% clay B, 15 wt% sand C and 20 wt% sand D, to which copper slag additions were made as shown, Table 13:

Body	% Slag	% Base body
A	0	100
B	20	80
C	40	60
D	60	40
E	80	20
F	100	0

Table 13: Composition of experimental bodies on a raw material basis (wt%), [25]

The materials were predominately of an aluminosilicate nature. All the material blends were examined in powdered form (~63 μm), then the powders were pressed into tiles of 50 x 50 x 5 mm using a hydraulic press. The tile samples were fired at 1000, 1025, 1050 and 1075 °C for 1 hr in an electric furnace at a rate of 5 °C min^{-1}. The slag was experimentally determined to melt at 1040 °C, which means that this processing regime, even though presented as a glass-ceramic route is more like a viscous phase sintering process, an observation not explained in the text of the paper. This ambiguity is exaggerated by the presence of a silica rich glassy phase through the presence of a silica related peak on the XRD traces. Bend strength determination was conducted using four point bend tests with a span of both 20 and 40 mm; hardness testing was also carried out using a Vickers testing machine. As expected, bend strength values were a maximum at

the firing temperature giving the lowest water absorption and shrinkage. The material transformation and densification process was further complicated by the appearance of a fayalite ($2FeO.SiO_2$) peak on the XRD traces which disappeared at 600 – 1000 °C. Bloating was attributed to SO_2 formation, [25].

Gao *et al* (1999) at Ohio State University successfully generated glass ceramic materials from vitrified industrial wastes. The formulations employed maximised the incorporation of hazardous wastes, including both spent foundry sand and electric arc furnace dust which together made up a total of 73 wt% of the pre-calcined furnace charge. These waste materials did not exhibit a significant variation in composition or physical form, as they arose from industrial processes, subject to process control. The work was laboratory based, using 40 gram samples, and focused on the thermal analysis of the nucleation and growth of crystalline phases as a result of heat treatment. The two phases identified included a spinel solid solution and a meta-silicate augite ($CaMg(SiO_3)_2$), of crystallite size was 0.5 – 1.0 μm. The high hardness of the crystalline phase was claimed to increase the hardness to 620 kgf mm^{-2} and increase the fracture toughness of the product material. The addition of TiO_2 nucleating agents (< 5 wt%) and the use of heat treatment schedule variations were observed to have a significant effect on the morphological features of the glass-ceramic microstructure resulting in variation in the shape and volume fraction of phases. The product is claimed to have applications equivalent to high standard abrasive. The sample composition, based on a completely calcined basis, is given in Table 14.

Component	Composition (wt%)
SiO_2	33.36
Fe_2O_3*	24.25
MgO	11.45
Al_2O_3	9.81
CaO	9.01
ZnO	6.59
Cr_2O_3	3.58
PbO	1.21
Na_2O	0.63
MnO	0.10

Table 14: Sample composition on a flashed oxide basis, [8]

Samples were melted at 1500 °C for 2 hours and quenched for DTA analysis. The as-quench samples were annealed at ten selected temperature between 580 – 675 °C and DTA

was performed to temperatures up to 1250 °C. The temperature at which the nucleation rate peaked was determined to be 635 °C. The most important information is associated with the evaluation of TiO_2 as a nucleating agent. Electron micrographs show the effect of increasing TiO_2 additions on the XRD trace of the crystallised material. The distinct changes observed are confirmed when the electron micrographs are examined. The morphological features of the microstructure are changed completely and the structure is finer [8].

Berzina *et al,* (1999) at the Riga Technical University in Latvia researched the generation of environmentally friendly glass ceramic materials from metallurgical waste. Over 40 blends containing 100% wastes were considered; the blends were generated from peat ash, metallurgical slag, fly ash and cullet. XRD indicated that calcite, siderite, gehlenite, hemantite, larnite were present in the metallurgical slag, and spinel and sphalerite in the fly ash. The structure and properties of the resulting materials were systematically investigated. Glass-ceramic materials were generated from all of the wastes, the technologically valuable properties ranged from 0.14 - 3.23 wt% water uptake, with final densities of 2.60 – 3.05 gcm^{-3} and flexural strengths of 80 – 96 MPa. Here the most desirable properties were only produced with virgin material additions. The research indicated that it was only possible to generate useful products from waste materials using clay additions. This probably relates to the quantity of network forming oxides and the kinetic stability of the glassy phase. The work was laboratory based and on a small scale, [26].

To summarise all the papers relating to metallurgical wastes; the literature presents several examples where solid-state material transformation have been employed to successfully enhance the properties of the waste materials. The extent of improvement allows performance that is equivalent and beyond those of current industrially accepted products. The glass-ceramic route has been successfully employed in a variety of different ways; the use of nucleating agent has been successful in improving material properties. The results indicate that control at each stage of the process i.e. from batch preparation to final heat treatment and cooling, are important in defining the properties of the product. This in itself justifies the approach and topics covered in the context of this research.

3.3.2 Contaminated Soils

Rozenstrauha *et al* (2002) at the 7th Conference of the European Ceramics Society presented a new approach to waste treatment, combining composite materials science and waste material sintering. Here the wastes were blended with a reinforcing phase of clay and alumina platelets, however, the alumina platelets are quoted as having a density greater than the theoretical density. The secondary phase improved mechanical properties and broadened the sintering temperature interval, improving processing tolerance in relation to conventional industrial ceramic processing technology. The waste materials were employed as a sintering aid as they formed low temperature liquid phases. The material blends employed ranged from fly ash (10 – 30 wt%), peat ash (70 – 90 wt%), carbon free clay (20 wt%), to constitute a contaminated soil, since in addition to the base oxide constituents of the materials, the fly ash contained heavy metals. These toxic species were claimed to reside within the glass matrix, such that the leaching characteristics met the requirements for dense un-glazed pressed ceramic tiles (DIN EN 106). Milled powder blends were prepared with different levels of reinforcing phases at 10 wt%, 20 wt% and 30 wt% levels and also equivalent mass fractions of waste glass. DTA was used to assess thermal changes and the sintering behaviour of the prepared batches to define sintering parameters. Sintering temperatures of 1000 – 1200 °C were employed for durations of 60 minutes. The highest densities were achieved with an optimal 20 wt% alumina platelet addition at a sintering temperature of 1050 – 1070 °C, this was accompanied by a failure strength of 96.5 MPa, distinctly higher than the 54.5 MPa associated with the equivalent waste glass sample. The micrographs revealed irregular distributions of the reinforcing phases. The products were defined as being suitable for street tiles, floor tile and exterior tiles, confirming that processed wastes are viable for construction material applications, [27].

Tuan *et al,* (1996) considered the topic of in-situ soil vitirification (ISV), a process developed by the Battelle Memorial Institute's Pacific Northwest Laboratories (PNL) in the mid 1980's. The ISV process is claimed to transform contaminated soils into a glass-like material with a wide range of desirable properties that are unaffected by wet-dry or freeze thaw cycles. The materials tested include silty sand, clay and beach sand. Hence potential applications for the technology are slope stabilisation, groundwater removal, contaminated material stabilisation and the production of construction materials. This work is unusual as it was undertaken on a prototype scale using a single 100 kW or

240 kW non-transferred plasma torch, supplied by Plasma Energy Corporation (PEC). Material treatment temperatures were claimed to be in excess of 4000 °C, however the usefulness of such high temperatures in relation to the application described must be questioned, as the materials are not thermally stable at these temperatures. The use of a non-transferred plasma torches, would firstly have a negative effect on the efficiency and economics of the process, as it is a water-cooled device and, secondly, the process temperature delivered would not stabilize, but vaporise the material being heated. This brings into question the accuracy of the data.

Samples were taken from the vitrified materials processed into 5.1 cm diameter cylinders. The advances claimed in the process were associated with the increased heat fluxes, obtained through the use of water-cooled torches. This resulted in a shorter treatment time and a faster overall ISV process. This point is made as the research is aimed at addressing the US Air force mission needs for rapid runway construction or repair work. A 60 cm diameter, 90 cm high steel chamber was used to contain the test soil, the chamber being modular to allow easy retrieval of the vitrified monolith. The bulk of the vessel was refractory so that the active volume was only 7.6 cm in diameter and 15.2 cm thick. The images of the vitrified product presented show poor quality and in-homogeneity, as material properties and heat transfer would appear to have been neglected, this is reinforced by the fact that the paper indicates that the ceramic samples contained a number of hairline cracks and voids. Material characterisation results indicated that the elastic modulus was approximately 50 – 78 GPa and the compressive strength varied from 20 – 120 MPa. This represents a large material property range and indicates a high level of sample heterogeneity. The bulky nature of the ancillary equipment has not been addressed if the technology is to be used in military contingency situation, [28].

3.3.3 Low Level Radioactive Waste (LLRW)

Tzeng *et al,* (1998) reported the generation of a glassy slag with very low leaching characteristics from the processing of simulated calcium aluminosilicate radioactive wastes by plasma torch treatment. Glass and glass-ceramic slags of high quality were generated, and compositions were varied slightly. The compressive strengths of these slags are reported to exceed 125 MPa, the density of the slag is 2.75 to 3.1 g cm^{-3} and leaching indices were very low indicating that the cationic releases were low, ranging from $8.7x10^{-5}$ to $2.0x10^{-8}$ g cm^{-2} day^{-1} and was element sensitive. The surrogate wastes evolved from a

mixture of feldspar powder, polyethylene bottles and iron cans. The product had a black colouration and a vitreous lustre. X-ray diffraction investigation indicated an amorphous structure for most products. Some crystallisation was observed using X-ray diffraction investigations and anorthite and wollastonite phases were reported, [29].

Hoffelner *et al,* (1998) applied transferred DC plasma technology to the treatment of beta/gamma LLRW. By an appropriate control of oxidation potential, analysis indicates that up to 99% of the total radioactive isotopes remained in the melt, [30].

3.3.4 Heavy Metal Laden Wastes

Bernard *et al,* (1999) used a laboratory sized plasma reactor with a power level below 30 kW, which is low for an atmospheric plasma device. Material was contained in a graphite crucible located in a water-cooled controlled atmosphere chamber and the system was powered using a transferred arc plasma torch with argon stabilising gas. Here zeolite matrix material, with a composition of 87 wt% SiO_2 and 13 wt% Al_2O_3, was impregnated by chlorides, sulphates and nitrates corresponding to 2.5 – 7.5 wt% of volatile heavy metals such as lead and zinc. The impregnation of the material was facilitated by the porous structure of the zeolite. An Inductively Coupled Plasma (ICP) analysis system was used to monitor metal evaporation on line and monitor the composition of the off-gas generated continuously once steady state conditions were achieved. The aim of the work was to investigate the phase partitioning (volatilisation) of the heavy metals and quantitatively define the kinetics of reaction. The empirical observations indicated that the metal concentration decreased exponentially as treatment time increased for 5 wt% initial concentrations. This meant that metal concentrations could be reduced rapidly by two orders of magnitude in 4 – 5 minutes, but the remaining metal required more time to be evaporated. The main result of the experimentation is that plasma arc vitrification is a very useful and compatible tool [31]. This paper advocates the use of plasma technology through exploitation of input power manipulation independent of process chemistry, essential to control the phase partitioning of the heavy metals.

Cortez *et al,* (1996) developed a batch mode laboratory scale plasma arc furnace located at the University of Illinois. Their work focussed on the characterisation of the arising effluent waste streams. Real-time process data, dust samples and slag specimens were taken from each trial for comparative purposes. Experiments were conducted on nickel

and chromium laden surrogate wastes. The surrogate waste material was made up of a blend of 10 wt% metallic powder in a clay matrix (55.10 wt% SiO_2, 39.11 wt% Al_2O_3). Elemental volatility was examined as a function of oxygen partial pressure. Oxidising conditions reduced the total dust gathered for both nickel and chromium samples but dust samples were found to be metal enriched. Plasma treatment increased the leach-resistance of the slags by at least one order of magnitude as compared with the unprocessed waste samples. Energy Dispersive X-ray analysis and the Toxicity Characterisation Leaching Procedure (TCLP) analysis, were conducted on the slag specimens, [4]. The TCLP test is a leaching test performed on ground material samples that are exposed to acidified water and agitated.

Geimer *et al,* (1993) used the Plasma Hearth Process (PHP) for the treatment of heavy metal laden waste streams. The system focuses on the planned remediation of the Idaho National Engineering Laboratory (INEL) Sub Surface Disposal Area. The products were subjected to the Toxicity Characterisation Leaching Procedure (TCLP), which indicated that there was some lead and chromium present, but at acceptable levels. No units were given in respect to the tabulated leaching data. The line of investigation was extended to the Product Consistency Test (PCT), which indicated long-term stability by subjecting pulverised sample to seven days immersed in water at 90 °C, no glass forming additives were used in this work. All the product analysis work focussed on the acceptance of the product for ultimate disposal. The level of unconverted carbon was used to gauge the effectiveness of the heat treatment process; levels were commonly in the 1-2 wt% carbon region, [32]. As the carbon content of the treated material is relatively high the effectiveness of the process is low.

3.3.5 Municipal Solid Wastes (MSW) Ashes

M Hernandez-Crespo in collaboration with J Rincon and M Romero (2002) conducted additional research into a process for obtaining stoneware tiles from the recycling of granite and MSW incinerator fly ash using a sintering route. The product is described as Porcelainized stoneware (PS) which is a body densified in a vitreous state with almost zero residual porosity. Fly ash was employed in the research as it is contaminated with toxic heavy metals and trace organic pollutants, and the aim was to render the products environmentally benign. Here the fly ash was combined with granite machining residues, and the main objective of the research was to determine the chemical and mineralogical

composition of the final products and their physical and mechanical properties. The raw material compositions are presented in Table 15.

Species	Mud B	Mud C	Fly Ash	Clay	Industrial Feldspar
	Granite Muds				
SiO_2	74.85	65.20	13.10	64.01	70.21
Al_2O_3	13.50	11.85	14.00	31.49	16.63
Fe_2O_3	1.13	11.66	1.40	1.18	0.06
CaO	1.02	2.73	62.00	0.25	0.55
TiO_2	0.11	0.12	-	0.50	0.55
MnO_2	0.05	0.11	-	-	-
K_2O	4.77	4.29	2.60	1.86	10.26
Na_2O	3.40	3.06	4.60	0.29	2.30
MgO	0.23	0.31	2.40	0.41	0.06
Cl^-	-	-	15.26	-	-
P_2O_5	0.05	0.22	-	-	-

Table 15: Chemical composition (wt%) of the wastes and raw materials employed in the research for compositional blending, [33]

XRD analysis of the feedstock showed that the muds contained the mineral phases of α-quartz, albite and orthoclase. The fly ash contained $CaCO_3$, $Ca(OH)_2$, NaCl and $CaSO_4$ as well as feldspar anorthite. The materials were blended to obtain an oxide ratio of SiO_2/Al_2O_3 of 3.4. The as-blended materials were pressed at 40 MPa and heat-treated for 45 minutes at 1200-1230 °C. The sintering curves were determined from linear shrinkage measurements and water absorption measurement, both as a function of firing temperature. Good inter-technique correlation was obtained and changes were attributed to physical and phase transformations. Properties obtained were Vickers micro-hardness (H_v) values of 6.1 - 6.7 GPa, elastic moduli of 106 – 227 GPa and fracture toughness values of 2.3 – 2.5 MPa $m^{1/2}$, which are both high, and the density of the products ranged from 2130 – 2730 kg m^{-3}. The approach was significantly different from the vitrification route investigated extensively within the literature as sintering was employed to achieve densification, however the results advocate the glass-ceramic route for the processing of waste materials, as the properties are quoted as 'equivalent value properties to those of commercial products'. The paper does not attempt to address the most intrinsic material preparation barrier of a 'powder process', which is usually associated with more predictable processing material systems. This is significant problem in the context of the waste's physical form and the required treatment rates. The approach would not cope with

a diverse waste stream, however the concept of using different wastes as blending agents is attractive as it obviates the requirement for pure materials, [33].

Boccaccini and Rawlings, (2002) reviewed the importance of silicate residues in the recycling and reuse of industrial wastes. They referred to both bottom ash and fly ash from waste incinerators. They indicated that the main barrier to the acquisition of a cost effective and justified recycling route for these materials lies in the requirement to produce high-quality products that are of commercial viability. Here the limitations of conventional vitrification, were described as an energy intensive costly process that produces a low quality product. They clarified this statement, stating that the products should be competitive in application on a commercial basis. Focus was placed on the glass-ceramic route as an effective means of improving product properties without major alterations to the primary vitrification process, there the Silceram product developed in the 1970s and 1980s was used as an example [24]. They discussed the different routes available for the preparation of glass-ceramics from waste streams and typical material properties that can be obtained, this is extended through discussion focussing on secondary reinforcing phases such as SiC fibres and TiC particulates. The compositions of the waste materials employed in the research are given in Table 16.

Species	Incinerator Fly Ash	Coal Fly Ash
SiO_2	38.0	31.0
Na_2O	3.5	-
CaO	21.1	4.0
Al_2O_3	17.5	11.4
Fe_2O_3	8.0	43.5
ZnO	3.5	1.4
MgO	2.4	1.3
Cr_2O_3	-	0.9
TiO_2	1.7	2.3
K_2O	1.8	-
MnO	0.4	-
P_2O_5	1.6	-

Table 16: Chemical composition (wt%) of the coal ash and incinerator fly ash [34]

The mechanical properties quoted have a broad magnitude span and included flexural strengths ranging from 79 – 240 MPa, Young's moduli of 63 – 124 GPa and indentation fracture toughness values ranging from 0.5 – 1.7 MPa $m^{1/2}$. The bulk glass-ceramic

exhibits the most attractive values in all of the mechanical properties, unfortunately the values are not quoted in relation to a sample size or testing protocol. The results reinforce the advantages offered through the transformation of a vitrified product into a glass-ceramic product. Typical applications for the material include floors for industrial buildings and facings for buildings. In the future the group will address the issues of environmental chemical durability and 'toxic potential' which are essential if public acceptance is to be obtained and will enable exploitation [34]. The paper fails to appreciate the limitation of commercialised vitrification technology as a means of producing a high quality glass product, i.e. degassing and homogenisation are not purposely undertaken, which is essential for a viable glass-ceramic processing route.

Barbieri *et al,* (1999) investigated the melting of alkaline / alkaline-earth silicate glasses and glass ceramics. This was achieved at 1500 °C in a refractory crucible by introducing 10 and 50 wt% steel plant fly ash into a glass-cullet, a generic term used to describe waste glass, municipal incinerator slag and a diopside-anorthite glass ceramic. The glasses were quenched in air and then annealed by holding at temperatures close to the glass transition temperature for one hour, followed by slow cooling to room temperature. The higher additions of steel plant fly ash caused instability in the glassy phase through the formation of iron phases in the material obtained after melting. These phases increased the propensity for crystallisation to occur as shown through variations in the crystallisation temperature (T_c). Systematic characterisation was only performed on the completely amorphous products. A summary of the results is given in Table 17. The steel plant fly ash increased the tendency for crystallisation and reduced the glass transition and crystallisation temperatures of the municipal incinerator slag series because of the nucleating effect of iron. For the glass-ceramic the substitution of 10 wt% steel plant dust made the glass less viscous because the overall SiO_2 and Al_2O_3 content decreased, favouring the formation of crystalline phases at lower temperatures. The identity of the crystalline phases evolved from the parent glass, was a very strong function of its composition, but pyroxene (diopside and/or augite) was the most thermodynamically favoured phase. Material resistance/durability towards water, under both acid and alkali conditions was also considered. The overall conclusion was that vitrification followed by de-vitrification is a viable route for inorganic waste treatment [14].

Parameter	$T_{g\ (DTA/DSC)}$ °C	$T_{c\ (DTA)}$ °C	$T_{s(DIL)}$ °C	$\alpha_{100-500}$ 10^{-7} °C^{-1}	Hv (kg/mm^2)	Main crystalline phase
100wt% Cullet	540 / 556	None	623	109	6.2	None
90wt% Cullet 10wt% Steel Plant Ash	547/560	807	653	103	6.6	D+M+W
50wt% Cullet 50wt% Steel Plant Ash	560/551	748	607	108	-	-
100% MSW Slag	648/633	937	702	90	6.2	W+A+D+Au
90% MSW Slag 10wt% Steel Plant Ash	635/633	871	716	92	7.1	D+AU+M+Ma+F
50% MSW Slag 50wt% Steel Plant Ash	640/653	865	716	91	-	-
100 wt% diopside-anorthite glass ceramic	720/745	932	814	80	6.6	D+A
90 wt% diopside-anorthite glass ceramic 10wt% Steel Plant Ash	685/707	889	775	79	6.0	D+Au+A
50 wt diopside-anorthite glass ceramic 50wt% Steel Plant Ash	620/640	807	750	78	-	-

A=Anorthite [$(Ca,Na)(Si,Al)_4O_8$]; Au = Augite[$Ca(Fe,Mg)Si_2O_6$]; D = Diopside [$Ca(Mg,Al)(Si,Al)_2O_6$]; F = franklinite [$ZnFe_2O_4$]; M = magnetite [Fe_3O_4]; W = wollastonite [$CaSiO_3$].

Table 17: The thermal, physical and mechanical properties of the glasses studied and the main crystalline phases evolved as a glass ceramic [14].

Menzler *et al,* (1999) conducted work focussing on the two specific glass compositions for the vitrification of toxic products resulting from MSW incineration, e.g. the fly ashes. The work incorporates the formation of stable glasses through the addition of network forming oxides to the incineration ashes, followed by vitrification and leaching characterisation. They describe the legislation driven nature of the work, making particular reference to the 'Closed Substance and Waste Management Act', however the paper treats waste treatment by-products as non-recyclable. This is the opinion that this research aims to invalidate. The research indicates that thermal treatment is a growing component of the waste management industry. The MCC-IP leaching test was used, which is of a long-term predictive nature. The parameters varied in the experimentation were composition, temperature, time and leaching solution. Again all of the test work was conducted on a laboratory scale. The composition of the as-blended glasses is given in Table 18.

Species	Glass 56 (as batch)	Glass 63 (as batch)
SiO_2	56.13	66.62
Na_2O	15.0	13.30
CaO	7.0	4.45
Al_2O_3	6.0	3.17
Fe_2O_3	5.0	3.08
PbO	4.0	0.78
ZnO	3.5	1.85
MgO	2.0	1.08
CuO	0.8	0.24
Cr_2O_3	0.5	0.20
CdO	0.05	-
NiO	0.02	-
TiO_2	-	3.51
K_2O	-	0.89
MnO	-	0.12
BaO	-	0.70
Σ heavy metals	8.87	6.70

Table 18: Waste glass composition as oxides (wt%), [35]

Glass 63 is similar to that successfully used in previous experiments, glass 56 is higher in the level of heavy metals and lower in the amount of network formers, and could be predicted to be less stable. Glass 63 is used in the nuclear industry in France, Japan, USA and Germany, glass 56 is used in Germany for the vitrification of fly ash. Both glasses were melted in alumina crucibles at 1400 °C for 2 hours, upon solidification the samples were sectioned using diamond tooling to 1 x 1 x 0.1 cm and polished to allow surface control. Unfortunately the 'time at temperature' and assimilation of the containment material were not considered, hence the resulting glass composition was likely to vary significantly from that of the initial starting material.

The samples were immersed in water for between 1 and 91 days at 40 –120 °C. Both acidic and alkaline conditions were covered using buffer control and each test was conducted in triplicate. Weight loss data are presented and generally showed an increase in loss with both time and temperature. However, there was a threshold temperature at which the process became active. The affected surface layer was observed to be under tensile loading and de-lamination occurred at a critical thickness, [35].

Romero *et al*, (1998) conducted a study to assess the feasibility of recycling the solid residues from Spanish municipal waste incineration by producing a glass-ceramic. The main components of the inorganic waste form SiO_2, CaO and Al_2O_3 but nucleating agents, such as TiO_2, P_2O_5 and Fe_2O_3 were also present. They were able to manufacture a stable glassy phase by mixing 65 wt% ash with 35 wt% cullet. This is a very large addition of modifying material to ensure a controlled crystallisation sequences.

The optimum heat treatment schedule was determined to be 560 °C for 35 mins followed by crystal growth at 1000 °C for 120 mins, derived from examining the nucleation and crystallisation sequence in detail. The glass transition temperature of the material was determined to be 750 °C.

The semi-crystalline material contained several phases including clinoenstatite ($MgSiO_3$), the most stable phase, which possibly could have been a pyroxene phase that incorporated Ca, Mg and Al in its composition, and akermanite ($Ca_2MgSi_2O_7$). Again the microstructure was observed to contain both fibre-like and dendritic crystals, as in the case of several other studies. The compositional characteristics of the waste material and cullet used in the experimentation are given in Table 19.

Species	Waste Ash	Waste glass	Optimum blend (35 wt% cullet)
CaO	44.0	10.89	32.41
SiO_2	5.5	72.47	28.94
Al_2O_3	3.4	1.77	2.83
Fe_2O_3	0.7	1.19	0.87
MgO	1.5	1.30	1.43
Na_2O	3.7	12.38	6.74
K_2O	2.9	0.84	2.18
P_2O_5	0.8	0.02	0.53
TiO_2	0.5	0.08	0.35
ZnO	0.65	0.01	0.43
L.O.I	29.3	-	19.05

Table 19: Chemical analysis (wt%) of the waste ashes and waste glass as determined by ICPOES method, [36]

Mixing the two components in varying proportions, and melting these blends at 1500 °C for 30 minutes, produced different results. This is a very short melting interval, as only

limited homogenisation would have been observed in this time, additionally material sampling and pre-treatment was not considered. However, stable glasses were claimed to be produced with sufficiently low viscosities and melting temperatures.

As the proportion of cullet, used in the melt blends, was reduced, the resulting material became too refractory and crystallisation was generally unavoidable. The optimum material composition used incorporated 35 wt% of cullet, the overall composition being given in Table 19.

The glass melts were poured onto a metal plate and held at 600 °C for 2 hours then slowly cooled to room temperature. Some additional samples were quenched in water to examine the effect of cooling rate on crystallisation, which indicated that cooling rate had limited effect on the crystallisation process.

A thermal approach was used to estimate the optimum temperatures and times for both nucleation and crystallisation. Variations in crystallisation temperature with material physical size were taken to indicate that surface crystallisation predominated in the finer material, however the heat transfer mechanism and the time dependence in obtaining steady state thermal conditions were not considered, i.e. temperatures of transformation increased with increasing particulate size. The crystallisation process was evaluated using X-ray diffraction data, which is an indirect form of evaluation, as the microstructural features evolved were not considered in terms of frequency size and distribution. Hence, the statements made cannot be considered as a definitive assessment for enhancing the material properties. Crystallisation resulted in the surface growth of $CaSiO_4$ and bulk crystallisation occurred with a fibre-like morphology; the length of the fibres was 200 μm and the width of the crystals was 2 - 7 μm. In some areas there was a well defined dendritic structure. The crystallisation process resulted in diffusion of material to the crystalline areas and a rejection of the foreign species into the glassy matrix. Again there was ambiguity between the XRD and SEM-EDX results which indicates that solid solutions could be present, for example instead of $MgSiO_4$, a pyroxene phase was suggested, such as augite ($CaMg(SiO_3)_2$+$(Mg,Fe)(Al,Fe)_2SiO_3$). Limited mechanical property evaluation was undertaken but the fracture toughness was claimed to be 1.5 $MPa.m^{0.5}$ [36]. The experimentation was based on a laboratory evaluation of these

materials, and was of a scientific nature, no emphasis was placed on material forming or the end product specifications.

Shawn *et al,* (1995) investigated the processing of a range of inorganic wastes, which were made up of magnesia, silica, calcia, alumina and iron oxide. Composition adjustments were made to allow for the evolution of specific phases and melting in the range of 1400 – 1465 °C. The glasses were cast into graphite crucibles and annealed. The samples were crystallised at 975 – 1000 °C forming enstatite, forsterite, hercynite, magnesioferrite and pseudobrookite. Micrographs of the formed material indicated that phase separation occurred at 850 °C with crystal growth occurring from 'droplet' like precipitates. Optimum conditions were claimed to give rise to a uniform microstructure with low porosity. Higher melting temperature materials were claimed to give rise to easier processing through limited adhesion of the slag to refractories, which is probably due to physical wetting contact defined by heat transfer. The work did not address the problems of refractory deterioration, which would alter material composition. The compositions of the main wastes employed are presented in Table 20. These waste material compositions were subsequently individually adjusted to lie in the cordierite - enstatite - forsterite phase eutectic triple point at 1360 °C.

Constituent*	Slag (wt%)	Baghouse Dust (wt%)	Filtercake solid (wt%)
CaO	1.73	1.66	1.63
MgO	49.68	37.09	1.92
Al_2O_3	2.34	1.99	6.24
Fe_2O_3	3.12	2.74	2.14
TiO_2	2.48	3.10	0.29
SiO_2	5.68	5.33	82.48
P_2O_5	18.68	16.95	0.61
Na_2O	11.44	21.70	3.82
K_2O	4.65	9.44	0.86

* Trace element details were also given.

Table 20: Chemical composition of the waste materials employed [37]

Attempts were made to modify the base glass by the addition of TiO_2 to enhance nucleation. This adjustment resulted in the overall batches being only 45 wt% waste in total, i.e. more virgin material was used in preference to waste materials. The batches were 100 grams each, melted in a silica crucible using a retractable hearth furnace. Material was added to the furnace until they were three quarters full, then they were allowed to

homogenise for one hour. This meant that the overall residence time in the crucible was high and compositional modifications would be likely. The resulting melts were discharged onto a graphite mould at 450 °C and annealed at a temperature of 550 – 700 °C for eight hours to relieve the casting stresses.

XRD gave evidence of a nucleation phenomenon at 600 °C and crystallisation at 900 – 1000 °C. The phases evolved have already been summarised. The densities of the resulting materials are given in Table 21, showing an increase in density after crystallisation.

Composition	Glass Specimen ($kg\ m^{-3}$)	Recrystallised Specimen ($kg\ m^{-3}$)
Slag	2650	2790
Baghouse Dust	2600	2690
Filtercake	2710	2790
Mixture	2650	2690

Table 21: Average densities of the glass and crystallised specimens [37]

Only the slag and bag-house dust samples showed mechanical improvements in the crystalline state relative to the glassy state. The slag had a glassy compressive strength of 79.3 MPa, which increased to 114.6 MPa in the crystallised state, [37].

Chapman *et al,* (1995) plasma treated both MSW and sewage sludge waste (SSW) with three different DC twin arc plasma reactor configurations. The work focused on the demonstration of ash melting plasma reactors to generate non-toxic slag products, thermal destruction of persistent organic species and to provide information for scale up of the process. The test work demonstrated the flux-less melting of the ashes and the vitreous slags produced were environmentally safe. The MSW ashes used were shown to contain quantities of persistent organics (i.e. dioxins and furans). The plasma reactor processes reduced the level of these persistent organics to $< 0.1\ ng\ g^{-1}$. The process was successfully scaled up to pilot plant operation ($200 – 300\ kg\ hr^{-1}$). Table 22 gives the chemical analysis of the ashes used.

Species	MSW Feed (grate ash)	MSW Slag (grate ash)	MSW feed (fly ash)	MSW slag (fly ash)	SSW feed (fluidised bed)	SSW slag (fluidised bed)
Bulk Oxides / Wt%						
SiO_2	47.0	50.5	26.0	42.0	46.0	46.0
TiO_2	1.0	1.0	1.8	2.4	1.0	1.0
Al_2O_3	9.8	12.0	13.0	17.3	15.0	15.0
Fe_2O_3	11.5	12.0	3.5	3.5	10.5	11.5
MnO	0.1	0.1	0.1	0.2	0.1	0.1
MgO	0.2	2.0	2.2	3.0	2.1	2.1
CaO	13.0	13.5	21.8	26.1	8.0	8.0
P_2O_5	1.0	1.0	1.5	1.5	10.0	10.0
Total C	3.0	0.5	2.5	<0.1	1.0	1.0
Na_2O	4.5	4.5	3.1	1.9	1.0	1.0
K_2O	1.5	1.0	3.1	1.3	2.0	2.0
Trace Metals / ppm						
Mn	950	950	880	1000	1050	1000
Cr	250	240	100	550	1500	1400
Ni	160	160	50	130	115	120
Cu	5600	5800	660	400	750	750
As	40	40	90	150	70	36
Cd	15	<1.0	150	<1.0	3	<1.0
Zn	4000	600	6400	1300	3750	2600
Pb	2450	110	2740	<1.0	850	200
Chlorides	3400	70	28628	130	60	25
Flourides	7.5	<1.0	5.0	<1.0	1.5	<1.0
Sulphates	2075	1500	6712	4000	2360	600
Organics / ppb						
Solvent Extract	5000	<50	800	<50	110	<50
Phenol	2.5	<0.1	0.5	<0.1	0.5	<0.1

Table 22: Feed and slag analysis from the plasma treatment of MSW and SSW ashes [38]

The material products were not subjected to physical or mechanical testing, the experimentation only characterised the material in terms of environmental stability. Leaching characterisation indicated that all slags were environmentally stable when tested in accordance with the DIN 38414 S4 (R3) leaching method. The leachate data for the MSW fly ash for both the feed material and associated slag product are shown in Table 23. The table also includes the guidelines for eluate limits for hazardous and inert wastes as proposed by the EC draft landfill directive. A distinct improvement in product conformity is noted upon plasma treatment, [38].

Species	MSW* Feed Fly Ash (mg/l)	MSW Slag Product (mg/l)	Proposed EC Directive	
			Hazardous Waste Range (mg/l)	Inert Waste Range (mg/l)
Ar	0.15	<0.05	0.2 – 1.0	<0.1
Pb	4.81	<0.05	0.4 – 2.0	Total < 5
Cd	0.15	<0.05	0.1 – 0.5	
Cr	0.64	<0.05	0.1 – 0.5	
Cu	0.11	<0.05	2 – 10	
Ni	<0.05	<0.05	0.4 – 2.0	
Hg	<0.05	<0.05	0.02 – 0.1	
Zn	0.5	<0.05	2 – 10	
Phenols	0.2	<0.01	20 – 100	<10

* maximum levels

Table 23: DIN 38414 leachate standard test results [38]

Suzuki *et al,* (1991) filed a patent based around the treatment of sludge and municipal solid waste materials. In this work melting, rapid cooling and subsequent annealing of glass like materials was used to generate a product with a specific microstructure. This microstructure contained needle shaped crystals of anorthite ($CaO.Al_2O_3.2SiO_2$) and β-wollastonite ($CaO.SiO_2$) in a vitreous matrix. The product was claimed to have superior mechanical and aesthetic properties to that of naturally occurring equivalents. The stages of the process covered in the patent are feed composition adjustment and the allowable bands of composition are given in Table 24. The basicity criteria employed ensured the fluidity of the melt for casting. The ranges presented are based on the molecular formulae of the mineralogical phases developed and the practical processing limits imposed by the equipment.

Species	Waste Compositional Ranges (wt%)	Typical Waste Starting Composition (wt%)
SiO_2	35 – 55	40.72
Al_2O_3	5 – 20	14.80
Fe_2O_3	2 – 15	9.56
CaO	5 – 30	8.24
MgO	-	2.97
P_2O_5	-	12.97
Na_2O	-	1.25
K_2O	-	1.44
C	0.2 – 5	Sum = 8.05
S	0.2 – 6	

Table 24: Glass compositional adjustment ranges [39]

Degassing at 1200 – 1400 °C, then cooling into a glassy state followed melting at 1300 – 1500 °C was employed. No reference was made to heat transfer and thermal stress at this point or subsequently for the crystallisation process. The patent is specific as reference is given to a specific XRD trace and thermal expansion curves. Nucleation was accomplished by holding the vitreous material at 800 – 900 °C for longer than 15 mins to allow FeS to precipitate colloidally. Crystallisation occurred between 1000 – 1200 °C. After crystallisation 40 – 60 vol% of the vitreous constituents were retained. The role of carbon is indicated to encourage the development of sulphide species as opposed to sulphate species in the nucleation phase of the process. Generally, it is observed that crystallised materials that contain wollastonite, as opposed to anorthite, had superior mechanical properties. Examples are given of flexural strength in the range of 65 – 73 MPa and Mohs' hardness in the range 6.5 – 7.0.

The invention relates specifically to the production of crystallised glass from waste materials, and builds on the current aggregate production technology available worldwide at the time of publication, i.e. aggregate quenching in water baths and globalisation and slag casting into moulds without controlled crystallisation. The work emphasises the importance of having bulk, as opposed to surface specific, crystal growth. In essence the invention is claimed to generate a high-grade building material from a waste, [39].

3.3.6 Sewage Sludge Waste (SSW)

Ekonomakou *et al,* (2002) investigated the use of water works sludge as a precursor for producing ceramic products (bricks). The material was described as a sludge containing solid, organic matter, chemicals and flocculants. The work has been driven by the increasing awareness of the EU of the requirements for an acceptable long-term disposal methodology for sludges, other than discharge at sea. The work characterised the properties of the sludge, and investigated its use as a recycled additive for building bricks. The influence of fractional sludge additions on both the physical and mechanical properties were determined. The sludge was substituted at the 10 wt% level, for the clays which contain on average 60 wt% SiO_2, 20 wt% Al_2O_3, 5 wt% Fe_2O_3 and 8 wt% CaO. The blends employed are described in Table 25.

Raw Material (%)	Mix A	Mix B	Mix C	Mix D	Mix E
Extruded Mix	-	-	-	-	-
Aspropyrgos Sludge	-	10	-	10	-
Galatsi Sludge	-	-	10	-	10
Clay No 1	35	25	25	35	35
Clay No 2	26	26	26	26	26
Clay No 4	15	15	15	5	5
Clay No 6	24	24	24	24	24

Table 25: Batch mixing specifications for roof tile blends [40]

The waste sludge compositions were examined for a period of one year and significant variations were noted. Confusingly, there is a significant amount of alumina present in the material but the mineralogical analysis did not show the presence of any crystalline aluminium compounds (it was claimed to be present as a colloidal amorphous suspension), nor can it explain the high loss-on-ignition. All specimens were dried at 110 °C for 24 hours and then heated at a rate of 250 °C hr^{-1} to 930 °C and held at temperature for 2 hours. The unfired specimens were characterized in terms of dry shrinkage and the sintered specimens were characterized in terms of mineralogical phase by XRD, density and three point bending strength. Unfortunately, the sludge additions had a negative influence on both the physical and mechanical properties of the fired brick. The modulus of rupture dropped from 13 MPa to 7 MPa and 11 MPa, [40]. The work shows that waste materials can be incorporated into commercial production regimes when the waste properties are similar to those the usual materials employed. Unfortunately this is a 'low grade' application and compatibility is only achieved in terms of material physical displacement.

Takeshi *et al*, (1992) investigated the production of glass-ceramic materials from incinerated sewage sludge ashes. In this study inorganic incinerated ash was used as the main raw material, and the global composition was modified with virgin material additives e.g. lime, carbon and soda, the crystalline phase aimed at was anorthite ($CaO\text{-}Al_2O_3\text{-}2SiO_2$). Fundamental processing features were examined including compositional requirements for crystal formation and process thermal history. The work was conducted on a small laboratory scale, melting was achieved in an electric resistive furnace, the samples being contained in alumina crucibles. Samples were cast onto iron plates and cooled in an electric furnace at 600 °C to solidify as a glass material. These glassy samples

were then thermally treated; crystallisation hold temperatures were varied between 1000 – 1100 °C. The composition of the starting ash is given in Table 26.

	Raw Ash		Experiment Number									
Species	Contents (Wt%)	Normalised (wt%)	1	2	3	4	5	6	7	8	9	10
SiO_2	48.2	67.8	49.4	46.7	55.7	53.1	50.5	60.6	57.7	54.9	46.9	44.9
Al_2O_3	18.7	26.3	22.3	19.7	20.0	19.2	18.5	18.9	18.3	17.8	25.5	24.5
Fe_2O_3	3.6	-										
Na_2O	0.6	-										
K_2O	0.9	-										
CaO	4.1	5.8	28.2	33.5	24.3	27.7	31.0	20.5	23.9	27.3	27.6	30.7
MgO	1.9	-										
MnO_2	0.4	-										
TiO_2	1.8	-										
ZnO_2	0.5	-										
CuO	0.2	-										
P_2O_5	5.6	-										
C	0.3	-										
S	2.6	-										
Others	5.6	-										
Experimental Results												
Crystal Growth Temp (°C)	1050	X	A	A	A	C	A	A	A	A	C	A
	1100	X	A	A	A	A	A	A	A	A	C	A

A = Homogeneous crystals formed (High Strength), B = Homogeneous crystals formed (low Strength , C = Crystals formed only at the surface, X = No crystals formed.

Table 26: Chemical composition of the incinerated sewage sludge ash material [6].

The samples were analysed using electron microscopy and compressive strength measurements. Thermal treatment indicated that at the lower crystallisation temperatures the crystallite size was smaller and the extent of crystallisation was limited. The situation generally improves, as the crystallisation temperature is increased, but no quantitative data is presented. The quality of the product improved as the proportion of virgin material increased, or the level of impurity decreased. For example, when the level of lime addition exceed 20 wt% (<40 wt%) crystallisation was reported to occur uniformly. In a similar manner quartz additions appeared to improve the compressive strength of the materials produced. Nucleating agents did not have a significant effect on the formation of crystals or product quality. The presented explanation accounted for this observation through the fact that the ash contains significant amounts of C and S, and that the FeS nucleating phase would probably form in-situ.

Similar experimentation was performed using various wastes as composition modifying additives, e.g. concrete scrap and grit. XRD indicated that the main crystalline phases formed were anorthite and pseudo-wollastonite. It was found advantageous to adjust the basicity to 0.2 – 0.7 to lower the melting point and viscosity, (basicity = CaO/SiO_2). The overall outcome was very similar to the previous experimentation.

The material was evaluated for use as an aggregate and was found to meet all the requirements of the JIS-A-1100, a Japanese leaching standard. The results are shown in Table 27. The product was claimed to have high mechanical strength and high acid resistance [6][1]. The values of flexural strength seem extraordinarily high for this class of material.

Property	Crystallised Glass	Marble	Granite
Flexural Strength (MPa)	500	110	150
Specific Gravity (gcm^{-3})	3.0	2.7	2.7
Mohs' Hardness	6 – 7	3	5 – 6
Acid Resistance (%)**	0.1	10.3	1.0

*Weight loss when immersed in $H_2SO_{4(aq)}$ solution

Table 27: The properties of waste glass-ceramics compared with natural materials [6].

Endo *et al,* (1997) studied the production of glass ceramic tiles from sewage sludge waste, this work followed the original engineering tasks performed by TSK, where a 150 ton-blend/day plant had been installed and commercialised. Here the composition of the sewage sludge was adjusted into the anorthite region of the $CaO\text{-}SiO_2\text{-}Al_2O_3$ phase diagram. Melting was performed at 1450°C, the slag was cooled in a mould and then reheated to between 1000 –1100 °C to form an anorthite phase crystallised product. Crystal nuclei were attributed to components contained in the original material, namely FeS, eliminating the requirement for nucleating agent additions. The sludge ashes used and the compositional adjustment made are covered in Table 28.

[1] Related press articles are given in references 76 and 77.

Raw Material	Incinerated Ash	
Species	A	B
SiO_2	51.9	26.6
Al_2O_3	15.6	26.0
CaO	6.2	8.6
MgO	2.3	2.1
Fe_2O_3	7.3	5.0
Na_2O	0.4	1.2
K_2O	0.6	0.7
P_2O_3	9.2	23.9
LOI	0.5	0.5

Table 28: Compositional analysis of the ash [41]

To ash 'A' a 15 w/w% addition of CaO was made and to ash B a 29 w/w% addition of CaO was made to adjust the composition of the sewage sludge into the anorthite phase field. Metallic element retention trials showed that the trace elements were successfully incorporated into the slag, and a leaching trial indicated that the immobilisation of heavy metals was effective. Table 29 summarises the material characterisation work undertaken, which successfully confirms the materials' usefulness as a building material relative to Japanese standards, [41].

Property	Crystallised Slag A	Crystallised Slag B
Compressive Strength (MPa)	167	120
Thermal Expansion ($10^{-7}°C^{-1}$)	67	80
Water Absorption (%)	0.0	0.2

Table 29: Physiochemical properties of the crystallised slag [41]

3.3.7 Medical Wastes

Chu *et al,* (1998) vitrified mixed surrogate medical wastes in a plasma reactor built in the Institute of Nuclear Energy Research (INER) in Taiwan, Republic of China. The process was described as being indirect, which is assumed to indicate that the plasma heat source was of a 100 kW DC non-transferred water-cooled torch. The system was described as being laboratory based and the material samples weighed 400 – 500 grams. Efficiencies of 85 % were quoted but unfortunately not defined. The work was undertaken to address the changing nature of waste disposal practices associated with progressively more stringent regulations, a topic addressed within the context of this research. Particular emphasis is

placed on biomedical concerns associated with this class of waste stream, such as acquired immune deficiency syndrome (AIDS). Hence this treatment route is thermally excessive, but justified in terms of the heterogeneous nature of the waste, i.e. medical waste is currently handled by lower temperature autoclave, incineration and microwave technology. After heat treatment a 'monolithic metal nugget', termed a 'heal', was separated from the vitrified slag as a result of gravity effects. The vitrified product consisted of mostly vitreous SiO_2 that had taken other components into solid solution.

No macroscopic phase segregation was noted in the resulting material. This observation was taken to indicate the presence of good mixing condition during vitrification. The formation of secondary phases, i.e. the metallic nuggets, was related back to the metallic constituents of the furnace charge, using density measurements. Leaching characteristics indicate that the product had encapsulated these metallic species successfully, according to the TCLP leaching testing protocol, [42]. The leaching results were not interpreted in relation to the bulk material composition of the materials. ZnO was used as a source of Zn for the tracking of metallic species, but the volatility of this metallic element, the forced air gas stream and high temperatures present in a plasma reactor are not referred to in the text. Hence it is not surprising that the leaching results were favourable.

Plasma Energy Application Technology (PEAT) used a plasma system for the treatment of Medical Waste in 1995, [12]. The vitrification treatment took place at 1550 °C and lasted for 15 minutes. The product of the thermal treatment is described as vitreous, however the electron micrographs would appear to indicate the presence of a second phase well above the concentration of any additions made. Slag densities were determined to be 2700 to 2800 kg m^{-3}, correlations are presented between increases in density and the metallic component of the charge. This suggests that density cannot be used as a sole measure of slag quality. The dispersed phases included spheroids, plates, needles and irregular shaped phases. Additionally not all of these features are consistent with surface free energy minimisation effects associated with highly fluid components. The work concludes indicating that effective mixing is achieved within the plasma reactor in the absence of external agitation that results in a homogenous vitreous product, [12].

3.3.8 Other Industrial Wastes and Summary Publications

Chang, J *et al*, (2001) reviewed the growing application of plasma technology in the treatment of gaseous, solid and liquid wastes. The advantages offered are claimed to include high treatment and energy efficiencies, smaller space volumes and lower costs. They state that in addition to the advantages quoted, for the adoption and commercialisation of the technology there is a requirement to improve all the characteristics further and the products must be re-usable and production rates must increase. This will only be achieved by understanding the fundamental mechanisms and optimisation of the key process components. Plasma processing is presented as a desirable alternative to landfill with the advantage of producing harmless products and/or reusable products. In the context of this review, atmospheric plasma generated by DC torches is important, and relative to other plasma devices this offers the advantage of extremely high plasma densities, locally high electron temperatures, high gas temperatures and low electrical fields. They are claimed to have found a niche market in the treatment of solid and liquid wastes and also in the treatment of thermally stable gaseous species such as ozone depleting substances (ODSs), volatile organic compounds (VOCs) and toxic gases and are regarded as effluent clean up devices.

In contrast, the lower pressure devices, e.g. electron beam, packed bed reactor, corona radial injection, are claimed to be unreliable and troublesome for the primary production process as they lead to contamination. In the context of solid waste treatment two definite distinctions were made; firstly for combustible matter the process was considered to produce a gasified product referred to as a syngas ($CO_{(g)}$ and $H_{2(g)}$ rich), after thermal treatment in a reducing environment. Secondly oxidative thermal treatment was reserved for the detoxification of non-combustible solid wastes. Encouragingly, the main conclusion of the paper is that plasma is well positioned to address the changing face of the waste treatment industry, this is associated with the complex nature of wastes, often of a mixed nature, that are produced by high technology materials industries, e.g. semiconductors and glass fibres, [43].

Tanaka M *et al*, (1999) investigated the production of glass-ceramics from waste granite for use as a construction material. Here waste stone was heated to 700 °C in an electric furnace and quenched in water. Subsequent crushing resulted in particles smaller than

270 μm. Batches were prepared by mixing the following constituents together in the same proportions, Table 30.

Species	Weight Percentage (%)
Waste granite	57.6
$CaCO_3$	31.7
Na_2CO_3	5.8
Na_2SO_4	3.2
C (graphite powder)	0.6
ZnO	1.2

Table 30: Batch mixing mass ratios [44]

As in most cases a black glass was produced by melting the material at 1450 °C in an electric furnace, which was cast onto a steel plate. After cooling to room temperature the glass was reheated to 850 °C for 1 hr to effect nucleation and 1050 °C for 2 hrs to allow crystal growth. The experimentation progressed past this laboratory stage to a prototype stage. Scanning electron microscopy was used in conjunction with powder XRD to confirm that β-wollastonite ($CaO.SiO_2$) was the main crystal phase. The microstructure was composed of prismatic 2-3 x 10-20 μm crystals that were homogeneously entangled. The chemical composition of the waste granite is given in Table 31.

Mass % Composition			
SiO_2	69	TiO_2	0.3
Al_2O_3	15	MnO_2	0.04
Na_2O	4.1	P_2O_5	0.07
K_2O	4.9	SO_3	0.01
CaO	2.4	Cl	0.03
MgO	0.6	SrO	0.03
Fe_2O_3	3.6	ZrO_2	0.02

Table 31: Chemical composition of the waste granite [44]

This places the material composition in the phase field between β-wollastonite and anorthite as in many earlier studies. Nucleation and crystal growth phenomena were examined in an arbitrary manner, large temperature windows were examined in a coarse way. Nucleation processes were examined between the temperatures of 750 – 950 °C and crystal growth between the temperatures of 950 – 1150 °C in 100 °C intervals. The

nucleation phenomenon was attributed to the formation of FeS and ZnS, the former precipitating first with a slight overlap with the crystal growth peak and the ZnS peak occurring simultaneously with wollastonite crystal growth, hence the first peak was subsequently used to engineer the microstructure. The data were presented in a qualitative form. DTA analysis indicated a very distinctive exothermic crystallisation peak, with a maximum at 968 °C, which was used to define heat treatment schedules. A summary of the glass ceramic heat treatment schedules employed is presented in Table 32.

		1hr @ Nucleation Temperature (°C)		
		750	850	950
Crystal growth Temp (°C)	950	G	G	G
	1050	S	P	S
	1150	S	P	S

P = Prismatic crystal homogeneously entangled, S = Crystallised from the surface, G = Glass

Table 32: Effect of heat treatment on the crystallisation process [44]

XRD traces showed that specific peaks developed at the expense of others, as in previous studies. To give an overall outcome to the work; the properties of this synthetic glass-ceramic material were examined relative to those of two other naturally occurring building materials, namely marble and granite. This is summarised in Table 33.

Property	Glass-Ceramic	Granite	Marble
Density (kg m^{-3})	2700	2700	2700
Acid resistance (mg/cm^2)*	10	4 – 6	31
Flexural Strength (MPa)	70 – 80	15	11 – 17
Mohs Hardness	6	5 -6	3 –5
Water absorption	0.0	0.35	0.30

*weight loss in 1% H2SO4aq, 50ml, 90 °C, 24 hr

Table 33: Properties of the glass ceramic and natural stone [44]

As can be observed the properties of the glass-ceramic material are superior to those of the natural material. However, the limited specific gravity values would indicate that some further improvements could be achieved. Property enhancement is also confirmed by subjecting the material to a crystallisation heat treatment, [44].

Omar *et al,* (1999) examined the fabrication of glass-ceramics of the cordierite (magnesium aluminosilicate $2MgO.2Al_2O_3.5SIO_2$) spodumene system using inexpensive industrially available raw materials. As with much of the literature presented in this document, the mineralogical constitution of the crystalline product and microstructure was examined in relation to the chemical composition of the glass and the parameters of heat-treatment. The catalytic effects of TiO_2 on the microstructure and the phase constitution of the resulting crystalline materials were also evaluated with some success. In this work, glass compositions were manipulated to generate a specific amount of desired mineralogical phases, these being cordierite in the proportions of 50 – 90 wt% in 10 wt% increments. Some of the glasses were also prepared containing different nucleating agents e.g. TiO_2. Table 34, presents the range of material samples presented.

Sample ID	Nominal Phase Composition (wt%)	Calculated Oxide Components (wt%)				Starting Materials
		SiO_2	Al_2O_3	MgO	Li_2O	
1	Spodumene – Cordierite	52.68	34.11	12.40	0.80	Clay, $MgCO_3$, Li_2O_3 (and sometimes Quartz sand) 2% Boric acid was added to facilitate batch melting
2	Spodumene – Cordierite	54.00	33.37	11.03	1.61	
3	Spodumene – Cordierite	55.32	32.62	9.65	2.41	
4	Spodumene – Cordierite	56.65	31.87	8.27	3.21	
5	Spodumene – Cordierite	57.97	31.13	6.89	4.01	

Table 34: The compositions of the examined glasses and starting materials, [45].

Melting was conducted in alumina crucibles at 1450-1500 °C for 3-5 hours. Crystallisation investigations were undertaken on a laboratory scale and both one and two stage heating profiles were used. Heat treatment schedules were based on the outcome of the DTA traces. The proportion of thermodynamically predicted crystalline phases were found to favour different mechanisms of crystal growth. Samples 1 to 3 inclusive, with high corderite contents, were noted to crystallise from the surface. In contrast samples 4 and 5, with higher spodumene contents, were observed to crystallise uniformly across their entire volume. Generally the degree of crystallinity was observed to increase with time and temperature.

Microstructural features are described as being short prismatic, spherulitic, dendritic and/or fibre like. Complex phase assemblies were observed and the evolved crystalline phases were very dependent on processing condition and base glass composition. It was observed that the first phase(s) to evolve had modified solid solution characteristics, then further heat treatment transformed them into the more stable pure form of the phase leading to component rejection and further crystallisation due to local variations in composition. TiO_2 was observed to increase the crystallisability of the glass at lower temperatures, stimulating volume crystallisation leading to the formation of fine grained microstructures. It was also noted that glasses containing > 2 wt% TiO_2 showed enhanced glass-in-glass phase separation, being more potent, as a nucleating agent, relative to ZrO_2 and P_2O_5. The product material analysis was limited and only thermal expansion data was presented, the quoted values being 9.1 x 10^{-7} $°C^{-1}$ at 300 °C and 24 x 10^{-7} $°C^{-1}$ at 900 °C. Again the work presented here was limited as no reference was given to the method of containment and assimilation of the containment material into the contained glass [45].

Diaz *et al* (1999) investigated the production of Cordierite ($2MgO.2Al_2O_3.5SiO_2$) glass-ceramics from Geothermic Waste. This type of waste material is produced world wide in power plants e.g. in the ducting / piping used to convey steam in the production of electricity. The particular residues considered here have a high SiO_2 content and a low percentage of sodium and potassium salts and sulphur. Purification gave a 99.4 wt% pure SiO_2 product and twelve tonnes of this material were produced per month. This material has been substituted into a glass-ceramic blend as an inexpensive raw material. TiO_2 and ZrO_2 were selected as nucleating agents, hardeners were ZrO_2 plus polishers of ZnO and SrO, that improve the quality of the upper surface. The batch melting was conducted in aluminosilicate crucibles heated to 1450 °C for 2 hours, the resulting glass was cooled over water. The glass was pulverised and added to another glass cullet in 100 (VC-1), 75 (VC-2) and 50 (VC-3) wt% proportions, employed as a secondary agent, Table 35.

Weight %			
SiO_2	56	TiO_2	5.95
Al_2O_3	16.9	SrO	4.2
Na_2O	0.18	ZnO	4.62
K_2O	0.19	ZrO_2	2.28
CaO	0.17	MgO	8.58

Table 35: Chemical analysis of the glass obtained as VC – 75 [46]

Four thermal treatments were applied to the resulting glasses; 1145 °C for 30 mins; 1145 °C for 30 mins + 800 °C for 30 mins, 1145 °C for 30 mins + 800 °C for 30 mins + 900 °C for 240 mins and 1200 °C for 30 mins + 900 °C for 240 mins, the applicable heating rate in all cases was 10 °C min^{-1}. Experimental observations again presented the fact that the glass was homogeneous with no evidence of un-melted material. Chemical analysis showed a composition close to that of the original charge, however no quantitative data were presented so the assimilation of the crucible lining cannot be discounted as a negligible effect. DTA was used to determine the temperature of glass transformation (T_g) at 740 °C and of crystallisation at 870 and 970 °C. De-vitrification was claimed to be homogeneous and complete, the overall extent of de-vitrification being inversely related to the level of dilution. The surfaces of the samples showed the presence of un-melted spots, however a transverse section of the samples revealed the absence of bubbles and/or internal pores.

The phases identified in the materials were corderite (in its high and μ polymorph) and α crystobalite. The microstructure showed defined crystals in a glassy layer of feldspar composition of the anorthoclase type. Glass VC-1 was crystallised to the lowest extent. Finally, the mechanical properties, namely hardness, elastic modulus, fracture toughness, were determined, Table 36, some of which are questionably high. The research is promising as it suggests that this waste material can be incorporated into a commercially available glass-ceramics leading to property enhancement. The property values quoted in the text of the publication are detailed in Table 36 [46].

Sample	H_K (GPa)	H_v (GPa)	E (GPa)	K_{1C}(MPa.$m^{0.5}$)
VC-2	5.74	6.82	291.44	4.82
VC-3	4.60	5.88	100.02	2.14

Table 36: Mechanical properties of the glass-ceramics obtained [46]

Zaghloul *et al,* (1995) reviewed the current situation in the field of waste processing in the USA, reference is made to a limited number of government-funded initiatives of a similar nature including the Superfund scheme [47]. The private organisations pursuing the technology are Westinghouse's Plasma Waste Cupola, Plasma Energy Corporation and Retech, who were examining the capability of the plasma technology. Unfortunately the

paper claims that the technology was developed more than 25 years ago, however the history of plasma technology goes back much further, [12, 48, 49]. The advantage of plasma processing over competing fossil fuel technology is described and explained, particular emphasis is placed on the size and capacity of the off-gas handling equipment. The paper also covers work conducted at the University of Illinois already described in detail [4]. The work is aimed at quantifying the effectiveness of conversion and destruction of waste, the data from the work being used in a predictive manner for scale up purposes. The evolutionary structure of the research within the USA is qualitatively presented.

The effects of processing pressure and temperature changes are covered in this research, the importance of on-line data acquisition is presented in the context of processing condition – material property correlations. The paper highlights the possible future problem of asbestos containing wastes in the US, a material verified as having carcinogenic properties. Legislation is being extended from schools into public and commercial buildings. The paper however does not indicate that these undesirable properties are associated with the physical form and specifically the aspect ratio of the fibres. Such properties can be actively removed using a lower temperature sintering process that causes that material to globularise. Concluding remarks say that this project has been managed well and is now at a phase 2 level, where the practicalities associated with a mobile unit are being considered, called the mobile Plasma Asbestos Pyrolysis System (PAPS). Another similar system is in development called the Mobile Asbestos Vitrification (MAV), [12].

The next subject described is the Army Material Command (AMC) Unique Military Waste Experimental Program, the plasma component of this work was undertaken by Retech in a small cylindrical reactor. This research went on to the larger Retech system covered in [47]. Here the de-militarisation of arms was undertaken, i.e. munitions waste. This test work highlighted the problem of cross–contamination between experiments in a refractory lined furnace, a problem addressed within the context of this research. This larger scale unit was the Plasma Arc Centrifugal Treatment (PACT) Furnace. High material recoveries were obtained in the context of phase partitioning and accountability. This work has been extended to improve plasma device lifetime and the effect of waste composition on these factors and general operability. The topics addressed in this study were extended to a US

Navy shipboard system, aimed at the pyrolysis of shipboard waste. This project was intended to produce a land based prototype system by 1997. This broadened to consider electromagnetic compatibility issues and unit size and footprint. Particular attention was given to the impact on shipboard communication equipment, as a lot of plasma devices require frequency modulated electrical power, [12].

The US Department of Energy (DOE) activities extended the previously described work, to the treatment of low level and mixed radioactive waste, the work being conducted by Retech. Interest in this research was fuelled through the potential for large waste remediation contracts. The Georgia Institute of Technologies Construction Research Centre is conducting trials on low-level simulated radioactive waste at their Savannah River Site (SRS). Another large DOE project was undertaken by Science and Application International Corporation (SAIC), using the Plasma Hearth Process (PHP). This work involved the customisation of several PHP systems for specific processing aims, the pilot scale work was planned for 1995, with the objective of lowering the technology performance risk, the field scaled system being planned for 1997, installation being intended for Argonne National Laboratory-West (ANL-W), [12].

Westinghouse Science and Technology Center (WETC) is claimed to be the leader in Plasma-fired Cupola Technology. Tests have been conducted on low level radioactive sludge. The work gave rise to sales in 1994 where WETC sold four systems to IHI Japan, for installation on municipal solid waste incinerators, for the purpose of ash vitrification, [12].

Vursel *et al,* (1995) reviewed the plasma activities in Russia and in the Newly Independent States (NIS), emphasis was placed on solid waste treatment in a plasma furnace. The main centres of research.

(i). Institute for Petrochemical Synthesis, Moscow, Russia, scientific basis of plasma chemistry

(ii). Moscow Institute of Chemical Engineering, Plasma Reactors, thermodynamics of plasma processing

(iii). Institute of Thermophysics, Novosibirsk, and institute of Heat and Mass Exchange, Belorussia, Electric Arc Plasmas

(iv). Institute of Energy, Alma-Ata, Kazachstan, Thermal Plasma Reactors

Plasma research effort focuses on waste utilisation and for the design of ecologically compatible industries. The factors of importance for the success of a plasma installation are ecological safety, productivity, possibility for treatment of different wastes and economics. The review makes specific reference to waste and specifically fly ash and grate ash from MSW incinerators, then addresses work in the field of radioactive waste. The conclusion is not clear but seems to present a treatment route that generates a product that can be fed back into the plasma reactor as a fuel. The main outcome of the research is that solid wastes are the easiest to treat and the most effective furnace arrangement was a shaft furnace where liquid slag is recovered. The system described used singular and multi 'plasma-jet technology' and computer code was used to model spatial temperature distribution, layer height and melting zone, [48].

3.4 Production of Coloured Glass-Ceramics from Wastes

Kitaigorodskii *et al,* (1970) synthesised coloured glass ceramics using compounds of Ni, Co, Cr, V, Fe and Mn that were added to the original glasses in amounts of 1 – 9 wt%. The pigmenting power of Ni and Co resulted from the formation of the aluminates $NiAl_2O_4$ (greenish blue) and $CoAl_2O_4$ (dark blue), which are minerals of the spinel group. However, this led to a shortage of Al_2O_3 for the other mineralogical phases. The generation of a brown coloration on the addition of 4 wt% Fe_2O_3 was accounted for by the formation of the $FeO.Al_2O_3$ spinel. The vanadium compound V_2O_5 entered the glassy phase of the glass ceramic giving a yellow coloration [16].

In the Former Soviet Union glass-ceramics based on blast furnace slags have been coloured by sulphide compounds, [15]. The main crystalline phases were wollastonite and pseudo-wollastonite. Manganese sulphide gave a green, and iron sulphide a black coloration. These phases were claimed to be the only colouring phases in the material and therefore determine its colour. The overall colour of the material was defined by the proportion and identity of each phase, and their spatial distribution. It was claimed that by adding zinc oxide to the batch the following exchange reaction could be accomplished:

$$(Mn, Fe)S + ZnO = ZnS + (Mn, Fe)O$$

The resulting material was a pleasant "warm white", since zinc sulphide is virtually colourless [15]. The properties of the resulting glass-ceramic 'slagsitall' are given in Table 37:

Material	Density (g/cm^3)	Coefficient of linear expansion α ($°C^{-1}$)	Flexural Strength σ_f (MPa)	Tensile Modulus (GPa)	Micro hardness ($kg\ mm^{-2}$)
Slagsitall	2.70	$65x10^{-7}$ (40-650°C) $83x10^{-7}$ (650-900°C)	93	90	560

Table 37: The properties of slagsitall, [15]

M. Wang *et al*, (1988) used blast furnace slag as a raw material in a glass melting experiment, in which the emphasis was placed on the colour of the resulting product. The transmission curves of the glass were examined at different wavelengths. The blast furnace slag employed was comprised primarily of CaO, SiO_2, Al_2O_3 and MgO and the intended application was food/drink container ware. No data was presented on the hygiene requirement of long-term storage. The blast furnace slag was examined in the context of three potential applications;

(i) as a major constituent in glass melting

(ii) as a glass colorant exploiting its contained elements

(iii) as a fining or refining agent

The slag works as a fining agent in a different way from conventional agents, by encouraging bubble removal, here reduction of surface tension of the molten glass was obtained by the addition of slag and a redox reaction involving the sulphur contained in the slag. Various batches were prepared with a wide range of compositions and the chemical composition of the slag is given in Table 38.

CaO	40.25	MgO	7.80	S	0.50	K_2O	0.51
SiO_2	34.32	FeO	0.61	TiO_2	0.53	Na_2O	0.16
Al_2O_3	14.71	MnO	0.55	P	0.005		

Table 38: Composition of the blast furnace slag (wt%) [17]

The prepared powder batches, weighing 200 - 300 grams, were melted in alumina crucibles at 1420 °C. The samples were cast onto a stainless steel plate at 400 °C and then

transferred to an annealing furnace at 400 °C for 2 – 4 hrs. At this point it should be noted that the annealing intervals appeared to be arbitrary with no specific scientific basis. The colours of the glass products were transparent amber to yellow-green. After annealing, bar specimens about 1 x 1 cm in cross section and 2.5 cm long were manufactured to evaluate the softening temperature and thermal expansion coefficient. Leaching characteristics were also evaluated under both acid and alkaline conditions. Percentage transmission was measured using a spectrophotometer for wavelengths of 320 – 1000 nm, encompassing the application specific parts of the ultraviolet and infrared spectral regions.

Sample preparation involved extensive polishing, resulting in specimens of 3 x 1 x 0.2 cm. The variations of softening and transition temperatures were evaluated as a function of specific flux content, the species considered being ZrO_2, Li_2O and Na_2SO_4. Li_2O was observed to be the most effective fluxing agent in aiding viscous flow. The presented transmission characteristics of the glasses are all similar; 60% - 69% for a 2 mm thickness and the dominant wavelengths were λ_d = 574.2 to 577.1 nm.

Since the colours produced by transmission, as opposed to reflection, are associated with rare earth elements, correlations were made with synthetic base glass compositions. They compared poorly, giving no real application information and elements with more than one valence state produced colours that were dependent on the redox potential of the melt, but this was not assessed. Colour centres in amber glasses were attributed to ferric ions, sulphide and sulphur; hence, the ferrous-ferric and sulphide-sulphate redox couple was considered. Overall the paper concludes that the glass may be suitable for container applications, where the adverse effects of ultraviolet radiation on colour and flavour could be avoided in use. Chemical durability in the context of specific liquids was considered and both positive and negative leaching characteristics were noted in relation to specific solutions. The paper concludes by indicating that it was possible to generate coloured glasses with slag contents between 40 - 50 wt%, a conclusion that has been drawn from a wide amount of similar literature but with higher waste contents [17].

Kazumasa Matusita, Junya Kinefuchi and Manabu Koide, (1996) prepared glasses from sewage sludge waste and incinerator ash by melting at high temperatures. Melting was achieved in a muffle furnace at 1450 °C for 3 hours with the samples contained in alumina crucibles as 50 g batches. The samples were removed from the furnace and cooled in air,

which would introduce significant thermal stress into the material thereby influencing the attenuation of light. The glasses obtained from both wastes were almost black, and not transparent, although the content of iron oxide was only 0.4 mol% in the glasses produced from incinerator ash and 5 mol% from the sewage sludge. Glasses of the same compositions were prepared from quartz sand, alumina, calcium carbonate and ferric oxide, and the absorption spectra of the glasses were compared and analysed to estimate and identify the origin of the colours. These samples were melted in a similar fashion, however they were transferred to an intermediate muffle furnace at 600 °C for three hours. Unfortunately the overall composition of the materials was not reported. The experimental samples were prepared by either cutting strips of glass 0.1 – 0.5 mm or by blowing 0.05 mm thick glass films. The samples were examined in the range of 350 - 750 nm wavelength and optical absorption spectra acquired. Through a comparison of the two materials it was deduced that the absorption coefficient was two orders of magnitude higher for the waste materials, i.e. iron oxide was not the predominant colour contaminant. It was concluded that the colouring contaminant is iron oxide in the glass from sewage sludge and finely divided carbon from the incinerator ash, which accounts for the abnormally strong colour.

The argument presented focuses on the fact that, although the waste materials investigated contained a large number of components, most were volatile and evaporated during melting. The amount of other transition or rare earth components present was very low and formation of colloidal metallic particles was suggested, but disregarded. Carbon particles or embryonic clusters may be retained in the glassy matrix as they are derived from organic precursors heated under reducing conditions, this being a common feature of glasses prepared via the sol-gel route where metal alkoxides are the precursors. This view was confirmed by crushing the glasses and re-heating them under oxidising conditions, here final re-melting gave rise to glasses with lower absorption coefficients, [18].

3.5 A Chemically Pure Example of the Waste System Approach

Wang *et al,* (1993) investigated the effects of additions of CaO to the Li_2O-Al_2O_3-SiO_2-TiO_2 (LAST) system, in the preparation of lower thermal expansion coefficient glass-ceramic materials. This system was examined due to its technological importance in the preparation of low thermal expansion materials, and similar information was available on the addition of MgO to the system. Here progressive weight percentage substitutions of

CaO for SiO_2 were made at constant ratios of Li_2O, Al_2O_3 and TiO_2. The experimentation indicated that the thermal expansion decreased with the addition of CaO. X-ray diffraction confirmed that the major crystalline phases were β-spodumene, with a minor titanate phase. Here, as in many waste treatment papers, TiO_2 was used as a nucleating agent. The material investigation was undertaken on a laboratory scale and analytical grade reagents were used to make up 200 – 300 gram batches. Table 39 gives the oxide composition of the glasses melted where CaO additions were made in 4 wt% steps through the substitution of silica. Melting was conducted, in an electric furnace, in a platinum crucible at 1500 °C for 4 hrs. The resulting melts were quenched in water crushed and re-melted. This re-melted material was cast onto stainless steel plates at 400 °C, all of which was transferred to an annealing furnace at 400 °C for 2 – 4 hours. A clear, transparent amber-coloured glass was obtained.

Oxides					
Sample	SiO_2	Al_2O_3	CaO	Li_2O	TiO_2
A	68.0	13.6	5.0	6.4	7.0
B	64.0	13.6	9.0	6.4	7.0
C	60.0	13.6	13.0	6.4	7.0

Table 39: Chemical composition of glasses (wt%) [50]

Again DTA traces were used to show the glass transition temperatures, crystallisation and melting temperatures. A heating rate of 10 °C min^{-1} were employed. The glasses show a transition temperatures T_g of about 560 – 570 °C for all samples. The glasses showed a two-stage crystallisation temperature and also two melting endotherms in all cases. Crystallised glasses were prepared using soaking at a temperature 50 °C higher than the second endothermic peak. The crystallisation temperatures of the major and secondary phases were significantly influenced; both increased in temperature with CaO content. This effect was interpreted in terms of high temperature viscosity modifications accounted for through the effect of CaO at these temperatures. The similar shift of both peaks would indicate that the glass retained with the appearance of the first crystalline phase was more viscous than the starting LCAST glass. The properties of the glass are summarised in Table 40.

Properties			
Sample	T_g (°C)	T_{DSP}(°C)	α (10^{-6}°C^{-1})
A	560	585	8.17
B	570	590	8.27
C	570	600	8.32

Table 40: The temperature of transition, dilatometric softening point and thermal expansion coefficient (from 25 to 500 °C) of the LCAST glasses [50]

The addition of CaO to the glass system was observed to increase the thermal expansion coefficient, and simultaneously, the difference between the glass transition temperature and the dilatometric softening point decreased smoothly. The trend was taken to indicate that phase separation had not occurred; hence the compositions did not lie in the region of immiscibility. This paper importantly summarises phase development studies in the LAS, LMAS and LCAST glass systems. Crystallisation was observed to start at the surface and then proceed towards the interior of the glass matrix. The appearance of the material was recorded to change to white and opaque as a result of crystallisation. Sectional differences in appearance of the material led to the conclusion that the core of the samples remained essentially glassy. Coarsening phenomena were observed to occur if heat treatment times were extended beyond 3 hours. The variation of the properties including density and thermal expansion coefficient are also included. The plateau of the trends observed in the presented graphs is a good indication of the point at which crystallisation approaches completion [50]. This paper summarises the characteristic of a specific material, and in this light is very similar to other papers on this subject. The scope of the work is comprehensive.

3.6 Discussion

The limitations imposed by a waste stream, either industrial or domestic, in term of composition, complexity and variability are prohibitive in terms of colour formation, Section 3.4. Waste materials exhibit limited compatibility with the production of coloured materials, unless variations in colour, similar to those associated with naturally occurring products, are accepted. The literature indicates that reproducibility of colour is associated with purity and consistency and simultaneous control of the wide number of processing variables. The cited research employed very small quantities of waste, and it is

questionable whether this is representative of larger scale production or is a rigorous demonstration of a waste treatment technology. The appearance of the formed material products must be acceptable in application, and therefore appearance will define potential applications.

The cited pilot plant scale experimentation and laboratory work was plagued by refractory erosion problems, which had an uncontrollable effect on the constitution of the melts, that was not quantified. These problems were exaggerated with increases in the size of the reactors and their operating power densities. The effect was magnified, as material property scatter was observed due to inconsistencies in batch preparation.

The hypothesis that improvements in material properties can be achieved using waste materials that have been processed in accordance with the glass-ceramic preparation route remains valid. Limitations are imposed by the complex compositional characteristics of the starting wastes. Normalised compositional manipulation can only provide a rough guideline for processing, and dynamic process control is required in conjunction, for commercial success. The opinion is validated, as excessive crystallisation has been found to give deterioration of material properties due to structural disruption.

The literature presented an appreciation of the limitations associated with current vitrification technology; as a means of producing a high quality glass product. The processing stages of degassing and homogenising are essential for the production of high quality glass precursors for glass-ceramic production.

It is also apparent that the limitations imposed by product dimensions have not been considered; including heat transfer and thermal stress as well as the volumetric dependence of mechanical properties. Therefore extrapolated data should be interpreted with scepticism. Similarly, the homogeneity of the vitrified products was not assessed and limited emphasis was placed on material forming or end product specifications. Re-usable and saleable products, produced at increased rates, are claimed to be the key to technological success and commercial adoption.

The experimental work has moved gradually away form the laboratory, into prototype scale installations, but overall progress has been limited. The bulk of the research lies

firmly within the laboratory, especially within the field of atmospheric DC plasma. Consideration of the thermal control within a single melting chamber is apparent, but not during sample transfer from the melting chamber to the heat treatment furnace, which has a significant potential to influence material properties, as there is often only a limited temperature window between the melting temperature and optimum heat treatment temperature.

The material physical property data does indicate improvements upon thermal treatment and crystallization, but does not quantify the statistical scatter of the results, which is a questionable oversight in the field of waste treatment. The most successful work and products originated from industrial processes, and were therefore subject to process control. This has aided experimental success, but casts doubt over the technological applicability to municipal waste streams.

Leaching characterisation focussed on long-term storage criteria, however the same type of investigation could be considered as data for the assessment of stability in re-use. Limited emphasis is placed on the influence of thermal processing on leaching phenomena, and at no point have several material been assessed relative to each other, produced from different waste using the same technological route. This places question marks over the generic characteristics of the processes described.

3.7 Literature Conclusion

This review covers the material and process developments in the field of waste treatment, and the research can be described as either agricultural or scientific and focussed. However, it is felt that an intermediate approach is most justified in this field. Within the literature an accepted approach for the systematic evaluation of crystallisation is evident, employing standard techniques for material evaluation.

Analytical ambiguities exist in the vast majority of the research work, conducted on waste streams, due to the erosion of refractory and graphitic liners typically used in pilot-scale and laboratory-scale processing chambers. This produces difficulty in obtaining an absolute material baseline within the research, as composition is not measured after processing, and relative property changes can be significant, as containment materials are often network formers. These effects are exaggerated by the small samples sizes often

employed. Variations in the waste composition will influence the identity of the crystalline phase(s) evolved as well as the extent of crystallisation itself, and is a critical factor in glass-ceramic processing. It is a factor that is not readily addressed in the literature along with the scalability of the processing route.

To address these issues cold skull melting was employed in this work to eliminate the refractory wear problem on a prototype scale. This was used in combination with an upper melt surface plasma heat source, which gave dynamic control that addressed the limitation imposed by complex waste characteristics. The furnace achieved the requirements of the glass melting operation, including the required thermal cycles. This minimised random and systematic material property and preparation uncertainties. Material compositional analysis before and after the furnace confirmed success and the solidified vitreous products were evaluated for physical homogeneity and the statistical scatter of mechanical properties.

Nucleating agents are essential for the uniform formation of crystals in a large product. Without a nucleating agent, crystals will grow predominantly in one direction, from the surface towards the interior of the product. In some cases, the crystals will not reach the interior of the product, hence, crystallisation will be incomplete and the product will show a large degree of inhomogeneity. This will adversely affects the mechanical properties of the material due to phase incompatibility and anisotropic response. This is exaggerated as product sizes increase, thus laboratory experimentation poses limitations. The vast majority of the literature available makes no reference to the extent of the body and the mechanisms and time dependence of heat transfer. This is a key topic that must be addressed in respect to product formation and technology scale up, if crystallisation is to be achieved uniformly. Therefore the end products evaluated here were of realistic sizes and thorough mapping of crystallisation process occurred.

The research has shown that the external addition of nucleating agent(s) influences material properties positively, and beyond the level that can be acquire by intrinsic nucleation means. To address these issues a nucleation agent will be used and application-sized articles will be produced for product evaluation. The work will aim to acquire an understanding of the relationship between waste composition, processing conditions,

microstructure and properties. This is hoped to deliver the basis of a robust generic technology.

Colour is one of the least important 'barriers to entry' for plasma waste processing technology and its products entry into commerce. Colour should be stated and not engineered in this context. Basically black is acceptable, it masks significant variations and is widely utilised in industry, alternatively more traditional topographic colouring technologies should be considered in combination, e.g. glazing and cladding etc.

Ecological compatibility for these products will be defined primarily by their leaching characteristics. It is essential that the material is tested under simulated application conditions and the data related to the extent of the body and the physical and chemical nature of its service environment. To confirm ecological acceptability the waste material products must be compared with natural materials.

It is considered that only limited research has been undertaken on a prototype scaled processing plant and therefore limited success has been achieved in transferring the technology from the laboratory into industry. The research undertaken here will address these issues and make the process more tangible to the waste processing industry. The cited review papers present plasma waste processing technology in a positive light and it is hoped that the growing international voice of acceptance and adoption means that the research is industrially applicable and timely.

4 Fundamental Scientific Background

The word 'glass' should be treated as a generic term as virtually every class of material can now be formed in a glassy or amorphous state [4, 7, 84]. A glass should not be regarded as an atomic or molecular property dependent on chemical or physical properties, but a phenomenological effect dependent on re-arrangement kinetics. This can be understood through the fact that, for specific systems, there are well defined compositional and processing ranges where glass formation can occur, the limits of these ranges are commonly associated with changes in the primary phase of crystallisation, [51]. *Turnbull et al* examined the definition and properties of glasses in significant detail, ultimately describing a glass as a solid material formed by the continuous hardening of a cooled liquid, [52].

Glasses are materials that have properties intermediate to those of crystalline solids and liquids. The structure lacks long-range periodic order, but exhibit some short-range order as indicated by typical atomic distribution function variations. No sharp phase transitions are noted, as in the case of the formation of crystalline phase materials or in phase transitions of state. One of the most important features of the glassy state is the isotropic nature of material properties. Glasses are usually obtained by cooling a liquid, below its freezing or liquidus temperature, at a sufficiently fast rate in order to avoid spontaneous crystallisation. Other externally imposed stimuli can result in similar transitions, e.g. pressure. Hence, glass formation is described through an understanding of cooling, heat transfer phenomena, material dimension and phase transformation kinetics. Materials that readily form glasses are usually those that are very viscous at the melting point and have complex structures that are difficult to re-arrange, however these are not always sufficient criteria.

The relationship between crystalline solids, liquids and glasses can be explained using a volume – temperature diagram, Figure 1 below.

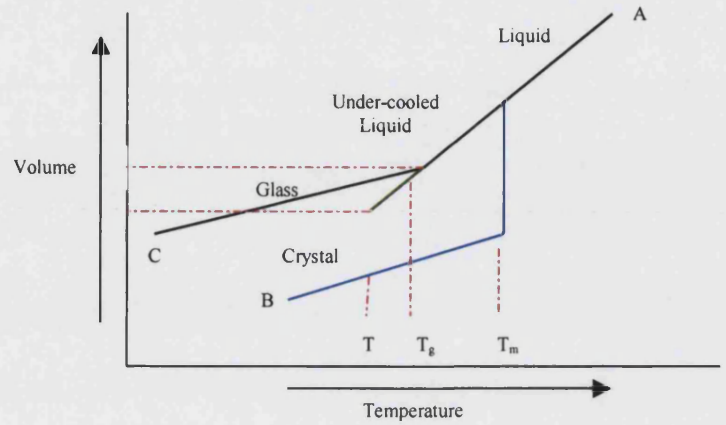

Figure 1: The volume temperature relationship between glass, liquid and solid states

On cooling a liquid from point A along the black line, the volume will decrease steadily. If the rate of cooling is slow and nuclei are present, crystallisation will occur and the cooling path will follow the blue line at the solidification temperature T_m. Here it is observed that a sharp volume change occurs, which is attributed to the formation of a dense crystalline phase and the loss of free volume, the crystalline solid then continues to cool towards point B. However, if the rate of cooling is sufficiently rapid crystallisation will not occur and the material will cool from point A, and follow the black line, to point C. Here the material is firstly under-cooled and then there is a change is slope associated with the glass transition temperature T_g. Below T_g the material can be considered as a glass.

If the temperature is held below T_g at a temperature T the volume of the material will change as a function of time[1], which is an extension of the primary part of the black line from point A to C, involving a loss of free volume. This illustrates that properties may change as a function of time in the vicinity of T_g, and all of these changes are grouped together under the term 'stabilisation effects'. This is not the case above T_g where no such time dependence of material properties is observed.

[1] in accordance with the green line

In silicate glasses, viscous flow is thermally activated and will be discussed in Section 4.4. The viscosity associated with the liquidus temperature is ~ $1x10^5$ poise and typically the viscosity associated with glass transition region (T_g) is ~ $1x10^{13}$ poise. The terminology used when describing ceramic oxide glasses includes the following:

(i) 'Glass formers' which are oxides that readily form glasses on their own and provide the backbone of any glass network, e.g. P_2O_5, B_2O_3, GeO_2 and SiO_2.

(ii) 'Intermediate oxide' or 'conditional glass formers' which will participate in a glass network, in the presence of sufficient amounts of other oxides, but will not form one on their own, e.g. V_2O_3, MO_3, Bi_2O_3 and Al_2O_3.

(iii) 'Network modifiers' disrupt the glassy network, increasing the incidence of non-bridging oxygen atoms, e.g. Na_2O and K_2O.

Several approaches have been taken in trying to explain the glass forming capabilities of materials. These have been based on factors such as relative atomic size, bond geometry, directionally of bonding and bond strength, examples include;

(i) Goldschmidt's radius ratio criteria [51, 52]

(ii) Zachariasen's random network hypothesis [51, 52]

(iii) Smekal's mixed bonding hypothesis [51, 52]

(iv) Sun's bond strength criterion for glass formation [51, 52]

However, no unified hypothesis capable of explaining the phenomenon of glass formation in all systems has been developed since in each case non-conforming occurrence exists [20, 51, 52]. For example, Sun's bond strength criterion would suggest that because the V-O and Sb-O bond strengths are high they would be glass formers, but this is not the case and V_2O_5 is an exceptional poor glass former.

Whether or not a given liquid will crystallise, during cooling through the glass transition temperature (T_g) range, is strictly a kinetic problem. On the one hand it involves the rate of nucleation and crystal growth, and on the other, the rate at which energy can be extracted from the cooling liquid hence reducing its temperature.

4.1 Phase Transformations in Glass

Phase transformations in glasses can be split into two distinct primary categories; firstly, crystallisation and secondly, liquid-in-liquid phase separation. Crystallisation is defined as the growth of a crystalline phase from a liquid and it can be a surface (at the glass-

atmosphere interface) or volume (nucleation occurs at sites within the bulk of the material) phenomenon, each case justifying a separate treatment. Volume crystallisation can be further sub-divided into homogeneous and heterogeneous crystallisation, depending on whether the initiating site is indigenous or exogenous to the bulk material, respectively.

Liquid-in-liquid phase separation is defined as the growth of non-crystalline phases that have a different composition from the original liquid, hence this mechanism is reserved for complex and not single component systems and usually occurs homogeneously. Spinodal decomposition is a complex phenomenon in which separation into two liquid phases, one of the phases shows no energy barrier to nucleation and phase separation is limited only by diffusion.

4.2 Nucleation (Classical Theory)

Although phase transformations can be divided into two principal types, crystallisation and liquid-liquid separation, the transformation manipulated in this work is crystallisation and will now be described.

When a material is cooled below its thermodynamic melting or liquidus temperature the stability of crystalline nuclei and the rate of nucleation increases with under-cooling. Crystallisation occurs at a specific rate from a finite number of nuclei. Glass formation can be attributed to either a low rate of nucleation and/or a low rate of crystal growth. For truly homogeneous nucleation the process is controlled by two factors; surface/interfacial and volumetric free energy changes. For a spherical nucleus the free energy change, ΔG_r, associated with a singular nucleation event is given by:

$$\Delta G_r = -\frac{4}{3}\pi r^3 . \underline{\Delta G} + 4\pi r^2 \sigma$$

Equation 1

where: $\underline{\Delta G}$ is the free-energy change, per unit volume, for the crystal – liquid phase transformation ($J\ m^{-3}$)

r is the radius of the spherical nucleus (m)

σ is the interfacial surface free energy of the liquid – crystal interface ($J\ m^{-2}$)

The transformation will be thermodynamically favoured, i.e. spontaneous, if the overall change in free energy is negative. The interfacial free energy term opposes the phase change while the volumetric free energy term drives the change. If r is small the surface term dominates and the transformation is unfavourable, where if r is large the volume term dominates and ΔG_r becomes negative, making the transformation favourable. The critical radius, r^*, can be equated with a maximum in the graph of ΔG_r versus r; Equation 2.

$$\frac{d(\Delta G_r)}{dr} = -\frac{12}{3}\pi r^2 \underline{\Delta G} + 8\pi r\sigma = 0$$

Equation 2

$$\text{Hence: } r^* = \frac{2\sigma}{\underline{\Delta G}}$$

This point is associated with the change of an unstable embryo ($r<r^*$) to a stable nucleus ($r>r^*$) as growth is associated with a further decrease in free energy. Hence, by substituting r* into Equation 1 we arrive at a value of the free energy barrier for nucleation, Equation 3.

$$\Delta G_{\text{hom}}{}^* = \frac{16\pi\sigma^3}{3(\underline{\Delta G})^2}$$

Equation 3

If v is the volume of the atomic species and n is the number of atoms in a nucleus, then the number of atoms in a critically sized nucleus, n^* is given by:

$$nv = \frac{4}{3}\pi r^3 \quad and \quad n^* = \frac{32\pi\sigma^3}{3v(\underline{\Delta G})^3}$$

Equation 4

Even though the formation of an embryo involves an initial increase in free energy, the event still occurs because the entropy of the system can be increased, and therefore, the free energy is decreased by the formation of a small number of ordered clusters. Their occurrence can be related to the presence of local thermal gradients. Assuming an ideal solution, the entropy change will be equal to the free energy change for the transformation, thus the overall free energy change associated with the formation of a number (N_r) of nuclei (ΔG_n) is given by Equation 5, [51, 65].

$$\Delta G_n = N_r \Delta G_r + kT\left(\frac{N_r}{N_r+N}\ln\frac{N_r}{N_r+N} + \frac{N}{N_r+N}\ln\frac{N}{N_r+N}\right)$$

Equation 5

where N is the number of atoms per unit volume and N_r is the number of clusters of radius r per unit volume and k is Boltzmann's constant. At equilibrium $\Delta G_n = 0$, $\Delta G_r = \Delta G^*_{hom}$ and $N_r <<< N$ giving Equation 6.

$$N_{r^*} = N \exp\left(\frac{\Delta G^*}{kT}\right)$$

Equation 6

The addition of a single atom from the parent phase to the critically sized nucleus results in a stable nucleus. Hence, the rate of formation is the product of the number of critically sized nuclei present per unit volume and the rate at which atoms are attached to the embryo, i.e. across the interfacial region. The frequency with which an atom attempts to cross the embryo - parent phase interface is given by the vibrational frequency of the atom, *kT/h*, where *h* is Planck's constant. The probability, *P* with which an atom attempts to cross the embryo/parent phase interface is given by:

$$P = \exp\left(-\frac{\Delta G_a}{kT}\right)$$

Equation 7

Only atoms that are adjacent to the interface are in a position to allow growth, if this number is N_s, then the frequency at which the atoms cross the interface is given by:

$$frequency = N_s \frac{kT}{h} \exp\left(-\frac{\Delta G_a}{kT}\right)$$

Equation 8

Thus the rate of nucleation, *I* is the product of the number of nuclei of critical size, Equation 6, and the number of atoms that cross the interface per second, Equation 8, resulting in Equation 9.

$$I = N_s \frac{kT}{h} \exp\left(-\frac{\Delta G_a}{kT}\right) . N \exp\left(-\frac{\Delta G^*}{kT}\right)$$

Equation 9

The first factor on the right-hand-side of Equation 9 is of kinetic character. ΔG_a is often referred to as the *kinetic barrier to nucleation* and is analogous to activation energy for assimilation of atoms/molecules across the growth interface. It is often taken to be equal to the activation energy for viscous flow or diffusion of the slowest associated species along its fastest path. The second factor involving ΔG^* is referred to as the *thermodynamic*

barrier to nucleation. If the free energy of crystallisation increases in magnitude with falling temperature below the melting point at a rate given by:

$$\frac{d\left(\underline{\Delta G}\right)}{dT} = -\Delta S_f$$

Equation 10

Where ΔS_f is the entropy of fusion, which is assumed to be independent of temperature. At the melting temperature, T_m, we have.

$$\underline{\Delta G_m} = \Delta H_f - T_m \Delta S = 0$$

$$\underline{\Delta G} = \left(T_m - T\right)\frac{\Delta H_f}{T_m}$$

Equation 11

where ΔH_f is the heat of fusion per unit volume. By combining Equation 3, Equation 9 and Equation 11 it is seen that the rate of nucleation is extremely sensitive to temperature, as depicted in Figure 2. As temperature decreases, the thermodynamic driving force increases and atomic mobility decreases, which means that a maximum occurs at a finite temperature below the melting or liquidus temperature. Similar observation can be made about the crystallisation process all of which leads to the classical 'Tamman' curves, Figure 2.

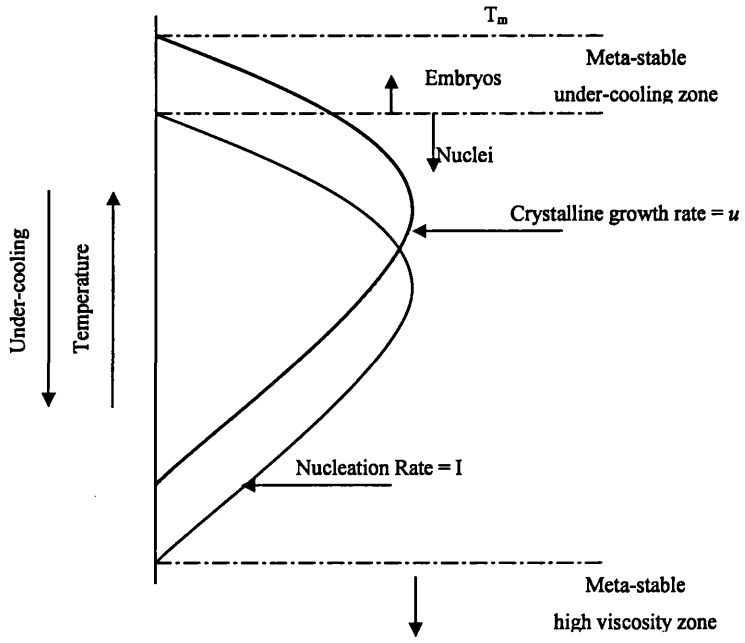

Figure 2: The variation of homogeneous nucleation rate and growth rate of a crystalline phase with temperature

The primary assumptions made in this treatment are that the nuclei can be treated as bulk material and their boundaries are sharp with defined surface energies. An understanding of nucleation and crystal growth temperature windows can be used to engineer the microstructure. For example, if a uniform and fine microstructure were required, then a high rate of nucleation combined with a moderate rate of crystal growth would be employed. Similarly if both the maximum nucleation and crystallisation rate are employed then the shortest processing time will be achieved but a coarser and segregated microstructure would evolve.

4.3 Heterogeneous Nucleation

Here growth occurs on a foreign interface, which may be a solid interface or a solid dispersed throughout a liquid. An embryo or cluster forms on this solid surface with a contact angle θ. The free energy change associated with the formation of the cluster now shows a more complex surface free energy characteristic, giving Equation 12.

$$\Delta G_r = \frac{v_c}{v_m}\underline{\Delta G} + S_{lc}\sigma_{lc} + S_{cs}(\sigma_{cs} - \sigma_{ls})$$

$$where \quad \sigma_{ls} = \sigma_{cs} + \sigma_{lc}\cos\theta$$

Equation 12

where:

v_c is the volume of the cluster (m^3)

v_m is the molar volume of the crystalline phase (m^3 mol^{-1})

S_{lc} and S_{cs} are the surface areas of the liquid-crystal and the crystal-substrate interfaces respectively (m^2), and

σ_{lc}, σ_{cs} and σ_{ls} are the interfacial energies (J m^{-2})

It should be noted that the free energy term $\underline{\Delta G}$ is a molar (J mol^{-1}) quantity as opposed to volumetric quantity, which was used for homogeneous nucleation.

The interfacial terms have a positive influence (i.e. they contribute a negative component to the free energy change) on the transformation if interfacial area is removed and a negative influence when interfacial area is created. For a spherical cap cluster, of radius r, on a planar surface, a static equilibrium can be described as follows, [20, 51].

$$\sigma_{ls} = \sigma_{cs} + \sigma_{lc}\cos\vartheta$$

$$v_c = \frac{4}{3}\pi r^3\left(\frac{2-3\cos\vartheta+\cos^3\vartheta}{4}\right)$$

$$S_{lc} = 2\pi r^2(1-\cos\vartheta)$$

$$S_{cs} = \pi r^2\sin^2\vartheta$$

By substituting these equations into Equation 12 the following equation, relating ΔG to r, can be derived.

$$\Delta G_r = \left(\frac{\pi r^3\,\underline{\Delta G}}{3v_m} + \pi r^2\sigma_{lc}\right)\left(2-3\cos\vartheta+\cos^3\vartheta\right)$$

Equation 13

As in the case of homogeneous nucleation by differentiating with respect to *r* and equating to zero, an equation for *r** can be obtained, which is identical to the expression obtained for homogeneous nucleation.

$$r^* = -\frac{2\sigma_{lc}v_m}{\underline{\Delta G}}$$

Equation 14

When this expression is substituted into Equation 13, for ΔG_r, it is possible to determine the equation for ΔG_{het}^*, the thermodynamic barrier to heterogeneous nucleation, Equation 15.

$$\Delta G_{het}^* = \frac{16\pi\sigma_{lc}^3 v_m}{3.\underline{\Delta G}^2}.\left(\frac{2-3\cos\vartheta+\cos^3\vartheta}{4}\right)$$

Equation 15

The part of the equation in parentheses is often referred to as f(θ), this function is always less than 1 and shows highest values for 'poor wetting' conditions and lowest values for 'good wetting' conditions, i.e. when the contact angle approaches zero. The following graph illustrates this variation of f(θ) with contact angle in radians.

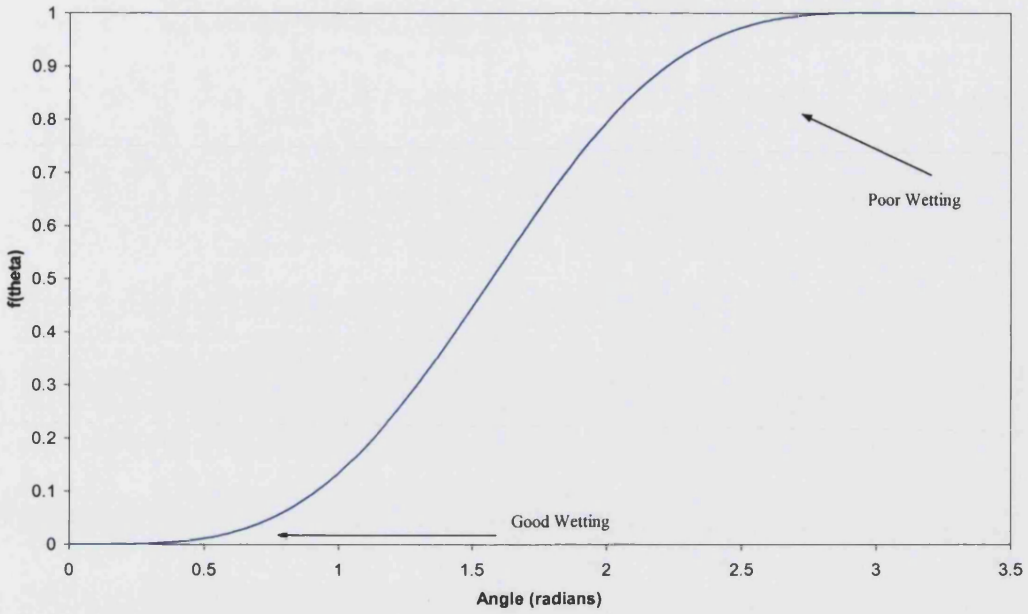

Figure 3: The variation of f(θ) with the contact angle

It is observed that the critical size of an embryo in both homogeneous and heterogeneous nucleation is the same. However, in the case of heterogeneous nucleation, the additional surface contribution reduces the thermodynamic barrier to nucleus formation. The advantage obtained is very dependent on the wetting characteristics of the phases involved, but practically, the mechanism leads to a reduction in the critical level of under-cooling.

This indicates that nucleating agents, purposely added to under-cooled glasses, should lead to epitaxial growth or oriented overgrowth. Hence, the seeding additions made should have low index (Miller indices) planes of high atomic density that have similar atomic arrangements and spacing to that of the crystalline phase(s) to be nucleated. The unit cell dimensions and crystal structure should be similar, in the case of glass ceramics a maximum disregistry of 8% is the limiting extent of crystalline mismatch. Disregistry (δ) is defined as:

$$\delta = \frac{a_c - a_0}{a_c}$$

Equation 16

Here the subscripts, c and a, refer to inter-atomic distances within the crystalline and substrate phases respectively.

The importance of heterogeneous nucleation in glass-ceramic processing can be seen through micro-structural examination. A crystallite size of 1μm implies $1x10^{18}$ nuclei m^{-3}. The types of nucleating agents employed in glass-ceramic technology can be broadly classified into two types:

(i) Substances that are capable of forming minute crystals of low solubility in the glass. These materials reduce from their ionic form into a neutral metallic nature in the melt, e.g. Pt, Au, Cu.

(ii) Oxide substances that are soluble in silicate glasses in significant proportions (1 – 20 wt%). These materials rarely crystallise upon cooling as independent oxides, but precipitate incipiently as complex compounds, e.g. P_2O_5, Li_2O, TiO_2 as $MgTiO_3$ or Li_2TiO_3, [8, 9, 36, 45, 50, 51].

Heterogeneous nucleation is influenced by the interaction between the embryo and substrate crystal. The contact angle is the important parameter, and has been postulated to be a function of the chemical bond type, strength and level of disregistry. However, for both types of nucleation, work must be done to create a surface between the new phases and the matrix, and hence make a positive contribution to the free energy of the system. Super-saturation of the matrix phase by the precipitating phase can aid this process [9].

4.4 Crystal Growth Kinetics

The rate of crystal growth is dependent on the rate at which atoms arrive and remain at the surface of the nuclei. When a nucleus is microscopic, but above its critical size, crystal growth rate will be affected by the curvature of the growth interface. However this effect can be neglected when the crystalline phase becomes macroscopic in size and can be considered a crystal with a planar interface.

Under 'normal growth' conditions atoms arriving at the growth interface are able to join the crystal at all points on the interface, so it can be described as atomically rough. For this process to occur the atoms must overcome the activation energy, ΔG_a. The number of atoms, i, crossing the interface per unit time is given by, [51].

$$\frac{di}{dt}(g \rightarrow c) = sv_0 \exp\left(-\frac{\Delta G_a}{kT}\right)$$

Equation 17

Here 's' is the number of atoms in the glassy material 'g' adjacent to the crystalline phase 'c', and v_0 is the frequency at which each atom vibrates due to thermal energy, as defined by Equation 8. Thus the exponential term represents the probability of finding an atom with sufficient thermal energy for the process to occur. Once an atom has accomplished this change in position, its energy is reduced by $\underline{\Delta G}(v/v_m)$, where $\underline{\Delta G}$ is a molar quantity. Thus for the reverse process to occur, the required activation energy increases to $(\Delta G_a+\underline{\Delta G}\, v/v_m)$. This means that the number of jumps per unit time from the crystal to the glassy phase can be expressed in a similar manner. The net transfer of atoms from the glassy matrix to the growing crystal can be expressed as follows, using the mathematical laws of indices, Equation 18:

$$\frac{di}{dt}(g \rightarrow c) - \frac{di}{dt}(c \rightarrow g) = sv_0 \exp\left(-\frac{\Delta G_a}{kT}\right)\left[1 - \exp\left(-\frac{v\underline{\Delta G}}{v_m kT}\right)\right]$$

Equation 18

If 's' atoms are transferred then the crystal grows by λ, where λ is approximately one inter - atomic spacing with the crystal phase. Equation 19 defines the growth rate 'u', of the crystalline phase, [51, 52]:

$$u = \lambda v_0 \exp\left(-\frac{\Delta G_a}{kT}\right)\left[1 - \exp\left(-\frac{\underline{\Delta G}}{RT}\right)\right]$$

Equation 19

$kv/v_m = 1/R$, where $R = N_a.k$ and is the gas constant. This equation predicts that a maximum in growth rate will be observed because the thermodynamic term in square brackets increases with under-cooling whereas the kinetic term decreases with undercooling. Importantly, for a given temperature, the growth rate will be a constant with time. The maximum in growth rate occurs at higher temperatures than the maximum nucleation rate, as shown in Figure 2. Other, more complex, growth models are contained within the literature [51], e.g. 'surface nucleation growth'. Here the first atom to arrive at a smooth surface takes up a more unfavourable site than any other subsequent atom associated with adjacent positions in the monolayer until the process is started again by the initiation of another monolayer. In 'screw dislocation growth', a fraction of surface imperfection sites act as growth initiators and their features are extended by the growth processes, [20, 51].

These complex models do not give any more understanding of the complex nature of the waste systems under consideration in this research. The systems under study are multi component systems and the crystallising phase is predicted to differ in composition from that of the original glassy phase. Continual growth of the crystalline phase requires long-range diffusion, the effective diffusion distance being given by $\sqrt{Dt}$, where D is the diffusion coefficient ($m^2 s^{-1}$). This varies with temperature in accordance with Equation 20 and can be calculated using the Stokes-Einstein relationship, [51]:

$$D = D_o \exp\left(-\frac{\Delta G_a}{kT}\right)$$

Equation 20

In addition to this effect the preferential segregation of the materials between the two phases, i.e. glassy and crystalline phases, results in a continuous alteration of matrix phase composition, which will in term, lead to variations in the thermodynamic driving force for crystallisation and thermal variations due to specific heat changes. These features of the system will be taken into consideration so that a robust treatment process can evolve.

4.5 Liquid-in-Liquid Phase Separation

In some silicate melts dual liquid phase formations are observed. This immiscibility can occur above and below the liquidus temperature, the latter being referred to as metastable immiscibility and is usually observed for melts with S-shaped liquid phase boundaries, as shown in the free energy diagram, Figure 4. Binary oxide systems, comprised of divalent metal ions, usual exhibit immiscibility above the liquidus and the spontaneity of the process implies that separation of the phases has produced a lowering of free energy. The free energy of mixing is given in Equation 21.

$$\Delta G_m = \Delta H_m - T\Delta S_m$$

Equation 21

If ΔH_m has a large positive value then there is departure from the classical two fully miscible liquid systems giving a composition region with favourable immiscibility due to the deflection of the free energy curve. In this zone the free energy of the system will be lowered by the separation of any singular liquid into two liquids with adjacent compositions. This is in accordance with the intersection point of a horizontal line with the phase boundary as observed in the lever rule. This transformation is reversible, as the

entropy term is temperature dependent, allowing thermal control of the process. This situation is depicted in Figure 4.

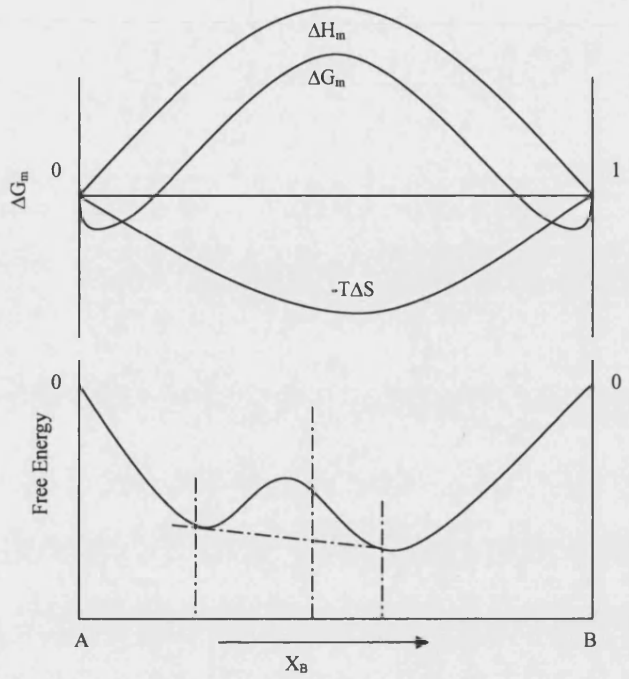

Figure 4: A graph of free energy versus composition for an immiscible system where ΔH_m is positive.

From graphs such as those in Figure 4 it is possible to construct a phase diagram of the immiscibility dome. This is achieved by plotting the liquid phase compositions as a function of temperature. The inner dome is referred to as the spinodal, and a melt within this dome spontaneously separates if the mobility of the ions is high enough due to a net reduction in free energy. Whereas, the outer part of the dome, defined by the region lying between the points of inflection and minima's of the free energy versus composition curve, will require nuclei formation for immiscibility to occur as phase transformation is associated with an increase in free energy. Therefore, the compositions that lie between the two points of inflection on the free energy curve define the chemical spinodal. Outside the dome classical nucleation and growth theory apply.

4.6 Kinetics of Glass Formation; Simultaneous Nucleation and Crystal Growth

Fundamental theory has been used to obtain expressions indicating how material parameters and external state properties influence both nucleation and crystal growth processes. However, these two dynamic events may and will take place simultaneously, as depicted in Figure 2. For this reason several researchers have used the Johnson-Mehl relationship to understand the kinetics of simultaneous nucleation and growth, [20, 51]:

$$1 - x_t = \exp\left(-\frac{\pi}{3} u^3 I t^4\right)$$

Equation 22:

where: x_t = fraction transformed ($v_{crystal}/v_{glass}$)

u = crystalline phase growth rate (m s^{-1})

I = nucleation rate (m s^{-1})

t = time (s)

This relationship has an extended derivation associated with it, and will not be included here, however it does apply to isothermal conditions and both the nucleation and growth rates are assumed to be constant with time. The treatment refers to an initiating non-productive time interval called the induction or incubation period. The Avrami modification, in which the nucleation rate is assumed to be time independent under isothermal conditions, has been used for the experimental comparison of different waste and virgin material systems, Equation 22. The general form of the equation is referred to as the Johnson-Mehl-Avrami equation and its exact form depends on the assumptions made about nucleation and growth processes during its derivation. The exponent of 't' can vary between values of ~1 to 4, e.g. a value of 1 denotes surface crystallisation and a value of 3 implies bulk crystallisation. This approach has been successful in providing guidance in the field of glass formation where theoretical temperature-time-transformation (T-T-T) curves have been generated by selecting a particular crystallised fraction and calculating the times, at different levels of under-cooling, to achieve it. The 'nose' of the T-T-T curves indicates the orders of magnitude of the critical cooling regimes [$(dT/dt)_{critical}$ = $undercooling_{nose}$/incubation period], this being the cooling regime required to avoid the crystallisation processes.

The fundamental processes of nucleation and crystal growth have been discussed. The processing of glass-ceramics and plasma technology will now be described.

4.7 The Glass-Ceramic Process

A glass-ceramic is a polycrystalline solid prepared by the controlled crystallisation of a glass material, using a controlled heat treatment schedule. A blend of material is firstly melted at a temperature of ~100 °C above the liquidus temperature of the material so that the nucleating agent dissolves into the glass forming a homogeneous mass. During melting cords (off composition glassy regions) and stones (refractory inclusions) are assimilated, bubbles escape and homogeneity of composition, temperature and density of the glass melt is acquired. Shaping of the glassy product is then achieved at a working temperature under low viscosity conditions; less than 10^4 - 10^7 poise, [20, 51]. The temperature of the article is lowered to the annealing temperature of the glassy material, i.e. at a viscosity of $10^{13.4}$ poise, where the body acquires dimensional stability without internal stresses. The temperature of the material is then raised so that nanometric particles of the nucleating agent precipitate, which usually occurs at a temperature approximately 50 °C higher than the annealing point of the glass. The glass is held at this temperature for a desired time so that the nuclei are generated. The nucleation process can be intensified by reducing the temperature at which nucleation occurs, which increases the degree of under-cooling. The nucleated glass is then heated at several degrees per minute until the formation and growth temperature of the primary crystalline phase is observed, (commonly 100 – 200 °C below the nucleation temperature). The glassy body is then held at this temperature for several hours until the crystallisation process approaches its desired completion stage. The rate of heating at this stage must be carefully controlled to avoid distortion through dimensional change and the development of the skeletal crystalline network counters this dimensional deformation by reducing viscous flow.

The stabilised glass-ceramic is then cooled to room temperature. The exact format of the thermal history of the samples can have a profound effect on the micro-structural properties of the glass-ceramic. Synthetic glass-ceramics differ from natural rocks as they have a very fine structure with a lower number of crystal types, the size of the crystals commonly not exceeding 2 μm [16].

4.8 Characteristics of Plasmas

A plasma, sometimes referred to as the fourth state of matter, is an ionised gas comprised of ions, molecules, electrons, photons and atoms (in their ground state and various excited states). Overall, a plasma is electrically neutral, a property which is termed quasi-neutrality. As additional energy is added to atoms in the gaseous state, the atoms collide with each other with more energy and with greater frequency. At about 2,000 °C molecules dissociate into atoms and at about 3,000 °C, these collisions result in electrons being ejected and the atoms become ionised, [53]. During steady state electrical conditions the plasma has a rate of ionisation balanced by the rate of recombination. The overall degree of ionisation therefore depends on the energy content of the plasma. In this ionised state the gas is electrically conducting and can be confined by an electromagnetic fields and has an almost liquid-like viscosity.

There are two different types of plasma; the equilibrium or thermal plasma ("hot" plasma) and the non-equilibrium or non-thermal plasma ("cold" plasma). The two important distinguishing features of 'hot' thermal plasmas are firstly the equality of the heavy gas particle (T_{gp}) and electron temperature (T_e), i.e. ($T_e = T_{gp}$), and secondly 'chemical' equilibrium. T_h is often referred to as the sensible temperature, this is the temperature that would be experienced by material when exposed to the plasma through both heat and mass transfer mechanisms, i.e. a mass average particulate temperature. In 'cold' non-equilibrium plasmas there is a strong deviation from kinetic equilibrium ($T_e >> T_g$). The sensible temperature T_h is very close to room temperature, which means the effective temperature of the electrons is considerably higher than that of the ions. The temperature of the particles in a plasma are defined by its mean kinetic energies:

$$\frac{3}{2}kT_x = \frac{1}{2}\overline{m_x v_x^2}.$$

Equation 23

where:

k is the Boltzmann's constant = 1.38054×10^{23} J/K

m_x is the mass of a particle (kg)

v_x the velocity of the particle (m s^{-1})

T_x absolute temperature of the particle (K)

This definition can be made more complex by the introduction of the statistical treatments required to describe the large number of various species and collision processes that govern individual kinetic energies within thermal plasmas. Generally the number of collisions within a given volume of plasma is proportional to the density of particles, consequently the collision frequency will depend on its pressure since increases in pressure increase the density of particles and the collision frequency. Electrons are lighter than either molecules or intact or fragmented nuclei, hence, the effect of an externally applied force, e.g. an electric field, will have a greater impact on the velocity of electrons. Thus, there can be a large deviation between the kinetic energy of electrons and ions, hence thermal plasmas are those that are at sufficiently high pressure to be in thermal equilibrium. Figure 5 graphically illustrates the differences in thermal and non-thermal plasmas. The inset box within Figure 5 highlights the pressure and temperature characteristics at which the experimentation occurred.

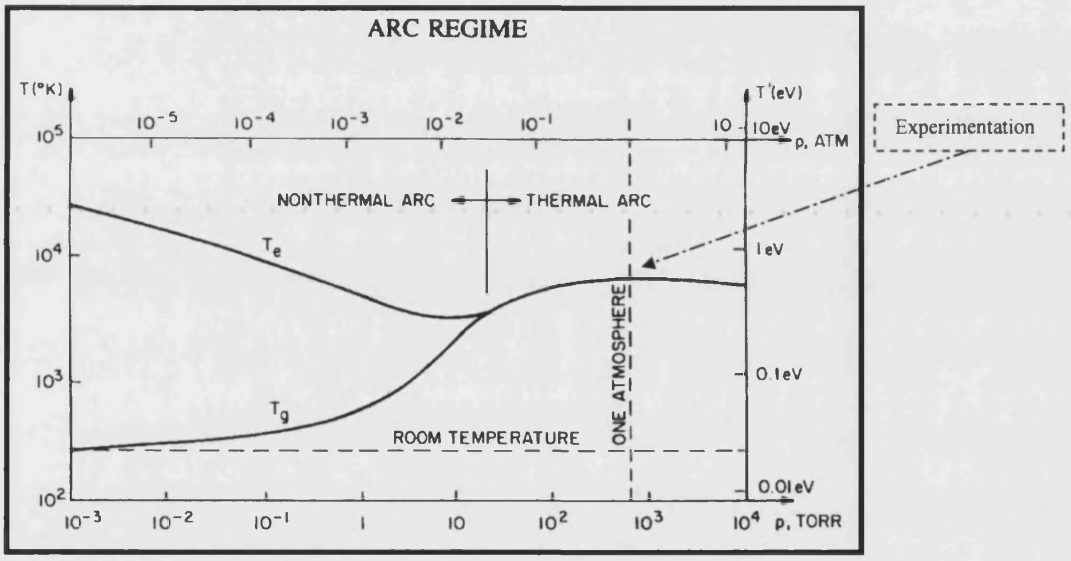

Figure 5: The separation of electron and heavy-particle temperature as a function of pressure (experimental operating regime indicated). [53, 54]

In summary thermal plasmas are gases that are electrically conductive and are at a high enough pressure such that the ion and electron temperatures are within a few percent of each other. In practise thermal plasmas are produced by constrictive arc devices, in which there is a profiled and forced gas flow. These are the factors that determine the spatial and electrical stability of industrial plasmas, other factors, such as power supply specification and control logic, tending to be equipment and control specific.

The unique characteristics of thermal plasmas; such as their energy content (enthalpy), high temperature and density has attracted scientists and engineers to apply thermal plasma technology to industrial processes. While fossil fuel combustion with air has an upper practical temperature range of ~ 2,000 °C, industrial thermal plasmas can produce temperatures of ~ 20,000 °C or more. It is precisely this order of magnitude increase in the temperature, and thus enthalpy content, of thermal plasmas over fossil fuel devices that has led to their industrial utilization and attempts to apply thermal plasma technology to the treatment of various wastes.

4.9 Generation of a Sustained Thermal Plasmas Between Two Electrodes.

The passage of an electric current through a characterising gas, e.g. argon in the case of argon plasma, generates plasma, which together become an electrical discharge. It is this characterizing gas that distinguishes a plasma from an electrical arc, as the gas identity and flow patterns improve stability. While at room temperature gases are extremely electrically insulating, a small fraction of charged species can have the effect of making the gases electrically conductive, a process referred to as electrical breakdown. Here a conducting path is established between a pair of electrodes, i.e. an anode (+ve) and cathode (-ve). Note this can also be achieved by an electrode-less means such as induction (magnetic) and RF (electromagnetic) excitation. There are a number of features that characterise steady-state thermal plasmas:

(i) A relatively high current density, $1x10^6$ A m^{-2} can be reached in the arc column which is even more pronounced at the electrodes where plasma attachment can occur at spots leading to current densities in excess of $1x10^{10}$ A m^{-2}. This gives associated heat flux densities of $1x10^{10}$ Wm^{-2}.

(ii) Secondly the potential distribution in a thermal plasma has a particular form; with rapid changes being associated with the interfacial electrode locations termed 'electrode fall regions'. This is very much a boundary layer phenomenon, as depicted by d_c^1 and d_a^1, Figure 6. The cathode fall 'V_c' is commonly 10V, which is relatively low and a feature of more efficient thermionic emission (cf. 100 V for a glow discharge plasma).

(iii) Thermal plasma has a very high luminosity, provided the pressure is sufficiently high ($p \geq 1$ kPa).

Initiation of the thermal plasma arc can be achieved in four fundamental ways:

(i) Electrode contact.

(ii) Pre-ionisation of the electrode gap, with a high frequency and voltage energy source.

(iii) Applying a source of ionising radiation close to the electrode gap.

(iv) Bridging the electrode gap with a thin wire that is ultimately vaporized forming a conductive species.

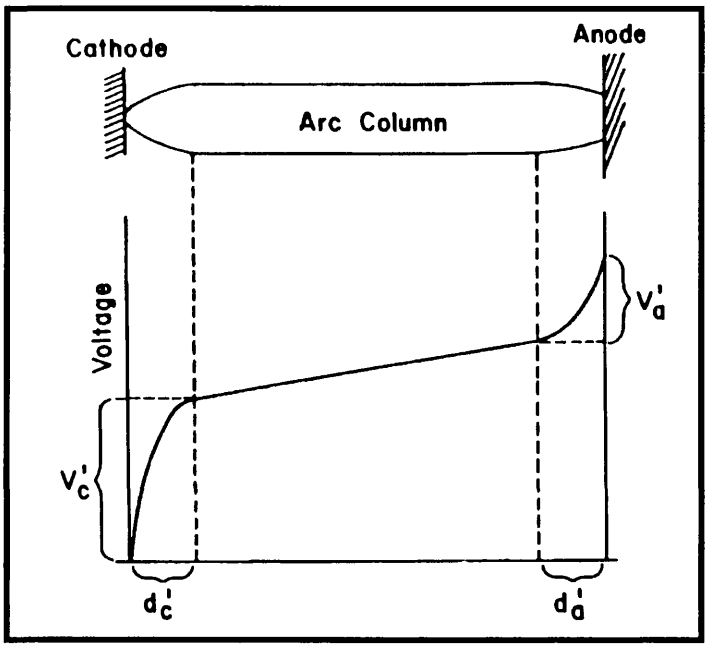

Figure 6: Typical potential distribution along a thermal plasma arc column (thickness of electrode drop regions have been exaggerated, it assumes arc length ≥ arc diameter). [53, 54]

The relevant approach in this research is 'electrode contact', when electrode contact is made an electrical potential is applied across the electrodes. A short circuit current flows over the contact bridge between the electrodes. This heats the contact point sufficiently to allow thermionic emission to occur from the cathode, i.e. the work function of the material is overcome and electrons are emitted. Simultaneously, electrode material is evaporated and ionised at the contact point, which provides the required charge carriers for the development of the stable plasma as soon as the electrodes are separated (i.e. drawing of an arc). The thermal plasma arc current can be described as being made up, nearly entirely, of electron motion due to the imbalance of electron and ion mobilities. In this work argon gas

is also injected through central electrode cavities in graphite electrodes to further stabilize the plasma.

The 'attachment' of the arc to the cathode electrode face influences the nature of plasma, and of most significance, it can be divided into two categories. Firstly, a diffuse / low intensity attachment, without evidence of single or multiple cathode spot attachments that are stationary or slow moving contact points. This mode is attributed to thermionic emission, which is described by the following Richardson-Dushman equation, Equation 24, [54, 55].

$$j_s = AT^2 \exp(-e\phi_c / kT)$$

Equation 24

where:

ϕ_c = material work function = height of potential surface step (eV or V).

ε = electronic charge (C)

A = constant (A K^{-2} m^{-2})

T = Absolute cathode surface temperature (K)

j_s = Saturated 'zero potential' Surface flux of electrons (Am^{-2})

k = Boltzmann's constant

This mode of emission is thermally driven, for carbon A = 150 $kAm^{-2}K^{-2}$ and ϕ_c = 4.5 V, this being the material of electrode construction in this project. Additionally a further increase in anode potential causes a positive field at the cathode surface; this lowers the potential barrier slightly and increases the current.

Secondly, a high intensity attachment, in the form of one single or multiple cathode spot attachments. Here the attachment spots move randomly with high velocities over the cathode surface. Electron liberation here is achieved by 'field emission'. The equation is rather more complex and is primarily driven by electrical field strength, [54, 55].

The industrial use of plasma follows the development in electrical power generation and has always found application in high temperature and environmentally controlled situations. The development of the technology will be described in the following section.

4.10 Historical Development of Plasma Waste Processing

The history of plasma materials processing is essentially as old as the history of electricity, where the influence of electrical discharge on the physical and chemical properties of materials began to be investigated. Inorganic reactions, equipment and patents have tended to dominate in the field of plasma chemistry. Hence all the literature would appear to start from 1867 with the invention of the electric generator. The practical use of arcs for bulk melting began in 1878 when Sir W. Siemens developed the DC furnace. The concepts used in this design are still incorporated into modern commercial furnace design [48, 49]. The key to the successful melting operations was the optimisation of plasma heat transfer to the furnace charge and this is achieved in the transferred arc configuration where the plasma arc(s) actually attaches to the surface of the conductive molten material. Here energy is dissipated predominantly in the gas phase, through resistance heating of bulk condensed phases and through electron transfer at the arc attachment point. Graphite electrode furnaces differ from electric arc furnaces because there is always a specific gas introduced through the electrode(s) to extend, stabilise and control the arc, resulting in a clean, directional heat source that can be controlled independently of process chemistry. Thermal plasma technology is now an established alternative for the high temperature treatment of wastes, but the technology is orientated towards ultimate disposal of the processed waste.

Plasma technology has been successfully used in many industrial applications, from the processing of ores to the welding and cutting of metals. As far back as 1923, the Huls process, designed around a water-cooled plasma torch, was used for producing acetylene. The needs of the chemical production industry, metallurgical process industry, ore processing industry, and the requirement for high enthalpy gas heaters for the testing of aircraft and space vehicles has led to advances in plasma torch and furnace design [48, 49]. In the application for space vehicles, the primary motivation has been to simulate the high temperature atmospheric re-entry environment as they travel at great speed through the earth's atmosphere. These tests, and hence, the equipment designed for them, was only required to last a relatively short period of time. Thus extensive research and development followed this primary use, to allow industrially reliable devices to evolve. During the 1960's thermal plasma systems were being applied to the metals processing industry for ore reduction, scrap metal recovery, and high temperature alloying. Thermal plasma provided technology advantages including the fact that electrical energy can be provided to

the system independently of the partial pressure of oxygen in the system, so that reducing, oxidizing and inert atmospheres can be employed. This gives a distinct advantage over combustion systems where the processing chemistry is directly linked to the net power input achieved. Higher processing temperature and energy fluxes can also be achieved with spatially directed plasmas. High temperatures and a controlled atmosphere are important in producing high quality products such as titanium, tungsten, and steel alloys.

It was recognized that, with some modifications, thermal plasma metal-processing systems could be applied to the safe processing of a variety of hazardous wastes [43, 48]. Thermal plasmas provide a heat source for keeping a molten slag bed at a high enough temperature. With this heat source, organic wastes can be separated and pyrolysed from a feed of soils, mixed scrap and persistent organics, such as dioxins and furans can be destroyed, while allowing for the recovery of metals. Additionally the use of plasma heating instead of fossil fuel heating devices has the effect of greatly reducing the volume of effluent gases, giving rise to more compact gas handling facilities at lower capital cost [12].

In the field of waste management it has been difficult for plasma technology to achieve an economic advantage over conventional incineration and land filling. This has occurred because plasma installations have had to compete with lower cost disposal approaches such as land-fill and sea disposal. However, general environmental awareness, legislation and long term potential liabilities are changing this. Whenever, a technology is effective, economics will dictate the usage of the technology, unless special circumstances prevail. To date the niche applications of thermal plasma technology, in the field of waste treatment, have been in the treatment of mixed nuclear waste, the treatment of hazardous (non-radioactive) waste, in the demilitarisation of ordnance and chemical weapons. In addition, technology adoption has promoted the generation of valuable products and regulatory driven requirements. The last factor, i.e. legislation, has recently given rise to the most significant response, resulting from the adoption of the landfill directive, incineration directive, hazardous waste directive and the green energy regulations that encourage generation of energy from waste.

The next chapter will introduce the laboratory methods use to characterise and define the manufacturing parameters of the glass-ceramics, produced from the selected wastes.

5 Laboratory Experimentation

Four waste materials were selected using the following criteria: availability, generic waste classification, process suitability and technological importance in the field of waste treatment. The waste materials included Classified Municipal Solid Waste (C-MSW) grate ash, Russian MSW fly ash (RFA), German Harbour Sediments (GHS) and British China Clay (BCC) mining waste and were all of a calcium magnesium alumino-silicate nature, with other elements in small proportions, such as iron, sodium, chromium and titanium. The C-MSW was classified with a magnetic drum separator to reduce the magnetic iron and iron oxide content of the waste, which inhibits heat transfer. The other materials were used in their as delivered state. The raw waste materials were characterised to produce a baseline for further experimentation e.g. compositional manipulation and phase evolution. Glasses were produced from the four waste materials. The wastes were blended with virgin materials, to comparable normalised bulk oxide compositions, before conversion into glass. The laboratory experimentation started with the performance of a number of melting trials. All the samples were heated in an electric furnace under an ambient atmosphere and soaked at 1500 °C for 2 hours. The resultant liquids were then quenched to avoid nucleation. Computer data logging facilities were used to record the 'real time' thermal history of the experimental specimens through their entire heat treatment cycle. A proportion, integral and differential (PID) controller complemented the acquired data through accurate control of the muffle furnace thermal cycle to ± 5 °C. The glasses were analysed using Differential Thermal Analysis (DTA) to identify the characterising phase transformations and crystallisation exothermic peaks. The identities of the crystalline phases were confirmed using X-ray diffraction (XRD). The elemental compositions of the crystalline phases were identified using a JOEL 6310 Scanning Electron Microscope (SEM) with Oxford ISIS Instruments Energy Dispersive X-ray Analysis (EDS). A backscattered electron detector was used to investigate the morphology and spatial variations of composition in the microstructure, produced by atomic number contrast. Laboratory based experimental melting trials were accompanied by a continual review of relevant literature, Section 3.

5.1 Waste Material Characterisation

There were variations in the type of compositional analysis supplied with the waste materials, obtained from different industrial and geographical locations, e.g. mineralogical,

trace elements and bulk earth oxides. This necessitated the requirement for verification analysis to be undertaken, as interpretation relied on uncorroborated assumptions, e.g. fully oxidised basis. Inconsistencies associated with analysis conducted in different geographical locations using different analytical techniques in relation to various calibration standards were addressed. In the work the waste material's composition has been fully characterised in accordance with the following methodology. The most promising waste materials were those deemed to be readily available and most likely to be successful in the generation of semi-crystalline glass ceramic products.

5.1.1 Raw Wastes Sampling Procedure

The preparation and analysis of the raw waste materials were undertaken and is detailed in this section. The wastes were grab sampled in ~5 kg batches. These samples were thoroughly mixed and representative sub-samples ~2 kg were taken. The sub-samples were dried in an oven at 150 °C and milled to < 250 μm particle size. Further sub-samples were taken for chemical analysis. It was assumed at this point that the material samples were representative of the wastes and sufficiently homogeneous to be compatible with the requirements of the analytical techniques and their preparation procedures. This allowed the information to be used for compositional computations. The basis of this sampling procedure is ISO 11464 / BS 7755 which is of particular relevance to soil-like samples.

5.1.2 Trace Metal Analysis

Hydrofluoric (HF) acid digestion of the solid waste samples was conducted under microwave radiation, due to the aggressive nature of the preparation technique and its ability to take the materials into solution. This procedure allowed a direct comparison of the untreated ash and solidified melt products to be made. An aqua-regia digestion medium (HCl/HNO_3 @ 3:1 w/w) was initially attempted but was found to be ineffective for taking silica into solution. Trace element analysis was carried out by inductively coupled plasma optical emission spectroscopy (ICP-OES) as described by Thompson and Walsh, (*Handbook of Inductively coupled Plasma Spectrometry, 2nd Edition*, Chapman and Hall 1989). Laboratory standards were used to calibrate the equipment.

The samples were completely acid digested to dissolve trace metal components and subsequently analysed by ICP-OES, to evaluate their compositions. Here, hydrofluoric

acid was used to dissociate the silicate matrix and to dissolve the trace metal components. The resulting solution was passed into a plasma source in a flow of argon gas. Excitation of the elements present within the sample, and subsequent relaxation to their ground states, resulted in the emission of characterising elemental spectral lines. These were detected by a photometer, the intensity and wavelength of the emission being directly proportional to the concentration and identity respectively of the element in question.

5.1.3 Bulk Oxides Analysis

X-ray fluorescence spectrometry (XRF) was used to determine the bulk oxide concentrations; again the instrument was calibrated using relevant laboratory standards. The samples were prepared by drying at 150 °C after which a smaller sample (2 g) was taken and soaked at 1000 °C for 1 hour. A mass of 0.4 g of the prepared materials was analysed for major component oxides on a dry basis using a technique developed from that reported in: T Padfield and A Gray, *A simple fusion method*, Philips Analytical Bulletin F535. HF dissolution with ICP-OES can also be used as an alternative.

5.1.4 Total Carbon and Sulphur Analysis

Carbon and sulphur were measured in a Leco analyser using relevant standards. Powdered samples of the wastes were preheated to 2000 °C in the oxidising environment of an induction furnace and the carbon and sulphur contents were measured by infrared detection with reference to the emission of the gaseous species CO_2 and SO_2 respectively. It was also possible to quantify the 'total loss on ignition' (LOI), i.e. the weight fraction of the sample that partitions to the gas phase upon thermal treatment.

5.1.5 Waste Characterisation Results

5.1.5.1 Trace Element Analysis by ICP - OES

The ICP-OES analysis results indicated that it was more appropriate to perform waste analysis using a combination of XRF for the major oxide constituents and ICP-OES for the trace elements. ICP-OES is most suited to concentrations of < 5000 ppm (0.5 wt%), requiring the waste and glass samples to be significantly diluted prior to analysis, which increases errors. Difficulties were found in measuring bulk oxide analysis data, despite employing acidic digestion processes to improve the silica dissolution and accountability.

	C-MSW Grate Ash				Harbour Sediment (GHS)				MSW Incinerator Fly Ash (RFA)				China Clay Waste (BCC)
Species	wt %		wt %		wt %		wt %		wt %		wt %		wt %
Oxide Species	**XRF**		**ICP-OES**		**XRF**		**ICP-OES**		**XRF**		**ICP-OES**		
Al2O3	11.90		8.50		10.50		10.80		11.20		14.08		33.20
CaO	14.40		13.74		3.40		6.40		15.60		29.24		0.05
Co3O4	0.01												
Cr2O3	0.07		0.03		0.02		0.01		0.10		0.03		
CuO	0.32		0.25				0.01		0.10		0.09		
Fe2O3	8.10		8.43		5.10		5.05		2.00		2.36		1.76
SrO	0.03				0.02				0.06				
MgO	2.60		1.63		2.30		1.80		2.10		1.79		0.42
MnO	0.23		0.22		0.16		0.18		0.13		0.15		
NiO	0.01		0.01				0.00				0.01		
P2O5	1.90		0.98		0.32		0.23		2.40		0.09		
PbO	0.30		0.18				0.00		0.43		0.32		
SiO2	35.80		0.27		47.50		0.31		18.80		0.57		51.60
SnO2	0.07		0.02						0.14		0.06		
TiO2	1.60		0.86		0.56		0.33		1.80		1.44		0.08
ZnO	0.80		0.44		0.03		0.03		1.30		1.05		
K2O	2.40		0.61		2.30		0.42		4.60		3.67		3.97
Na2O	2.00		1.35		1.40		1.43		4.30		4.75		0.02
ZrO2	0.04				0.04								
Sb2O3	0.02								0.02				
CdO	0.00		0.00		0.00		0.00		0.00		0.00		
BaO	0.21				0.02				0.26				
V2O5					0.02								
SO3	5.20				1.20				6.20				
Cl	1.40				1.60				7.50				
SUM	89.42		37.53		76.47		27.01		79.03		59.70		
L.O.I. @ 450°C	6.06	-			14.41	-			12.09	-			8.90
C+H+O	4.32	-			9.05	-			8.32	-			
TOTAL	99.797	-			99.932	-			99.444	-			
Trace metal	**Flame**				**Flame**				**Flame**				
	Photometry	L.O.D	Range		**Photometry**		L.O.D	Range	**Photometry**		L.O.D	Range	
Metals	ppm	mg/kg	mg/kg		ppm		mg/kg	mg/kg	ppm		mg/kg	mg/kg	
Na	10000	4	(4-60)		10600		4	(4-60)	35200		4	(4-60)	
K	5100	4	(4-60)		3500		4	(4-60)	30500		4	(4-60)	
Carbon & Sulphur	**Leco CS444 carbon / sulpur analyser**				**Leco CS444 carbon / sulpur analyser**				**Leco CS444 carbon / sulpur analyser**				
	%	L.O.D	Range		%	L.O.D	Range		%	L.O.D	Range		
Total C	1.26	0.02%	0.02-100%		2.62	0.02%	0.02-100%		2.47	0.02%	0.02-100%		
Total S	0.96	0.02%	0.02-100%		0.4	0.02%	0.02-100%		1.25	0.02%	0.02-100%		
Trace metal / element	**ICP / 1**	**ICP / 2**	**ICP / 3**	L.O.D.	**ICP / 1**	**ICP / 2**	**ICP / 3**	L.O.D.	**ICP / 1**	**ICP / 2**	**ICP / 3**	L.O.D.	
ICP-OES + HF Digestion	ppm	ppm	ppm	ppm	ppm	ppm	ppm	ppm	ppm	ppm	ppm	ppm	
As	61	24	61	<1	56	36	56	<1	11	24	11	<1	
Cd	10	6	28	<1	<1	<1	28	<1	84	84	84	<1	
Cr	242	195	264	<1	68	73	68	<1	182	235	182	<1	
Cu	2802	2203	3192	<1	44	39	44	<1	971	811	971	<1	
Hg	<1	<1	<1	<1	<1	<1	<1	<1	<1	<1	<1	<1	
Zn	4246	3546	5912	<1	285	232	287	<1	7210	8439	8415	<1	
Mn	1543	1498	2045	<1	1127	1278	1120	<1	948	1009	957	<1	
Ti	5038	5136	5767	<1	1837	1965	2484	<1	7622	8638	7497	<1	
Pb	2088	1691	2506	<1	51	36	51	<1	2867	3007	2942	<1	

Table 41: Sample XRF and ICP-OES analysis summary table

The trace element analyses were conducted in triplicate, the results of the work are presented in Table 41. Data consistencies within the same order of magnitude were obtained which is acceptable for waste materials. The ICP-OES bulk oxide analysis results in Table 41 show a low level of consistency, in reporting SiO_2 concentration, with respect to the XRF techniques. The BCC analyses were comprehensive and accurate when supplied by Imerys of Cornwall England so they were not duplicated. They are included in Table 41 for comparison.

5.1.5.2 Bulk Oxides Analysis by WD-XRF

The SiO_2 concentration analysis errors described in Section 5.1.5.1 were resolved using Wavelength Dispersive X-ray Fluorescence Spectroscopy (WD-XRF). The samples were prepared as pressed pellets using cellulose binder and analysed using the UniQuant™ program developed by Omega Data Systems. This is a standard-less program that is suitable for the semi-quantitative analysis of unknown materials. Initial instrument calibration was achieved using pure oxide component samples, used in the program's configuration. The known loss-on-ignition values and the non-volatile carbon, hydrogen and oxygen fractions were added to the sum before normalisation. The carbon values have been converted to carbonate as the rest of the analysis is given in a fully oxidised format. Table 41 gives the analysis results, drawing comparison with the ICP-OES results. The results were normalised with respect to the Al_2O_3-SiO_2-CaO ternary oxide system, as these species were most abundant in the waste materials, Table 42.

Species	BCC		GHS		RFA		C-MSW	
	Wt%	Mol%	Wt%	Mol%	Wt%	Mol%	Wt%	Mol%
SiO_2	60.81	72.45	77.36	82.85	41.23	44.65	57.65	61.47
Al_2O_3	39.13	27.47	17.10	10.79	24.56	15.67	19.16	12.04
CaO	0.06	0.08	5.54	6.36	34.21	39.68	23.19	26.49

Table 42: Normalised waste compositions acquired using WD-XRF

The high proportion of Al_2O_3, SiO_2 and CaO meant that the wastes could be considered as single points on a ternary liquidus phase diagram, so that phase stability and melting characteristics could be predicted and controlled with compositional adjustment. The ternary phase diagram of the Al_2O_3-SiO_2-CaO system is given in Figure 7. The presence of MgO, the next most abundant oxide (<3 wt%), has an effect on the relative stability of the predicted mineralogical phases. The significance of the effect is presented diagrammatically in Figure 8, here it is observed to suppress anorthite formation.

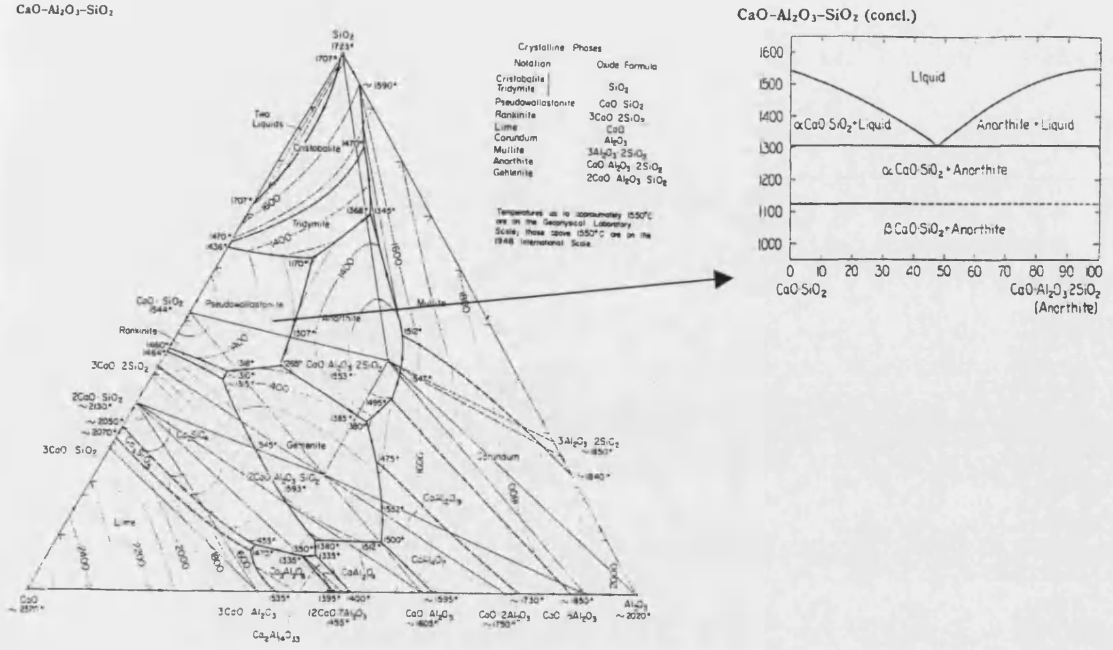

Figure 7: Ternary phase diagrams of the Al_2O_3-SiO_2-CaO system [56]

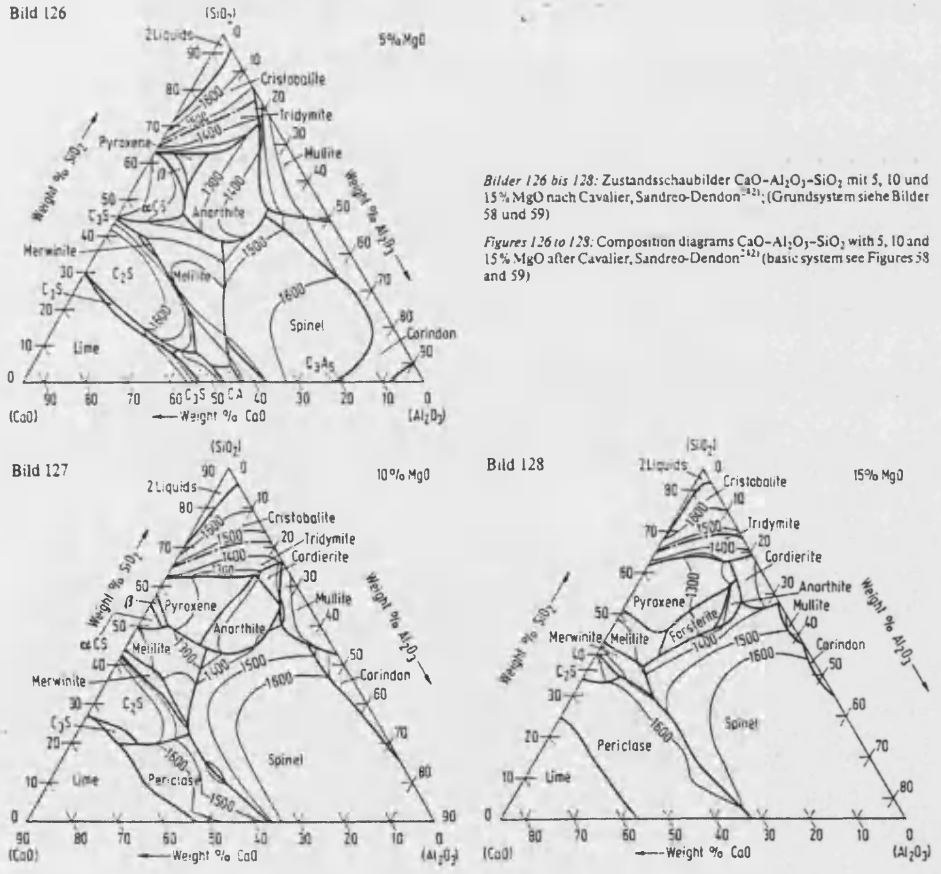

Bilder 126 bis 128: Zustandsschaubilder CaO–Al_2O_3–SiO_2 mit 5, 10 und 15 % MgO nach Cavalier, Sandreo-Dendon[342]; (Grundsystem siehe Bilder 58 und 59)

Figures 126 to 128: Composition diagrams CaO–Al_2O_3–SiO_2 with 5, 10 and 15 % MgO after Cavalier, Sandreo-Dendon[342] (basic system see Figures 58 and 59)

Figure 8: The influence of MgO on the phase stability of the Al_2O_3-SiO_2-CaO system [57]. The anorthite region is reduced as the MgO content is increased.

The results of the Leco carbon and sulphur analyses and the flame photometry sodium and potassium analyses, are also included in Table 41. To establish the accuracy of the acquired WD - XRF results, certified reference materials (BCR 176), that had similar matrix compositions, were analysed to simulate native interferences. The outcomes of the analyses are given in Table 43.

Standard Material Species	Standard BCR 176 City Waste Incineration Ash (Wt %)	WD-XRF Analysis Results (Wt %)
SiO_2	30	28.9
TiO_2	1.42	1.5
Al_2O_3	19.2	18.2
Fe (total)	2.13	2.1
Fe_2O_3		
CaO	12.3	11.8
MgO	3.62	3.4
Cr_2O_3		
MnO	0.18	0.17
V_2O_5		
P_2O_3 (total)	1.27	1.2
Na_2O	5.8	3.7
K_2O	5.42	5.5

Table 43: The certified BCR 176 standard and WD-XRF acquired analysis results

A high level of consistency in the characterization results is observed, with a maximum error ± 0.5 wt%. It is important to note that species such as TiO_2, P_2O_5 and Fe_2O_3 are present in amounts >1 wt%, which is also observed in the raw waste materials used in this work. This compositional data was an essential qualification for undertaking melting trials to allow glass characterisation work to be undertaken.

5.1.6 The Experimental Procedure (Laboratory to Plasma Furnace)

The preparation of a glass-ceramic requires, firstly the formation of a homogenous glass. Secondly, the glass product is shaped and, finally, the application of a controlled heat-treatment process converts the glass into a glass-ceramic material with properties superior to that of the parent glass. To demonstrate that the technology was scalable, robust and generic, the conditions determined in the laboratory were replicated in the prototype plasma-melting furnace. The laboratory experiments allowed different waste systems to be quantitatively compared after similar processing and this information was used to select the

waste system that was used in the prototype plasma furnace. The generic features and terminology of the process will now be discussed:

For glass formation a number of raw materials were mixed and heated together to form a 'batch'. The temperature was high enough to allow the materials to diffuse and to form a homogeneous melt, avoiding the formation of 'cords' and 'stones'. Sufficient fluidity was generated to allow the dissolved gases to escape as bubbles, a process referred to as 'refining'. Complex temperature profiles were employed at this stage of the process, by varying the power input, to ensure that vigorous reactions and assimilation occurred, which ultimately led to the avoidance of micro-structural flaws such as micro-cracks and porosity. The refining stage is governed by the rate of bubble rise, a kinetic process that is directly proportional to the square of the bubbles' diameter, hence large bubbles rise much faster than fine ones. This stage wipes the melt clear of finer bubbles referred to as 'seed'. The overall composition was adjusted to make the whole process of shaping and casting economically and technologically viable, in terms of melting temperature and specific energy requirements. In this case the material system was also compatible with the prototype melting facility; in terms of physical form, power/specific heat requirements and treatment temperatures.

The glass was superheated in the plasma furnace so that its fluidity was sustained during casting and mould filling. Control of the glass composition was essential, as relatively small variations in glass composition had profound influences on both the glass melting and crystallisation characteristics. Consequently raw materials were accurately weighed and metered. This work was purposely conducted within a robust material environment, i.e. small variations in composition did not have a profound effect on the properties of the system.

The problem of refractory liner erosion, observed in the laboratory work, was addressed by using 'cold-skull' melting technology to eliminate the problem. Agitation of the melt was accomplished by the action of convective currents and through the turbulence arising from the escape of gaseous species. The plasma's gas and current surface impingement also enhanced these effects, as the plasma arcs were transferred during steady state processing. Rapid temperature control was achieved due to the dynamic nature of the operative heat transfer mechanisms, i.e. the system was responsive.

The melts were cast into preheated cast iron moulds, to produce simple, flat shapes with high quality top surface finish. Preheated flat plates were also used to cast buttons for laboratory experiments. Internal stresses within the solidifying glassy body were removed by annealing. This stage was important, as externally applied stresses, superimposed on the internal stresses developed during processing, would limit the performance of the materials in service. Annealing was achieved by holding the material during cooling at a temperature sufficient to remove stresses by viscous flow relaxation, which occurs at viscosity values of 10^{12} to 10^{14} poises [20, 51], and below the dilatometric softening point. After annealing the glass was cooled sufficiently slowly to avoid the build up of thermal gradients. Uncontrolled de-vitrification was avoided as annealing occurred outside the higher temperature crystallisation zones at a lower temperature to T_g, which was determined during the experimentation. Cooling to the annealing temperature occurred as a step change, the material moving quickly through the glass transition range.

The next stage in the process was to convert this glassy material into a glass-ceramic. Having nucleated the glass, preferential crystallisation sites were formed, and allowed crystal growth to occur uniformly at higher temperatures. The rate of temperature rise was controlled to avoid deformation, however crystal growth had to be sufficiently rapid to ensure that a rigid crystalline reinforcing framework evolved. Stress evolution in the material was attributed to the differences in the density of the crystalline phases with respect to that of the glassy phase and thermal expansion mismatch between the phases.

The optimum nucleation temperature usually corresponds to viscosities of 10^{11} to 10^{12} poises, which are usually 50 °C above the dilatometric softening point (T_{DSP}) and requires a soaking duration of 0.5 – 2.0 hours to be effective [20, 51]. This was used in the laboratory work and experimentally determined in the prototype experimentation.

5.1.7 Laboratory Melting Trials

The small-scale laboratory melting trials aimed to improve the quality of the refined melts. Homogeneous, translucent and solidified samples were generated from the blended waste materials. The laboratory work was conducted in ceramic crucibles. The conditioning stage of the glass melting process was empirically optimised resulting in the virtual elimination of off-composition cords and entrapped gas bubbles, which occur through the

evolution of gaseous species and the variable viscous/solubility of the mineralogical species originally present. Homogenisation was found to be essential in ensuring the uniformity of the glass-ceramic product and in the generation of associated mechanical and thermo-physical properties, as homogeneous glassy bodies are required for the formation of uniform and fine microstructures. The crystallisation of these glassy materials was successfully achieved without deterioration of the sample's mechanical integrity and surface finish. The variables of 'melting atmosphere' and 'melt containment medium' were found to have a major effect on the appearance and microstructure of the products generated. The basis of the laboratory trials was to develop/define conditions that could be replicated in the prototype plasma furnace.

Reliable melting and refining heat treatment schedules were defined which enabled the crystallisation process to be tailored to specific products within the laboratory, in terms of an engineered microstructure incorporating a known crystalline phase. This was achieved without interference from variations in the glass formation process with morphology.

5.1.7.1 Laboratory Melt Preparation of the Raw Materials

The essence of glass-ceramic production is the growth of a semi-crystalline material from a glass. Glass formation was confirmed using empirical correlations, pouring experiments and XRD. A common normalised waste blend composition and processing regime were employed so that a stable glass could be formed from the different waste materials, with limited tendency to de-vitrify.

A stable glass was obtained by reducing the nucleation rate in the crystallisation temperature range, by reducing the diffusion rate in the glass through manipulation of the proportion of network forming and intermediate oxides, e.g. SiO_2 and Al_2O_3 respectively. This approach was supported by the introduction of TiO_2 to broaden the separation of the Tamman curves, Section 4, as it was renowned for its ability to form heterogeneous nuclei, [9]. Liquid phase separation of sulphide compounds, e.g. FeS, was not observed.

The four waste materials were dried in an oven at 150 °C overnight and ball milled to < 250 μm particle size, over a period of five hours, using alumina milling media. To minimise the effect of particulate composition heterogeneity the powdered waste materials were blended with other chemically pure oxide additives so that their normalised oxide

composition and associated liquidus temperatures were similar. The pseudo-wollastonite - anorthite compositional region employed was chosen due to its success throughout the literature in the field of slagcerams, Figure 8, [9]. The system had a robust nature with a relatively flat liquidus surface, which minimised melting difficulties and problems associated with the assimilation of oxide species due to temperature variations. The viscosity versus temperature curve in this region is relatively flat and allowed control during melting, casting and heat treatment, [62], and will be discussed in Section 5.1.7.10. Blending allowed a reduction in the hot face working temperature of the laboratory furnaces, reducing health and safety risks with practical control measures.

A SiC radiant element furnace was used for melting powder blends at 1450 °C using high purity alumina (> 99.5 wt%) crucibles. The samples, ~80 grams, were removed from the furnace and poured into preheated and machined brass moulds, some of which were thermally monitored. The resulting solidified buttons were transferred to a pre-heated annealing oven and annealed for 12 hours at 300 °C, after which time the furnace was switched off, and allowed to cool to room temperature before opening. Various sample shapes and sizes were cast to meet the configuration requirements of the analytical techniques. This complex preparation procedure produced good quality glass products from all four waste materials. The normalised composition required for all four base glasses was 43.1 wt% SiO_2, 29.2 wt% CaO and 27.7 wt% Al_2O_3. On a molar basis this is 47.5 mol% SiO_2, 34.5 mol% CaO and 18.0 mol% calculated from the chemical analysis results of the different wastes, Table 41. The blending additions made to achieve the desired composition are given in Table 44. Additions of between 10 and 44 wt% were made.

	Waste Material	Oxide Addition	Overall Virgin Oxide Addition
Sample ID	Waste ID	Per 100g of Waste	(wt%)
93 TET	BCC	23.5 CaO	19.0
94 TET	RFA	11.0 SiO_2	9.9
95 TET	GHS	46.9 CaO 32.6 Al_2O_3	44.3
96 TET	C-MSW	13.9CaO 19.9 Al_2O_3	25.2

Table 44: Base glasses compositional characteristics.

Glass cooling rates, i.e. the difference between using an annealed sample and a quenched sample, and their effect on crystallisation phenomena were not considered here as the effect was observed to be negligible by previous researchers [9, 36]. Temperature differences of 5 K were noted in the crystallisation peak temperatures, from DSC, of the different waste samples, which can be considered to be negligible in light of the level of process control employed. All laboratory samples were melted under ambient atmospheric conditions in 80 gram batches. The melting crucibles were coated with a boron nitride aerosol release agent to aid casting. A proportional, integral, differential (PID) controller controlled the thermal cycle of the muffle furnace to the following format for producing glass buttons: ramp from room temperature at 6 °C min^{-1} to 1450 °C, dwell at this temperature for 120 mins, then furnace cool to 1300 °C at approximately –2 °C min^{-1} and dwell for 15 mins, re-heat at 6 °C min^{-1} to 1450 °C then pour the samples into a metallic mould heated to 300 °C.

An addition of TiO_2 was made to all samples during blending, to promote the formation of nucleation sites. At concentrations above 5 wt%, TiO_2 forms compounds with other oxides rendering it ineffective as a nucleating agent, so an optimum 1 wt% TiO_2 addition was employed, [8, 9, 36, 45,50]. The ceramic crucibles used in the melt trials were investigated in detail. Figure 9 indicates that the level of wetting and dissolution were minimal, and that the composition of the samples was not grossly altered.

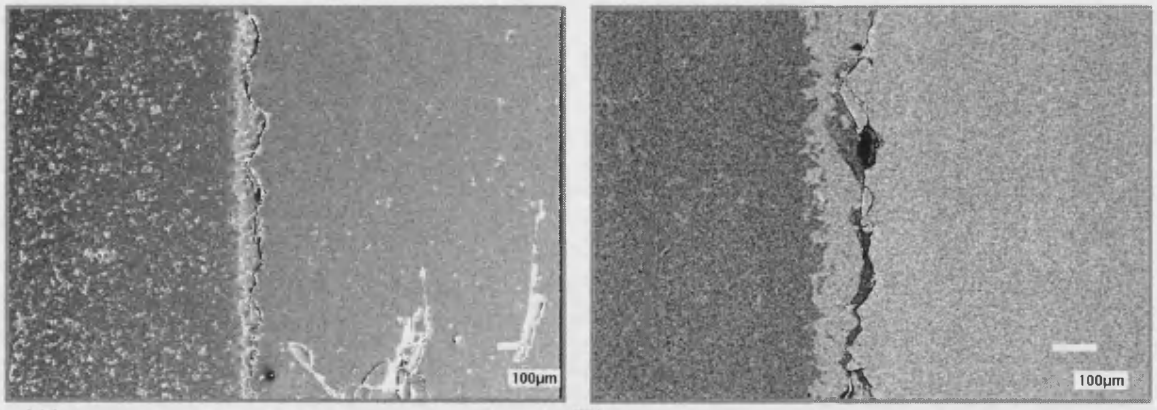

Figure 9: BCC sample (A) Secondary electron micrograph of the crucible-melt interface. (B) Backscattered electron micrograph of the crucible-melt interface. The crucible is shown on the left hand-side of the micrographs and the melt on the right

The crack defines the interface between the solidified glass and crucible formed due to the differential thermal contraction of the waste glass, relative to the crucible, during cooling.

5.1.7.2 Dilatometry

The coefficient of linear thermal expansion and the resulting dimensional changes that occurred with changes in temperature were important as they defined the thermal processing cycle and critical thickness of the cast products. A glass-ceramic was required with good thermal shock resistance, so the coefficient of thermal expansion was required to be as low as possible to minimise the strains resulting from temperature differentials. Crystallisation produces crystallites with different coefficients of thermal expansion to that of the parent glass, so the glass-ceramic was examined as a composite material. Its thermal expansion coefficient was defined by the elastic properties of the phases present and their volume fractions, Equation 25. The equation could also have been used to assess the phase proportions, if the identity and properties of the phases present had been known and significantly different enough, [20]:

$$\alpha = \frac{\frac{\alpha_1 K_1 F_1}{\rho_1} + \frac{\alpha_2 K_2 F_2}{\rho_2} + ...}{\frac{K_1 F_1}{\rho_1} + \frac{K_2 F_2}{\rho_2} + ...}$$

Equation 25:

Where: α = linear thermal coefficient ($°C^{-1}$)

K = bulk modulus (Pa), hydrostatic pressure / fractional volume change (elastic modulus can be substituted if Poisson's ratios are similar)

F = weight fraction of component

ρ = phase density ($kg\ m^{-3}$)

Difficulties arose because the process of crystallisation also altered the composition of the residual glass which was not possible to measure. Cylinders of 8 mm length and 6 mm diameter were cast using preheated metallic moulds. The as cast samples were cut to obtain parallel faces using a diamond saw. These samples were annealed at 300 °C overnight then placed in a high temperature Netzsch dilatometer with alumina sample furniture. The sample chamber was evacuated, to eliminate errors induced by convective currents, to an ultimate pressure of 1.5×10^{-5} mbar. Thermal expansion data was collected using a heating rate of 5 $°C min^{-1}$. The maximum temperature achieved for each sample

was ~50°C above the dilatometric softening point (T_{DSP}), which was the temperature at which viscous flow was exactly counteracted by thermal expansion during the measurement and the point at which problematic equipment wetting would occur. The traces produced have the strain as the ordinate and the sample temperature as the abscissa.

5.1.7.3 High Temperature Differential Scanning Calorimetry (DSC)

Chemical reactions and/or structural changes were identified, using high temperature DSC, through their evolution or absorption of energy within the semi-crystalline or glassy materials. DSC was used to investigate the crystallisation process to devise heat treatment schedules for crystallisation.

Samples were ground to powder, Section 5.1.7.1, then analysed using a Netzsch 404 high temperature DSC, in an alumina sample pan. Both silver and zinc standards were used to calibrate the equipment. Data collection was carried out at a heating rate of 10 °C min^{-1} under an argon atmosphere from ambient temperature to a maximum of 1300 °C. The traces produced had the specific rate of energy release as the ordinate and the sample temperature as the abscissa. Exothermic effects are indicated as peaks and endothermic effects as depressions in the curve.

5.1.7.4 Scanning Electron Microscopy (SEM)

A scanning electron microscope (Joel 6310) was used to investigate the micro-structural texture and crystallite morphology of the semi-crystalline materials. The samples were mounted in epoxy resin and cured at 40 °C for two hours, then their surfaces were ground with SiC paper and polished with a diamond paste. The metalographic polishing schedule is shown in Table 45:

Stage	Surface	Particle Size	Speed (rpm)	Force (ibf/sample)	Head Rotation	Time (mins)
Grinding	Paper	P320 Grit SiC	150	6	COMP	Until Planar
Sample Integrity Stages	Ultra-Pad	9 μm oil-based diamond	240	6	COMP	5
	Texmet 1000	3 μm oil-based diamond	240	6	COMP	5
	Texmet 1000	0.05 μm colloidal silica[1]	100	10	COMP	5
Polishing	Chemomet	0.05 μm colloidal silica[1]	100	3	COMP	5

[1] Buehler Mastermet 2, 0.05 μm colloidal silica suspension

Table 45: Metallographic Polishing Schedule

Heat was applied to the mounting resin after polishing to soften the resin and release the sample for thermal etching. The samples were heated to 600 °C for 15 minutes, which was approximately 150 °C below the sintering temperature, and the sintering temperature was taken to be two thirds of the sample's melting points, [58]. The thermally etched samples were mounted on stainless steel plates using a water based carbon dag compound. The samples were then sputter coated with gold using an Edwards 150B Sputter coater.

5.1.7.5 Hardness and Fracture Toughness Measurements

Micro-hardness measurements were made using a Zwick Vickers sharp indenter which met the relative dimensional requirements of the microstructure for fracture toughness analysis. The glassy samples were loaded at 50 grams for 15 seconds, while the semi-crystalline samples required loads between 150 – 200 grams to produce the necessary contact pattern. The size of the indentation and the radial crack profile was measured immediately, to limit slow crack growth. The reported values are the arithmetic means of the values taken from the two orthogonal radial directions, from five measurements. Quantitative evaluation of hardness and of fracture toughness was achieved by the application of elastic/plastic indentation fracture mechanics in conjunction with empirical observations.

Only geometrically consistent crack patterns were evaluated and as a minimum requirement, $c \geq 2a$, which defines a stable crack profile. Additionally, care was given to the limitations imposed by slow crack growth and by crack-microstructure interactions. Figure 10 is a schematic representation of the indentation deformation fracture pattern for the Vickers geometry. P' is the peak load and a and c are the characteristic dimensions of the plastic deformation region and the radial/median cracks, respectively.

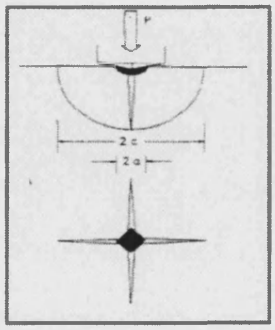

Figure 10: The Vickers indentation fracture system showing characteristic dimensions c and a of penny-like radial/median crack and hardness impression, respectively [59]

Typically, radial crack dimensions were of the order of 100 μm, so cracks intersected by heterogeneities greater than 1 μm gave error fluctuations in the *c* measurement. If the microstructure was visibly different in various areas of the sample, each region was tested separately. If the microstructure had coarsened to be comparable in size to the indenter, the fracture pattern would have been disrupted by local grain failure events and by crystalline anisotropy. The test specimens were annealed so that the surfaces contained no pre-existing stresses prior to indentation. The experimental approach adopted here was valid up to the load-chipping threshold, which is defined as the load at which the sub-surface lateral crack systems and the median/radial crack systems intersect at the surface under load causing fragmentation of the material.

The evolution of the crack profile indicated in Figure 10 was driven by the residual irreversible component of the stress field, and the radial cracks, grew to their final lengths as the indenter was removed. This approach has been observed to be valid empirically for a wide variety of ceramic materials including amorphous, poly-crystalline and mono-crystalline materials with an accuracy of ± 15%. The approach requires a Young's modulus to hardness ratio (E/HV); and E and HV were measured to within ± 5%. The equation used and the associated calibration constant are shown in Equation 26, [59]:

$$K_c = \chi_r \left(\frac{P^l}{c_0^{3/2}} \right) = \delta_v^R (E/HV)^{1/2} \left(P^l / c_0^{3/2} \right)$$

Equation 26

Where:

K_c =Critical stress intensity factor, (Pa $m^{0.5}$), fracture toughness

E = Elastic modulus, (Pa)

HV = Vickers hardness = $P/(2a^2)$, (Pa)

P' = Peak force (N)

c_0 = Equilibrium crack dimension (when $K_r = K_c$), (m)

δ_v^R = Calibration constant = 0.016±0.004, (dimensionless)

χ_r = Constant associated with material constants and loading geometry constants, (dimensionless)

The equation is derived from the mathematical representation of a crack system subjected to conditions of mechanical equilibrium both during and after the contact event, such that the radial cracks remain stable, i.e. $K_r = K_c$ and $c = c_o$.

5.1.7.6 Density Measurements

Density measurements were taken in accordance with BS1902, [85]. All samples were weighed to an accuracy of ±0.0001 grams. Archimedes' principle was used in conjunction with a purpose built balance bridge assembly to determine the dry weight (W_a), immersed weight (W_b) and soaked weight (W_c) of the samples. The immersion fluid used was deionised water of density (D_l). Equation 27 was used to determine the bulk density and apparent density of the solid.

$$\text{Bulk density} = \frac{W_a}{W_c - W_b} x\ D_l$$

$$\text{Apparent density} = \frac{W_a}{W_a - W_b}\ x\ D_l$$

Equation 27

Here the density of the immersion fluid was taken to be that of deionised water i.e. 1 g cm^3, it was noted that there were slight variations in the density of de-ionised water as a function of temperature. The density of a glass-ceramic lies between the densities of glasses and conventional ceramics and it is a function of the densities of the various crystalline and glassy phases present and their relative proportions. Thus, density measurements were carried out to indicate the level of porosity / structural integrity and SEM and XRD were used to map the extent of crystallisation.

5.1.7.7 Elastic Modulus Measurements

Ultrasonic pulse measurements were used to determine the elastic properties of the material samples generated. The wave velocity, c, of a pulse of longitudinal ultrasonic vibration travelling in an ideal elastic solid can be described using Equation 28.

$$c = \sqrt{\frac{E}{\rho}\frac{(1-\nu)}{(1+\nu)(1-2\nu)}}$$

Equation 28

where: E = Dynamic elastic modulus (Pa)

ρ = Density (kg m^{-3})

ν = Poission's ratio (dimensionless)

Re-arrangement gives an expression for elastic modulus, Equation 29, that was utilised in further engineering stress / strain calculations.

$$E = \frac{\rho c_l^2 (1+\nu)(1-2\nu)}{(1-\nu)}$$

Equation 29

The pulse velocity, c_l, of the ultrasonic signal was derived from the quotient of specimen dimension and the ultrasonic radiation transmission time. This time parameter was measured using the Portable Ultrasonic Non-destructive Digital Indicating Tester (PUNDIT) supplied by CNS Farnell, which complied with BS 1881 and ASTM C597. If the pulse velocity is independent of frequency (f), the wavelength (λ') of the pulse vibration is inversely proportional to the frequency:

C *(constant)* = f. λ' Hence λ' = constant/f

This means that the pulse velocity is a function of the material, due to the elastic propagation of the incident signal, allowing material property measurements. Measurements were made at 150 kHz and the higher frequencies gave a narrower beam of pulse propagation, but the attenuation was greater due to the shorter wavelength. Finally the technique has limited accuracy as significant error is produced at the point of coupling between the probe and detector. These factors are functions of surface pressure, surface finish, contamination and planar character, none of which were guaranteed.

5.1.7.8 Radial Solidification Temperature Profiles

Heat transfer through molten glasses was considered in the design of the products and the control of processing conditions at elevated temperatures. Due to the transparency of slags / glasses to infrared radiation, the heat transfer in such media is affected by radiative conduction. However in polycrystalline materials there are two independent mechanisms of heat transfer; namely thermal (phonon) conduction by the propagation of lattice waves; and radiative (photon) conduction by absorption and re-radiation of electromagnetic energy. At elevated temperature, heat transfer by photons predominates as lattice vibrations inhibit phonon conduction. From a mechanistic view point radiant energy

absorbed at the surface causes a mono-layer of atoms to become hot and to re-radiate energy which is absorbed by the adjacent layer of atoms and so on. Hence, a process of adsorption and emission of radiant energy gives rise to heat transfer. The Stefan-Boltzmann Equation mathematically describes this heat transfer, Equation 30:

$$E_r = \varepsilon.\sigma.T^4$$

Equation 30

where, for a non-black body:

E_r = radiant energy emitted by unit surface in unit time, (J m^{-2} s^{-1})

σ = the Stefan – Boltzmann constant, (J m^{-2} s^{-1} K^{-4})

ε = hemispherical emissivity, which is the ratio of the total emissive power of a non-black surface to the total emissive power of a black body at the same temperature

The same radiant conduction argument was applied to the cooling of glassy samples, and it is this phenomenon that produced the internal thermal gradients in cast products and the associated stress contours. Here, these gradients were quantitatively assessed as a function of material composition and sample size, to avoid fracture on the cooling of glassy products and ultimately the failure of the glass tiles.

The solidification temperature profile experiments, to assess thermal gradients, were conducted on all four glassy waste materials. The temperatures at different radial positions were quantitatively monitored as a function of time and the maximum temperature differential generated after a definite period were calculated. Temperature gradients developed in the glass as the radiant heat transfer mechanisms operative within the glassy materials were less effective than the surface heat transfer mechanisms. Internal material heat transfer was further inhibited because the glasses had a black coloration. This produced a residual stress due to differential thermal expansion. The experimentation was aimed at quantitatively evaluating the extent of the temperature profile responsible for the developed stresses under practical conditions. The stresses limited the dimensions of the products that could be formed from the black glass.

The apparatus used to evaluate the temperature profile is shown Figure 11. An analogue to digital thermocouple converter with a built in cold junction calibration was installed for

use with a K type thermocouple (100 –1200 °C). The PC data acquistion software 'Picolog' for the Windows 95 operating system was used to generate real time graphical representations of temperature.

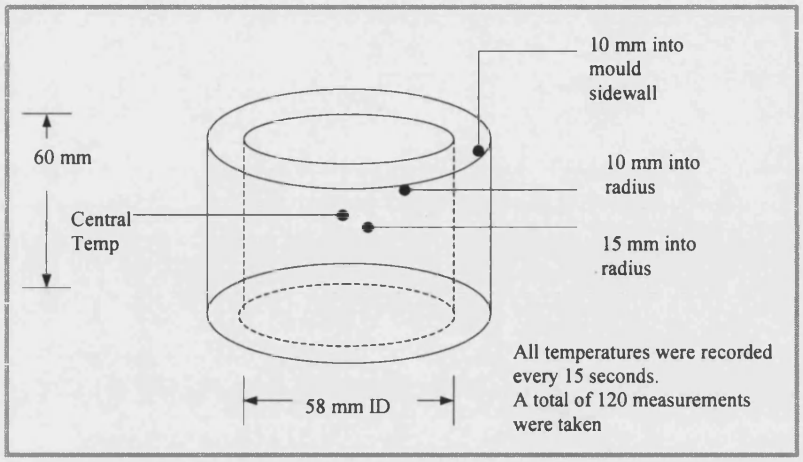

Figure 11: Radial solidification temperature profile experimental equipment (Positions of K type thermocouples are shown as black dots)

This thermal profile assessment is not the same as 'thermal shock', which is a generic term used to describe the stress that results from a body at a given temperature being rapidly cooled by an external medium to a lower temperature. An 'infinite quench' model is often used to model this phenomenon, [51,60].

5.1.7.9 X-ray Diffraction

X-ray diffraction measurements were obtained from as-cast solid specimens sectioned with a water-cooled diamond tipped cutting disc. The button specimens produced in the laboratory were sectioned radially to give two perpendicular surfaces. This specimen geometry complemented the X-ray source/detector configuration. A Philips X-ray diffractometer comprising a PW1730/00 4kW X-ray generator and a fine focus 2 kW copper target X-ray tube, was used at 40 kV and 25 mA. A Phillips PW1820/00 computer-controlled vertical diffractometer goniometer was used to acquire the intensity information in conjunction with Philips PW1877 PC-APD, version 3.5b, diffraction software. The resulting diffractograms were examined using powder diffraction file PDF-2 database sets 1 – 45, International Centre of Diffraction Data (ICDD). The samples were examined for values of 2θ of 5 – 60° with a step size of 0.02 ° in a continuous sweep. The important assumption was that the material was composed of an aggregate of tiny crystals in random

orientations with respect to each other, even though the materials appeared homogeneous on a macroscopic scale. As the major constituents of the system were SiO_2, Al_2O_3, CaO and MgO, the types of phase formed can be predicted according to the literature and thermodynamic data and diagrams. The predicted phases were melilite (a solid solution between gehlenite and akermanite), clinopyroxene, anorthite, spinels, merwinite and wollastonite. Other phases that do not appear on the equilibrium phase diagram are monticellite, rankinite, forsterite, periclase and oldhamite, their proportions and appearance being a function of composition and cooling rate [9]. Accurate determination of the lattice 'd' spacing was achieved using the following re-arrangement of the Bragg equation, Equation 31, which describes constructive interference [10]:

$$d = \frac{\lambda}{2\sin\theta}$$

Equation 31

The crystallites gave sharp X-ray diffraction spectra that were used to identify the crystalline phases. In contrast, the amorphous solids generated diffuse X-ray diffraction patterns with a complete absence of any sharp reflections. The most intense reflections were generated from the constructive X-ray interference, Equation 32:

$$n'\lambda'' = 2d\sin\theta$$

Equation 32

where:

n' = The order of reflection (indices)

λ'' = The wave length of the incident radiation (m)

d = Inter-crystallographic plane spacing (m)

θ = The Bragg angle (°)

Care was taken to account for possible distortion effects due to solid solution phenomena, meta-stability and residual stress. The potential for error gave rise to the decision to try to map out the crystallisation process using X-ray diffraction in combination with other techniques, i.e. phase changes and proportions as a function of time and temperature, Section 8. In order to compare X-ray intensities accurately it was necessary to keep factors such as exposure, time of irradiation and detector constant, to allow both qualitative and semi-quantitative comparisons to be made. A quantitative approach was not applicable as the materials had variable compositions and compositional homogeneity.

5.1.7.10 Viscosity of $CaO-MgO-Al_2O_3-SiO_2$ Melts

The viscosity of the multi-component oxide melts defined the liquid phase reaction rates and casting characteristics during the laboratory investigations and the plasma furnace operation. The basis of this quantitative approach was the application of the work carried out by Turkdogan *et al* [61]. This describes how the viscosities of complex blast furnace slag compositions have been measured extensively and correlated with structural changes in the case of liquid aluminosilicate melts. The data employed related to the $CaO-MgO-Al_2O_3-SiO_2$ system, i.e. the bulk composition of the waste materials employed. Complementary electrolysis measurements showed that the slag systems under consideration were electrically conductive when molten, so that the melts became an active part of a plasma circuit, allowing Joule heating to occur.

The structural basis of this approach was the molecular architecture of the tetrahedral bonding of Si-O and Al-O units, plus the rupture of these bonds by the addition of network modifiers (basic oxides). This defines the size of the resulting flow unit in the melt. The effect of temperature on the flow unit and activation energy was also considered. Rheological experimental inaccuracies were avoided, by employing non-graphitic containment, since colloidal graphite particles contaminate melts and change their composition. All measurements were made in the temperature range 1200 – 2000 °C, which was applicable to the plasma furnace operation.

The whole approach was based around 'equivalence' and in this particular case the silica equivalence of alumina. Both Al_2O_3 and SiO_2 have similar, but not identical, effects on the viscosity of industrially complex slags. It was assumed that in a basic slag the tetrahedral Al-O coordination is isomorphous to that of Si-O, so both Al and Si occupy similar lattice sites. The relationship is only valid for low Al_2O_3/CaO ratios, [61, 62]. Hence for a given temperature and viscosity, the silica equivalence of alumina can be written as follows.

$$N'_a = N'_{\text{SiO2 pseudo-binary equivalence}} - N'_{\text{SiO2 pseudo-ternary equivalence}}$$

Where:

N' = molar fraction

N_a=silica equivalence of Al_2O_3

Normalised Binary system = $CaO-SiO_2$

Normalised Ternary system = $CaO-SiO_2-Al_2O_3$

[MgO] + [CaO] = [CaO] + [CaO] when calculating

Empirical data indicate that alkaline earth oxides are also interchangeable in their effect on viscosity. Figure 12 describes the level of correlation achieved at the temperatures applicable to the plasma plant casting process for different slag systems [62]. It was valid to treat CaO and MgO as interchangeable in the derivation of N_a, as they have been determined to have equivalent effects on viscosity. To aid understanding of this approach, a plot of log η, i.e. viscosity in poise, versus absolute temperature for different $N_{SiO2}+N_a$ vales is given in Figure 12, in the temperature range 1150 – 2000 °C. Note that η is often expressed in poise, 1 P = 0.1 Nsm^{-2}. For the waste systems employed in this study, the following values were derived using this mathematical methodology, Table 46, [62].

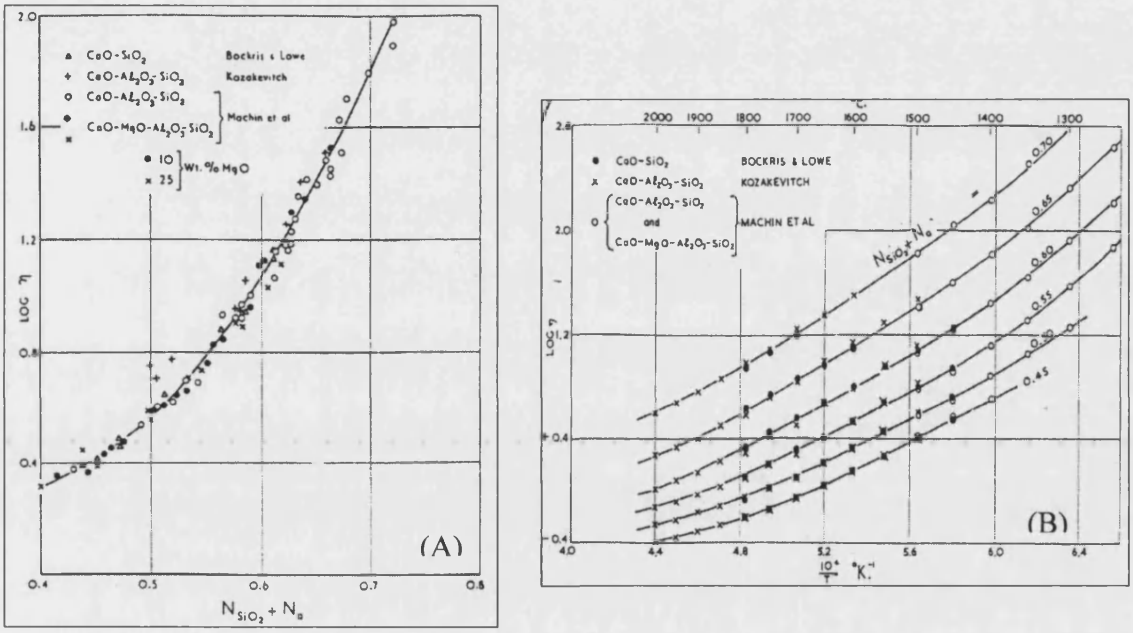

Figure 12: (A) Viscosity versus composition for CaO-MgO-Al_2O_3-SiO_2 melts at 1500°C, (B) Viscosity versus temperature and composition of molten silicates and alumino-silicates

Sample	Waste	N_{SiO2}	N_a	N_a+N_{SiO2}	*Log η (poise) @ 1600 ℃*
93TET	BCC	0.533	0.139	0.672	1.2
94TET	RFA	0.538	0.102	0.640	1.1
95TET	GHS	0.367	0.101	0.468	0.15
96TET	C-MSW	0.409	0.133	0.542	0.5

Table 46: Silica Equivalence Values for Viscosity Evaluation

The viscosity versus temperature curves for the different glassy materials used in this work are given in Figure 13. Viscosities of 10 P were sufficient to allow the slag to be tapped

from the plasma furnace. Here it can be noted that at temperatures of 1650 °C and above, all of the waste blend's viscosities were below the critical level of 20 poises. However, distinctly different curve configurations were obtained for the different waste materials, due to compositional differences. This was not meant to be an exacting approach but a way of assessing relative melt characteristics and validity of the experimental technique without the requirement for expensive high temperature rheological equipment.

To conclude, alumino-silicates behave as Newtonian liquids, i.e. their viscosity is independent of shear stress. Hence, the following Arrhenius type equation can be used to describe the temperature dependence of viscosity, Equation 33:

$$\eta = \eta_o \exp\left(\frac{E_\eta}{RT}\right)$$

Equation 33

The data used to construct Figure 13 were used to assess the material constants in the above equation to allow further extrapolation. In summary, on a molar basis MgO and CaO have the same effect on the viscosity of the melt. Al_2O_3 and SiO_2 affect the viscosity of the slags similarly, however the total acidic oxide concentration cannot be represented as the sum of the two molar species and the equivalence equation must be employed.

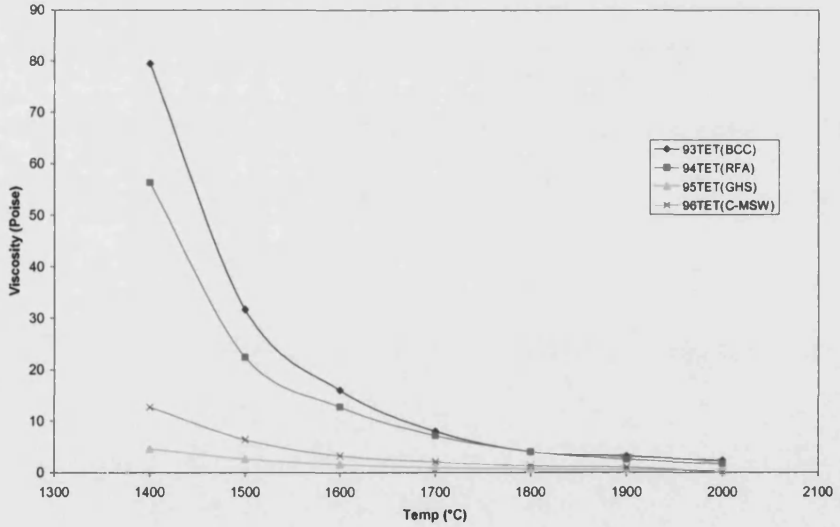

Figure 13: Variation of sample viscosity versus temperature curves

5.2 Experimental Results

The thermal expansion, DSC, micro-structural, compositional and mechanical analysis results, of the glasses produced from wastes, will now be described.

5.2.1 Thermal Expansion Characteristics

The linear thermal expansion curves (Δl/l versus temperature) acquired from the four annealed waste glasses produced at a heating rate of 5 °C min^{-1} are shown in Figure 14. The curves displayed similar features, but were distinctly different in magnitude.

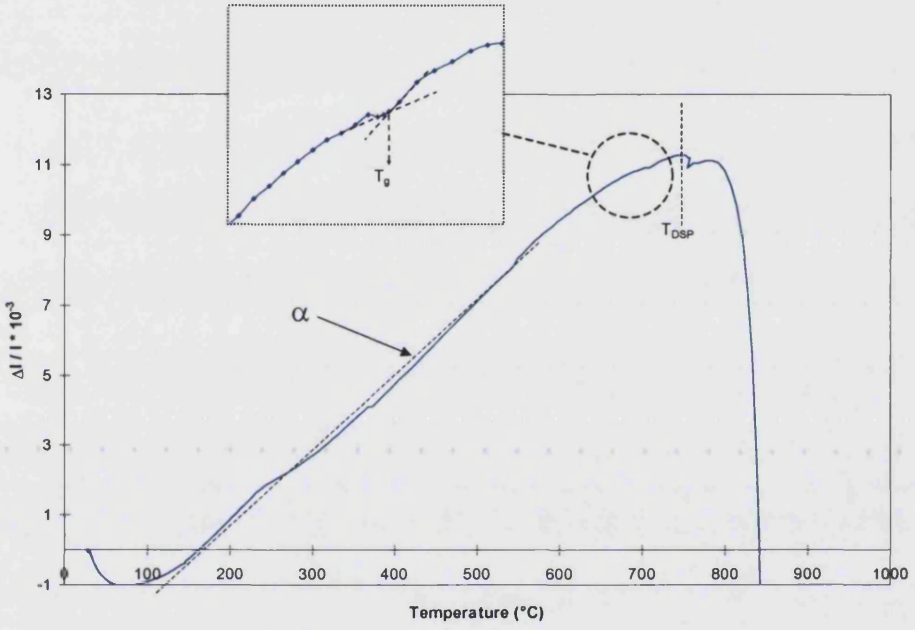

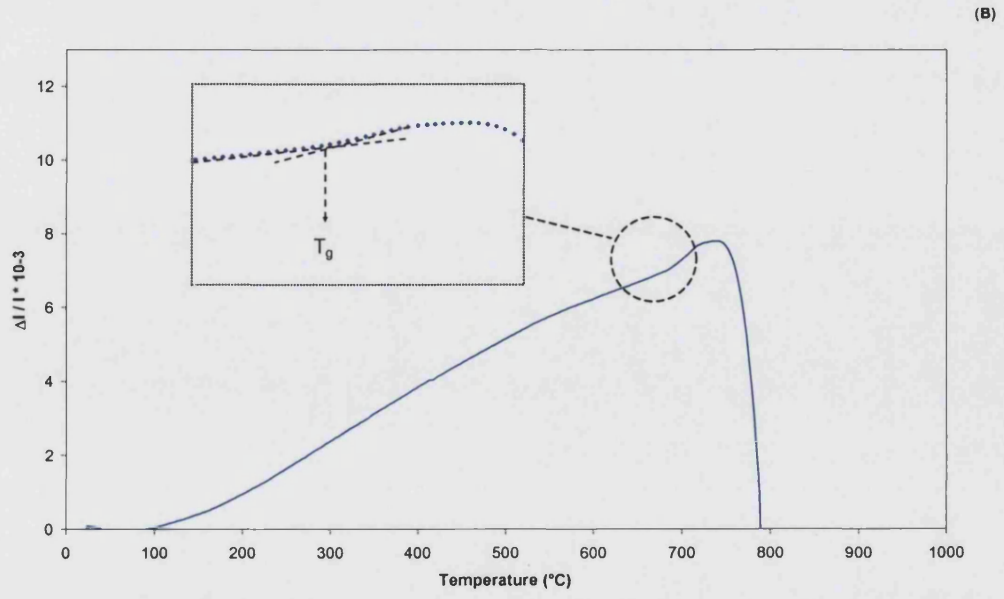

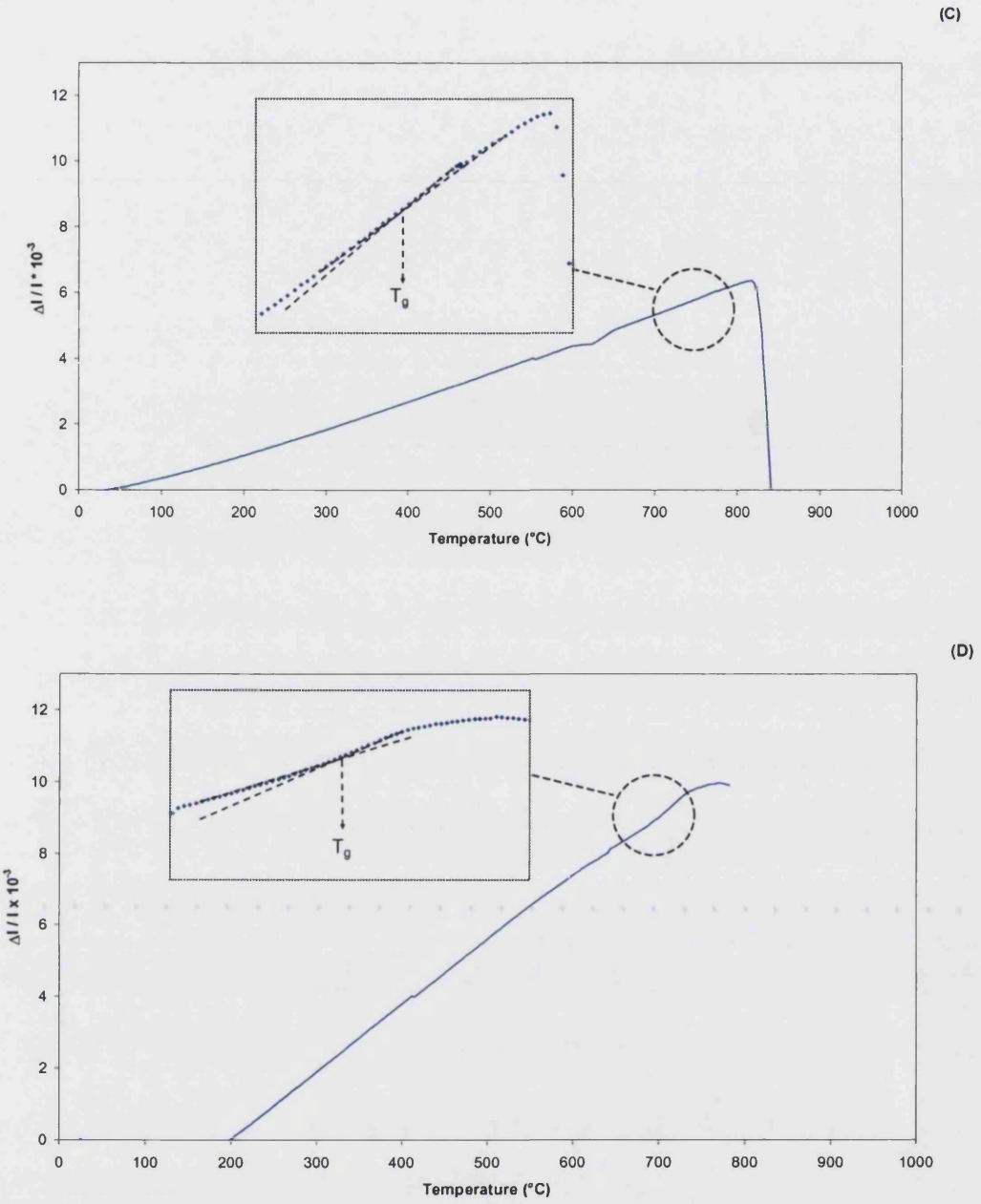

Figure 14: The uniaxial thermal expansion curves (A) 93TET, (B) 94TET, (C) 95TET and (D) 96TET, construction lines for T_g and T_{DSP} identification are included

All glasses exhibited glass transition temperatures (T_g) and dilatometric softening points (T_{DSP}). The former was determined as the point of intersection of the lines extrapolated from the adjacent sides of the point of inflexion of the curve, shown in Figure 14A. T_{DSP} was determined as the maximum of each graph, Figure 14A. The coefficient of linear thermal expansion (α) was determined in the temperature range 100 – 600 °C from the

slope in the linear part of the curve, Figure 14A. Deviations were observed at the extremities of the temperature scale, where Equation 34 which defines α, was not obeyed.

$$\alpha = \frac{1}{L}\left(\frac{\partial L}{\partial T}\right)_P$$

Equation 34

Where: α = linear thermal expansion coefficient ($°C^{-1}$)

L = specimen length (m)

T = temperature (°C)

Figure 14A is annotated to illustrate how the data were acquired. Higher temperatures were not examined, as the glassy samples underwent phase transitions resulting in softening and wetting. Material property values from the experimental measurements on the four wastes are given in Table 47.

Sample ID	Waste Precursors	T_g (°C)	T_{DSP} (°C)	α (x 10^{-7} K^{-1}) 100 – 600 °C
93 TET	BCC	708	760	210
94 TET	RFA	689	741	130
95 TET	GHS	750	817	80
96 TET	C-MSW	709	775	180

Table 47: Dilatometric properties of the glassy samples

The standard deviation of all of the materials' recorded T_g values was 25.7 °C. T_g gave an indication of diffusional atomic motion, a process that is thermally activated and chemically driven. The limited variations of T_g between the wastes validated the methodology used in the waste batch preparation and melting stages of the research, which were used to determine heat treatment schedules.

The standard deviation for all of the recorded T_{DSP} values was 30.1 °C. This temperature was employed in the determination of heat treatment schedule for the as-cast glassy tiles; it indicated when softening and shape deformation would start to occur.

Sample 95TET was considered to be the most thermally stable, with the highest T_g and T_{DSP} temperatures, and with the lowest coefficient of linear thermal expansion. This observation was consistent with the original compositional analysis work, where the GHS material was determined to have the highest proportion of network-forming oxides and

lowest fraction of network modifying oxides, Section 5.1.5. The coefficients of linear thermal expansion showed the most significant variation between wastes and had the most influence on the casting stages of the process.

5.2.2 High Temperature Differential Scanning Calorimetry (DSC)

The four waste glasses were analysed using high temperature DSC, the technique extended the temperature range of analysis to 1300 °C, going beyond of the scope dilatometric investigation. This allowed other phase transformations to be observed. Sample 93 TET (BCC) retained its shape during the test while the other samples melted and set solid in the containment pans. This was attributed to the open planar structure of the clay minerals and the low level of network modifying oxides present within the waste, Section 5.1. Exothermic energy releases were noted at different temperatures for the different samples. The DSC traces are shown in Figure 15, A to D, with the same scale for comparison.

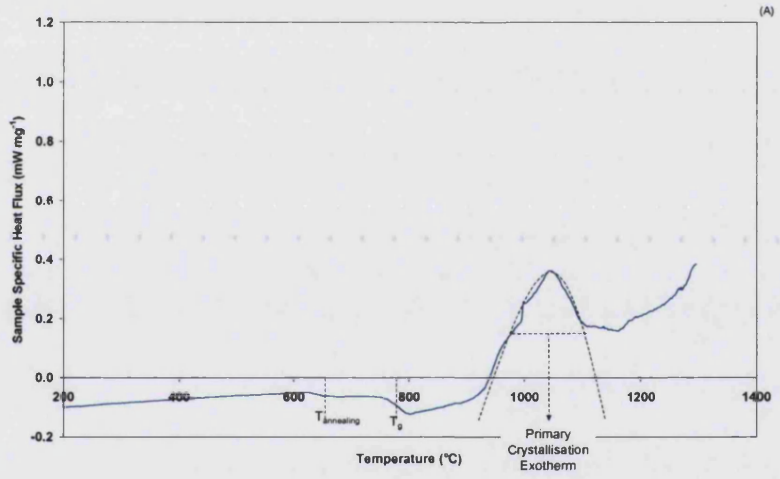

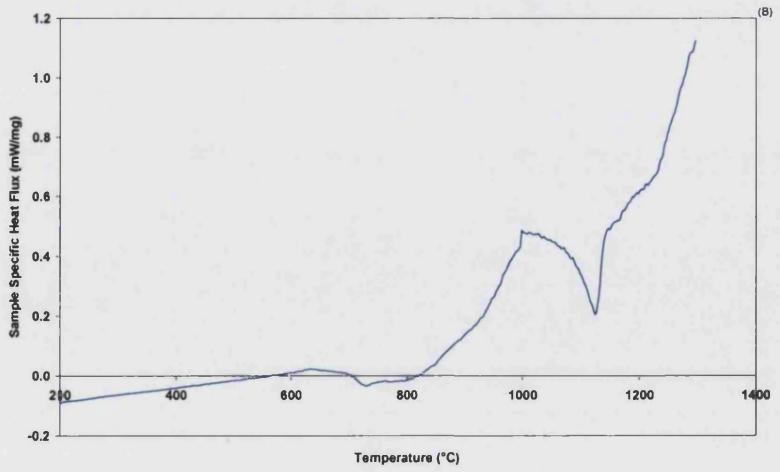

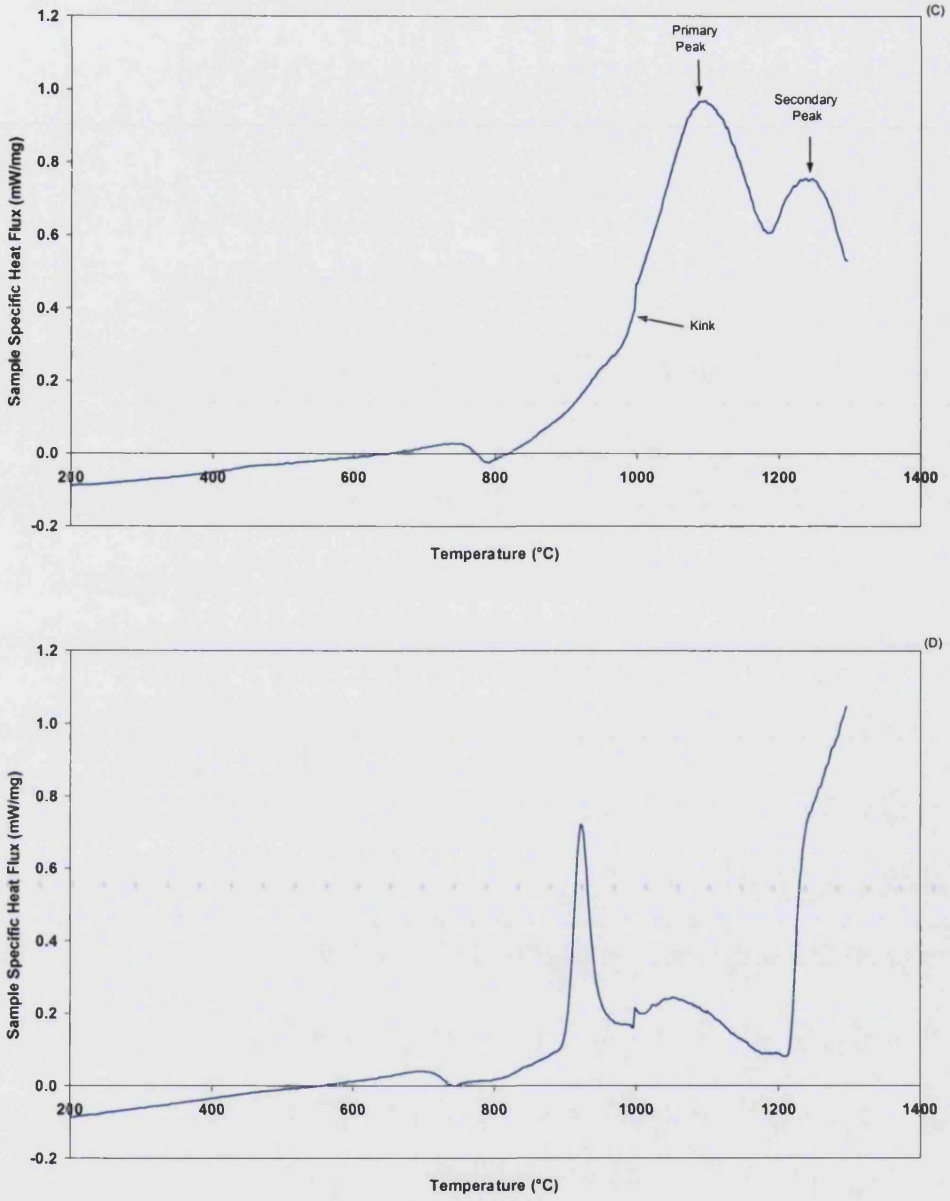

Figure 15: DSC of the glasses produced from the four waste material blends, (A) 93TET, (B) 94TET, (C) 95TET and (D) 96TET

Curve fitting techniques were used to assess peak heights, peak areas and the temperature at the peak's 'full-width-half-maxima' (FWHM). Figure 15A is annotated to illustrate how the data were acquired. The most significant point of inflection was used to assess T_g for the materials, the inflection being taken as that closest in temperature to the results from the dilatometric analysis. The discrepancies between the DSC and dilatometry data were

associated with the different heating rates employed and the lag in the detection system. The DSC results are summarised in Table 48.

Sample	T_g (°C)	Onset 1 (°C)	Peak 1 (°C)	Area 1 (J g^{-1})	Onset 2 (°C)	Peak 2 (°C)	Area 2 (J g^{-1})
93 TET	785	900	1045	206	1150	-	-
94 TET	715	800	999	305	1125	-	-
95 TET	765	900	1095	393	1175	1239	-
96 TET	726	900	923	110	1000	1051	48

Table 48: Summary of the DSC data of the waste glasses

'Onset' corresponds to the start of the exotherm. 'Peak' corresponds to the location of the exothermic peak and 'area corresponds to the area under the peak.

Sample 93TET, Figure 15A, had a T_g of 785 °C followed by two exotherms; the first started at 900 °C and peaked at 1150 °C; the second started at 1150 °C and did not peak within the measurement temperature range. A kink in the peak of the second exotherm, at 1270 °C, suggested that it was composed of two superimposed peaks. The specific energy release of this sample, determined from the area under the peaks when time is substituted for temperature, was lower than for the other samples within the temperature limitations of the equipment. Figure 15 has the same numerical scales on the axes to ensure that specific energy release can be compared.

Sample 94TET, Figure 15B, displayed a T_g of 715 °C followed by a broad exotherm starting at 800 °C and peaking at 999 °C, this peak had a very steep positive slope. As with sample 93TET a more pronounced second exotherm was observed at 1125 °C and peaked outside the experimental temperature range. The second exothermic peak had a kink at 1230 °C suggesting that it was composed of two superimposed peaks.

Sample 95TET, Figure 15C, exhibited a T_g of 765 °C. This was followed by an initial exotherm at 900 °C that peaked at 1095 °C. The second exotherm started at 1175 °C and peaked at 1239 °C. The two peaks were well defined with the first peak being more intense than the second. The first peak displayed a kink at 1000 °C.

Sample 96TET, Figure 15D, had a T_g of 726 °C, the first exothermic peak started at 900 °C and peaked at 923 °C with steep positive and negative slopes. This peak was significantly

narrower than those observed for the other samples. Additionally this sample gave a second, less pronounced exotherm at 1051 °C leading to the onset of a third peak at 1214 °C. This second peak had a very rough surface with a small exothermic feature at 1004 °C. The final peak started at 1214 °C and was significantly exothermic, this peak had a kink in the positive slope at 1240 °C.

When the sequence of peaks, summarised in Table 48, was ignored, it was observed that all samples had similar features in terms of peak onset and maximum temperature. They all had a peak with an onset between 850 – 900 °C and a maximum at 1100 – 1150 °C; peaks were also observed at 1150 – 1200 °C with a maximum at 1240 °C; commonly there was also a third peak. This observation confirmed that the methodology used to prepare the materials was reproducible. This outcome gave rise to similarities in processing characteristics, which aided the plasma furnace operation. Singular phase transition temperatures suggested the existence of compositional homogeneity in the quenched glass samples and material consistency. The presence of two exothermic peaks indicated that two different crystalline, or modified phases were precipitated within a very close temperature range and with some degree of overlap. Detailed crystallisation studies confirmed this to be the case, and will be discussed in Section 8. The information in Table 48 was used as the basis for devising sample heat treatment schedules for further experimentation; Section 5.2.3. The nucleation rate was predicted to become appreciable in the glass transformation range (T_g) and correlation between the DSC, dilatometry and viscosity experimentation was expected [9].

DSC was used to assess the thermal stability of the samples in relation to the crystallisation process, through an assessment of the difference between the dilatometric softening point and the onset of crystallisation, determined as the onset temperature of the first exothermic peak Table 49.

Sample ID	Waste	T_{DSP} °C (Dilatometry)	ΔT (°C) T_{DSP}-$T_{CRYST\ START}$
93 TET	BCC	760	140
94 TET	RFA	741	59
95 TET	GHS	817	83
96 TET	C-MSW	775	125

Table 49: The pre-crystallisation thermal stability of the waste glasses

The data indicated that samples 94TET and 95TET were the most stable in avoiding slumping problems on crystallisation, i.e. that crystallization would be possible without significant shape deformation.

5.2.3 Microprobe Examination of the Semi-Crystallised Materials

Electron microscopy samples were prepared in accordance with Section 5.1.7.4. Back-scattered electron detection was used for atomic number contrast, to allow the crystalline phase(s) to be distinguished from the continuous glassy matrix phase. Elemental compositional contours of the microstructure were produced using energy dispersive X-ray (EDX) spot, line and area mapping analysis. The data allowed segregation phenomena to be qualitatively defined. SEM-EDX (microprobe analysis) was used in conjunction with X-ray diffraction, to enable crystal formation to be quantified with respect to time and temperature. The microstructures of all the glassy samples were featureless under electron microscopy. During the laboratory phase of the work two crystalline samples were prepared from each base glass in accordance with the results of the DSC analysis, Section 5.2.2, hence a total of eight samples were prepared. Table 50 gives the preparation details, the crystallisation temperature employed were those determined using high temperature DSC analysis.

Sample ID	Waste	Nucleation Temp (°C)	Nucleation Time (mins)	Crystallisation Temp (°C)	Crystallisation Time (mins)
93TET1	BCC	796	30	1050	120
93TET2	BCC	796	30	1250	120
94TET1	RFA	752	30	999	120
94TET2	RFA	752	30	1150	120
95TET1	GHS	815	30	1095	120
95TET2	GHS	815	30	1239	120
96TET1	C-MSW	760	30	1050	120
96TET2	C-MSW	760	30	924	120

* A positive temperature ramp of 6 °C min^{-1} and a negative temperature ramp of -3°C min^{-1} was used for the heat treatment schedules. A two-stage traditional heat treatment schedule was employed.

Table 50: Thermal preparation details for the crystallised samples

5.2.3.1 Samples 93TET1 and 93TET2 based on BCC waste

The secondary electron micrograph of sample 93TET1, crystallised at 1050 °C was diffuse and showed acicular like crystallite morphology with orientated crystal growth features, Figure 16. The phase(s) grew to form interlocking networks of parallel lamellae crystallites. The boundaries regions of acicular growth impingement can be observed as featureless contrasting contours at lower magnifications. The aspect ratio of the individual crystallites were between 40 – 100, with the longest dimension being approximately 200 μm, and the perpendicular dimension between 2 and 5 μm. The crystallites had an internal skeletal structure.

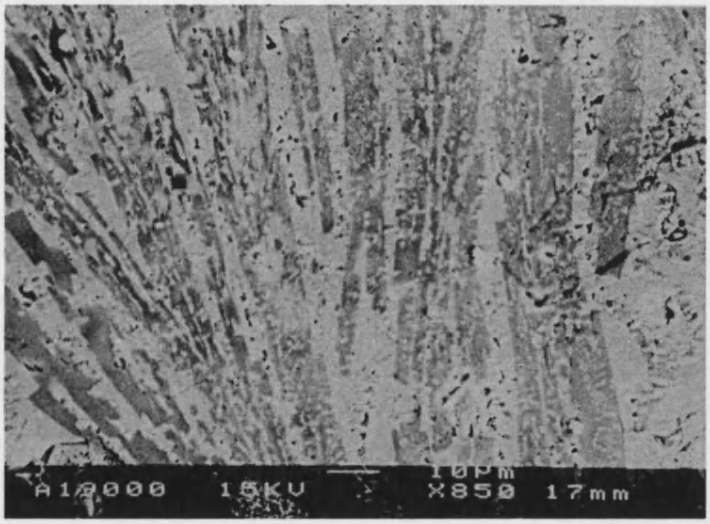

Figure 16: Secondary electron micrographs of sample 93TET1

The backscattered electron micrographs of sample 93TET1 gave greater contrast, and the internal structure of the crystalline regions was more distinguishable, Figure 17.

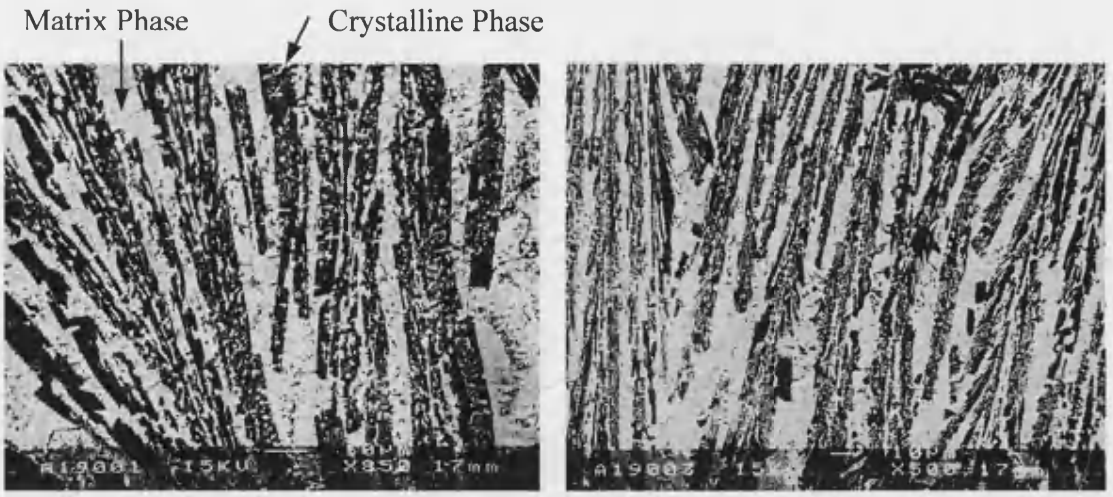

Figure 17: Backscattered electron micrographs of sample 93TET1

It can be postulated that the growth orientation resulted from favourable thermodynamics and lateral segregation within the localised micro-structural regions. EDX identified silicon, calcium and aluminium were the dominant oxide species within the crystallites, Figure 18, as would be expected. This was consistent with the bulk oxide composition of the material. The crystallite analysis was also observed to have a small titanium peak. This was indicating the presence of the nucleation medium, titania, within the glass. The amorphous phase was depleted in aluminium relative to the crystalline phase and enriched in silicon and calcium. It also displayed more pronounced titanium and potassium peaks, indicating that limited nucleation had occurred. Magnesium was not detected significantly in the EDX spectra.

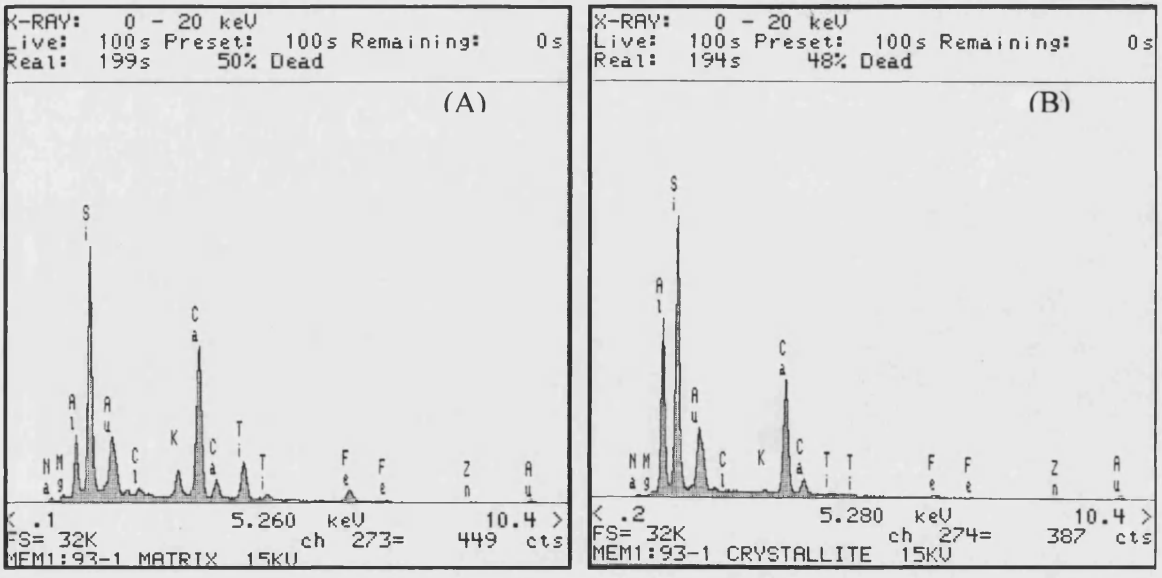

Figure 18: The EDX spectra of the matrix (A) and crystalline (B) regions of 93TET1

The backscattered electron micrographs of sample 93TET2, crystallized at a higher temperature of 1250 °C, are shown in Figure 19. Porosity was observed at the growth impingement regions, especially in areas of high crystallite density. It is likely that the growth of the higher density crystalline phase accounted for the generation of porosity within the material.

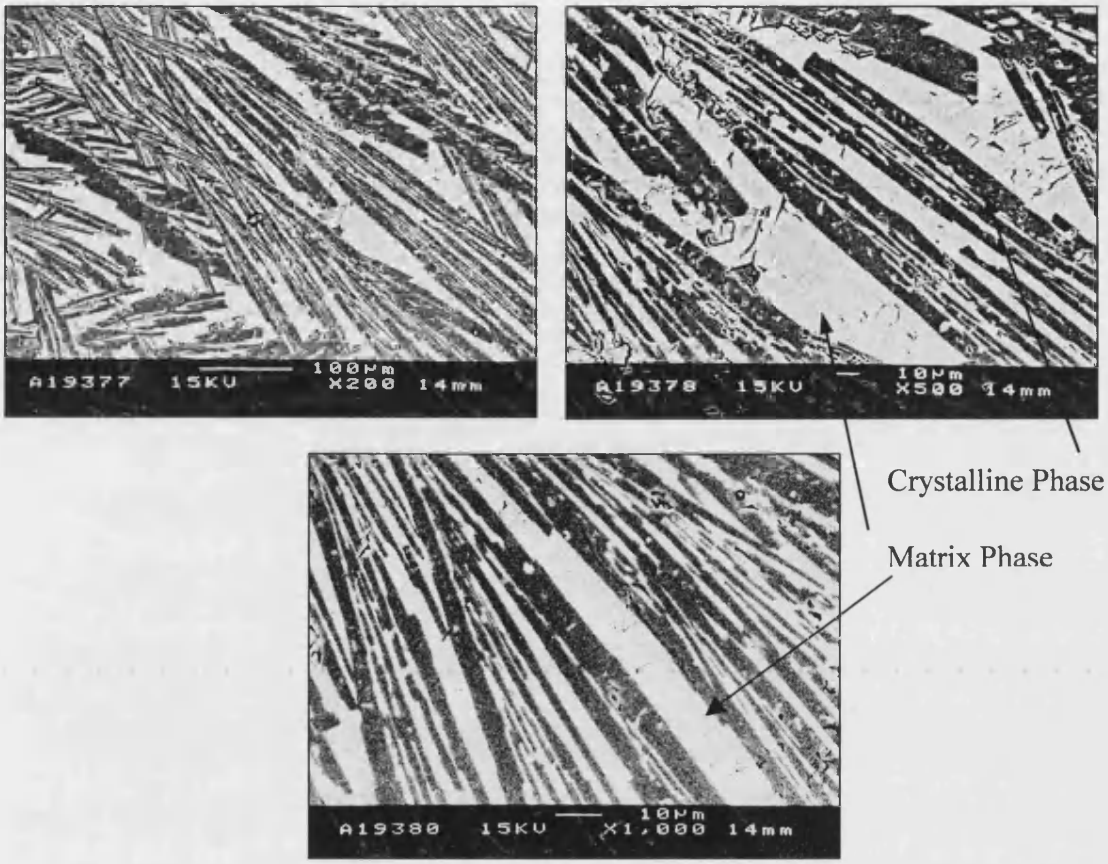

Figure 19: Backscattered electron micrographs of sample 93TET2

A lamellar orientated microstructure was observed, similar to that of sample 93TET1. The backscattered electron micrographs showed an acicular morphology with two different crystallites, with the newly evolved phase having a finer structure than the previously noted in sample 93TET1. The phase(s) grew to form an interlocking network of clumped parallel segments of crystallites. The aspect ratio of the newly formed crystallites was about 20-100, with the longest dimension being approximately 200 μm, and the perpendicular dimension varying between 2 and 10 μm, i.e. the microstructure has coarsened due to the higher temperature employed. Sparse matrix regions, of comparable dimensions to the newly formed crystalline phase, separated regions of crystal growth. Comparison of the semi-crystalline product with the microstructure of the alumina crucible indicated that the product had a high density throughout its cross-section. The interfaces

were well defined and displayed no evidence of columnar growth, Figure 20. Here the semi-crystalline product is on the left-hand-side and the alumina crucible is on the right-hand-side.

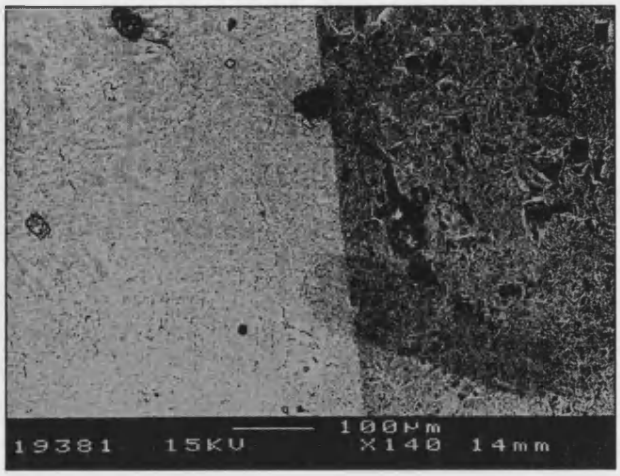

Figure 20: Secondary electron micrograph of the crucible-melt interface

Elemental silicon, calcium and aluminium were identified within the crystalline phases using EDX analysis, the peak proportions being consistent with sample 93TET1. The matrix phase was depleted in aluminium and showed more pronounced titanium, magnesium and potassium peaks, Figure 21, however magnesium was almost insignificant in intensity.

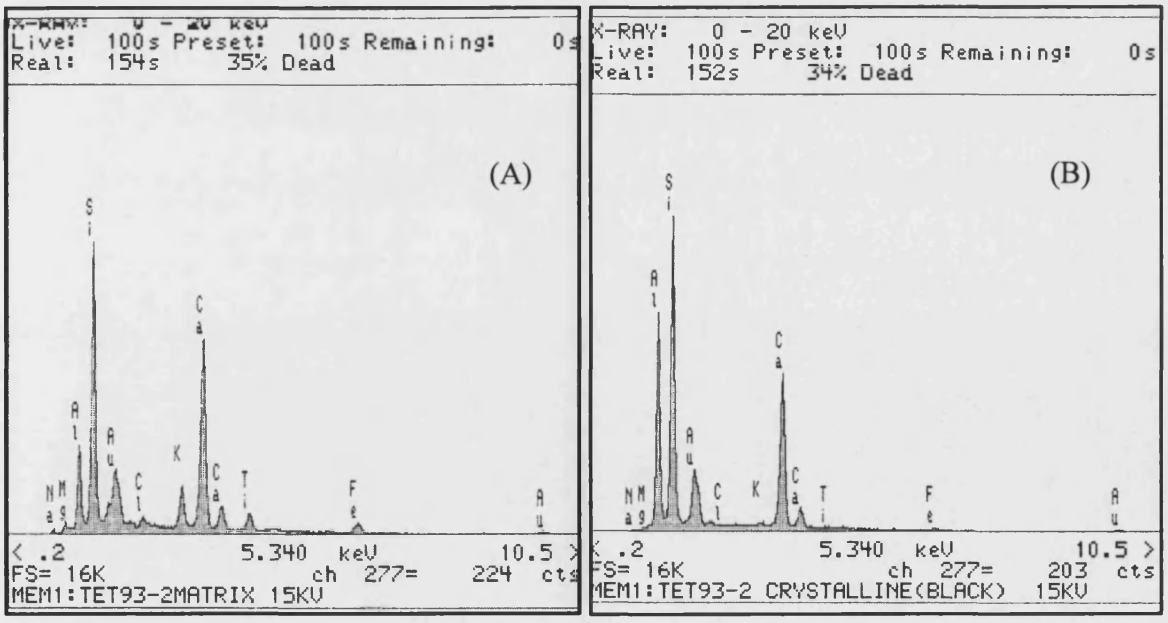

Figure 21: EDX spectra of the matrix (A) and crystalline (B) regions of 93TET-2.

These observations were complemented by X-ray diffraction data that showed the evolution of a secondary crystalline phase, through the appearance of some additional characteristic peaks, at the expense of the primary phase's peak intensities, Figure 22. Overall increases in crystallisation temperature led to increased sample crystallinity. The XRD data of all of the materials will be described in detail in Section 5.2.8.

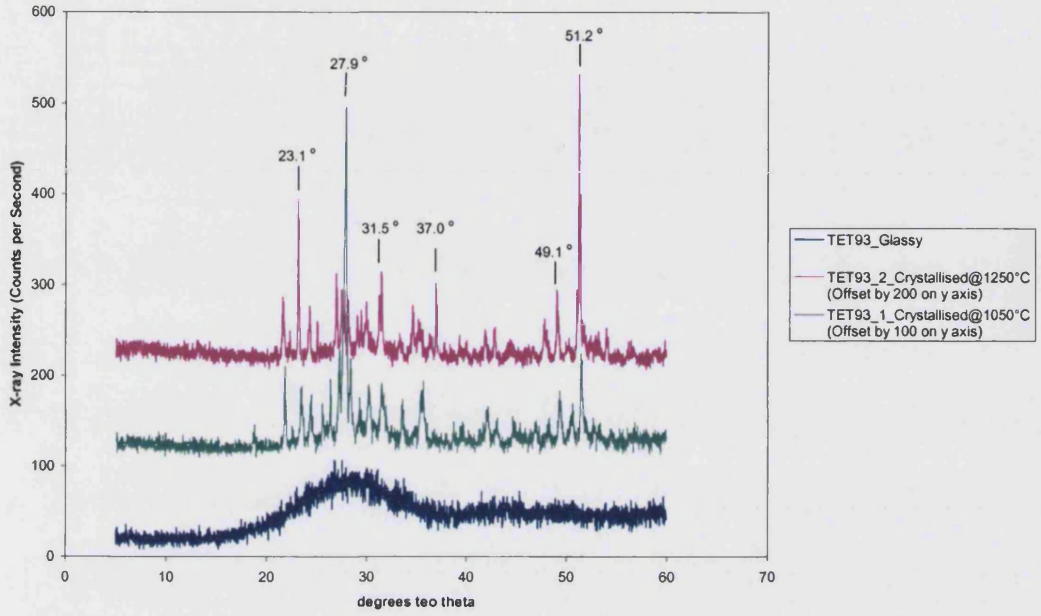

Figure 22: The XRD diffractograms of materials based on 93TET (BCC)

5.2.3.2 Samples 94TET1 and 94TET2 based on RFA waste

The secondary electron imaging of sample 94TET1, crystallised at 999 °C, gave no microstructural contrast and polishing imperfections were used to focus on an otherwise featureless surface. Backscattered electron micrographs identified the material as having a finely mottled surface structure, Figure 23, but the bulk was featureless. This inferred that the nucleating agent was ineffective for this material system. Further examination indicated that sporadic crystallisation had occurred throughout the bulk of the sample, however the surface region was most prominently crystallised. Contrast between the surface and the bulk of the material could be observed on a macroscopic scale. The crystalline surface structure was very fine with dimensions of a fraction of a micron; here the lighter phase was the crystalline phase. The crystalline phase was oriented and had dimensions ranging from 10 – 30 μm by 1 – 2 μm.

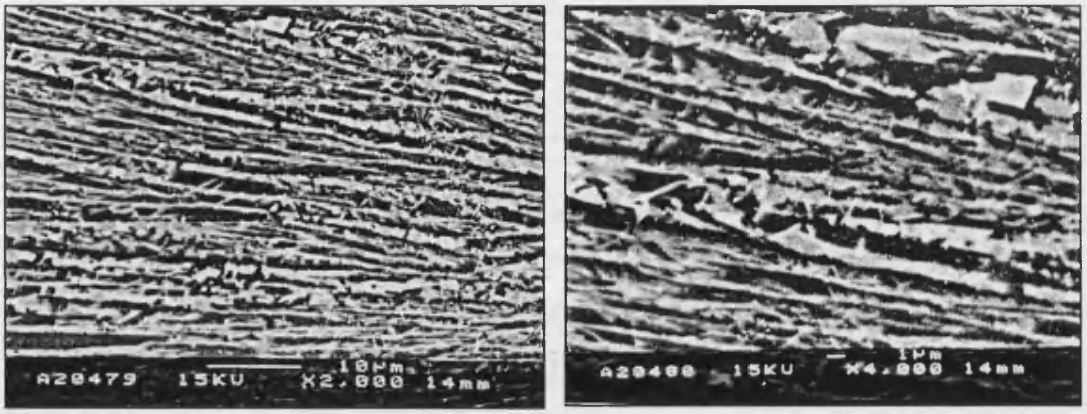

Figure 23: Backscattered electron micrographs of the surface region of 94TET1

The microstructure was different from that of samples 93TET1 and 93TET2. Qualitative EDX analysis indicated that the crystallite species contained silicon, calcium and aluminium cations. The limited spatial resolution of the EDX technique meant that it was difficult to differentiate between the matrix and the crystalline phases, relative to the dimensions of the microstructure, Figure 24.

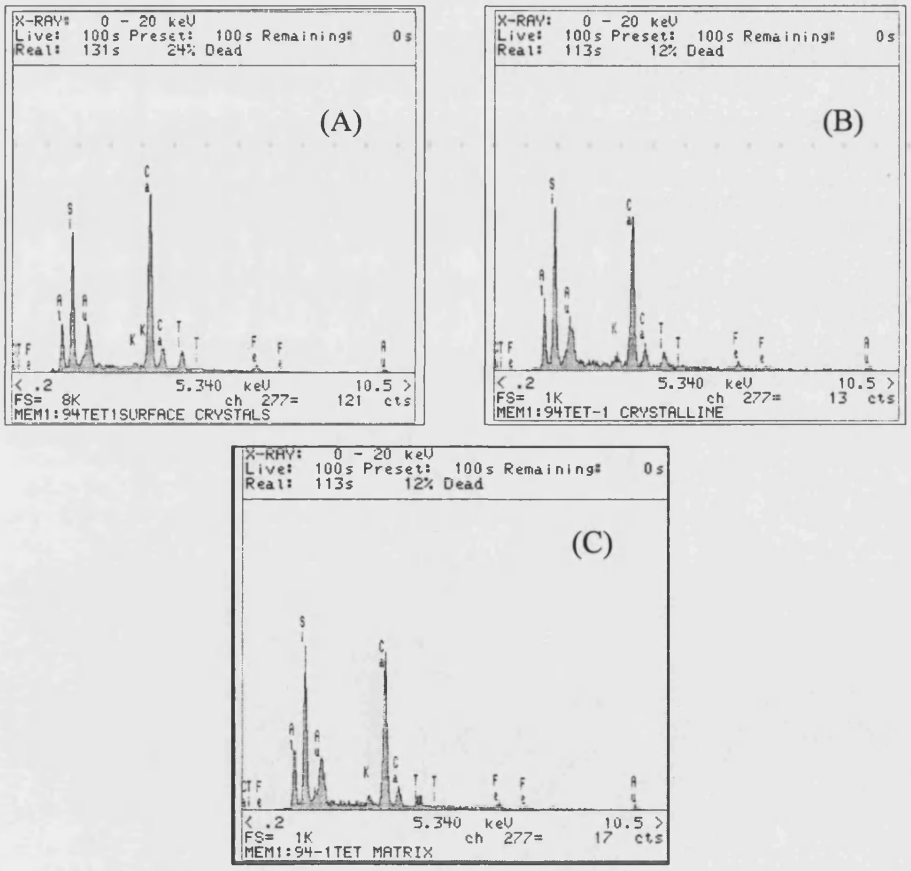

Figure 24: EDX spectra of the matrix and crystalline regions of 94TET1 (A) surface crystals, (B) bulk crystals and (C) matrix

The matrix and crystalline phases had a similar composition, however, the surface crystalline phase was enriched in calcium and depleted in aluminium. The XRD spectra for this material showed low peak intensities, which was consistent with these micro-structural observations of limited crystal growth. The peak locations are observed to be consistent with sample 94TET2, which was heat-treated at higher temperatures, Figure 25.

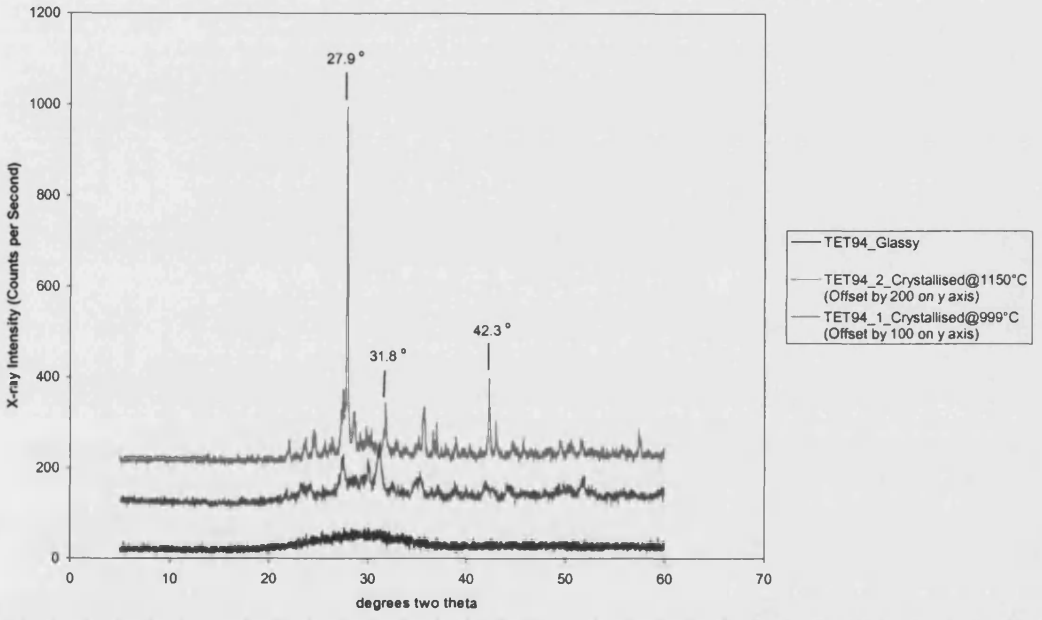

Figure 25: The XRD diffractograms of material based on 94TET (RFA)

Sample 94TET2, crystallised at a higher temperature of 1150 °C; exhibited features similar to those of 93TET1 and 93TET2. The secondary electron micrographs showed a very diffuse image, however, coarse dark crystalline features were present, Figure 26.

Figure 26: Secondary electron micrograph of 94TET2

Further examination indicated a coarsely crystalline and oriented microstructure. The whole sample was crystalline throughout its section. The crystallites were facetted with well defined interfacial boundaries. They appeared needle like with a longitudinal dimension of 200 μm and a width of 50 – 80 μm. The coarse nature of the microstructure produced increased local strains that caused the glass matrix to crack, Figure 26. At higher levels of magnification the matrix phase was observed to be crystalline. The crystallites had a fine whisker-like appearance and were contrastingly light in colour; with a length of 10 μm and a width of < 1 μm; Figure 27.

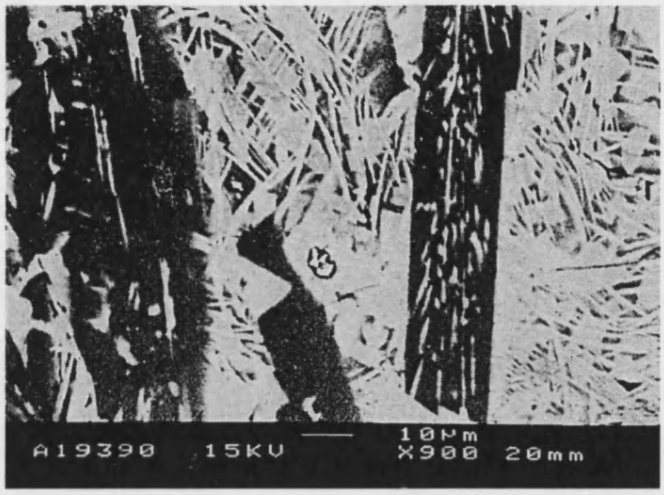

Figure 27: Higher magnification secondary electron micrograph of 94TET2

The microstructure bore little resemblance to that of sample 94TET1. EDX analysis indicated that the larger crystallite species contained silicon, calcium and aluminium with an additional small peak of titanium. The matrix phase had been depleted in aluminium and showed relatively pronounced titanium, magnesium, sodium and potassium peaks. The overall shift in relative proportions of the peaks was similar to those observed for samples 93TET1 and 93TET2 between the matrix and crystalline phases, where aluminium had segregated to the crystalline phase, Figure 28.

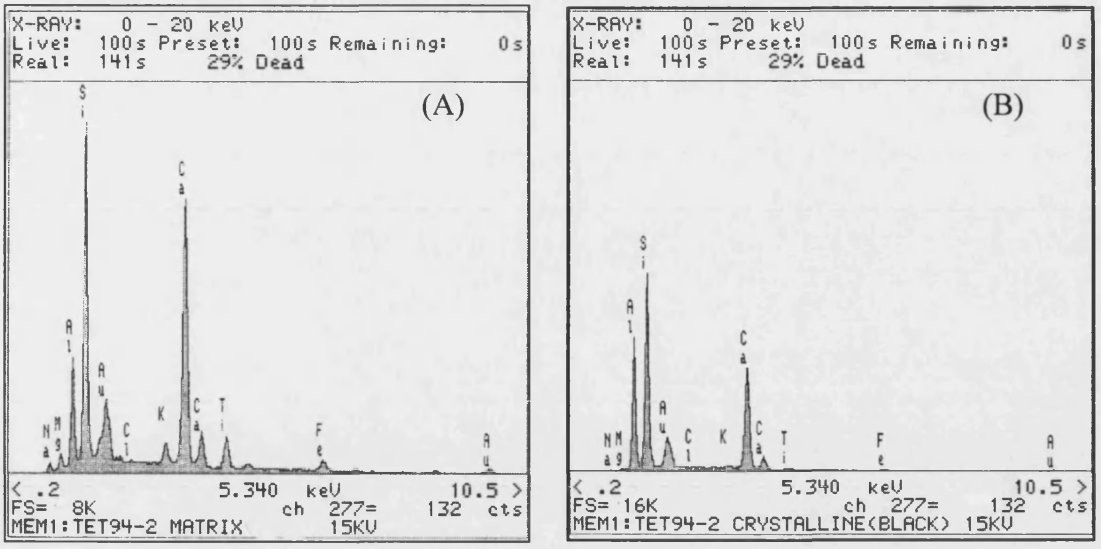

Figure 28: EDX spectra of the matrix (A) and crystalline (B) phases of 94TET2

This was not consistent with sample 94TET1, where the elemental silicon and calcium levels were higher. The XRD diffractograms indicated that there was consistency between samples 94TET1 and 94TET2, thus it was postulated that the secondary crystalline phase had the same identity as the surface specific phase associated with 94TET1 and the different dimensional characters were a result of the changing physical properties of the matrix.

5.2.3.3 Samples 95TET1 and 95TET2 based on GHS waste

The secondary electron micrographs of sample 95TET1, crystallised at 1095 °C, at relatively high levels of magnification showed an oriented crystal structure. The individual growth regions had 'grain like' boundaries between areas of different orientated growth impingement, which were observed as contrasting contours, Figure 29. The phase(s) grew to form interlocking networks of clumped, parallel segments of acicular crystallites. The micrographs showed the morphology of the crystalline phase(s), to have an aspect ratio of about 30, the greatest dimension of the crystallites being < 30 μm, while the perpendicular dimension varied, but was < 1 μm. Backscattered electron micrographs gave greater contrast between the glass matrix and the crystalline phase, Figure 30. Higher magnification primary electron micrographs showed the presence of grain-like triple point areas with micro-structural features similar to those associated with the solidification of a eutectic liquid forming lamellae of anorthite and pseudowollastonite, Figure 7.

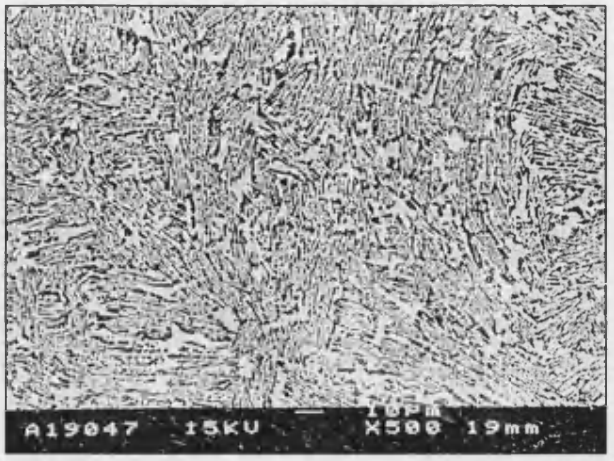

Figure 29: Secondary electron micrographs of 95TET1

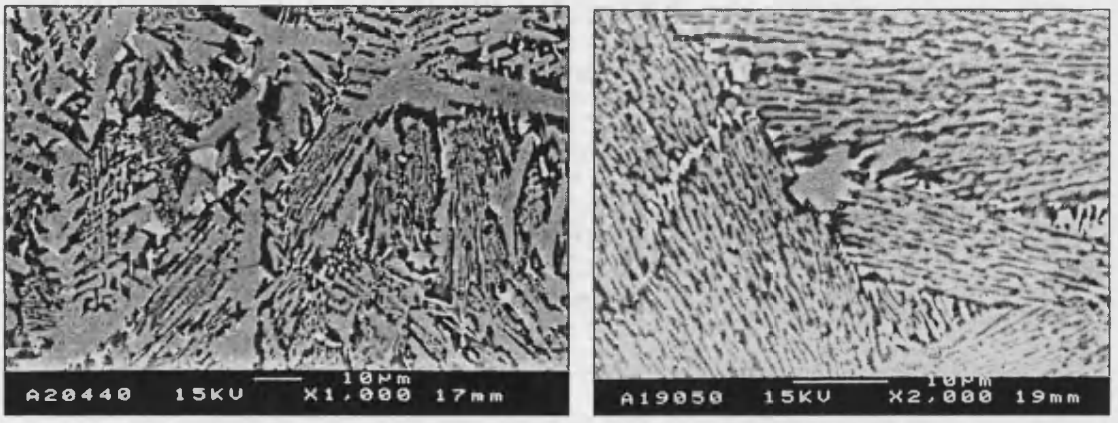

Figure 30: Backscattered electron micrographs of 95TET1

The application of EDX to assess the difference in composition between the glassy and crystalline phases was hindered by the fine nature of the microstructure. The analysis of the lighter crystalline phase indicated that it contained silicon, calcium and aluminium, consistent with the waste's bulk oxide composition and that of samples based on the glasses 93TET and 94TET, Figure 31. The crystalline phase was enriched in elemental calcium which was different from that observed in the previous materials. The XRD spectra for 95TET1 were well defined and showed a high level of consistency with the higher temperature sample 95TET2, Figure 32.

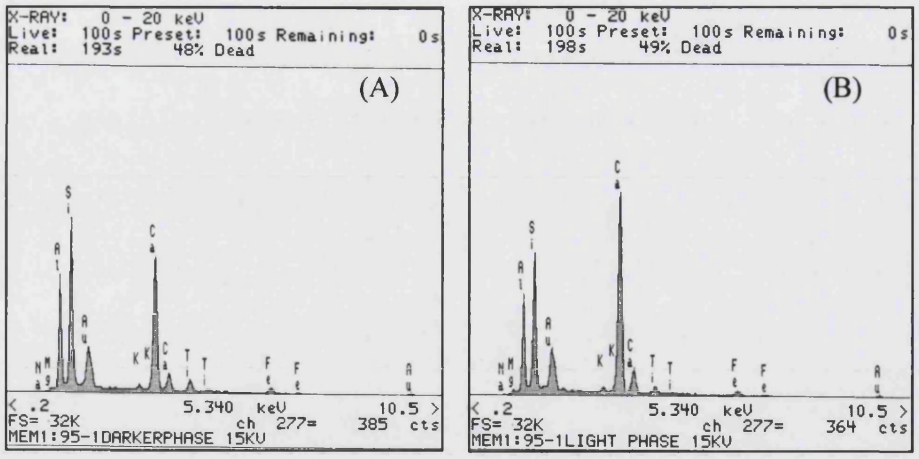

Figure 31: EDX spectra of the matrix (A) and crystalline (B) regions of 95TET1

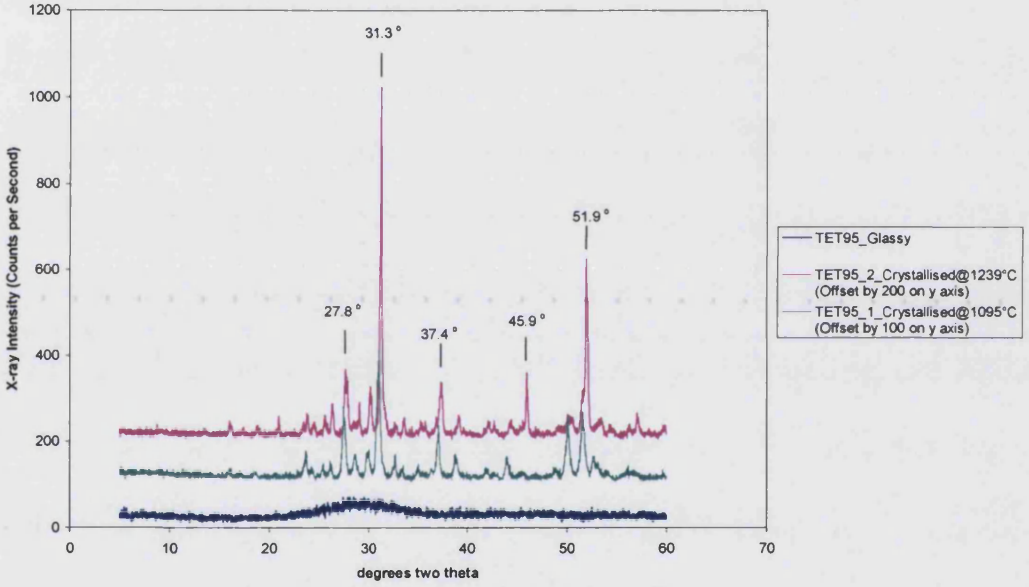

Figure 32: The XRD diffractograms of material based on 95TET (GHS)

The electron micrographs of sample 95TET2, crystallised at a higher temperature of 1239 °C, are shown in, Figure 33. Here, orientated crystal growth profiles were observed throughout the bulk of the sample and the crystalline phase's morphology was different and coarser than that of 95TET1. The phase exhibited more random crystal growth with lateral 'dendritic-like' features between the primary branches. The crystals showed a greatest dimension of ≤ 100 μm, with a perpendicular dimension of ~ 5 μm. The

crystallites had an internal structure of a skeletal nature possibly indicating a dendritic growth mechanism where lateral material rejection and enrichment had generated growth perturbations as the local compositions were modified. The growth regions still displayed 'grain like' boundaries between areas of growth impingement, which were observed as contrasting contours allowing the glassy region to be identified as the black phase.

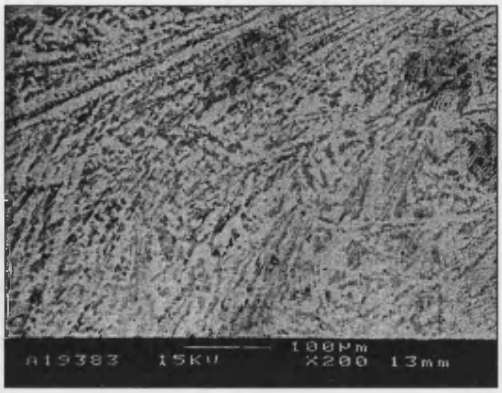

Figure 33: Secondary electron micrographs of 95TET2

The finer microstructure, which was present in 95TET1, had been transformed, and none of the features seen previously were retained at similar levels of magnification, Figure 34. The backscattered electron micrographs showed the difference in atomic number between the glassy matrix and the crystalline phase, with the crystalline phase being enriched in the heavier elements.

Figure 34: Backscattered electron micrographs of 95TET2.

At higher magnification it would be seen that the inter-primary crystalline phase regions were bridged by a second crystalline phase, which was 10 µm long and 1 µm wide. EDX analysis indicated that the primary crystallite again contained silicon, calcium and aluminium, and were enriched in elemental calcium and depleted in elemental silicon

relative to the matrix glass, Figure 35. The secondary crystalline phase was depleted in silicon and aluminium relative to the matrix material.

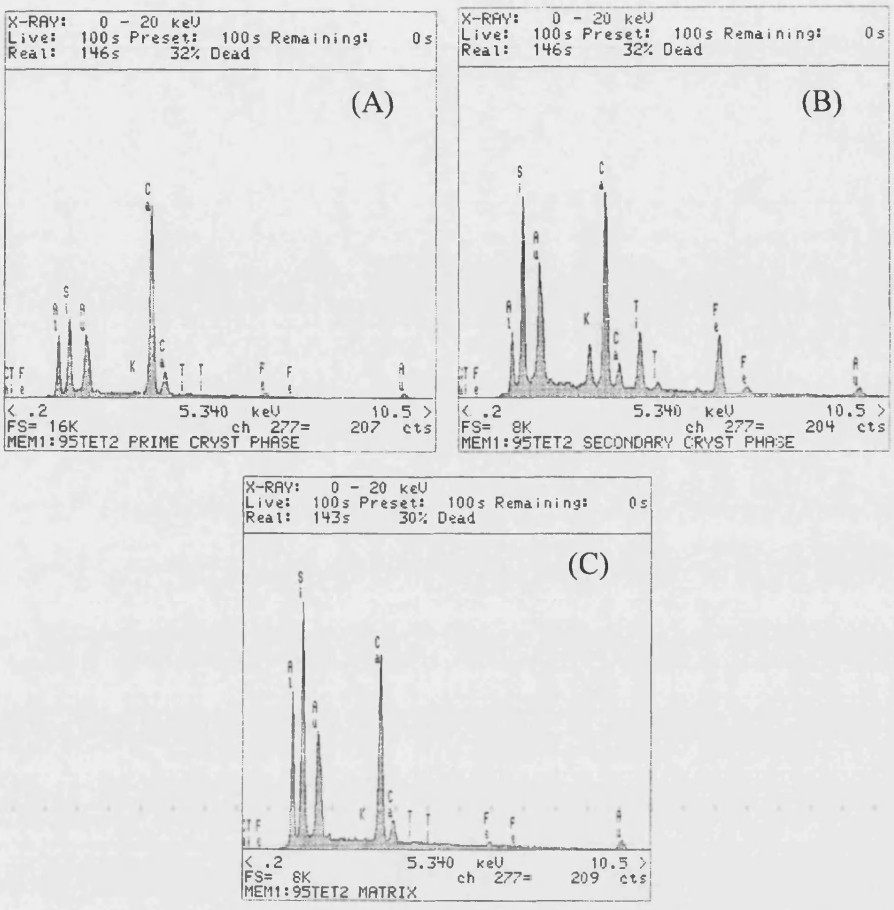

Figure 35: EDX spectra of the secondary crystalline phase (A), primary crystalline phase (B) and matrix (C) region of 95TET2

The XRD spectra of sample 95TET2 were more intense than 95TET1 indicating that a significant fraction of the crystalline phase was present, Figure 32. The peak locations on the diffractogram showed a high degree of similarity with sample 95TET1.

5.2.3.4 Samples 96TET1 and 96TET2 based on C-MSW waste

The secondary electron micrographs of sample 96TET1, crystallised at 1050 °C, were featureless, so backscattered electron detection was used to reveal the atomic number contrast. A fine mottled structure was observed within islands distributed throughout the bulk of the material, Figure 36. The structure was extremely fine, with dimensional features being only fractions of a micron in size. The island growth features had a radial distribution giving a spherulitic appearance, 50 μm in diameter, comprised of crystallites

with 1 – 5 μm in characteristic dimension. The surface microstructure was similar to that of sample 94TET1, with a very fine whiskery structure in the peripheral regions of the sample. The crystallites were approximately 10 μm in length and 1 μm wide.

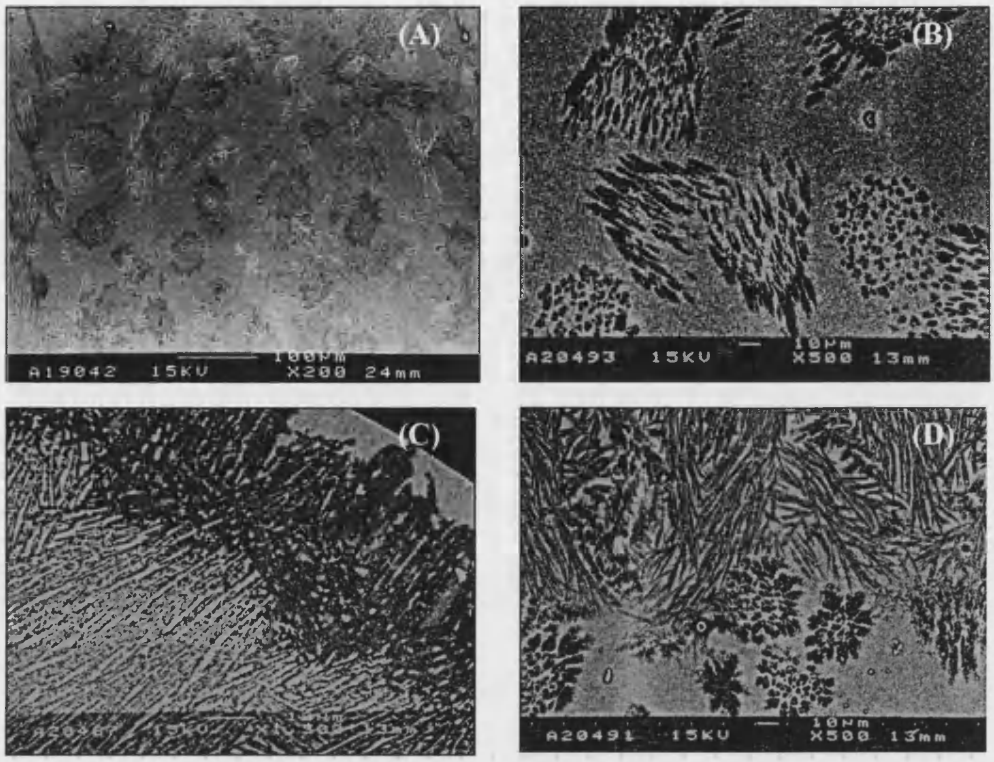

Figure 36: Backscattered electron micrographs of 96TET1
Bulk sample of (A) and (B), surface region (C) and (D).

The EDX analysis, was similar to 94TET1, and indicated that the surface crystalline phase was enriched in calcium relative to atomic silicon and aluminium, Figure 37. However, the spherulitic bulk crystalline phase was enriched in silicon and aluminium relative to calcium. There were common spectral features between the XRD diffractograms of sample 96TET1 and 94TET1, Figure 38, which were consistent with the similar micro-structural features of the material.

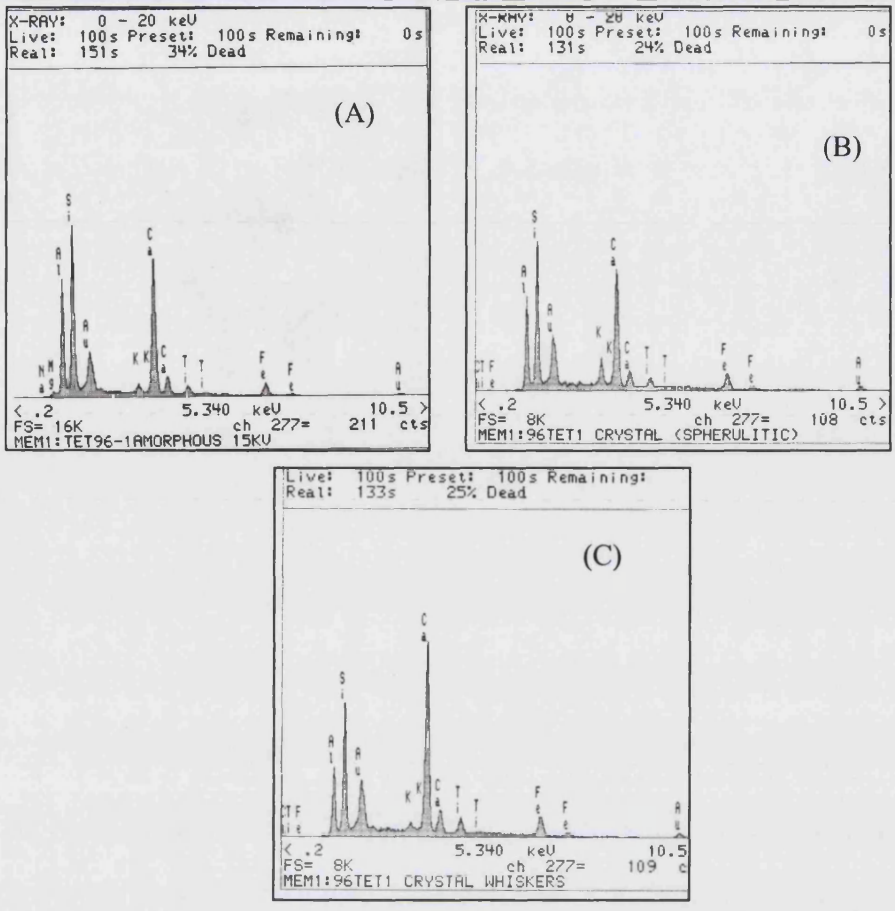

Figure 37: EDX spectra of the matrix (A) and crystalline (B and C) regions of 96TET1

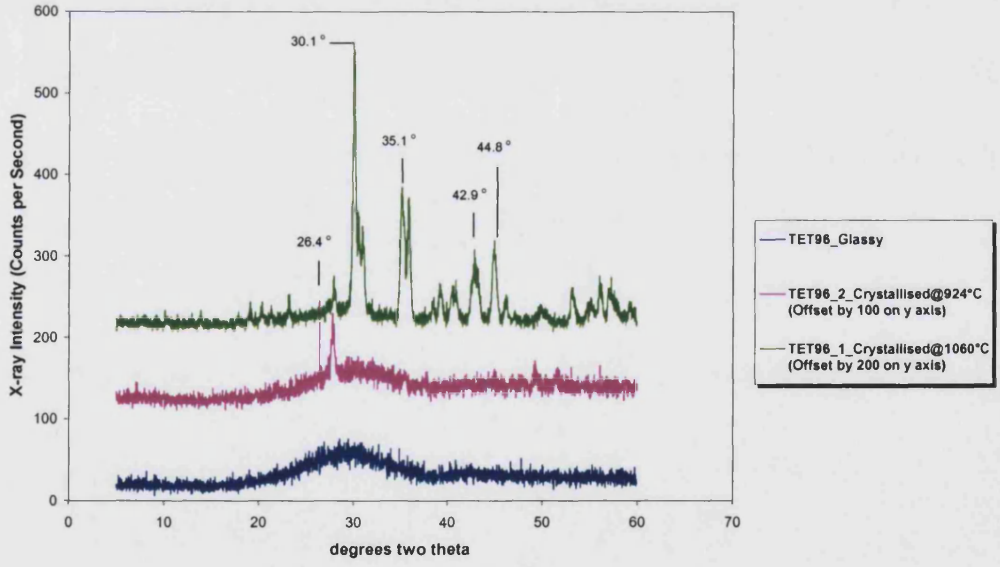

Figure 38: The XRD diffractograms of material based on 96TET (C-MSW)

The backscattered electron micrographs of samples 96TET2, crystallised at a lower temperature of 924 °C, had little micro-structural contrast. This was expected, as 96TET2 was the lower temperature version of 96TET1, so there was less disappearance of the crystalline phase. Topographic secondary electron images were used to examine the material's microstructure, Figure 39.

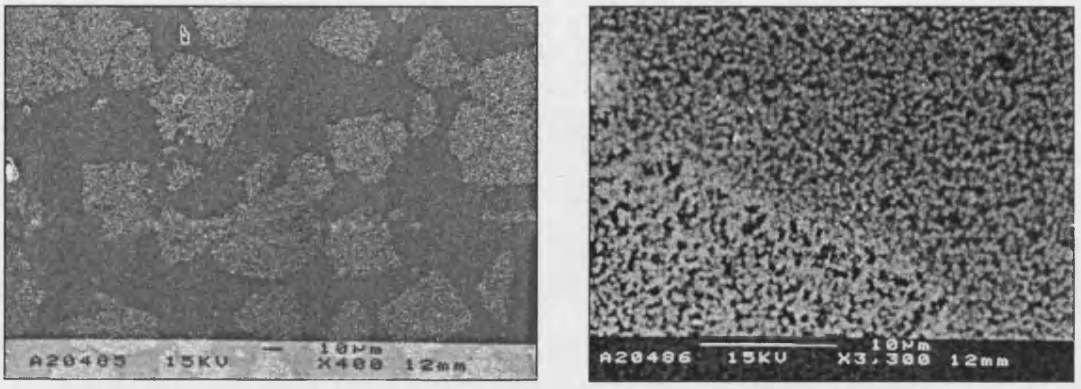

Figure 39: Secondary electron micrographs of 96TET2

The structure was very fine, due to the lower temperature employed, with dimensions of less than a micron. Limited similarity with 96TET1 was observed. The microstructure had uniform growth features that were randomly orientated, with 10 – 30 µm crystalline regions throughout the material. Crystallization was limited and displayed a limited crystallite number density towards the centre of the body which was consistent with the lower temperature attained during crystallisation. This was consistent with the low intensity of the XRD peaks in Figure 38. The application of EDX to assess qualitatively the difference in composition between the glassy and crystalline phases indicated that the crystalline species contained primarily silicon, calcium and aluminium, with the crystalline regions being depleted in calcium, Figure 40.

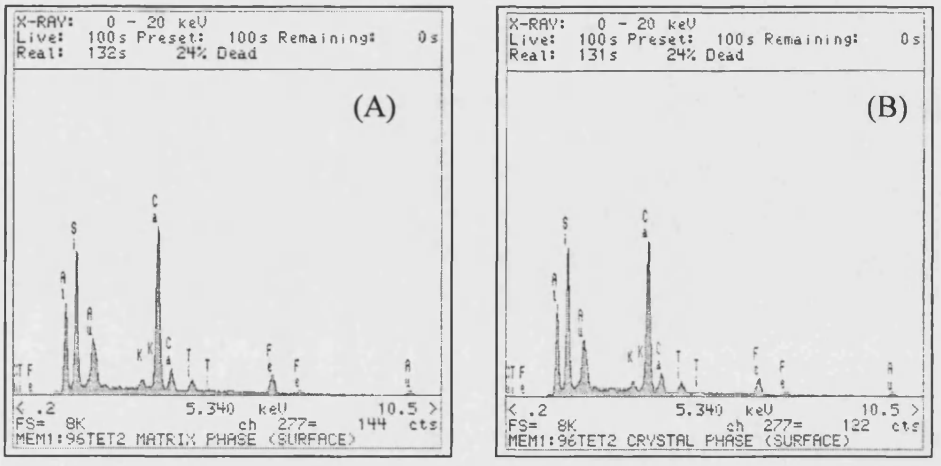

Figure 40: EDX spectra of the matrix (A) and crystalline (B) regions of 96TET2

5.2.4 Hardness and Toughness Test Results

Hardness is considered to be of importance in determining a material's resistance to abrasion and wear, however the subject and mechanisms are complex. The glassy samples, formed by quenching and annealing the blended waste materials, were tested for hardness and toughness using eight replicates. Hardness and toughness results are summarised in Table 51. Reference should be made to Figure 10 when interpreting the data. Arithmetic mean values of the eight readings are shown.

Sample ID	2a (mm)	2c (mm)	Weight (kg)	*HV	K_{1C} (MPa$\sqrt{m}$)
93TET	0.0650	0.1386	0.5	220	0.76
94TET	0.0290	0.0510	0.3	650	0.99
95TET	0.0338	0.3235	0.5	772	0.10
96TET	0.0373	0.0802	0.5	660	1.02

*HV = Vickers Hardness Number

Table 51: Glassy sample hardness characteristics

Large variations in material properties were noted for the different waste materials, and the low indentation fracture toughness values obtained for 95TET were possibly an error due to there extremely low values which were not representative of the samples handled. These values were used as a base line for examining the properties of the heat-treated semi-crystalline materials. The fracture toughness values compared favourably with the data reported for other aluminosilicate glasses, [59]. This confirmed the success achieved in the material preparations stages of the work. The hardness and toughness of the crystallised samples prepared in accordance with Table 50, is shown in Table 52.

Sample ID	2a (mm)	2c (mm)	Weight (kg)	HV	K_{1C} (MPa$\sqrt{m}$)
93TET-1	0.063	0.176	1.0	475	0.60
93TET-2	0.059	0.132	1.0	533	0.45
94TET-1	0.030	0.114	0.2	404	0.23
94TET-2	0.026	0.107	0.2	549	0.11
95TET-1	0.05	-	1.5	733	-
95TET-2	-	-	-	-	-
96TET-1	0.050	-	1.0	858	-
96TET-2	0.060	0.170	1.0	1092	0.99

Table 52: Semi-crystalline sample hardness

Large inaccuracies were observed in the fracture toughness data because it was difficult to assess the radial crack profile dimensions accurately, and sometimes the profile did not appear. In these cases fracture toughness values are not reported. The analysis was undertaken several times but the consistency of the reading did not improve. However, the crystalline samples generated from 93TET and 96TET showed increased hardness values. Increases in both hardness and toughness were expected for the glass-ceramic with respect to the glass, [21, 22, 39, 59].

5.2.5 Density Measurements

Density measurements were taken for all of the glassy samples and the arithmetic mean values of three experiments each are given in Table 53.

Sample ID	Apparent Density ρ (g cm^{-3})	Waste Precursor
93TET	2.73	BCC
94TET	2.82	RFA
95TET	2.86	GHS
96TET	2.83	C-MSW

Table 53: Density data for the glassy waste samples:

The density values were high, indicating that porosity and flaw levels were low and a high degree of consolidation had been achieved. These values were compared to those of the semi-crystalline samples acquired in an identical manner, Table 54:

Sample ID	Apparent Density ρ (g cm^{-3})	Relative Change (%)
93TET-1	2.73	0.0
93TET-2	2.76	1.1
94TET-1	2.87	1.8
94TET-2	2.84	0.7
95TET-1	2.89	1.0
95TET-2	2.88	0.7
96TET-1	3.17	12.0
96TET-2	3.13	10.6

Table 54: Density data for the semi-crystalline waste samples

An increase in density after crystallisation was observed for the majority of the samples. The change in density was most pronounced for sample 96TET, generated from C-MSW

grate ash. The dimensional changes associated with this change in density were not quantified.

5.2.6 Elastic Modulus Determination

Ultrasonic pulse velocity measurements were undertaken using 150 kHz transducers and a metallic calibration standard which had a transmission time of 21.3 μs. The time taken for a pulse of ultrasound radiation to pass through a material of uniform sections was determined. Each experiment was repeated four times and arithmetic average values are quoted, Table 55.

Sample ID	Transmission Time	Sample Thickness	Transmission Velocity	Density ρ	$E_{(range)}$*
	(μs)	(mm)	(km s^{-1})	(g cm^{-3})	(GPa)
93TET	2.08	8.32	4.00	2.73	32.4 - 40.2
94TET	2.00	7.81	3.91	2.82	32.0 - 39.7
95TET	2.05	8.18	3.99	2.86	28.4 - 35.2
96TET	2.00	8.06	4.03	2.83	34.1 - 42.3
93TET1	1.63	7.50	4.59	2.73	42.8 – 53.0
93TET2	3.40	8.00	2.35	2.76	11.4 – 14.7
94TET1	1.70	7.10	4.19	2.87	37.5 – 46.5
94TET2	3.63	4.70	2.20	2.84	10.2 – 12.6
95TET1	2.05	7.30	3.57	2.89	27.4 –34.0
95TET2	1.75	8.00	4.57	2.88	44.7 – 55.4
96TET1	1.50	7.50	5.00	3.17	59.0 – 73.1
96TET2	1.45	7.50	5.17	3.13	62.2 – 77.1

* $E_{(range)}$ is based on Poisson's ratio values in the range 0.18 – 0.30

Table 55: Ultrasonic pulse velocity data used to calculate elastic modulus values

In the majority of cases there was an increase in elastic modulus when the glass was transformed to a glass-ceramic. The exceptions were 93TET2 and 94TET2 with significant reduced moduli. The range of elastic modulus values were directly attributed to the range of Poisson's ratio values used in the calculation, as defined in Section 5.1.7.7. This information was used in conjunction with other empirically acquired data to predict the extent of thermal stress developed within the materials on cooling and heating. The modulus values compare favourably with published reference data, [59].

5.2.7 Radial Solidification Temperature Profiles

Glassy samples were cast into preheated metallic moulds as described in Section 5.1.7.8. A quantitative understanding of the thermal gradients developed in the tiles as a function of both material type and time after casting was obtained. Temperatures were measured at defined points, used to calculate differential temperatures. The data for glass 96TET are included in Figure 41, here temperature readings are displayed as a function of time for different radial positions. The temperature differences between the central thermocouple and the thermocouples at 15 mm and 10 mm into the mould inner diameter were considered to be representative of the differential temperature observed in tiles of 28 mm and 38 mm thick respectively, i.e. the mould had an inner radius of 29 mm. The experimental results are summarised in Table 56.

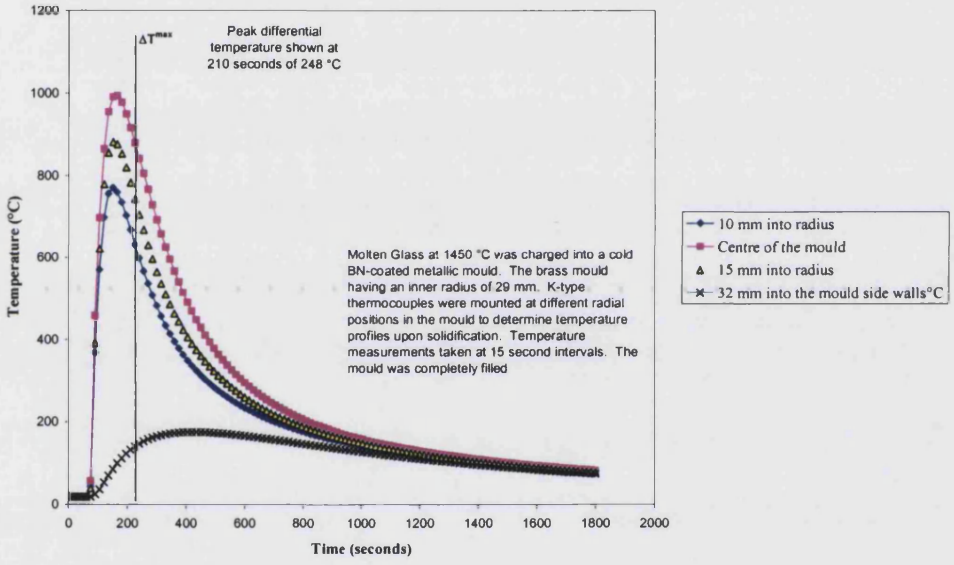

Figure 41: Mould radial solidification temperature profile of 96TET

	Equivalent Tile Thickness		α	Max thermal strain α.ΔT (38 mm tile)
	28 mm	38 mm	(x 10^{-7} K^{-1})	
Sample ID	[ΔT^{max} (°C),-time (secs)]	[ΔT^{max} (°C),-time(secs)]	100 – 600 °C	(%)
93TET	[170.6, 195.0]	[203.0, 210.0]	208	0.42
94TET	[210.3, 225.0]	[267.5, 240.0]	134	0.36
95TET	[156.5, 225.0]	[243.1, 240.0]	82	0.20
96TET	[135.3, 255.0]	[247.8, 210.0]	181	0.45

Table 56: Radial solidification temperature differential data

Table 56 shows that the largest temperature differentials generated were associated with samples 94TET and 96TET (247.8 °C). 94TET had the most severe temperature differential of 267.5 °C after 240 seconds for 38 mm of probe displacement. When the measurements were examined in relation to the materials' experimentally determined coefficients of linear thermal expansion, the thermal strains were the most severe for sample 96TET and exceeded the fracture strains commonly associated with ceramics, i.e. < 0.1 %. During the experimentation all samples failed due to the harsh cooling regime purposely employed and their large sections. The information was extrapolated to predict the likelihood of failure for the engineered tile product, but precise answers were not obtained because of the unknown behaviour of the mechanical properties of the glass products. However, the data was used to define the maximum acceptable tile thickness in the formed product, this was material dependent and lay between 9 mm and 19 mm. The calculation was undertaken with an assumed failure strain of 0.1% was used in conjunction with the coefficient of linear thermal expansion and temperature differential trends.

5.2.8 X-ray Diffraction Data

The processing route was intended to form a stable glass, hence the primary aim of using XRD was to confirm the avoidance of crystallisation in the cast glasses. All of the four laboratory glasses were analysed using XRD, Figure 42, which show that all of the four waste stream glasses had amorphous structures.

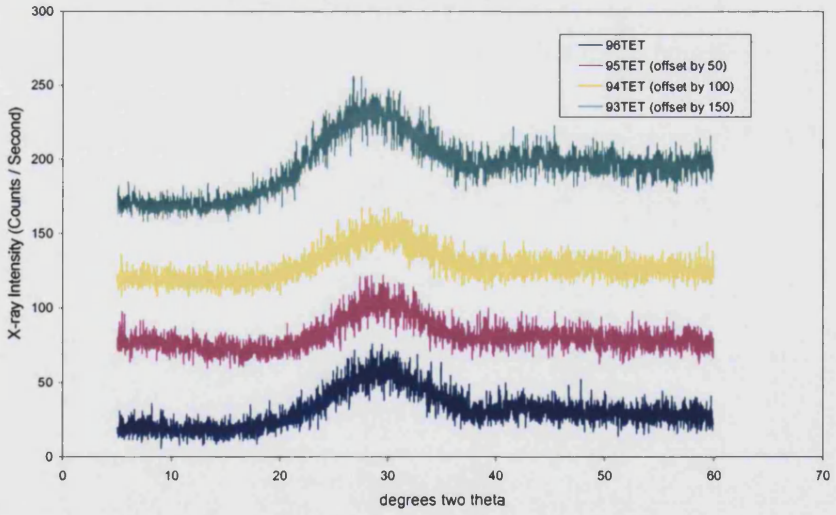

Figure 42: The XRD diffractograms of the waste glasses

The XRD data acquired from the crystallised samples is now discussed.

5.2.8.1 Samples 93TET1 and 93TET2 based on BCC waste

The X-ray diffraction spectra of sample 93TET1 and 93TET2 are presented with that of un-crystallised 93TET in Figure 22. Here the appearance and disappearance of peaks was linked to the heat treatment schedule.

Sample 93TET1 was crystallised at 1050 °C and had identifiable peaks in the X-ray spectrum. The five most intense peaks were positionally consistent with the JCPD standard diffraction pattern of anorthite $(Ca)(Al,Si)_2Si_2O_8$. This is a member of the feldspar group and plagioclase subgroup, which falls within the Tectosilicate classification of common rock forming minerals [63]. The Greek word 'Tecto' means framework, and the minerals have a three-dimensional network structure consisting of wrapped chains of four membered rings extending uni-directionally. They are joined together by ionic bonds by calcium ions, hence the mineralogical formula is written as $Ca(Al_2Si_3O_8)$. The compound is commonly found in solid solution with Albite $Na(AlSi_3O_8)$, forming continuous solid solutions at high temperatures. Anorthite has a triclinic structure and the crystals are commonly prismatic and elongated. They are formed through a transformation labelled *exsolution* resulting in a structure referred to as *microperthite*, i.e. micro-structural intergrowth. Here lateral rejection of material on crystallisation leads to segregation, and therefore alternating growth features. The XRD spectrum exhibited close consistency with the high temperature modification of the structure, which agrees with the material preparation route. Anorthite has a high hardness and a density of 2760 kg m^{-3}, [63]. It is a rock-forming mineral found in metamorphic and igneous deposits and its natural occurrence is commonly associated with the crust of ejected volcanic rock, and is similar in nature to granite [1]. The high angle (lower 'd' value) reflections showed consistency with the ordered and disordered JCPDS files. The location of the peaks was more consistent than were the relative intensities. This could be from the oriented microstructure of the material and the preferential orientation effects expected in the diffraction spectrum, Section 55.2.3.1. The samples were mechanically sectioned and not in powdered form, which is assumed to produce the random orientation of crystals.

The outcome of the waste material analysis results, combined with the bulk oxide compositional adjustment, in accordance with phase diagrams prior to melting, gave a high level of confidence in the phase identification, i.e. this is the phase the material was

blended to achieve, Figure 43. This was reinforced by the qualitative elemental analysis results from EDX analysis. Hence for this waste material enough control was maintained to allow micro-structural engineering to occur.

Sample 93TET2 was crystallised at 1250 °C and had an identifiable X-ray spectrum. The most intense peaks were positionally consistent with the JCPD standard diffraction pattern for anorthite $(Ca)(Al,Si)_2Si_2O_8$ and with reference to sample 93TET1 it can be observed that this is the case, Figure 22. The microstructures, EDX and XRD information were all consistent and increases in hardness and density were determined. The secondary phase was most probably wollastonite $Ca(SiO_3)$ or its high temperature (>1200 °C) modification pseudo-wollastonite. The conclusion was arrived at by examination of the slope of the liquidus; here solidification or lateral segregation upon solidification would produce wollastonite below the pseudo-binary eutectic temperature of 1370 °C, Figure 43. This mineral falls into the Inosilicate classification (The Greek word 'Ino' meaning chain or thread) and is the phase boundary that the glass would move towards after primary crystallisation. Here simple chains are generated by the sharing of oxygen atoms in alternate SiO_4 tetraheda to form bands of double chains. The structural differences arise because the silicon cation has three-fold coordination, as opposed to the four-fold coordination in anorthite. Wollastonite is a member of the pyroxenoid subgroup [63]. It is characterised by a fibrous habit and a triclinic structure. It has a high hardness and density of 2800 – 2900 kg m^{-3}, both of which have been empirically observed in the material. In nature it occurs with the calcium feldspars, i.e. anorthite, [63].

5.2.8.2 Samples 94TET1 and 94TET2 based on RFA waste

The X-ray diffraction spectra of sample 94TET1 and 94TET2 are compared with that of the untreated amorphous material 94TET in Figure 25. The superposition of the graphs gave an indication of the phase transformation sequencing within the material.

Sample 94TET1, was crystallised at 999 °C and had a noisy X-ray spectrum. The five most intense peaks were consistent with the JCPD standard diffraction pattern of anorthite $(Ca)(Al,Si)_2Si_2O_8$ and matched identically with sample 93TET1 when the spectra were superimposed. The intensity of the peaks was not consistent with those observed in 93TET1 and 93TET2, which could be explained using preferential orientation. To confirm the identification, the EDX traces were also compared and found to be similar. The

microstructures were different which would be accounted for by the differences in heat treatment schedule. For example, the crystallisation temperatures were higher for samples based on 93TET, and the heat transfer characteristics were assessed to be different. Anorthite formation has already been described for 93TET1; it is a member of the feldspar group and the plagioclase subgroups, and it has a prismatic and elongated crystal form [1], which was consistent with the micro-structural features that were observed. This conclusion was further confirmed on examination of the higher temperature transformed microstructure of 94TET2.

Sample 94TET2 was crystallised at 1050 °C and the micro-structural features of the whole sample were dramatically different than those of 94TET1 (999 °C). The microstructure displayed features that were consistent with those of sample 93TET1 and 93TET2, where a prismatic primary phase and whisker-like secondary phase were observed. The XRD spectrum of 94TET2 showed that some additional features present were consistent with those of 93TET2, indicating the formation of a secondary phase. The XRD spectrum of 94TET2 showed peaks of intensities that were consistent with the JCPD standard for anorthite $(Ca)(Al,Si)_2Si_2O_8$. Whereas the secondary phase peaks resembled the standard for wollastonite $Ca(SiO_3)$. EDX analysis confirmed this identification in that the darker primary phase was enriched in silicon and aluminium, and depleted in calcium relative to the matrix region. Further work is required to establish the exact identity of the secondary phase.

5.2.8.3 Samples 95TET1 and 95TET2 based on GHS waste

The X-ray diffraction spectra of sample 95TET1 and 95TET2 were compared with that of 95TET in Figure 32. The XRD spectrum of sample 95TET1 had many well-defined peaks, indicating a high degree of crystallisation and indicated that the crystalline phase was enriched in calcium relative to silicon and aluminium, compared to the matrix. Again, the XRD spectrum showed consistency with that of anorthite $(Ca)(Al,Si)_2Si_2O_8$, in terms of normalised intensity and position, but was not sufficient to justify un-ambiguous identification with certainty. However, anorthite will form a range of solid solutions with orthoclase $K(AlSi_3O_8)$ and albite $Na(AlSi_3O_8)$. The material was distinctly different in microstructural characteristics, resembling only the surface structure of 94TET1. The XRD spectrum showed similar characteristics for akermanite $Ca_2(Mg,Al)(Si,Al)_2O_7$ which is a range of solid solutions of melilite $Ca_2(Mg,Al)(Si,Al)_2O_7$ with gehlenite $Ca_2Al_2SiO_7$,

formed between 1200 – 1400 °C. This was consistent with the material's origin as it was processed at 1500 to 1600 °C within the laboratory. Further examination of this sample is required for definite identification. The fine intergrowth features of the microstructure were similar to the solidification microstructure of a eutectic liquid. The sample's composition was very close to the anorthite – gehlenite binary eutectic phase boundary, Figure 43 where the sample's composition is indicated, however the spectral peaks did not show positional consistency with gehlenite.

Sample 95TET2, crystallised at 1239 °C had an X-ray diffraction pattern showing consistency with several crystalline phases. Firstly rankinite, $Ca_3Si_2O_2$, shows positional consistency for all of the lines with variable intensity correlation, however some other intense lines were unaccounted for. Gehlenite, a calcium aluminium silicate, $Ca_2Al_2SiO_7$, showed consistency in both position and intensity for the first three low angle reflections, and then became less accurate in terms of intensity. As before, the spectrum was similar to the anorthite standard spectrum when wollastonite was superimposed. When the morphological features and atomic composition were considered, the primary phase was labelled as either anorthite or gehlenite. Hence a similar transformation to samples 94TET1 and 94TET2 was observed.

Augite, $Ca(Mg,Fe,Al)(Si,Al)_2O_6$, showed positional accuracy for all reflections but no agreement in terms of relative intensity. The material's secondary crystal phase was most likely to be augite as the EDX trace indicated the presence of a significant amount of iron in the secondary crystalline phase. It must be remembered that the microstructure of these materials are oriented, so preferential orientation effects would be expected in the spectrum, as mechanically sectioned samples were analysed. Augite falls into the inosilicate classification (Greek meaning chain or thread) and pyroxene subgroup. Simple chains are generated by the sharing of oxygen atom in alternate SiO_4 tetrahedra to form bands of double chains. Augite is formed from a complete solid solution series between diopside and hedenbergite and is a rock-forming mineral often naturally associated with basaltic lavas, which is consistent with the material's composition and high temperature processing regime.

5.2.8.4 Samples 96TET1 and 96TET2 based on C-MSW waste

The X-ray diffraction spectra of sample 96TET1 and 96TET2 were compared with that of the amorphous 96TET material in Figure 38. Sample 96TET2, was crystallised at 924 °C and had an X-ray pattern with only four peaks at relatively low intensity. Firstly, rankinite $Ca_3Si_2O_7$ showed positional consistency for all of the lines with variable intensity correlation, however some intense lines were un-accounted for. Diopside $CaMg(SiO_3)_2$ also showed a high level of consistency, however magnesium was not observed in the EDX spectra. The two most intense peaks were consistent with the diffraction pattern of albite, (Na, Ca)$(Si,Al)_4O_8$, a mineralogical phase formed by the combination of albite and anorthite as a continuous solid solution series and described as a disordered structure of high temperature origin. The pattern also has some features similar to that of anorthite $(Ca)(Al,Si)_2Si_2O_8$ which is also a closely related member of the feldspar group and plagioclase subgroup already described. Further work is required to give a definitive outcome; for example, a more pronounced X-ray spectrum would have been a more desirable starting point. The crystalline morphology was consistent with that of albite, which falls into the tectosilicate classification of common rock forming minerals [1]. Albite has a three-dimensional network structure consisting of wrapped chains of four membered rings extending in one direction, joined together by ionic bonds from sodium ions. It has a triclinic structure and high hardness and density, 2620 kg m^{-3}, [63]. Albite is a rock-forming mineral that occurs with potash feldspars and is found in both metamorphic and igneous rocks, e.g. granites.

Sample 96TET1 was crystallised at 1060 °C and had a X-ray diffraction pattern with prominent peaks. The electron micrographs showed the presence of two phases with distinctly different morphologies. The surface crystalline region was enriched in calcium relative to the matrix, and the spherultic bulk crystalline phase was depleted in calcium. Augite, $Ca(Mg,Fe,Al)(Si,Al)_2O_6$, showed agreement for all reflections but the relative intensities were not consistent. However, augite was the most likely phase and has already been described as forming solid solutions with diopside. Augite is naturally associated with metamorphic rock forming minerals. Diopside, a calcium magnesium aluminium silicate $Ca(Mg,Al)(Si,Al)_2O_6$, also shows agreement with the X-ray diffraction pattern details.

In summary two distinctly different kinds of microstructure were observed in the samples produced and the microstructural features have been related to phase identity through XRD classification. The target mineralogical phases, of anorthite and wollastonite, were obtained using different waste materials with normalised compositions achieved by the addition of oxides. Even though the bulk oxide compositions of the materials had been normalised and altered within the Al_2O_3-SiO_2-CaO system, their actual compositions determine the actual transformation characteristics and resulting microstructure. These 'as blended' compositions were presented, using the most applicable phase diagram, in Figure 43 and phase diagram consistency has been obtained.

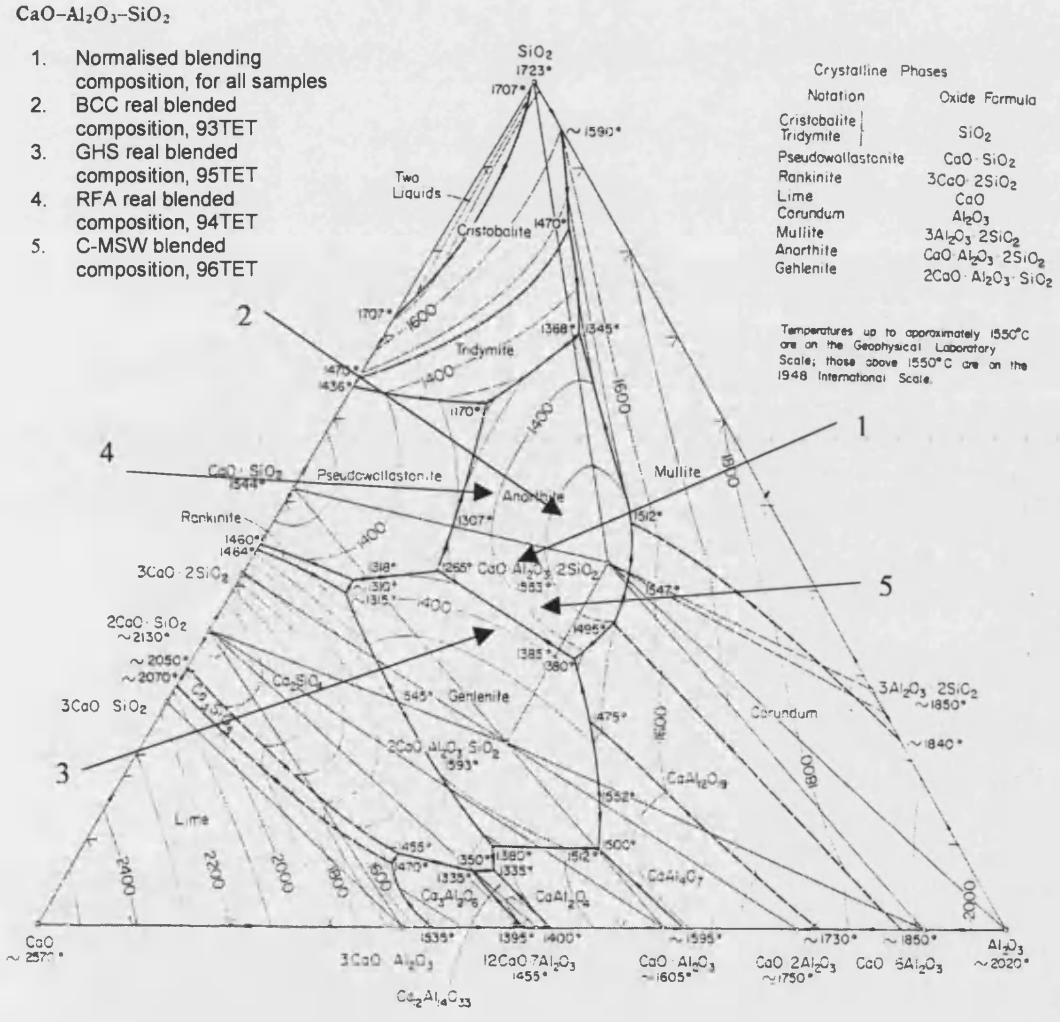

Figure 43: The actual sample compositions displayed on the Ternary phase diagram of the Al_2O_3-SiO_2-CaO system [57]

5.3 Laboratory Experimental Work Conclusion

The requirements of the laboratory assessment were to determine the most suitable material and heat treatment schedule for use in the extended plasma furnace trials. Samples 93TET1 and 93TET2 acquired a uniform grey colour upon crystallisation, but unfortunately they slumped and adhered to the supporting furnace furniture. There was also micro-structural contrast between the centre and surface of the sample, so they were not considered suitable.

Material based on 94TET produced from the RFA, were not available in enough quantity to allow the plasma furnace experimentation to be feasible. The high chlorine content of the waste material would limit industrial suitability, as large volumes of acid gases would have hinder process operation as a result of corrosion problems and the formation of persistent organics such as dioxins and furans.

Sample 95TET1 acquired a uniform green coloration on crystallisation; indentations were noted at the supporting points after crystallisation, but there was no gross material deformation indicating that the heating rate was slightly too high. In contrast, sample 95TET2 had a brown coloration that was micro-structurally uniform throughout its section. The material did slump, but not severely, and had a low level of porosity.

Samples 96TET1 had a brown/green mottled colour after crystallisation and sectioning revealed the bulk of the material was porous. Finally, sample 96TET2 acquired a uniform grey colour upon crystallisation and retained its physical shape and size indicating controlled crystallisation was achieved. This was a distinct improvement over sample 96TET1. Its high density (3170 kg m^{-3}), hardness (HV = 858) and fracture toughness (K_{1C} = 1 MPa$\sqrt{m}$) and its low coefficient of thermal expansion (180 x 10^{-7} K^{-1}), made it the obvious choice for the further plasma furnace trials and detailed crystallisation assessment.

6 The Prototype Plasma System

Thermal plasma arc technology has been applied in a wide variety of high-temperature, material treatment applications, as indicated by the extensive literature available, Section 3. Waste treatment is gaining increasing political and environmental importance, and is the subject of legislation on a worldwide basis. With this in mind the pilot plant plasma equipment was configured to achieve the following aims:

(i). To repeat the laboratory experimentation on a larger scale, in order to demonstrate the consistency of product attainable on an industrial scale.

(ii). To quantify the economic viability of the manufacturing process as a route for processing wastes and for simultaneously generating a glass-ceramic product.

(iii). To evaluate the process, operational characteristics, in order to obtain design information for the specification of larger plants.

6.1 Selection of the Reactor's Heat Source

Section 4.8 gave a phenomenological description of plasma technology, but made little reference to the processing equipment used in its generation. Thermal plasma arc reactors are generally classified in terms of their mode of arc-material interaction, (i.e. transferred, remotely coupled or non-transferred arc), the type of energy and mass transfer (dispersed or condense phase(s)) and the technology used for material containment (e.g. cold skull, refractory lined, levitated etc). The characterising features of the plasma reactor developed for this research will be defined, and its novel features are highlighted below.

The advantages of plasma processing and the reasoning behind the selection of plasma as the heat source were as follows:

(i). The gaseous environment was controllable and energy was provided to the system under oxidising, reducing and inert conditions.

(ii). Fine particle feed capabilities – the reactor and plasma arc configuration allowed direct feeding of particulate material into the reactor at the arc confluence (point of arc contact). This minimised entrainment and physical carry-over of the feed material to the exhaust gas stream.

(iii). The cold skull reactor allowed high temperatures and high energy fluxes for melt containment at elevated temperatures, i.e. well above the liquidus temperature of the glasses, in a relatively short period of time. The phrase 'cold skull'

containment describes the melt as being contained in a water-cooled copper crucible, so that within the crucible a solidified layer of glass forms at the containment interface due to heat transfer characteristics.

(iv). Graphite electrodes offer the advantages of low cost and high reliability. This allows the research effort to concentrate on the process and not the torches.

(v). The twin electrode configuration gives flexible operation. Two configurations were employed; remotely coupled between two electrodes in free space and directly coupled to a fluid melt. The latter allows ohmic heating of the melt, forming an additional heat dissipation mechanism. This configuration is the most suitable for heating a condensed phase due to its high current, low voltage characteristics. The remotely coupled configuration allowed the reactor to be started from cold, obviating the requirement for a conductive hearth.

(vi). The plasma reactors offer the combined advantage of being able to incinerate the combustible parts of wastes and to vitrify the non-combustible parts. This allows simultaneous volume reduction and effective immobilisation of heavy metals, transforming the contaminated wastes into safe, leach-resistant glasses, to protect against heavy metal contamination. The combustible, persistent organics present within the wastes were evaporated off and thermally destroyed (cracked), recombining down stream in the off-gas system as simpler, innocuous, molecules.

(vii). Arc instabilities were overcome during the pilot plant operation as the reactor used a pneumatically assisted gravity feed mechanism that was completely sealed. This eliminated the ingress of diatomic atmospheric gases which would cause destabilisation of the plasma discharge.

(viii). Plasma is the core technology of Tetronics Limited and their facilities were used to undertake the work, i.e. power supplies, control system, utilities and emissions control.

A tilting, twin electrode, cold skull, plasma reactor was used to produce glass-ceramic materials from waste ashes and sediments. The reactor produced a homogeneous and de-gassed melt over a skull of the same composition within a single chamber, which allowed the rapid attainment of steady state conditions. The as-cast tiles were subjected to a scientifically defined cooling and heat treatment cycle to encourage the formation of crystalline phases and a uniform microstructure. Dynamic process control, i.e. fast current control to regulate reactor temperature quickly, was used to compensate for the complex and variable nature of the waste streams.

6.2 The Plasma Processes Methodology

The process took blended and roughly crushed wastes, Section 6.3.1.4, and charged them, into the twin electrode plasma reactor, in a dry solid state, using a screw feeder. The system operated with two plasma arcs each operating at a given current, which therefore, achieved a higher power input than a single arc reactor. The crucible was fabricated from cast and machined copper and was water-cooled using an internal water channel. The material was melted and simultaneously contained in a frozen layer of itself (i.e. a skull), which eliminated refractory wear problems so that the bulk oxide composition of the melt was unchanged, neglecting volatile losses.

Within the reactor chamber the molten glass was conditioned using an empirically determined temperature - time cycle that resulted in a homogeneous and de-gassed melt. Argon fed into the reactor to provide an inert atmosphere limited the passage of undesirable feed components into the off-gas stream as a result of oxidation reactions. This meant, that to the greatest possible extent, heavy metal species were retained within the evolved glassy phase and persistent organic species were destroyed. An image of the plasma equipment is given in, Figure 44.

During the experimentation the reactor's power input and chemical melting atmosphere were adjusted independently, to give control and flexibility. When the material had been fully treated the whole reactor assembly was tilted, with plasma still running to maintain the melt's temperature. The melt was cast into pre-heated (600 °C) cast iron moulds and allowed to solidify under controlled conditions.

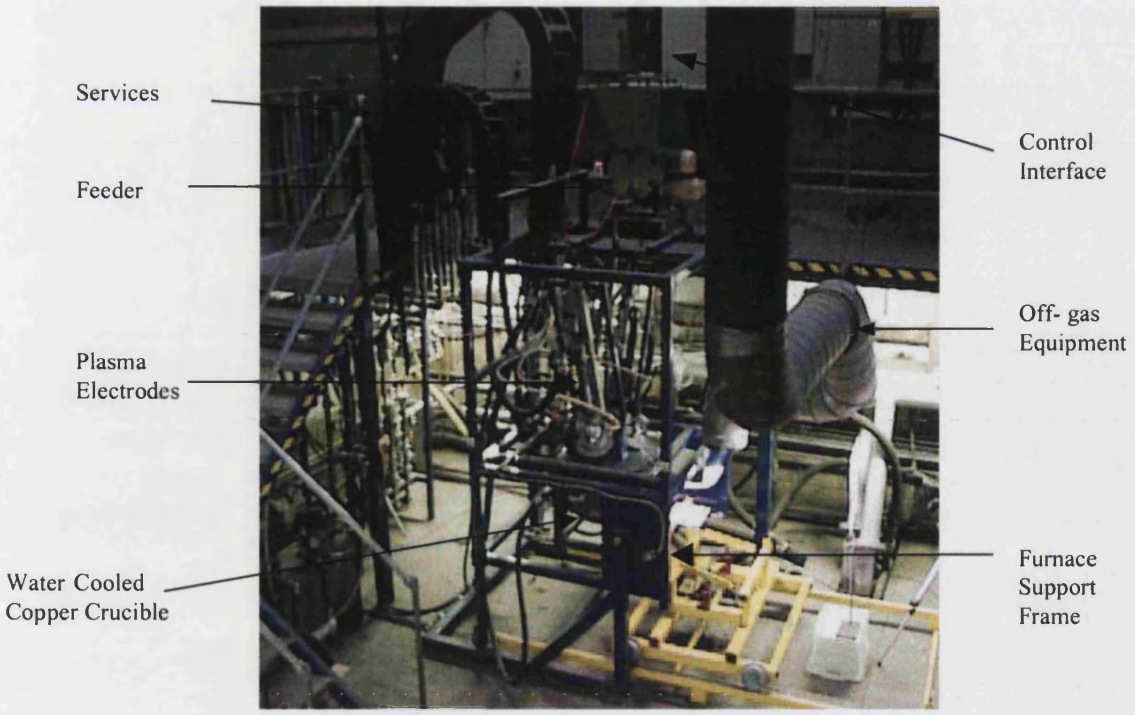

Figure 44: Twin torch plasma reactor

6.3 Process Design Parameters

The process design criteria were determined by the chemistry of the waste materials and the temperatures and times required for treatment as defined in the laboratory study. The key process design parameters are given in Table 57. The reactor, operated at a temperature of 1450 °C, with a material feed rate of waste of 50 kg hr^{-1} which required net and gross power requirements of 25 kW and 125 kW respectively. The net or theoretical energy was determined thermodynamically from specific heat data and latent heats of transformation. Compositional and phase stability data was therefore used to gain an understanding of the material's processing requirements. The gross energy requirement took into account the efficiency of the plasma heat transfer mechanisms and heat/thermal losses of the reactor's structure, i.e. the energy conducted to the water-cooled elements and retained in the off-gas stream. The power criteria are described further in Section 7.

Theoretical Energy Requirement (kWh kg^{-1} dry waste)	0.5
Estimated heat loss through reactor (kW)	100
Waste feed rate (max) (kg hr^{-1})	50
Gross power input to reactor (kW)	125
Operating temperature of the reactor (°C)	1450
Estimated Volts (V)	125-175
Estimated Amps (maximum) (A)	900
Temperature of metal mould interface (°C)	950

Table 57: Process design parameters for the plasma reactor

6.3.1 Equipment Specifications

6.3.1.1 Plasma Reactor

The twin electrode DC plasma furnace was designed to treat waste materials at up to 50 kg hr^{-1}. A cold crucible melting technique was employed due to the known chemically aggressive nature of the wastes to refractory materials. The low thermal mass crucible containment, allowed rapid material treatment, achievement of steady state and quicker reactor turnarounds, within a working day. The dynamic heat transfer characteristics of the crucible enabled control of the melting conditions, and the generic stages of glass melting were achieved within a single chamber.

The double skinned, water-cooled, hemispherical crucible was fabricated from cast high conductivity copper, Figure 45. The crucible was robust, and gave low maintenance costs. The crucible sections were joined to the roof by a bolted flange. The crucible was lowered and removed, using a hydraulically jacked platform, for servicing away from the main furnace frame. The water-cooled, conical furnace roof was lined with high-grade dense alumina refractory and fixed within the furnace supporting framework. The entire framework was capable of tipping up to an angle of 30 ° about the axis of rotation centred on the pouring spout, to ensure casting of tiles. Motion was controlled using a hydraulic ram operated from a locally mounted pendant, Figure 45.

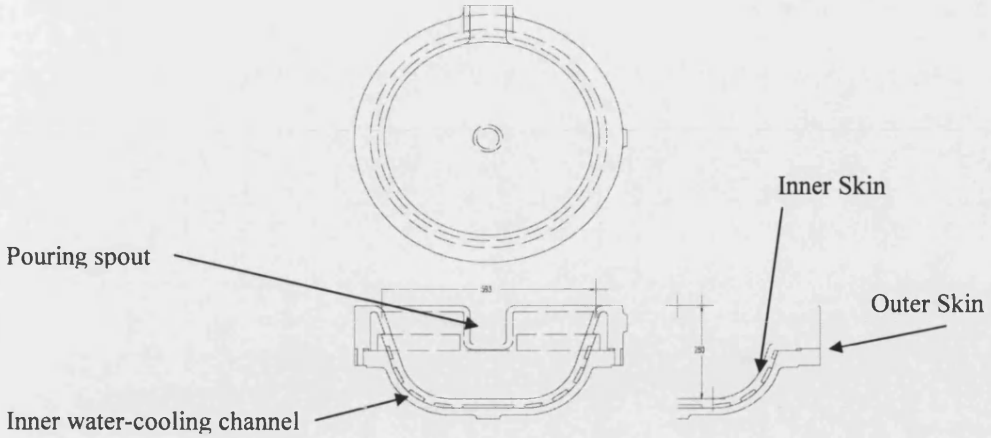

Figure 45: Schematic of the plasma reactor's cast copper crucible

The hot exhaust gases from the melting process were discharged to atmosphere via the pouring spout to an adjacent integrated off-gas handling system. Some key features of the reactor are as follows:

(i) External flange diameter: 780 mm
(ii) Internal cold crucible diameter: 600 mm
(iii) Melt volume: ~36 litres, 108 kg at a melt density of 3000 kg m^{-3}.
(iv) 5 roof ports: Two ports for electrodes, 1 sight port with CCTV, 1 feed port, one temperature monitoring probe port.

A high temperature B type (1800 °C) thermocouple was located in the internal roof space above the melt to indicate changes in reactor temperature. The cooling line's water flow rates and temperatures were monitored to determine the reactor's thermal losses, which gave a means of assessing thermal status and efficiency. Figure 46 gives a general assembly drawing of the plasma reactor with graphite electrodes and actuators in place.

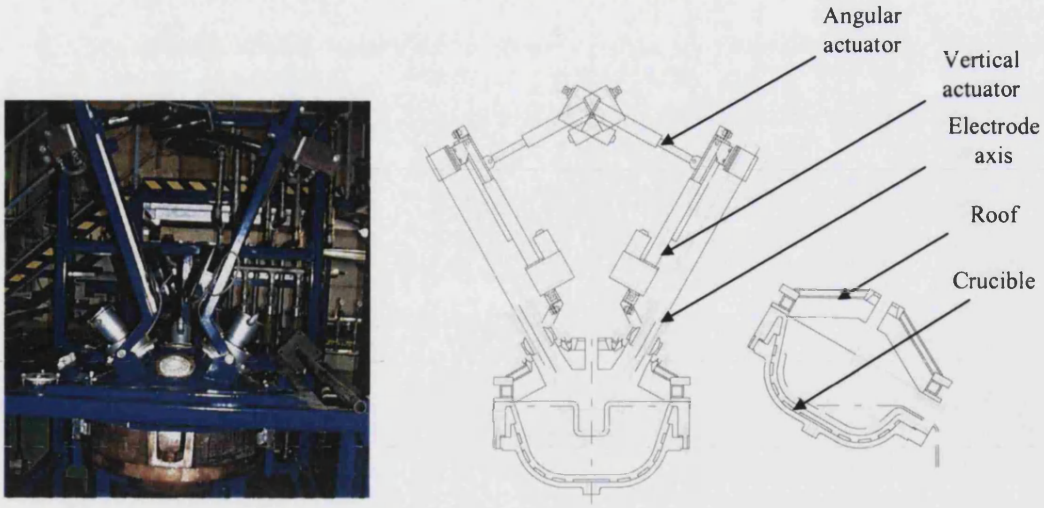

Figure 46: Schematic diagram and photograph of the plasma reactor

6.3.1.2 Casting and Heat Treatment

A key requirement in the production of economically viable material was to cast near-net-shape tiles with good surface finishes. The casting moulds were fabricated from cast iron, with machined inner surfaces', to give 'smooth' bases to the tiles. The moulds were coated with a boron nitride aerosol release agent to protect the mould's surface finish. The thermal expansion properties of the mould material and the tile were arranged to avoid fracture on cooling, i.e. the glass had the higher coefficient of linear expansion so that it shrank away from the mould. The dimensions of the cast tiles were 130 x 130 x ~10 mm, the 10 mm height of the tile being dependent on the quantity of material charged to the mould and varied between 10 mm and 20 mm. The moulds were thermally insulated and preheated to 600 °C in a muffle furnace prior to casting. In the interim period between mould positioning and casting the moulds were externally heated using an oxy-acetylene flame. The temperature of the mould was critical as it dictated whether the tile integrity was maintained and prevented un-controlled crystallisation on cooling. However, it was essential to avoid excessive cooling of the tile as this would have caused cracking as a result of thermal stress. After casting and solidification a controlled heat treatment cycle was applied for transformation into a glass-ceramic product.

6.3.1.3 Plasma Reactor Control System

A Mitsubishi programmable logic controller (PLC) continually interrogated the plasma operation including safety, measurement elements (temperature and positional analogue signals) and plasma power delivery. The main control screens included animated lights and push buttons to switch the services on and off, for operational start-up, interlock verification, system shut down, adjustment of plasma current and for electrode manipulator control. A 3 MW modular thyristor controlled DC plasma power supply (PPS) was used to delivered power to the furnace. The feeding equipment was self – contained with an integral control panel.

The master PLC, used for PPS control and safety, was a Mitsubishi type with a compatible local slave PLC, for reactor specific control. They communicated over an ether net communications link. All critical processing parameters, e.g. temperatures, cooling water inlet/outlet temperatures, voltage and current were acquired by the PLC's analogue and digital input modules for process control and monitoring. The slave PLC provided the safety system monitoring for the plasma reactor including water-cooling, reactor thermocouple temperatures, off-gas temperatures and gas supply flow verification. In particular, automatic cut-off of the plasma power and the feeder occurred upon deviation from the design intention. A human machine interface (HMI) was configured using a proprietary supervisory control and data acquisition (SCADA) software package. It provided control over the plasma operation, electrode movements, data acquisition and alarm/warning displays. It did not adjust water and gas flow rates automatically as these were manually adjusted at the start of each run on the manifold, and the set values were entered into the control system by the operator. The HMI allowed real time control and displayed customised process data based on operational requirements. A schematic of the control system is shown in Figure 47.

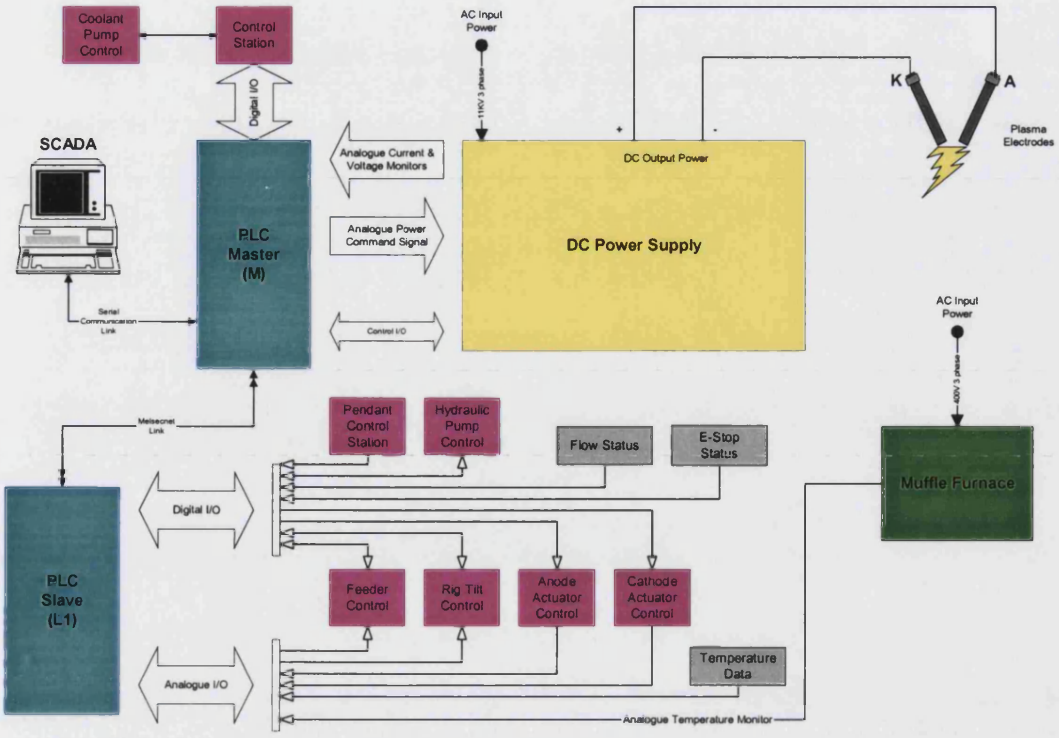

Figure 47: Schematic of the reactor's control system

6.3.1.4 Feeding System

The feed system was gravimetrically controlled, by a metering screw and load cell, i.e. each screw revolution delivered a set volume of material to the furnace, and motor speed defined feeding rate. The pre-blended and classified material was charged to the furnace at a controlled rate between 10 - 50 kg hr^{-1}. The maximum particle dimension was 5 mm, and the minimum particle size was < 1 μm. The feedstock was charged manually to the feed hopper which had internal agitators to minimise segregation. Material was only charged to the furnace and operated while the feeder was in a fully upright position, as this was essential for accurate load-cell operation. The feeder was mounted on the upper section of the furnace frame, Figure 44, and was electrically isolated from the plasma reactor using a plastic flexible inter-connection between the feeder front plate and the feed tube, located in the roof of the reactor. The feeder was fabricated from stainless steel with a gasket sealed hopper lid. It was fitted with an argon gas purge to minimise the potential for air ingress into the reactor and for the avoidance of plasma de-stabilisation and flashback, as the feed contained flammable material and to encourage the passage of feed into the furnace.

While the furnace was being tilted the integrity of the feed supply system was not compromised and an audible motion warning alarm sounded.

6.3.1.5 Plasma Graphite Electrodes and Manipulators

The twin electrode system was rated at a maximum power of 200 kW, however the maximum current allowable was 1200 A and voltage 600 V. Each cylindrical electrode was 1200 mm long and 50 mm in diameter and manufactured from extruded graphite. The twin electrodes were mounted in the roof of the reactor. The process current took alternative routes; either coalescence of the two arcs coupled in free space or through the melt, provided the melt was electrically conductive, i.e. molten. Changes in plasma arc spatial configuration were achieved through actuator movement.

The electrode manipulators incorporated the following features: both electrodes actuators were supplied with angular movement, giving displacements of +/- 13 °, relative to the normal of the flange mounting plate of the conical reactor roof, and a vertical travel of 130 mm relative to a set datum. Actuated movement was achieved with electrical motors and monitored using potentiometer devices. The electrodes were manipulated in a mirrored manner or separately, with direct or relative controls over positional changes.

6.4 The Waste Processing Thermal Plasma System Design

6.4.1 Reactor Copper Crucible Thermal Design

The design of the cold-skull melting furnace was a critical part of the experimental design. The crucible was successful in generating a thermally dynamic melting environment, which allow responsive control of melt temperature without significant time lags. To achieve this, the thermal gradients developed within the hearth region of the reactor were assessed to ensure skull formation. The basis of the design approach was conductive heat transfer theory, using a knowledge of heat flows from the higher temperature inner region to the lower temperature crucible interfacial region. The rate at which thermal energy was transferred by thermal conduction 'q_k' (W) was proportional to the product of the temperature gradient 'dT/dX' (K m^{-1}) and the cross-sectional area 'A' (m^2), i.e. the area normal to the direction of heat transfer, Equation 35.

$$q_k \propto A.{}^{dT}/_{dx}$$

Equation 35

The proportionality constant in Equation 35 is the thermal conductivity, k' (W m^{-1} K^{-1}) of the material. The overall result is the Fourier's equation, Equation 36:

$$q_k = -k'.A.{}^{dT}/_{dx}$$

Equation 36

The negative symbol signifies that a negative '*dT/dx*' is associated with the direction of positive heat transfer, i.e. increasing 'x'. The reactor was modelled as a one-dimensional heat transfer system, where planar heat transfer prevailed under steady state conditions. The following schematic diagram and mathematics illustrates how these assumptions were used to generate simplified equations by integrating Equation 36 to give Equation 37:

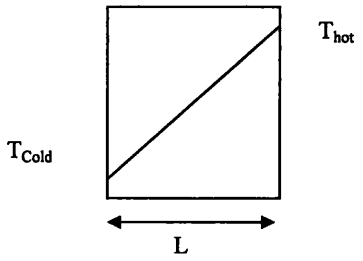

$$\frac{q_k}{A}\int_0^L dx = -\int_{T_{hot}}^{T_{cold}} k'.dT \ldots\ldots when\ x = 0, T = T_{hot}$$

If 'k' is assessed to be independent of temperature:

$$q_k = {}^{A.k'}/_{L}.(T_{hot} - T_{Cold}) = {}^{\Delta T}/_{\left({}^{L}/_{A.k}\right)}$$

Equation 37

A spreadsheet simulation of Equation 37 was used to investigate the mechanism. This assumed that the copper hearth area was constant and that the process power input and hearth heat flux density (Wm^{-2}) was controlled through plasma current changes. The evolved plasma power was transferred to the waste, and the sensible (thermal) energy of the waste was transferred to the water-cooled channel of the crucible by thermal conduction, which was monitored empirically at the manifold, Equation 38.

$$Heat\ flux\ density\ (HFD) = \frac{q_k}{A} = \frac{\Delta T.k'}{L}$$

Equation 38

Firstly, the dimensions of the crucible and system boundary temperatures were defined where possible, e.g. the water-cooling temperature determined the back face temperature of

the copper crucible. The working height of the melt was 150 mm, the diameter of the hemispherical crucible was 600 mm so the upper radius of the melt was calculated to be 250 mm. The maximum back face temperature of the copper crucible was assumed to be 100 °C, as dictated be the water-cooling mechanism and the requirement to avoid film boiling, i.e. local heat transfer difficulties cause by the localised boiling of a liquid resulting in reduced thermal conductivity. Additionally, the temperature of the melt at the interface between the solidified waste and inner liquid waste was defined by the fusion temperature of the melt, ~ 1300 °C, as acquired from phase diagrams, [56]. It had already been determined, in the laboratory, that a temperature of 1600 °C is required for the melt to have sufficient fluidity for casting, Section 5.2.

Next the heat flux density was defined at the skull/crucible interface and used in conjunction with the defined copper crucible back-face temperature and known thermal conductivity of copper [55], to calculate the working face temperature of the crucible, using the following rearrangement of Equation 38:

$$\Delta T = \frac{HFD.L}{k'}$$

The skull back face temperature, i.e. skull / air gap interface temperature, was calculated from a heat transfer coefficient (HTC) value based on the dimension of the air gap behind the skull and Equation 39:

$$HFD = HTC.\Delta T$$

Equation 39

A value of 500 $Wm^{-2}K^{-1}$ was calculated for the HTC and was determined to be realistic, [64] assuming the HTC to be equal to the thermal conductivity/thickness, and taking the value of k' = 0.037 $Wm^{-1}K^{-1}$ for dry air at 200 °C at atmospheric pressure, and an average skull gap of 74 μm, based on the machined surface finish of the crucible. The calculated heat transfer coefficient was conservative as the skull gap was found empirically to be larger than this. This conclusion was also consistent with a simple examination of the machined surface finish specifications, Table 58, and its effect on HTC.

Surface Finish	Size of surface roughness (μm)	Roughness Number	HTC ($W\ m^{-2}\ K^{-1}$)
Very rough machined	50	N12	740
Rough machined	25.6	N11	1450
Semi rough machined	12.8	N10	2890
Medium machined	6.4	N9	5780
Semi fine machined	3.2	N8	11,560
Fine machined	1.6	N7	23,130
Course ground	0.8	N6	46,250
Medium ground	0.4	N5	92,500
Fine ground	0.2	N4	185,000
Superfine lapped	0.1	N3	370,000

Table 58: Surface roughness specifications [57]

The next stage in the calculation was associated with the determination of the skull thickness from the slag fusion temperature and thermal conductivity, Equation 40:

$$L = \frac{k'\Delta T}{(HFD)}$$

Equation 40

The dimensions of the crucible and geometric formulae were used to evaluate the heat losses through the crucible to the cooling waters and the mass of fluid melt present assuming a slag density of 3000 $kg\ m^{-3}$. An illustration of the calculation is given in Figure 48, where it is shown that skull thickness reduces with increases in plasma heat flux density and decreases in heat transfer coefficient.

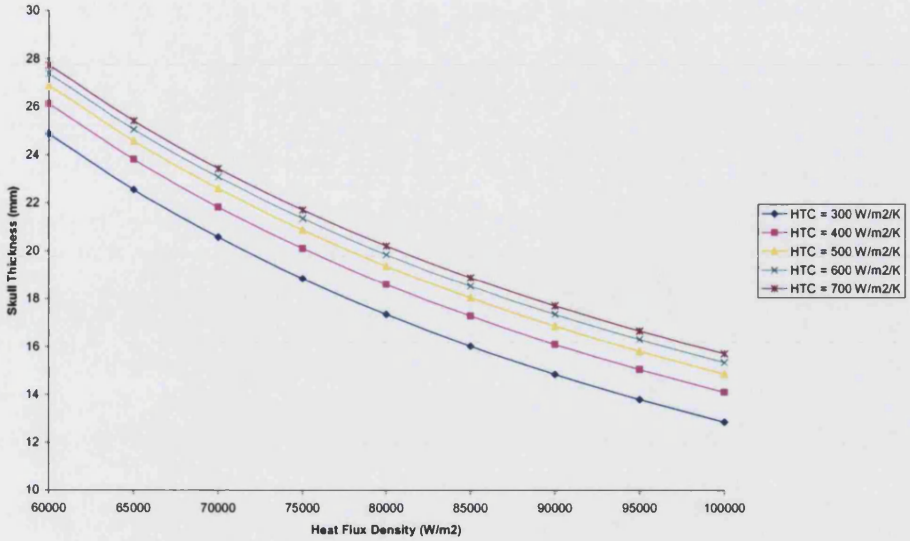

Figure 48: Crucible thermal design calculation results.
Skull thickness versus heat flux density for various heat transfer coefficients

Typical skull dimension of 2 mm were associated with power densities of; 350 kW m^{-2}. Which meant that the active working volume of the crucible would not be reduced significantly and the crucible would be protected from thermal damage.

6.4.2 Copper Crucible Pouring Spout Thermal Design

Once a satisfactory melt pool was established and conditioned within the plasma reactor it was essential to be able to discharge the melt into moulds in a controlled manner. The aim of the design of the pouring spout was to ensure that the melt was able to flow without excessive cooling and solidification.

To determine the performance of the pouring spout design a comparison was drawn between the heat contained within the molten slag, as superheat, at the nominal pouring temperature, with the heat estimated to be extracted by the water-cooled copper base and sides of the spout. The heat extracted was a function of the thickness of the solidified slag layer covering the spout and the heat transfer coefficient (HTC) between the slag and the spout. When the heat contained in the slag, as superheat, equalled the heat extracted from the solid / liquid interface of the pouring spout, the thickness of the solidified skull layer remained constant. Equation 41 was used to calculate the heat flux density (HFD):

$$HFD = HTC.\Delta T$$

Therefore

$$Heat\ Extracted = HFD.A$$

Equation 41

Where: ΔT = (glass underside temperature - spout temperature) (K).

A = melt / spout contact area (m^2)

Equation 41 was rewritten in terms of the heat lost from the glassy material, Equation 42:

$$Heat\ Extracted = P''.C_p.\Delta T_{lost}$$

Equation 42

Where: P'' = the material pouring rate ($kg\ s^{-1}$)

C_p = glass specific heat capacity ($J\ kg^{-1}\ K^{-1}$)

ΔT_{lost} = degrees of superheat lost (K)

An example of the calculation's structure and the values used are given below:

<u>Glass properties</u>	
Molten specific heat capacity ($J\ kg^{-1}\ K^{-1}$) [61, 62]	1,400
Melting point (°C) [62]	1,300
Interfacial heat transfer coefficient ($Wm^{-2}K^{-1}$)	500
<u>Inner pouring spout dimensions & properties</u>	
Inner pouring spout width (m)	0.1
Inner pouring spout length (m)	0.1
Skull depth on spout (m)	0.01
Interface temperature (°C)	200
Glass pouring rate ($kg\ s^{-1}$)	0.1
<u>Calculated Results</u>	
Skull underside temperature (°C)	1,200
Heat flux density ($W\ m^{-2}$)	500,000
Heat extracted (W)	6,000
Degrees of superheat extracted from the glass (°C)	42.9

The calculations showed that under the most unfavourable conditions, i.e. with a slow pouring rate and a high temperature difference between the underside of the solid glass and the upper surface of the copper spout, only 43 °C of superheat was extracted by the pouring spout. This was a relatively small loss of superheat and did not cause any practical difficulties, as the superheat requirement for the materials' fluidity was much higher. In practice a 7 – 10 mm skull built up on the lip but never hindered the pouring process. The most important conclusion to be drawn from the calculation is the reciprocal relationship between casting rate and lost superheat.

6.4.3 Tile Casting Mould Thermal Design

The thermal design of the tile moulds was based on the argument that the mould absorbed the sensible heat of the liquid slag. This occurred until the system attained thermal equilibrium and the ultimate temperature was between limiting values. The approach balanced the heat capacities and relative mass proportions of the tile mould and the contained slag, until thermal equilibrium was reached without peripheral heat loss. This allowed selection of an appropriate combination of mould material and pre-casting temperature for the tile. The adiabatic mould filling calculation was as follows:

<u>Glass properties</u>	
Temperature of slag (°C)	1300
Specific heat capacity (J kg^{-1} K^{-1}) [47, 62]	1400
Density (kg m^{-3})	3000
<u>Cast Iron properties @ 500°C</u>	
Specific heat capacity (J kg^{-1} K^{-1}) [55]	650
Density (kgm^{-3}) [55]	7500
<u>Tile dimensions</u>	
Length (m)	0.13
Width (m)	0.13
Thickness (m)	0.01
Mass (kg)	0.507
Heat contain in the tile (J K^{-1})	709.8

Mould Dimensions (base only)	
Base thickness (m)	0.01
Mass under tile (kg)	1.27
Heat contained under the tile ($J K^{-1}$)	823.9
Initial conditions	
Slag temperature (°C)	1300
Mould temperature (°C)	400
Heat content of slag (J)	922,740
Heat content of mould base (J)	329,550
Resulting equilibrium temperature (°C)	816.5

The resulting thermal equilibrium temperature, 816 °C, was for a cast iron mould, 10 mm thick, which was used in practice. It was assumed that the heat from the tile was only conducted downwards and was representative of the situation at the bottom central position of the tile. The calculation indicated that for a melt temperature of 1300 °C and a mould preheat temperature of 400 °C, the equilibrium temperature was 820 °C. This temperature was below the melting point of cast iron mould material (eutectic temperature is 1150 °C) and above the annealing temperature of the glass products (< 800 °C). The final mould design is presented in Figure 49.

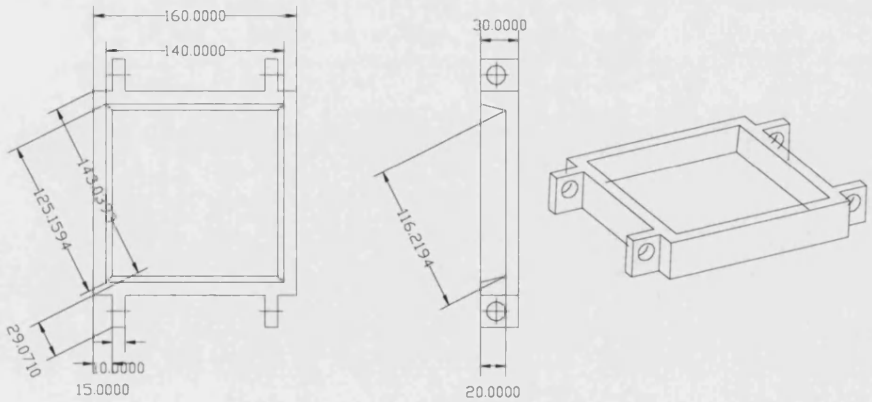

Figure 49: Cast iron mould design (dimensions in mm)

The equipment successfully achieved its design intention. The operation was reproducible, stable and robust and the reactor supplied all the operational data required for the experimental work. The reactor was operated safely and incurred no damage during the campaign. It was easy to service and clean and required minimal maintenance. The moulds were manually manipulated during casting and this produced operational variations in the tiles' dimensions and consistency. Automation of the casting process would improve quality and reproducibility of the tile's dimensions.

6.5 Detailed Process Description

Ash wastes were manually pre-blended with additives and fed at a controlled rate (50 kg hr^{-1}) to the plasma cold skull reactor, using a gravimetric screw feeder. Here the wastes were melted and conditioned at temperatures between 1450 - 1800 °C, giving high enough fluidity to allow casting. The roof of the furnace was water-cooled and lined with a castable refractory. The plasma reactor was heated using twin graphite plasma electrodes. The DC electrical power connections were made to the electrodes' using water-cooled copper clamps, with vertical and angular movements controlled by electro-mechanical actuators. Their point of entry into the furnace was located in the roof and sealed using water-cooled glands with an inner aluminium/graphite composite packing material. The water and gas services to the plasma reactor were controlled and monitored using distribution manifolds: these included pressure, flow rate and temperature measurement devices. The sensors with externally available electrical outputs were linked to a programmable logic controller (PLC). This communicated with a supervisory control and data acquisition system (SCADA), which provided the operator with an interactive graphical interface for process control and data acquisition. The system was visually interrogated using internal and external close circuit television (CCTV) and charged couple devise (CCD) equipment, respectively.

The plasma current was adjusted to maintain the melt at the required temperatures, here process voltage was dictated by the internal reactor environment. The twin plasma arc heater is shown in Figure 50. Crucible power densities of up to 450 kW m^{-2} were achieved. Variations in plasma voltage occurred due to entry of feedstock into the plasma arcs which increased the local resistivity, and the specific power input of the process. The reactor was periodically tipped to discharge parts of the melt into preheated moulds that were thermally insulated to limit the rate of heat loss by natural convection and radiation. The tiles cooling rate was controlled so that it was within the boundary conditions defined

by thermal stress evolution within the tile and the requirement of glass formation. The tiles were finally transferred to a pre-heated muffle furnace where they experienced a multi-stage, nucleation and crystallisation, heat treatment cycle.

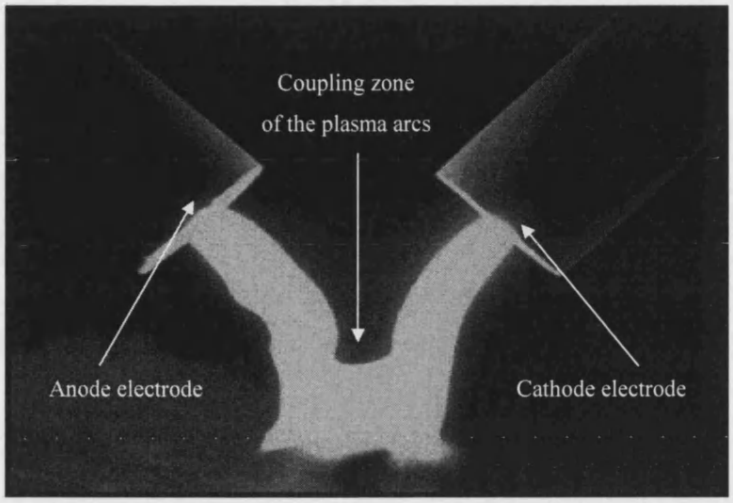

Figure 50: An image of remotely coupled twin arc plasma plumes
The electrode/torch diameters are 38 mm

7 Operational and Economic Assessment of the Plasma Furnace's Processing of Waste Materials

The treatment of harbour sediments, industrial wastes, mining wastes and municipal solid wastes, using dredging, cementation and incineration, is becoming increasingly expensive; for hazardous wastes e.g. contaminated soils, the treatment costs are likely to increase dramatically from ~£20/tonne to >£100/tonne in the near future. The cost of the landfill tax will also escalate it is widely expected to go from £15 to £25/ tonne by 2005/6, [2, 3]. The current cost of hazardous wastes treatment within Europe is ECU 200/tonne. These costs are being exaggerated by environmental concerns. Conversion of these residues into useful and environmentally compatible products offers the potential for economic recycling and reuse scenarios. Additionally, it obviates the requirement for material transport, and storage in, hydrologically engineered landfill sites, [2]. Treatment also reduces the potential for future social and economic liability promoting longer term industrial stability. The economic viability of cold skull plasma vitrification and refinement of waste materials has been evaluated. Prototype scale proof of concept trials were undertaken and evaluated.

7.1 Experimentation

The material residues for the prototype experiments included dry and classified German Harbour Sediment (GHS), Classified Municipal Solid Waste (C-MSW) grate ash and British China Clay (BCC) mining waste, as described in Section 5.1. These wastes were blended with virgin oxide additions to give bulk oxide composition with desirable melting, crystal growth and rheological properties, Section 5.1.

The Plasma Melting Furnace has a refractory lined and water-cooled roof and side-walls and a hemispherical, water-cooled, copper melting crucible. The ancillary equipment included:

(i) Water and argon gas supply, cooling, monitoring and distribution manifolds

(ii) Furnace, internal volumetric, material feeding equipment

(iii) Fume emission control and handling equipment

(iv) 3 MW modular DC plasma power supply (5000 Amps and 600 Volts maximum)

(v) Integrated programmable logic controller (PLC) and supervisory control and data acquisition (SCADA) systems

The furnace was designed to allow material to be fed at up to 50 kg hr^{-1} and had an electrical power capacity of up to 250 kW. The theoretical energy requirement (TER) for the plasma treatment of these materials was approximately 0.55 kWh/kg, i.e. based on the thermodynamic requirements only and neglecting thermal losses. The thermal analysis did not consider the reaction kinetics. The vitrified product was intermittently tapped from the furnace into pre-heated cast iron moulds. Photographs of the equipment and tapping process are shown in Figure 51.

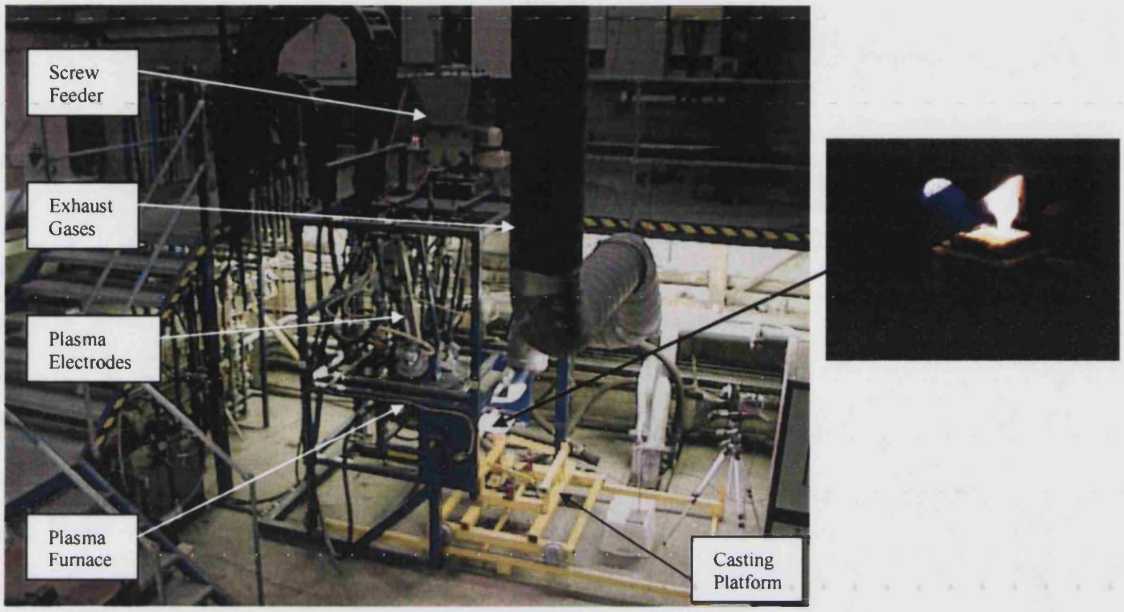

Figure 51: Plasma reactor installation with casting process insert

The photographs in Figure 51 appear to be very dark due to the high level of irradiance produced by the plasma in relation to the background level of light intensity. The intense light from the plasma required the use of eye and skin personnel protective equipment. The plasma light comprises of a wide range of wavelengths with peaks in the ultraviolet region. The plasma radiation was non-ionising, (as confirmed by the National Radiological Protection Board (NRPB)) because the applied potentials and potential fields were low, typically 400 V and always less than 600V, over a 300 mm arc length.

7.2 Method and Procedures

The dried, screened, as-received residues were extensively characterised to determine their physical properties and chemical composition, the analysis focused on compositional analysis including WD-XRF and ICP-OES, Section 5.1. The results are given in Table 41. Tap density data and loss on ignition (LOI) data were obtained, the latter by use of a thermal gravimetric balance.

The materials were prepared for the plasma furnace in accordance with the following procedure: isolated samples of the raw wastes, (~5 kg) x 20 = 100 kg, were made and thoroughly mixed, then coned and quartered to generate four sub-samples, each of 25 kg. Varying virgin material additions were made at this point, to adjust the overall bulk oxide composition in order to give more desirable melting characteristics and a predictable crystalline phase evolution, Section 5.1 and Section 8. All of the wastes were adjusted to fall in the same compositional phase region, Table 59 and Figure 43. The blending materials employed were Chinese bauxite, burnt lime and silica sand, all of industrial purity, i.e. 99.5 wt% pure. The materials were heated in a standard radiant element furnace so that the LOI, after calcination, was less than 5 wt%, including acid and volatile gases, oxidation losses for carbon and sulphur and the evaporated water content. All of these species could have de-stabilised the plasma operation by sporadically increasing the gas phase resistivity. Overall, the water content was lowered to 1 – 2 wt %. This preparation procedure ensured the correct material flow properties through the feeding equipment and the avoidance of refractory stones in the cast tile product. The materials were crushed and screened through a 10 mm square mesh sieve. Metered screw (auger) type feeding equipment was used in the experimentation.

ID	Waste	Virgin Material Addition	Overall Virgin Oxide Addition to waste
Lab Equivalent	ID	Addition per 100g of waste	(wt%)
93 TET	BCC	23.5 CaO	19.0
94 TET	RFA	11.0 SiO_2	9.9
95 TET	GHS	46.9 CaO 32.6 Al_2O_3	44.3
96 TET	C-MSW	13.9 CaO 19.9 Al_2O_3	25.2
Required As-Blended Waste Composition			
Oxide Species	SiO_2	CaO	Al_2O_3
Mass Comp (Wt %)	43.1	29.2	27.7
Molar Comp (mol%)	47.5	34.5	18.0

Table 59: Normalised material blending details

The 'as blended' materials had an apparent density of approximately 1200 kg m^{-3} which was assessed using a measuring cylinder and mass balance to obtain the mass of a known volume. During experimentation, the plasma furnace was firstly pre-heated, to allow the

inner chamber to reach a temperature of 1600 °C, before material was charged to the furnace. The intention was to allow a frozen skull to form from the molten material inside the furnace. The material was intermittently charged to the plasma furnace so that the small volume of the furnace did not become locally saturated in cold granular feed material.

The material was charged directly into the confluence of the twin plasma arcs. This approach was taken to aid material assimilation by delivering material directly to the hottest part of the furnace, and so avoiding the build up of thermally insulating mounds of feed material. During each trial, steady states testing conditions, defined by total energy accountability, were acquired after a relatively short period of time, and were held for the required duration. The feed material generated noticeable quantities of volatile matter upon entry into the hot furnace indicating the importance of the calcination pre-treatment in reducing the amount of volatiles generated. After the furnace was pre-heated, intermittent feeding occurred and the melt height increased. The melt was then homogenised, degassed and superheated for casting. Dynamic melt temperature control was achieved in a singular vessel by balancing the cold skull containment with the degree of top surface heating by the plasma. The crucible power densities ranged from 95 to 475 kWm^{-2} based on a crucible hearth interfacial area of 0.53 m^2 and the crucible's thermal losses to its inner water cooling circuit. These values are consistent with the conditioning and feeding periods of the process, respectively. Material entry into the plasma plumes, cooled the arc and increased local resistivity and arc voltage which, for a given operating current, increased the specific power input to the process. Hence the process temperature was controlled by varying the current, with the voltage being determined by the nature of the system.

The plasma furnace monitoring allowed the gross plasma power input to be determined from electrical characteristics, namely voltage and current. The thermal losses were calculated form the temperature increase seen on the different water-cooling furnace circuits. The difference in the gross power input and thermal losses and was the amount of power available for the treatment of the waste materials. The same information was used to assess plasma and thermal stability, processing costs and overall efficiencies. It also allowed the attainment of steady state conditions to be observed.

7.3 Plasma Experimental Results

A total of 17 plasma experiments were undertaken, including the heating, feeding, conditioning and cooling time. Equipment familiarity and experience improved the operating methodology, hence only the later trials are reported. Material mass balances for the plasma furnace operation are given in Table 60. The feed material was partitioned between the furnace melt, tile product, hopper residue and the physical and chemical gas phase carry-over. The crucible was designed to retain a residual volume of melt to avoid localised and intense heating of its structure.

	Trial 11 = 93TET		Trial 13 = 96TET		Trial 14 = 96TET		Trial 15 = 95TET		Trial 16 = 95TET	
Furnace Product	Weight (kg)	Phase (%)	Weight (kg)	Phase (%)	Weight (kg)	Phase (%)	Weight (kg)	Phase (%)	Weight (kg)	Phase (%)
1.Furnace charge (hopper/crucible)	79.77	-	80.00	-	87.11	-	52.06	-	49.05	-
2.Vitrified furnace residue	59.20	74.21	42.37	52.96	54.03	62.03	37.00	71.07	40.50	82.57
3.Tile weight	6.38 (7 tiles)	8.00	5.40 (6 tiles)	6.75	5.28 (6 tiles)	6.06	3.03 (6 tiles)	5.82	3.68 (6 tiles)	7.50
4.Hopper residue	13.00	16.30	23.74	29.68	23.39	26.85	8.52	16.37	0.00	0
5.Baghouse carry-over*	0.56	0.70	3.63	4.54	3.98	4.57	4.18	8.03	0.97	1.98
6.Electrode consumption	0.38	-	0.35	-	0.27	-	0.19	-	0.22	-
Accountability* (%)	98.5	-	89.38	-	94.94	-	93.25	-	90.07	-

*Accountability values do not include exhaust stream carry-over, these are calculated from the LOI values

Table 60: Material mass balance and phase partitioning over the plasma furnace

7.3.1 Plasma Trial 11 - 93TET (BCC)

Trial 11 comprised the primary heating of the plasma furnace equivalent to laboratory experiment 93TET, which is a BCC based material and included the primary 'furnace conditioning' period. To protect the copper components powdered waste material was placed in the crucible before the experiment started. The melting operation was stable which gave predictable electrical and thermal characteristics for a given feed type and rate. At a feed rate of 16 kg hr^{-1} of blended BCC a current of 900 A was used at a voltage of 167 – 221 V, the voltage was typically 170 V. The voltage decreased during the conditioning stages of the process, to a value of 70 V, so the current was increased above 900 A to sustain the power input to the furnace, as the system was thermal loss dominated. Figure 52 is a graph of plasma current, voltage and power as a function of time. The trial was controlled and no plasma outages occurred, i.e. the current did not drop to zero at any

point. The feeding period dominated the total time of the trial, the different stages of preheating, feeding, casting and cooling are indicated by the annotations within Figure 52.

The melt was visually uniform and flowed easily into the moulds, giving rise to seven physically intact tiles. The production economics will be pessimistic, as the process had to firstly achieve a steady state from cold, before going on to tile casting. More material was treated than actually utilised for tile production, Table 60. Feed-rates of up to 16 kg hr^{-1} were achieved but difficulties were experienced due to the fine nature of the clay waste material feed and physical carryover to the off-gas handling system, which produced an extended flame projecting from the furnace. Figure 53 is a graph of the thermal losses to different water-cooled components as a function of time, calculated using Equation 43. The furnace's thermal losses to water-cooled components were dominated by losses to the crucible. The overall power balance is presented in Figure 54, which is a graph of gross power input, total thermal losses and net power input as a function of time. The total energy usage of trial 11 was determined to be 267 kWh and was consumed in 3.5 hours. The capture and reporting of data was done at one minute intervals, data tags have been omitted from the majority of the graphs to ease interpretation.

$$Q_{loss} = K' \, x \, F_R \, x \left(T_{rtn} - T_{flw}\right)$$

Equation 43

Where Q_{loss} = Thermal loss (kW)

F_R = Water flow rate (l m^{-1})

T_{rtn} = Return water temperature (°C)

T_{flw} = Flow water temperature (°C)

K' = 0.07 (kW min $litre^{-1}$ $°C^{-1}$)

= Specific heat (C_p) of water corrected for volume flow and the units

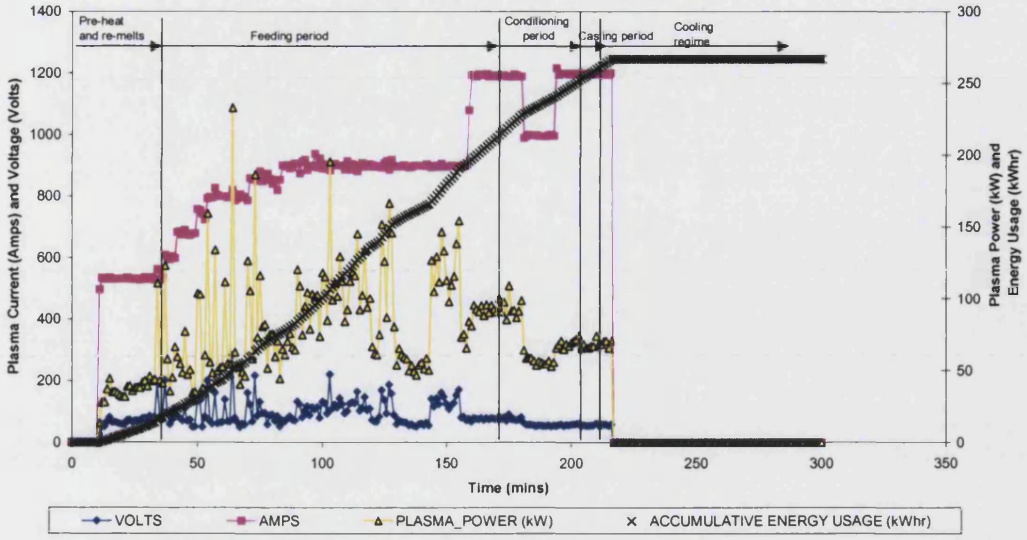

Figure 52: The electrical status and accumulative power consumption of Trial 11

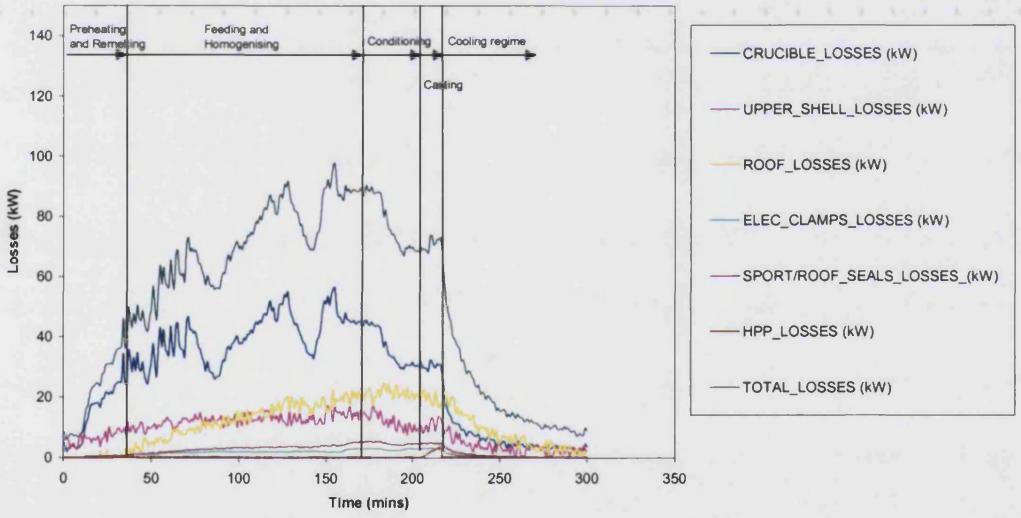

Figure 53: Thermal losses of Trial 11

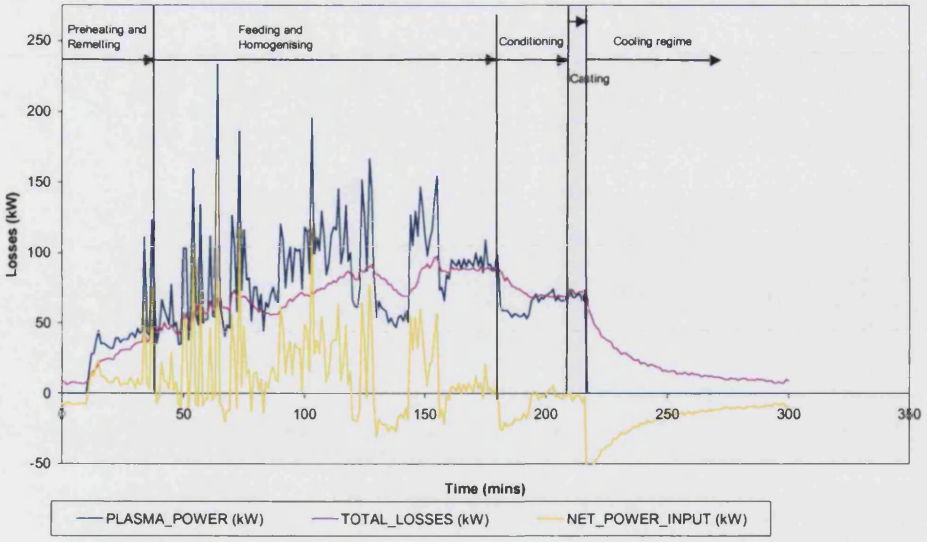

Figure 54: Thermal status of Trial 11 in relation to the balance of gross plasma power input and the total thermal losses of the plasma furnace

7.3.2 Plasma Trial 13 – 96TET (MSW)

Trial 13 was a secondary heat of the plasma furnace with C-MSW, equivalent to the laboratory experiment 96TET, and included a primary 'feed re-melting' period and a subsequent feeding period, because the residual material from the previous trial had to be re-melted prior to the introduction of new feed. It differed distinctly from Trial 11 in that the vitrified feed material of the previous trial, of the same composition and waste origin as the hopper charge, was retained in the crucible to protect the copper hearth. The melting operation was stable and gave predictable electrical and thermal characteristics for the feed type and feeding rate of 22 kg hr^{-1} C-MSW waste. No plasma outages occurred during trial 13, Figure 55, i.e. the current did not drop to zero. During feeding of material into the plasma typical currents of 855 A and voltages of 180 – 230 V were measured. The voltage peaked at 290 V when the feeding characteristics were locally intensified. The electrical characteristics of the process changed sharply during the conditioning stages of the process, where the voltage decreased 80-70 V over a period of 100 minutes. The current was increased to 1200 A during this period to maintain the power input to the furnace and the temperature and fluidity of the melt. The trial was not dominated by any specific stage

of the process and the electrical characteristics were similar to those of trial 11, validating the generic nature of the technology. The melt cast successfully due to the superimposed conditioning period of the previous trial with conditioning performed during trial 13. Five physically intact tiles were produced. Here the production economics are optimistic, as the crucible was partially filled with treated material before the trial started. In this case the utilisation of the material fed to the furnace during the trial improved. Feeding rates of 22 kg hr^{-1} were employed, after starting at 15 kg hr^{-1}, this accounted for higher processing voltages observed towards the end of the feeding period. The crucible dominated the thermal losses of the furnace, where they were observed to peak at 85 kW, Figure 56. The overall power balance of Trial 13 is presented in Figure 57, here the total energy usage equalled 327 kWh and was consumed in four hours and ten minutes. The three hour point saw the onset of conditioning and the attainment of steady state conditions, defined zero net power input, that were sustained for the remainder of the trial.

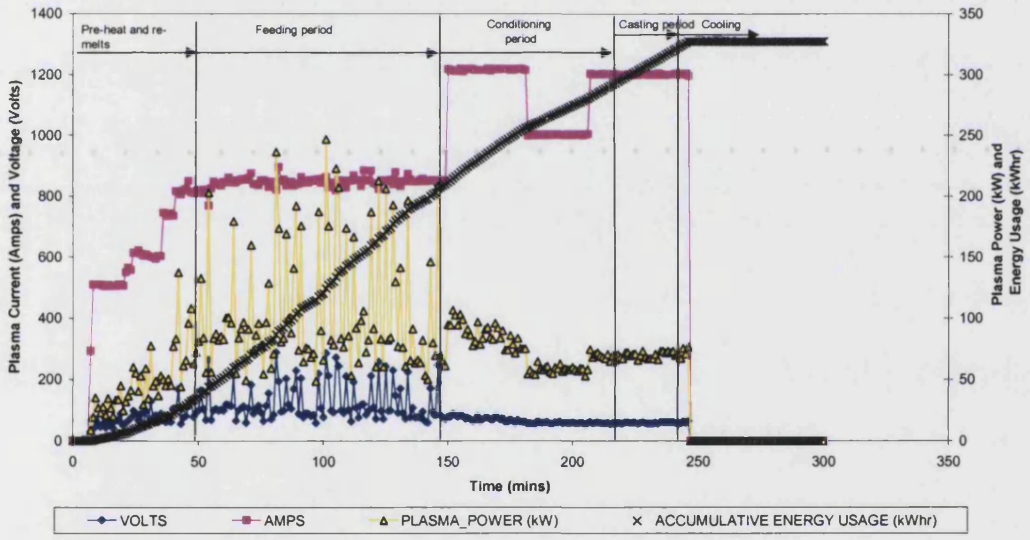

Figure 55: The electrical status and accumulative power consumption of Trial 13

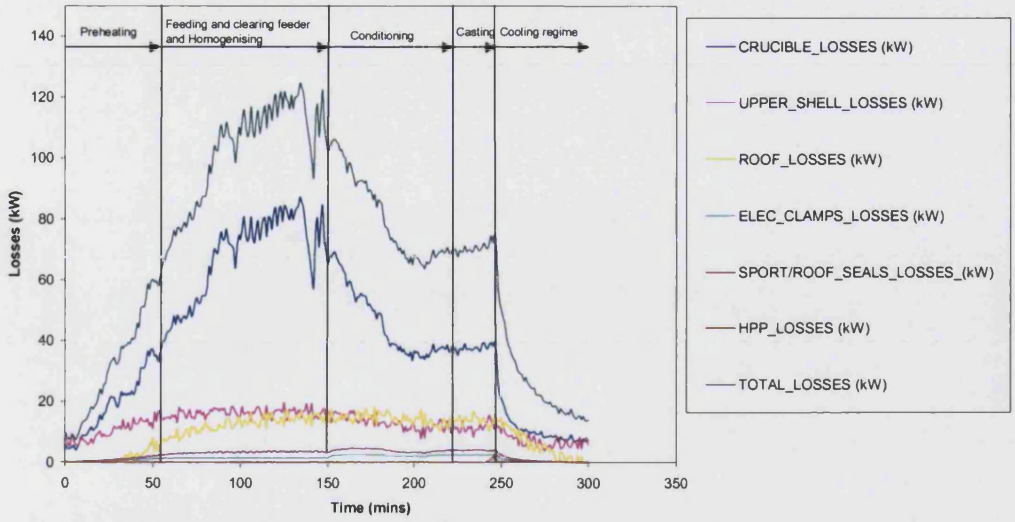

Figure 56: Thermal losses of Trial 13 showing the dominance of the crucible thermal losses

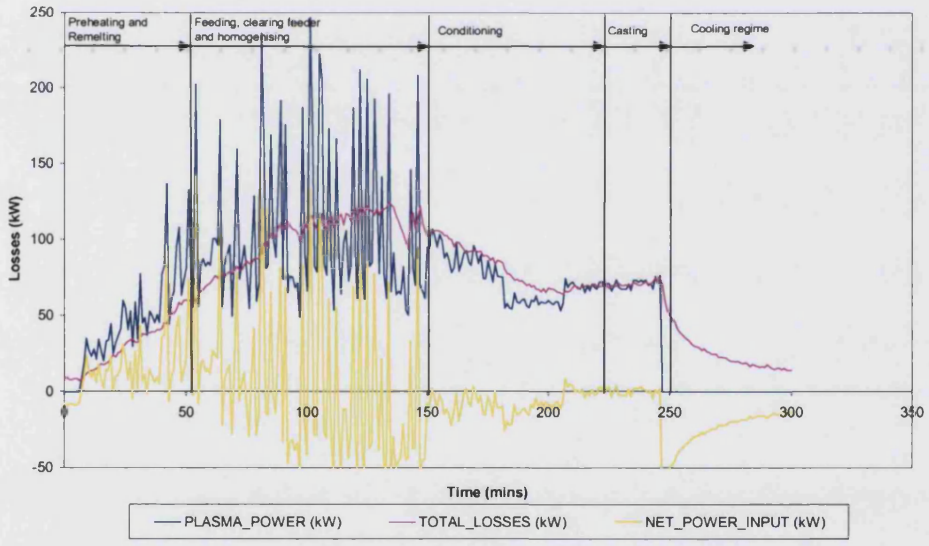

Figure 57: Thermal status of Trial 13 in relation to the balance of gross plasma power input and the total thermal losses of the plasma furnace

7.3.3 Plasma Trial 14 – 96TET

Trial 14 was a secondary heat of the plasma furnace containing C-MSW, equivalent to the laboratory experiment 96TET, and included the primary 'feed re-melting' period and subsequent feeding period. In this respect it is very similar to the previous trial 13, but condensed into 150 minutes. The melting operation was stable and gave predictable electrical and thermal characteristics with respect to trial 13 and no plasma outages occurred, Figure 58. At a feeding rate of 15 kg hr^{-1} C-MSW waste, typical currents were of 920 A and voltages of 120 – 190 V were measured. The voltage peaked at 220 V when the feeding characteristics were locally intensified. The electrical characteristics of the process changed sharply at the conditioning stages of the process, where the voltage decreased steadily from 88 V to 66 V over a period of 100 minutes. The current was increased to 1200 A during this period to maintain the power input to the furnace and the temperature of the melt, Figure 58. The different stages of the experiment were similarly proportioned to those of trial 13, but overall the trial was much shorter. The trial lasted a total of 150 minutes. The melt was uniform and cast well from the furnace, giving 6 physically intact and complete tiles. Here the production economics will be similar to trial 13 as the overall formats of the experiments were similar. Feed rates of up to 15 kg hr^{-1} were employed. Thermal losses to water-cooled furnace components are summarised in Figure 59. The crucible's losses were 130 kW, which is significantly higher than in the case of trial 13 and accompanies the intensification, and dominated the losses. The higher crucible losses were attributed to the higher melt level within the crucible. The overall power balance is presented in Figure 60, here the total energy usage equalled 218 kWh and was consumed in two hours and thirty minutes. Steady state conditions were acquired two hours into the trial where the electrical power input balanced the thermal losses, Figure 60. The time axis for all the trials has been held constant so that direct comparisons can be made easily.

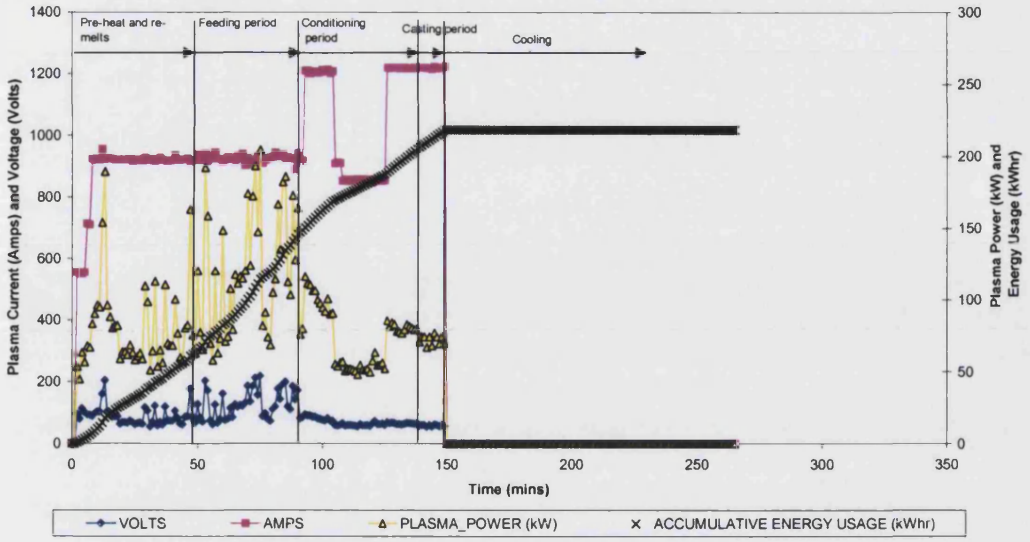

Figure 58: The electrical status and accumulative power consumption of Trial 14

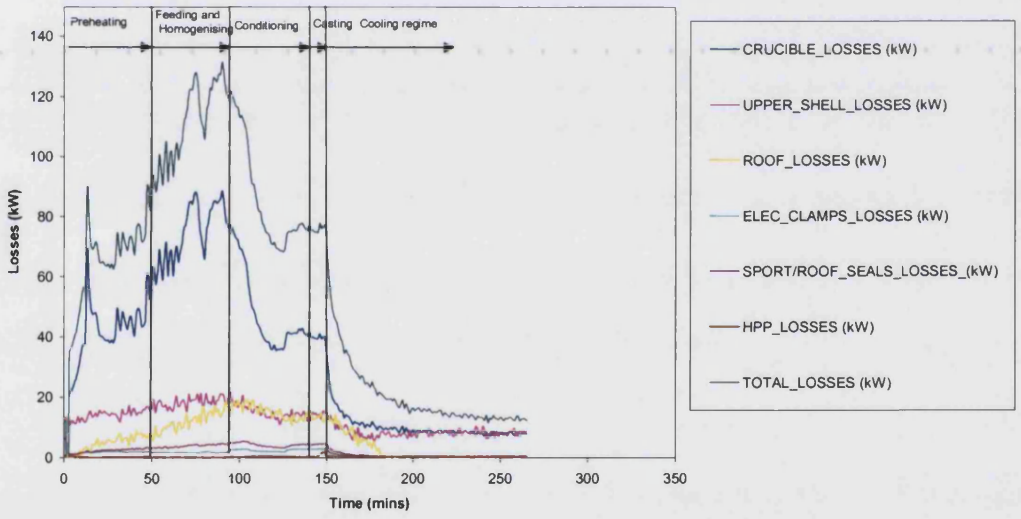

Figure 59: Thermal losses of Trial 14 showing the dominance of the crucible thermal losses

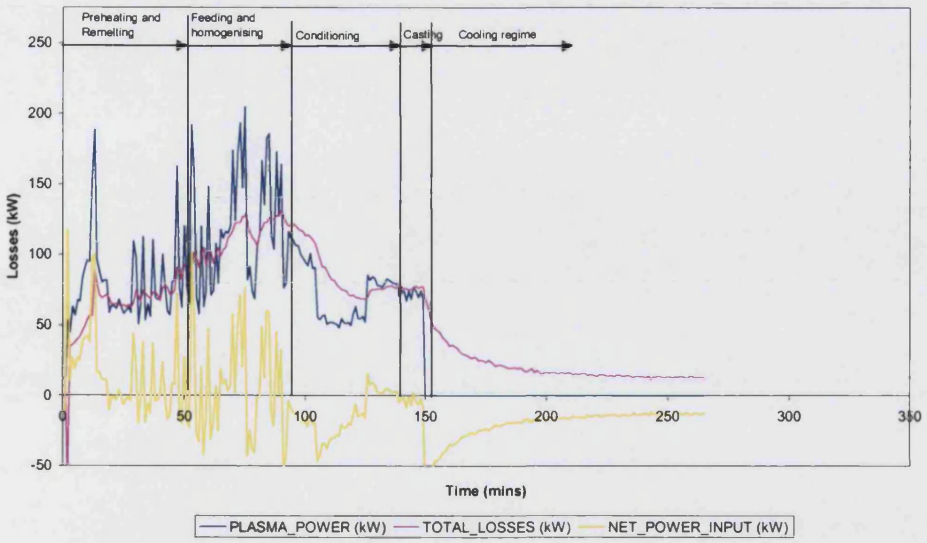

Figure 60: Thermal Status of Trial 14 in relation to the balance of gross plasma power input and the total thermal losses of the plasma furnace

7.3.4 Plasma Trial 15 – 95TET (GHS)

Trial 15 was a primary heat of the plasma furnace with GHS, it was equivalent to laboratory experiment 95TET, and included all operational stages encountered in starting the cold and empty furnace. Prior to the trial, granular material was placed in the crucible to protect its copper structure from intense localised heating. In general the melting operation was stable with gave predictable electrical and thermal characteristics. The feeding period dominated the lapsed time of the trial, lasting for approximately five hours, as indicated by the annotations in Figure 61. At a feeding rate of 22 kg hr^{-1} GHS waste, typical currents were 900 A with associated voltages were 195 – 290 V. The voltage peaked at 395 V with intensified feeding and overall higher voltages were noted for the GHS material for comparable mass feed rates of the other waste materials, Figure 61. The voltages were attributed to the high level of organic and combustible components present within the waste material, Table 41. The electrical characteristics of the process changed sharply at the conditioning stages of the process, where the voltage was stable at 65 V over a period of 1 hour. The current was increased to 1200 A during this period to maintain the power input to the furnace and the temperature of the melt. The trial lasted a total of 350

minutes. No plasma outages occurred during an extended operational period, demonstrating the robust nature of the plasma heat source. The feeding period dominated the lapsed time of the trial. The melt was fluid and cast well from the furnace, giving 6 physically intact and complete tiles. Here the production economics will give a pessimistic opinion of the process as a larger amount of material was actually treated than cast into tiles. The thermal losses to water-cooled components, are summarised in Figure 61, the crucible again dominated the process with a 162 kW loss. The losses are higher than in any other previous trial and can be attributed to the higher power input employed. The power balance is presented in Figure 63, and the total accumulative energy consumption was 510 kWh. Steady state conditions were observed towards the end of the conditioning section and were more difficult to acquire than for the other trials.

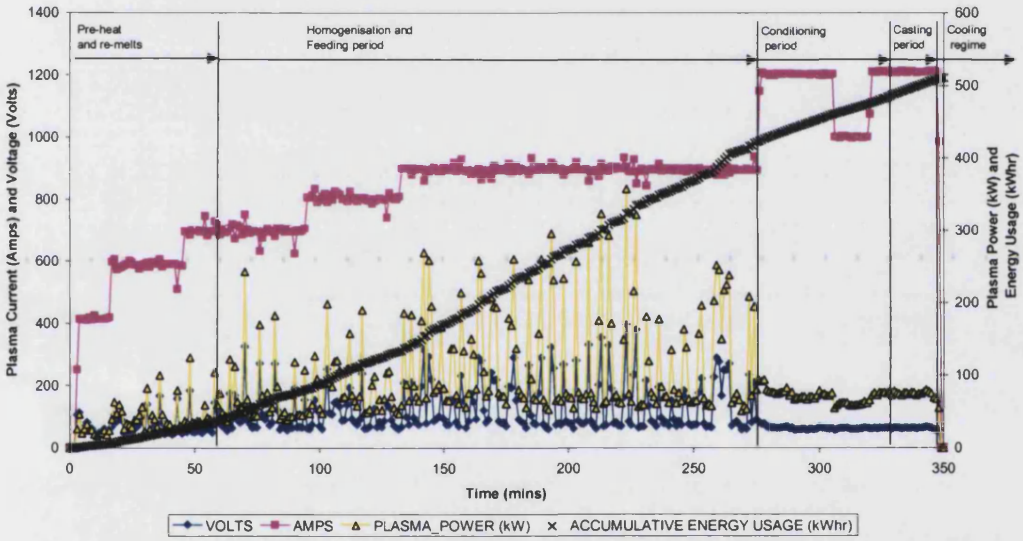

Figure 61: The electrical status and accumulative power consumption of Trial 15

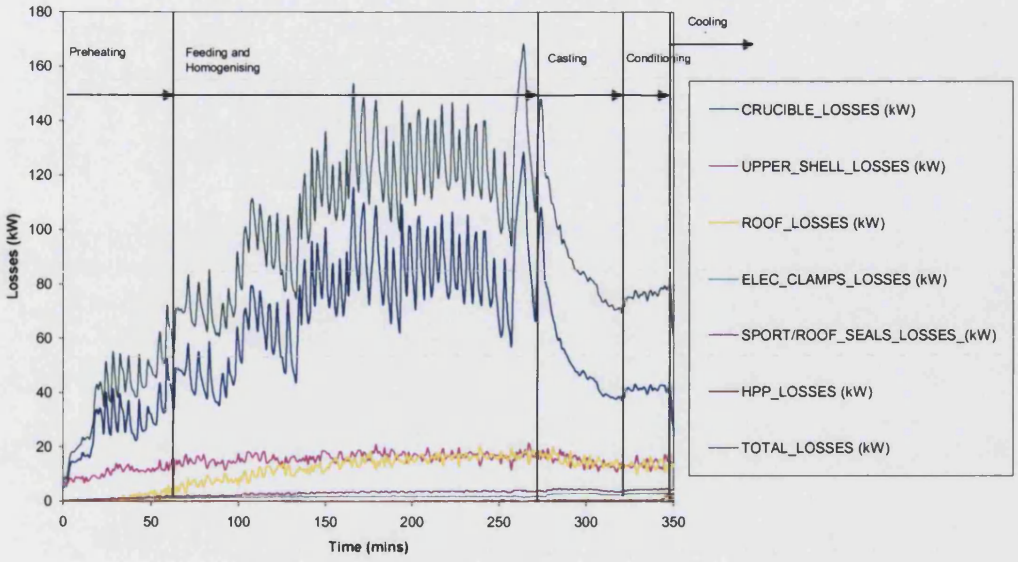

Figure 62: Thermal losses of Trial 15 showing the dominance of the crucible losses

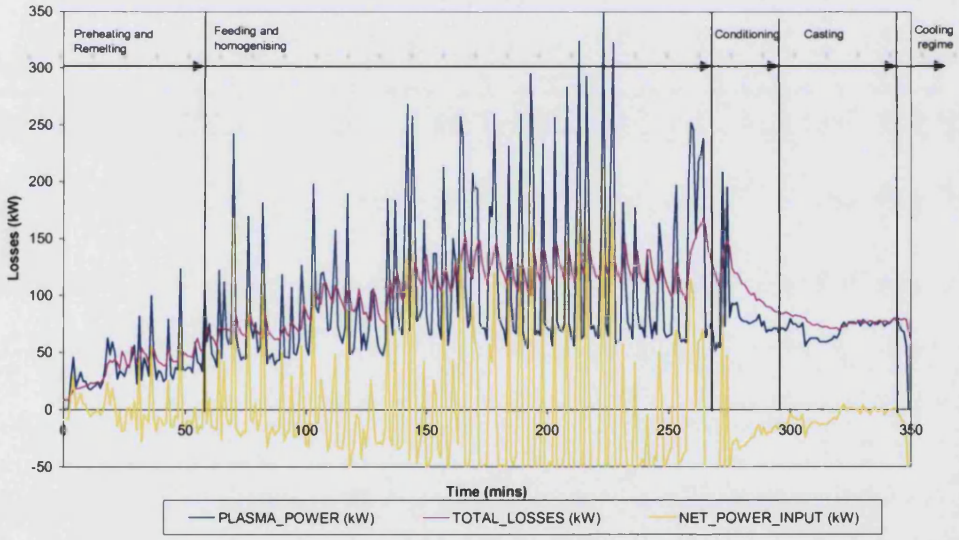

Figure 63: Thermal status of Trial 15 in relation to the balance of gross plasma power input and the total thermal losses of the plasma furnace

7.3.5 Plasma Trial 16 – 95TET

Trial 16 was the secondary heat of the plasma furnace with GHS, it was equivalent to laboratory experiment 95TET, and included the primary 'feed re-melting' period and subsequent feeding period and differed significantly from trial 15. Extended conditioning times were used to assess their influence on the processing economics and melt characteristics and the solidified furnace material was retained in the crucible from the previous trial and re-heated prior to feeding. In general, the melting operation was stable and gave similar characteristics to trial 15. For a feed rate of 15 kg hr^{-1} GHS waste, typical currents were of 910 A with associated voltages were 132 – 230 V, which is consistent with trial 15 when adjustment is made for the different mass feed rates. The voltage peaked at 270 V during the feeding stage of the trial, Figure 64, and was again attributed to the high level of organic and combustible species present within the waste material, Table 41. This voltage is equivalent to that acquired for a feed rate of 22 kg hr^{-1} with C-MSW. The electrical characteristics of the process changed sharply at the conditioning stages of the process, where the voltage was stable at 85 ± 15 V over a period of 1 hour. The current was increased to 1200 A during this period to maintain the power input to the furnace. An extended stable conditioning period was obtained under steady state conditions, Figure 64. The trial lasted a total of 255 minutes, of which conditioning consumed 140 minutes and dominating the lapsed time of the trial. The melt cast well from the furnace, however no visible differences in melt uniformity characteristics were observed. Six physically intact tiles were produced. Here the production economics will give a more optimistic assessment of the process when compared with trial 15, as the material utilisation was high. Thermal losses to water-cooled components, are summarised in Figure 65, the crucible dominated the losses at 130 kW. The power balance is presented in Figure 66, steady state conditions were observed towards the start of the conditioning section and were held for the whole period. The total accumulative energy consumption was 346 kWh, which is significantly lower than for trial 15.

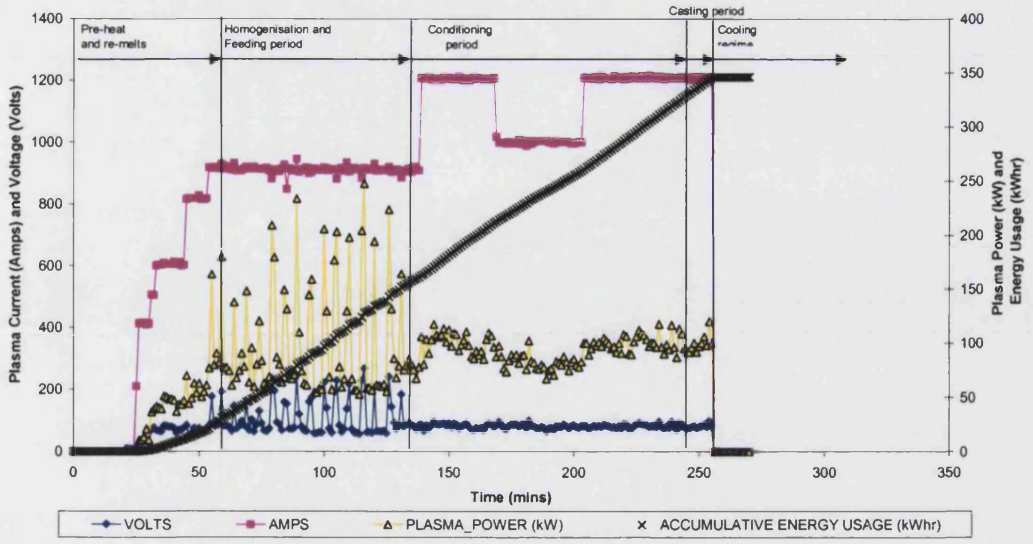

Figure 64: The electrical status and accumulative power consumption of Trial 16

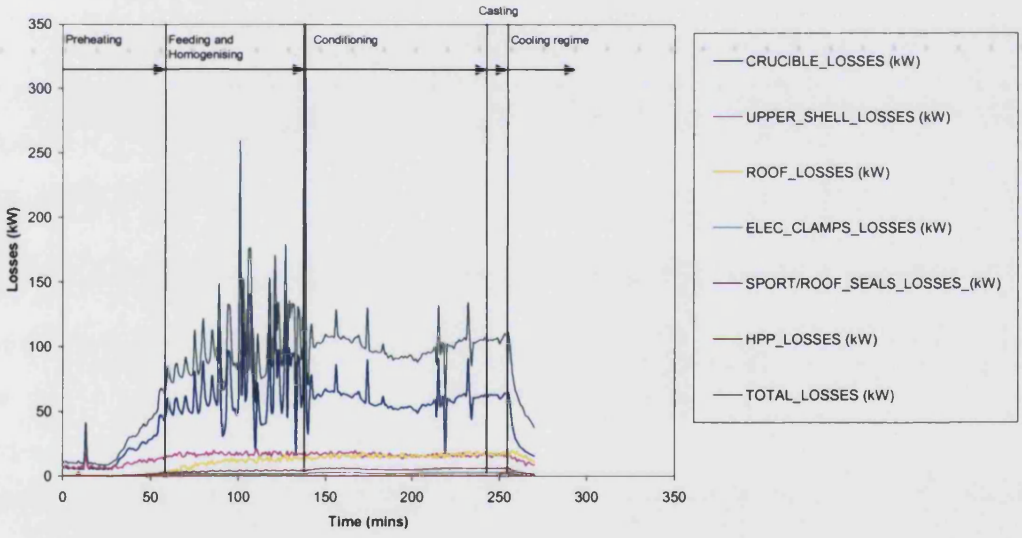

Figure 65: Thermal losses of Trial 16 showing the dominance of the crucible losses

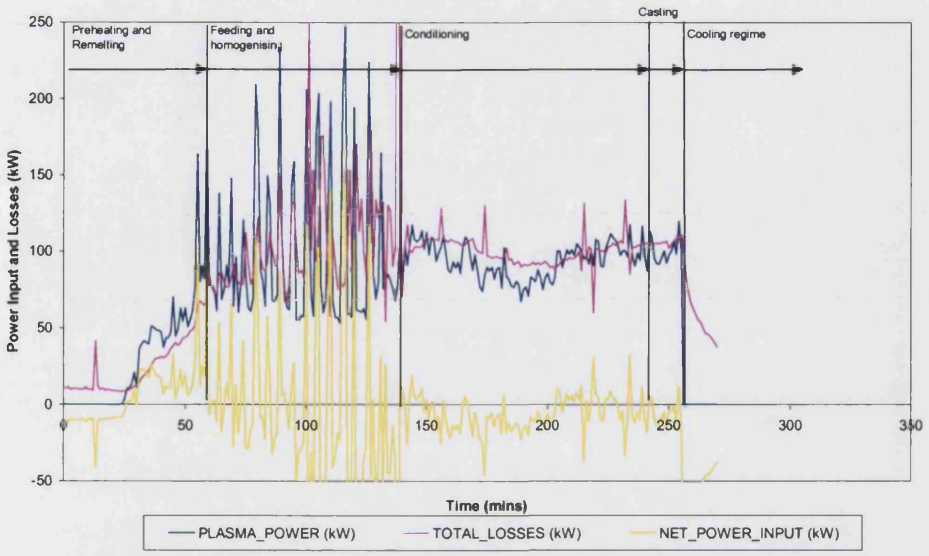

Figure 66: Thermal status of Trial 16 in relation to the balance of gross plasma power input and the total thermal losses of the plasma furnace

7.4 Tile Product Description and Production Costs

All tile products displayed limited macroscopic heterogeneity. Observed heterogeneities included off composition glass regions, surface / bulk porosity and metallic inclusions which originated form the waste. All of the trials discussed above produced glassy tile products with mechanical integrity. The last tile cast from each experiment, was generally of the poorest quality. This observation was taken to indicate that the plasma heat source, in the twin electrode configuration, had the most thermal influence at the upper melt region. This is consistent with the operative radiant heat transfer mechanism in the glassy body and the limited thermal conductivity of the melt. The plasma furnace has been shown to yield relatively uniform melt products in spite of the heterogeneous nature of the feed materials employed. A photograph of the typical material product of the furnace is shown in Figure 67. The two pairs of trials, 13 – 14 and 15 –16 demonstrated that the different waste materials exhibited different but reproducible processing characteristics. This enabled the plasma furnace's operation to be tailored to the waste material's requirements

so that the same overall objectives were achieved, e.g. melt temperature and specific power input.

Sectioned Tile (45x40x15 mm)	As-cast tile (130x130x15 mm)
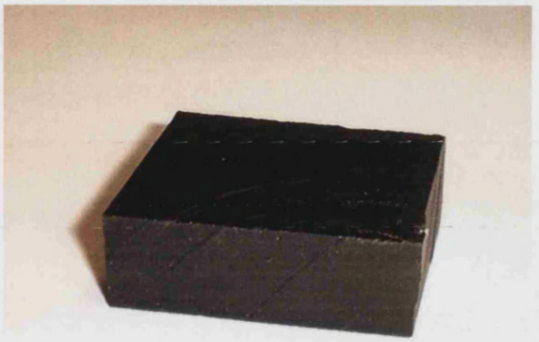	

Figure 67: Photographs of a sectioned and raw plasma furnace tile product

During casting, the fluid melt stream had a temperature of 1600 ± 50 °C, as determined using infrared pyrometry assuming an emissivity value of 0.7, [62]. The off-gas temperature at the immediate exit of the reactor was 970 °C, which was reduced to 80 °C by dilution with air in the off-gas duct prior to further filtering treatment. The tile products had an apparent density of 2700 – 3000 kg m^{-3}, measured in accordance with BS1902 using Archimedes' principle, giving a threefold reduction in volume compared with the blended waste materials. The product had a dense black vitrified appearance and was translucent in the thinner sections. Neither optical microscopy nor X-ray diffraction resolved any micro-structural features, Figure 68. Changes in material composition can be attributed to the evaporation of volatile components and the reduction of metal oxides within the melt. These variations are quantitatively defined in Table 61 using XRF for bulk oxide analysis and ICP for trace element analysis. In all cases the carbon content of the original feed material was significantly reduced, indicating the effectiveness of thermal treatment and mixing within the furnace inner chamber. There was a simultaneous decrease in the LOI. This indicates that there was a limited carbon contamination from the graphite electrodes.

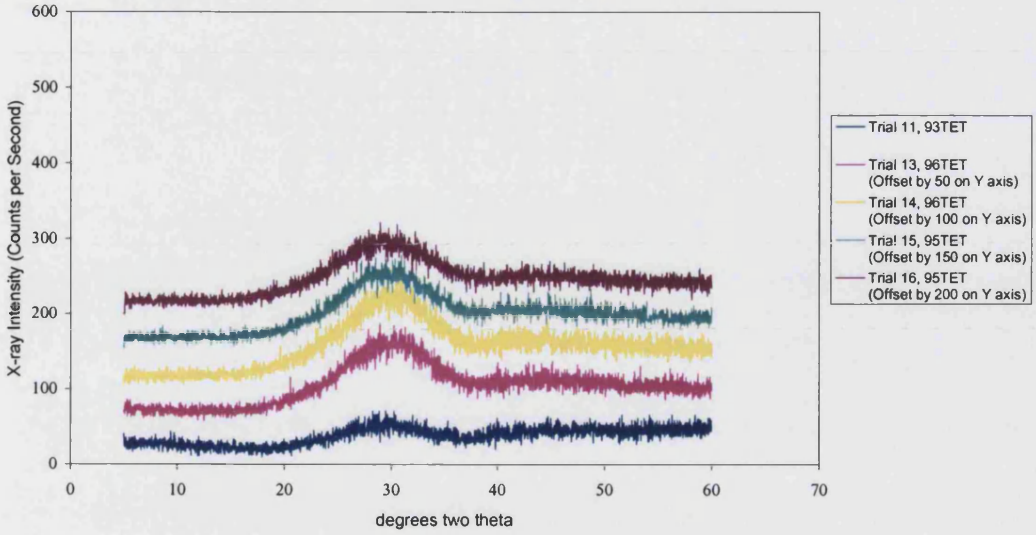

Figure 68: X-ray diffractograms of the glassy plasma furnace tile products

The 93TET trials, using BCC waste, gave good consistency between the blend and tile compositions. When the loss of volatile matter is taken into account the true, i.e. not normalized, calculated oxide fractions should be 29 wt% Al_2O_3, 20 wt% CaO and 45 wt% SiO_2. High lead retention also indicates that the inert environment was beneficial in promoting heavy metal encapsulation. The 95TET trials, using GHS waste, also gave good consistency between the blend and tile composition, except for SiO_2, which was higher than expected. The calculated true oxide fractions were 27 wt% Al_2O_3, 32 wt% CaO and 30 wt% SiO_2. The compositional data indicated a high degree of inter-trial consistency, particularly for the main bulk oxide species, and a very high level of heavy metal retention, e.g. Cr, Co and Pb. The 96TET trials, employing C-MSW waste, showed compositional consistency between the blends and tiles, except for SiO_2, which again was higher than expected. The calculated true oxide fractions were 26 wt% Al_2O_3, 23 wt% CaO and 29 wt% SiO_2. The products from the different trials are consistent and show a good retention of heavy metals, such as lead and chromium. Lead retention appeared to be limited to a threshold value of 40 – 50 ppm. For all plasma trials good retention of Ti as TiO_2 was seen, which is consistent with the ability of TiO_2 to form binary oxide minerals that are soluble within silicate matrices, [8, 37, 45].

Species	93TET DATA, BCC BASED			95TET DATA, GHS BASED				96TET DATA, C-MSW BASED			
	Raw Waste Analysis	Calculated blend composition	Tile Analysis Trial 11	Raw Waste Analysis	Calculated blend composition	Tile Analysis Trial 15	Tile Analysis Trial 16	Raw Waste Analysis	Calculated blend composition	Tile Analysis Trial 13	Tile Analysis Trial 14
XRF											
Na_2O	0.02	0.02	0.19	1.40	0.77	0.85	0.94	2.00	1.48	2.98	3.01
MgO	0.42	0.34	0.25	2.30	1.27	1.59	1.66	2.60	1.93	1.85	1.70
Al_2O_3	33.20	26.63	22.29	10.50	23.78	26.19	25.11	11.90	23.54	18.63	19.78
SiO_2	51.60	41.38	42.71	47.50	26.21	36.84	39.09	35.80	26.55	41.11	39.83
P_2O_5	-	-	<0.05	0.32	0.18	0.15	0.12	1.90	1.41	0.55	0.68
SO_3	-	-	<0.05	1.20	0.66	0.19	0.15	5.20	3.86	0.19	0.17
K_2O	3.97	3.18	2.06	2.30	1.27	0.77	0.86	2.40	1.78	0.82	0.85
CaO	0.05	18.85	28.75	3.40	27.76	28.94	27.01	14.40	20.95	24.13	24.02
TiO_2	0.08	1.05	0.68	0.56	1.30	1.68	1.62	1.60	2.18	2.25	2.01
V_2O_5	-	-	<0.05	0.02	0.01	<0.05	<0.05	0.00	0.00	<0.05	<0.05
Cr_2O_3	-	-	<0.05	0.02	0.01	<0.05	<0.05	0.07	0.05	0.07	0.08
Mn_3O_4	-	-	<0.05	0.16	0.09	0.10	0.11	0.23	0.17	0.13	0.13
Fe_2O_3	1.76	1.41	0.79	5.10	2.81	2.96	2.80	8.10	6.01	8.33	8.67
ZnO	-	-	<0.05	0.03	0.02	<0.05	<0.05	0.80	0.59	<0.05	<0.05
SrO	-	-	<0.05	0.02	0.01	0.06	0.05	0.03	0.02	0.06	0.05
Y_2O_3	-	-	<0.05	-	-	<0.05	<0.05	-	-	<0.05	<0.05
ZrO_2	-	-	0.07	0.04	0.02	<0.05	<0.05	0.04	0.03	<0.05	<0.05
BaO	-	-	<0.05	0.02	0.01	<0.05	<0.05	0.21	0.16	0.15	0.20
HfO_2	-	-	<0.05	-	-	<0.05	<0.05	-	-	<0.05	<0.05
ICP											
As	-	-	100 / 88	49.32	27.47	< 50 / < 50	< 50	48.52	36.29	< 50	< 50
Cd	-	-	< 25 / < 25	9.33	5.20	< 25 / < 25	< 25	14.56	10.89	< 25	< 25
Co	-	-	0.06% / 0.06%	-	-	80 / 78	69.00	-	-	68.00	73.00
Cr	-	-	< 25 / < 25	69.57	38.75	35 / 53	51.00	233.53	174.68	336.00	265.00
Cu	-	-	29 / 33	42.31	23.57	60 / 59	42.00	2732.33	2043.79	312.00	472.00
Mn	-	-	135 / 147	1175.00	654.48	0.07%	0.07%	1695.33	1268.11	0.11%	0.11%
Ni	-	-	< 25 / < 25	-	-	< 25 / < 25	< 25	-	-	< 25	< 25
Pb	-	-	32 / 37	45.85	25.54	47 / < 25	31.00	2095.00	1567.06	43.00	43.00
S	-	-	< 50 / < 50	-	-	0.12% / 0.11%	0.00	-	-	0.10%	0.11%
Sb	-	-	< 50 / < 50	-	-	< 50 / < 50	< 50	-	-	< 50	< 50
Sn	-	-	< 50 / < 50	-	-	< 50 / < 50	< 50	-	-	< 50	< 50
Ti	-	-	0.42% / 0.42%	2095.49	1167.19	1.06% / 1.04%	1.04%	5313.67	3974.62	1.44%	1.31%
Zn	-	-	< 25 / < 25	286.13	149.35	< 25 / < 25	< 25	4568.00	3416.86	155.00	344.00
C	-	-	0.30% / 0.31%	2.62	1.46	< 0.02	< 0.02	1.26	0.93	< 0.02	< 0.02
LOI @ 1025°C	8.90	7.14	0.29%	14.41	7.95	< 0.02	< 0.02	6.06	4.49	< 0.02	< 0.02

Oxides by XRF, % w/w, ICP analysis, ppm w/w, except where stated, on microwave-digestion and Carbon by Coulomat, % w/w on the as received material.

Table 61: Plasma furnace input and output material compositional data

The plasma power input and system losses for the five trials were monitored continuously and displayed in a 'real time' format to aid process control. A graphical representation of this information is presented in Section 7.3. Here it can be observed that after feeding, and during the conditioning stage of the trials, the furnace always achieved steady state conditions evidenced by the total energy accountability. Earlier in the experiment a negative net power input can be observed, i.e. the system losses exceeded the net power input. This can be attributed to exothermic reactions, but it was most probably due the time lag in the response of the system sensors. This is validated as the net power input troughs occurred after the peaks in the plasma power input as graphically presented in all of the thermal status graphs; Figure 54, Figure 57, Figure 60, Figure 63 and Figure 66. The attainment of steady state conditions during processing means that reliable economic predictions can be made on the basis of the test data, as the influence and uncertainties of transient conditions were minimised. The total losses of the system have been examined in detail and the proportion of energy transferred to each component has been assessed to account for the overall losses of the system.

The power input to the furnace can be apportioned to the different water-cooled structural components in accordance with Table 62. Here it was observed that the plasma reactor losses were dominated by the thermal losses to the copper crucible and accounted for 65-68 % of the heat loss. A number of different points in different trials were used to compile this data.

System Component	Losses (% of total)
Copper crucible	65 – 69
Upper shell	10 – 15
Roof	12 – 14
Electrode clamps	1.5 - 2.0
Electrode seals and sight port	3.0 – 4.0
Hydraulic Power Pack	0.1 – 0.2
Total Losses (kW)	80 – 120

Table 62: Furnace steady state power distribution profile

The electrical power required to melt the material was influenced by variables such as feed rate, plasma spatial configuration, reactor thermal design and thermo-chemical reaction. During the feeding periods the operating power ranged from 50 to 250 kW. The accumulative energy input for the process was assessed continuously and apportioned to the different stages of the process, as presented in Section 7.3.

The process had the following stages: pre-heat/re-melting, feeding, conditioning and casting. The slope of the energy usage curve changed for different stages of the experiment. The process as a whole had an average specific gross energy requirement (GER) of ~6,000 kWh tonne^{-1}, which is in accordance with the inefficient character of the reactor. For estimation on a continuous operational basis, i.e. removing preheating requirements and assuming continuous feeding (50% of the utilised feeding interval), the average specific energy requirement was reduced to ~3,900 kWh tonne^{-1}. Again this is an energy requirement, that takes into account non-steady state conditions, the intense water-cooling of the prototype plasma unit and the high surface area to volume ratio of the small plasma furnace. In vitrification processes the GER is lowered further because the requirement for the conditioning period is eliminated. These values are obtained using an assessment of the energy required to preheat and 50% of the energy required during the feeding stage. The energy consumption associated with each stage of the reported trials is summarised in Table 63, in each trial the feed stage accounts for the largest fraction of the energy consumption of the process.

	Trial 11 93TET, BCC		**Trial 13 96TET, C-MSW**		**Trial 14 96TET, C-MSW**		**Trial 15 95TET, GHS**		**Trial 16 95TET, GHS**	
Process Stage	Energy (kWh)	Energy (%)	Energy (kWh)	Energy (%)	Energy (kWh)	Energy (%)	Energy (kWh)	Energy (%)	Energy (kWh)	Energy (%)
Preheat / Remelting	36	13.5	48	14.7	57	26.1	26	5.1	21	8.0
Feeding	145	54.3	162	49.5	90	41.3	392	76.7	139	53.1
Conditioning	77	28.8	88	26.9	65	29.8	76	14.9	88	33.6
Casting	9	3.4	29	8.9	6	2.8	17	3.3	14	5.3
Total	267	100	327	100	218	100	511	100	262	100
Material (kg)	65.6	-	47.8	-	59.3	-	40.0	-	44.2	-
Process Gross Energy Requirements (GER)										
Actual Process KWh tonne^{-1}	4071	100	6841	100	3675	100	12,765	100	5930	100
Continuous Operation KWh tonne^{-1}*	2417	59.4	4142	60.5	1956	53.2	7220	56.6	3882	65.5
Continuous Vitrification KWh tonne^{-1}*	1016	25.0	1695	24.8	759	20.7	4896	38.4	1573	26.5

*Calculated based on the text defined assumptions

Table 63: Process energy consumption data

The pilot scale plasma system was designed to hold a residual amount of material to avoid localised overheating of the crucible. Each trial processed more waste than was utilised, so enough material was treated in order to generate a larger number of tiles than were actually produced. Under continuous operational conditions the material would be utilised, so it

has been included in this economic assessment. The energy usage of the current system and scale of operation for the melting, conditioning and casting of tiles is summarised in Table 64. Here it is observed that the trials closest to the true steady state operating condition give similar specific tile energy costs.

Trial N°	Mass Treated (kg)	Average Tile Mass (kg)	Potential number of Tiles produced	Energy Consumed (kWh)	Specific Tile Energy Cost (kWh/Tile)
11 = BCC 93TET*	65.6	0.91	72	267	3.7
13 = C-MSW 96TET	47.8	0.90	53	327	6.2
14 = C-MSW 96TET*	59.3	0.88	67	218	3.3
15 = GHS 95TET	40.0	0.51	78	511	6.6
16 = GHS 95TET*	44.2	0.61	72	262	3.6

*Trials that are closest to true steady-state operation

Table 64: Energy cost per unit tile

The plasma process operational cost assessments are given in Table 65. These are based on dry feed material prepared in accordance with the plasma furnace feed specification, Table 59. All the assumptions associated with the calculation are included. The cost of producing one tile in the prototype plasma furnace is estimated to be £1.82 for BCC (93TET), £1.72 for C – MSW (96TET) and £1.34 for GHS (95TET), which is a very strong function of material density, and the GHS is least dense so more tile is produced per unit weight. The production costs per unit weight gave a different ranking and C-MSW treatment was most favourable and GHS sediment least favourable, because of the high material pre-treatment costs and high gross energy requirements associated with the GHS. Again it must be remembered that the prototype plasma unit had limited energy efficiency due to its intense water-cooling. Hence, large 'economies of scale' are associated with the use of thermally engineered refractory lined furnaces and favourable surface area to volume ratios. No allowances have been made for landfill cost avoidance and possible revenue received through the product material having a beneficial use and saleable value. These factors will further improve the economic case and profitability of the process. In a similar manner it has been assumed that the product is environmentally benign. This issue was evaluated using environmental leaching test data and will be reported in Section 9.

General plasma costings have been extended to take into account both the primary mechanical and secondary thermal drying applied to the GHS. These costings have been incorporated into the plasma treatment costs, as they are considered essential for furnace operation. The other wastes only need limited processing to make them compatible with the feeding equipment. Hence, focus has been placed upon the GHS for scaled operating cost data, as this represents the worst-case situation. The technologies employed include primary membrane filter de-watering and secondary swing drying to take the water content of the sediment to below 2 wt%. Overall the 'break even point' of the process occurred at production scales of 1000's tiles per hour or £100 tonne^{-1} processing costs. This assessment is based on comparisons with current production/treatment costs of other materials, Section 7.

Here the cost per tile is ~20 pence, which is acceptable, as equivalent natural raw materials are a lot more expensive, typically £30 - £50 per square metre. The tiles are currently 130 x 130 x ~10 mm in dimension, so this cost can be converted into a 'per unit area' quantity, £11.8 m^{-2}. Any additional value that can be assigned to the product will shift the 'break even point' to lower tonnage through-puts increasing the potential scope of market applicability. To conclude the document presents four, balanced and focusing facts:

(i). The cost of the material product is significantly lower than existing commercial materials and wastes are removed from traditional disposal routes.

(ii). A reliable prototype plasma system has been engineered, and could be the foundation for further experimentation and commercial utilisation.

(iii). The equipment and process is capable of handling a wide range of waste materials in a similar manner and the technology is robust and generic.

(iv). The material processing costs can offer economic advantage over current waste disposal routes if implemented on a large enough scale.

Enhanced material properties and consistency, in combination with ecological compatibility will increase potential product value and improve the likelihood of technological adoption. The size of the viable plasma furnace will be defined by the 100 tonnes per day break-even point. This implies that there are economic arguments for localised process installation and larger centralised facilities based on demographic criteria.

Plant Details	BCC Current Trial 11	C-MSW Current Trial 14	GHS Current Trial 16	Commercial Plants Predictions for GHS		
Plant Capacity (tpd)	0.6	0.6	0.6	10.0	100.0	240.0
Annual Plant Capacity (tonnes)*	175.2	175.2	175.2	2920.0	29200.0	70080.0
Hourly throughput (kg/hour)	25.0	25.0	25.0	416.7	4166.7	10000.0
Allowed Average Power Density (kW/m^2)**	450.0	450.0	450.0	256.0	256.0	256.0
Required Furnace Hearth Area (m^2)	0.13	0.11	0.22	1.95	15.02	29.30
Furnace Diameter (m) Assuming hemispherical shape, $A = 2*Pi()*r^2$	0.3	0.3	0.4	1.1	3.1	4.3
Plant Power (MW)	0.06	0.05	0.10	0.50	3.85	7.50
Theoretical Energy Requirement (kWh/tonne)	600.0	600.0	600.0	600.0	600.0	600.0
Gross Energy Requirement (kWh/tonnne)***	2417	1956	3882.0	1200.0	923.1	750.0
Feed Costs £/hr						
Raw Waste Material	£0.0	£0.0	£3.5	£25.2	£126.3	£233.0
Blending Additions CaO and Al2O3 (kg)	4.8	6.3	11.1	184.6	1845.8	4430.0
CaO hourly addition (kg)	4.8	2.6	6.5	108.9	1089.0	2613.7
Al2O3 hourly addition (kg)	0.0	3.7	4.5	75.7	756.8	1816.3
Blending Addition Cost (£)****	£0.2	£0.5	£0.8	£13.0	£130.1	£312.3
Utilities Costs £/hr						
Electricity @ £0.03/kWh	£1.8	£1.5	£2.9	£15.0	£115.4	£225.0
Water	£0.0	£0.0	£0.0	£0.0	£0.0	£0.0
Argon gas (6000 Gas litre/hour for commercial plant) @ £0.65/Nm3*****	£7.8	£7.8	£7.8	£3.9	£3.9	£3.9
Graphite electrode Consumption (0.01 kg Graphite/ kg blended Waste)******	£4.0	£3.1	£3.5	£1.6	£15.7	£37.8
Direct labour (2 man labour @ all times for commercial plants) @ £20/hr	£20.0	£20.0	£20.0	£40.0	£40.0	£40.0
Plant Maintance and Labour Costs (£/hr)						
Labour (1 mans labour @ all times for commercial plants) @ £20/hr	£5.00	£5.00	£5.00	£20.00	£20.00	£20.00
Materials	£1.60	£1.60	£1.60	£3.90	£11.02	£19.38
Depreciation (10 yr life)	£3.50	£3.50	£3.50	£12.25	£36.70	£61.27
Other Cost	£1.00	£1.00	£1.00	-	-	-
Number Of Tiles Produced Per Hour	24.73	25.57	36.89	528.90	5,288.99	12,693.58
Operating Cost (£/hr)						
Total hourly Operating Costs (£)	£44.98	£44.00	£49.59	£134.88	£499.20	£952.64
Cost Per Tile (£)	£1.82	£1.72	£1.34	£0.255	£0.094	£0.075
Waste Treatment Cost (£)						
Blended Waste Treatment Cost (If applicable) (£/tonne)	1799.25	1759.80	1983.61	323.72	119.81	95.26

*80% overall annual availability assumed
**Based on commercial refractory wear knowledge and 80% heat transfer efficiency through the hearth
***Efficiency factors of 0.5, 0.65 and 0.80 assumed, respectiviely for commercial plants in Japan
GHS Mechanical dewatering costs £/tonne = $1198.4(t/yr)^{-0.3007}$ (membrane filtration followed by swing drying) to 2 wt% water
****Blending additons assumed to be at £0.1/kg Al2O3 and £0.05/kg CaO with bulk bag delivery
*****The Plasma Reactor uses 12000 Gas litre/hour, as it is very open
****** VN machined graphite £27.8/kg, Commercial graphite consumption is 10% of the plasma reactors @£3500/tonne.
The Tetrotile reactor will cost £700 to reline every six months. Other cost are 3% capex over 10 years on hourly basis
The plasma Plant is assumed to cost £300K on the smaller scale, which includes all ancillaries
90% Material utilisation assumed

Table 65: General economic assessment (hourly operating costing determined on a 24 hour operational basis, with 80% annual availability)

8 Experimental Investigation of the Crystallisation Process

The requirement of the crystallisation process is to facilitate the production of a polycrystalline ceramic material with improved mechanical properties, relative to those of the parent glass. This requires the attainment of a fine-grained microstructure and control of the volume fraction and composition of the retained glassy phase. This means that a quantitative assessment of the process must ensure that:

(i). Nucleation occurs uniformly throughout the material and that the nuclei display similar crystallographic characteristic to the required crystalline phase.

(ii). The required addition of nucleating agent is made for the development of heterogeneous nucleation sites.

(iii). The temperature and time required to produce a high nucleation rate upon reheating are defined.

(iv). Controlled intermediate crystal growth rates and efficient utilisation of the nuclei are achieved without the activation of coarsening mechanisms.

(v). The overall process does not cause excessive structural and dimensional changes to the material product and cracking is avoided from density mismatch or thermal stresses.

(vi). The overall process is economic in terms of time at temperature.

During the plasma melting of the waste materials, TiO_2 was added purposely as a nucleating agent. The material has been reported to be effective in combination with Li_2O, MgO and other divalent metal oxides where it precipitates at low temperatures as a titanate phase either conventionally or through a glass-in-glass phase separation. This mechanistic description validates its use in the content of the waste streams under consideration, [8, 20, 37, 45]. The multiple functionality TiO_2 has been attributed to its ability to obtain different coordination numbers in a silicate structure [65].

8.1 Experimental Methodology

The investigative approach taken for crystallisation was 'indirect' because the formation of nuclei was not observed directly. Crystal growth was required to allow the feature to be observed using SEM after standard metallographic preparation. This was considered to be the most desirable approach: firstly, it removed the requirement for the use of a TEM and intricate sample preparation and secondly, it allowed direct measurement of the number of

nuclei that were successful in growing to form a crystal, [20, 24, 36]. The specimens were all produced from the plasma furnace products and supported on refractory edges so that the level of dimensional deformation could be evaluated, and the heating rates (°C min^{-1}) regulated, to avoid its occurrence. The thermal stability of the material was predicted to change during the thermal cycle because of the crystalline identity, volume fraction and refractoriness of the phase precipitated. To determine the optimum thermal treatment schedule, specimens were heat-treated in a systematic manner. Here specimens were held for fixed periods at specific temperatures, within the nucleation range to utilise the nucleation process, then ramped to a crystallisation temperature, to grow the nuclei, and removed from the furnace after a two hour period. The specimens were then 'quenched' to arrest the crystal growth process, by immediate removal, at temperature from the furnace into the laboratory. Electron microscopy and XRD were used to assess the number of growth centres, the identity of the crystalline phases and the crystallite dimensions. After the optimum nucleation temperature (ONT) was determined the nucleation time (ONt) and crystal growth parameters were subjected to the same type of systematic evaluation. Similarly the optimum crystallisation temperature was abbreviated to (OCT) and time (OCt). The primary function of the nucleation time study was to obviate the occurrence of diffusion controlled coarsening processes. The crystallisation study was aimed at defining the highest and most economic processing temperature without deformation of the material, as judged from the relative temperature positions of the crystallisation exotherms and the melting endotherms.

From the laboratory study, specimen 96TET-2 was identified as the most desirable to work with because of the product's attractive appearance, dimensional stability and improved material properties. This included increased density, fracture toughness and elastic modulus, all of which were consistent with its fine microstructure. This material is based on the C-MSW waste ash and requires an intermediate material blending addition, totalling 25 wt% virgin material, including Al_2O_3 and CaO. It also processed desirably during plasma furnace operation, forming a fluid melt and low levels of volatile species. The heat treatment schedule employed in the laboratory was based around the location of the first exothermic peak, as observed using DSC, Section 5.2.2. Dilatometric analysis indicated that a large window of glass stability, of 125 °C, was available between the glass transition temperature and the first crystallisation exotherm, Figure 14D. The nucleation temperature

employed in the laboratory trials was approximately 50 °C above T_g and just slightly below the T_{DSP}, which is considered to have been within the optimum nucleation temperature range [20, 51, 52]. The specific experimental parameters used in this investigation are given in Figure 69.

Part 1: Nucleation temperature study, defining the optimum nucleation temperature (ONT)

Specimen ID	Nucleation Temp (°C)	Nucleation Time (hrs)	Temperature ramp (°C hr^{-1})	Crystallisation Temp (°C)	Crystallisation Time (hrs)
96TET-2-N1	550	0.5	360	950	2.0
96TET-2-N2	575	0.5	360	950	2.0
96TET-2-N3	600	0.5	360	950	2.0
96TET-2-N4	625	0.5	360	950	2.0
96TET-2-N5	650	0.5	360	950	2.0
96TET-2-N6	675	0.5	360	950	2.0
96TET-2-N7	700	0.5	360	950	2.0
96TET-2-N8	725	0.5	360	950	2.0

Part 2: Nucleation time study, defining the optimum nucleation time (ONt)

Specimen ID	Nucleation Temp (°C)	Nucleation Time (hrs)	Temperature ramp (°C hr^{-1})	Crystallisation Temp (°C)	Crystallisation Time (hrs)
96TET-2-NT1	ONT	0.1	360	950	2.0
96TET-2-NT2	ONT	0.2	360	950	2.0
96TET-2-NT3	ONT	0.3	360	950	2.0
96TET-2-NT4	ONT	0.4	360	950	2.0
96TET-2-NT5	ONT	0.5	360	950	2.0
96TET-2-NT6	ONT	0.6	360	950	2.0

Part 3: Crystallisation temperature study, defining optimum crystallisation temp (OCT)

Specimen ID	Nucleation Temp (°C)	Nucleation Time (hrs)	Temperature ramp (°C hr^{-1})	Crystallisation Temp (°C)	Crystallisation Time (hrs)
96TET-2-C1	ONT	ONt	360	900	2.0
96TET-2-C2	ONT	ONt	360	910	2.0
96TET-2-C3	ONT	ONt	360	920	2.0
96TET-2-C4	ONT	ONt	360	930	2.0
96TET-2-C5	ONT	ONt	360	940	2.0
96TET-2-C6	ONT	ONt	360	950	2.0

Part 4: Crystallisation time study, defining the optimum crystallisation time (ONt)

Specimen ID	Nucleation Temp (°C)	Nucleation Time (hrs)	Temperature ramp (°C hr^{-1})	Crystallisation Temp (°C)	Crystallisation Time (hrs)
96TET-2-CT1	ONT	ONt	360	OCT	0.5
96TET-2-CT2	ONT	ONt	360	OCT	1.0
96TET-2-CT3	ONT	ONt	360	OCT	1.5
96TET-2-CT4	ONT	ONt	360	OCT	2.0

Figure 69: Crystallisation heat treatment experimental schedule details

8.2 Experimental Results

All of the specimens were prepared and heat-treated in a SiC element muffle furnace, capable of 1600 °C with a proportion integral differential (PID) controller acting on the signal of a B type thermocouple input. Each specimen was analysed in an identical manner. Firstly, SEM was used in backscattered detection mode to give atomic/phase contrast at magnification levels of x 1,000, x 2,000 and x 4,000. This allowed the morphology and size of the crystallites to be determined as well as the number of growth centres pure unit volume. This was complemented with an EDX facility for qualitative spot analysis of atomic composition. A lineal intercept technique was employed that is applicable for two-phase polycrystalline ceramics, [66]. The equation governing this technique is:

$$D_{grain} = 1.56\frac{C}{MN''}$$

Equation 44

Where:

D_{grain} = average grain size (m)

C = length of the test line (m)

M = magnification of the electron micrograph

N'' = number of intercepts

1.56 = proportionality constant for tetrakaidecahedrally shaped grains with a log - normal size distribution.

To correct for the two-phase characteristics of the microstructure, where the secondary phase is of a non-continuous nature, a correction to the 'C' term is made and the different

types of phase intercept distinguished. The assumption, that the proportion of the line on the secondary phase, equals the volume fraction of the second phase, corrects the test line length to C_{eff}, given by:

$$C_{eff} = C(1-v) = C(1-l)$$

Equation 45

where: v = volume fraction of the phase under analysis

l = lineal-intercept fraction of the phase under analysis

For confirmation of the approach, the same result can be acquired from the measurement of densities and a rule of mixtures calculation. However, Equation 44 must be further modified to allow for the two types of test line intercepts, [66]. The effective number of test line intercepts associated with grain boundaries of the phase under consideration is given in Equation 46:

$$N_{eff} = N_{aa} + 0.5N_{ab}$$

Equation 46:

where: N_{eff} = the effective number of intercepts

N_{aa} = intercept boundaries of continuous grains of the primary phase

N_{ab} = intercept boundaries between primary and secondary phases

This means that the modified version of the lineal intercepts equation becomes:

$$D_{eff\,grain} = 1.56\frac{C_{eff}}{MN_{eff}}$$

Equation 47

To extend the data obtained from the analysis the number of growth centres per unit volume of material was calculated using Equation 48:

$$N_r = \frac{(N_{eff})^3}{(C)^3}$$

Equation 48

To complement this approach the samples were also analysed using XRD, here the characteristic spectral features were used to assign an identity to the crystalline phase(s) present. The intensity of the signal is directly proportional to the volume fraction of the

phase(s) present, and therefore should vary in accordance with the lineal intercept analysis of the SEM micrographs.

8.2.1 Results of the Nucleation Temperature Study (ONT)

Material samples were prepared and analysed in accordance with the laboratory work and the description in Section 8.2. SEM analysis indicated the presence of three phases including the matrix phase. The crystalline phases appearance and spatial distribution indicated that the first phase to precipitate produced composition segregation and changed the composition of the retained matrix as justified by the EDX analysis of composition. Therefore the identity of the thermodynamically favoured phase to be precipitated from the matrix changed, as seen in the literature [14, 33, 36, 44]. Backscattered electron micrographs for sample 96TET2-N5, the sample treated at the optimum nucleation temperature (ONT) of 650 °C for 0.5 hours, are presented in Figure 70. The ONT is defined as the temperature that produced the highest density of small nuclei that were successful in promoting crystal growth.

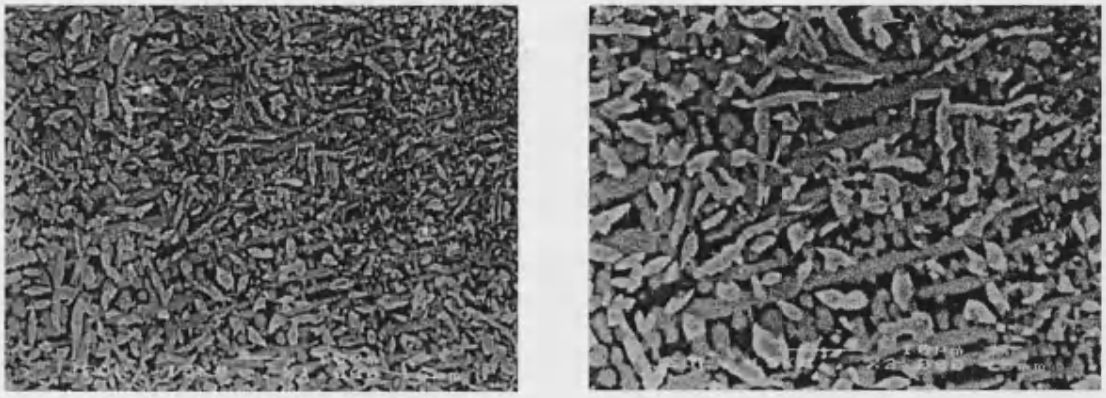

Figure 70: Backscattered electron micrograph of samples 96TET-2-N5, on the LHS (x 1,000) and on the RHS (x 2,000). Two crystalline phases and the matrix phase are shown

Similarity is noted between these micrographs and those observed in the laboratory phase of the research, confirming experimental consistency from the laboratory to the plasma furnace. The material has been crystallised to a high degree and the crystallites are frequent within the microstructure, the number of growth centres per unit volume of material was 1.6×10^{17} m^{-3}. All of the different nucleation temperatures employed, which ranged from 550 – 715 °C, produced similar microstructures with two contrasting

crystalline phases, Figure 70. The XRD analysis of the samples is summarised in Figure 71, where acceptable intensity levels have been obtained as the characteristic peaks were readily identified relative to the background spectral noise. The lineal intercepts analysis of the microstructure gave a transformed material fraction of 81 vol%.

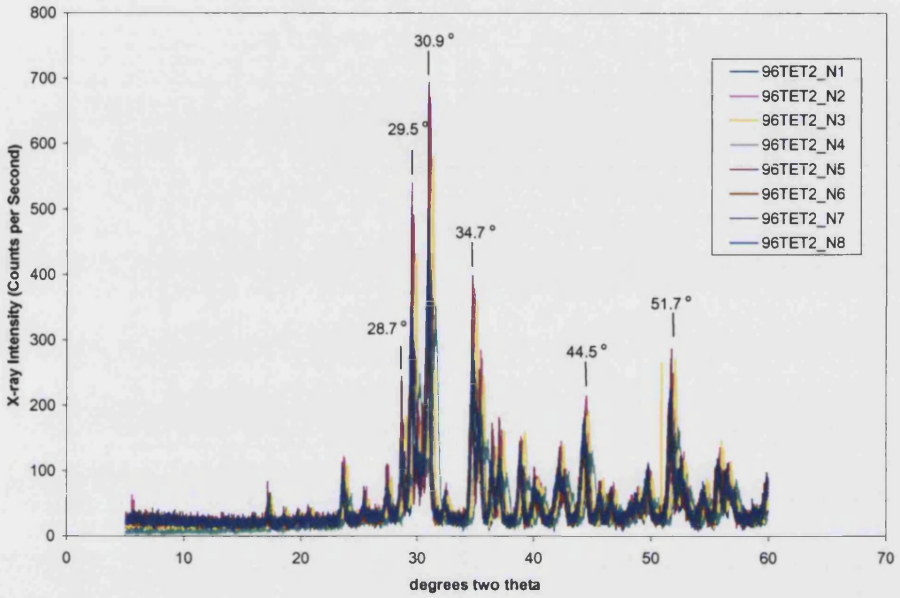

Figure 71: The X-ray diffractograms obtained in the assessment of nucleation temperature

The most intense peaks are those at 2θ values of 30.9° and 29.5°, these peaks are pronounced relative to the other spectral features. Firstly, rankinite $Ca_3Si_2O_7$ shows positional consistency for all of the lines with variable peak intensity correlations, as some intense lines are not present. Diopside $CaMg(SiO_3)_2$ also shows a high level of consistency, however atomic magnesium was not observed in the EDX spectra in the laboratory phase, however it is a light element, and relative intensities may be deceiving. The two most intense peaks are consistent with the diffraction pattern of albite, $(Na, Ca)(Si,Al)_4O_8$. This mineralogical phase shows a complete range of solid solutions with anorthite and is a member of the feldspar group and plagioclase subgroup. It is described as a disordered structure of high temperature origin. The pattern also has some features similar to that of anorthite $(Ca)(Al,Si)_2Si_2O_8$ which is also a closely related member of the feldspar group and plagioclase subgroup, already described in Section 5.2.8. The crystalline morphology can be observed to be consistent with that of albite, [63]. Albite is a rock-forming mineral that occurs with potash feldspars, it is found in both metamorphic

and igneous rocks, e.g. granites. The outcome of the visual and micro-structural analysis of the samples is summarised in Figure 72, which shows the variation of X-ray diffraction peak intensity and nuclei density with nucleation temperature.

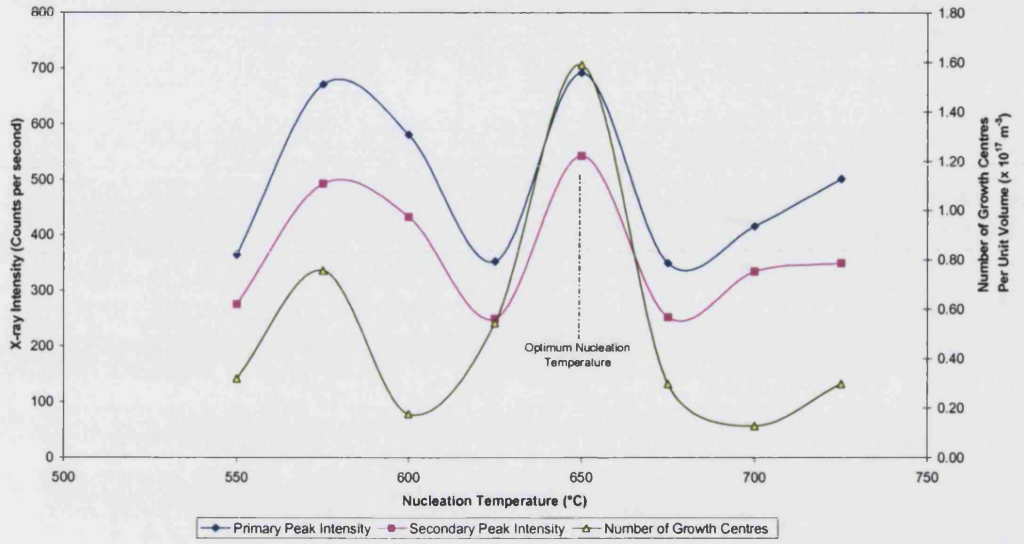

Figure 72: Micro-structural characteristics versus nucleation temperature obtained in the nucleation temperature assessment (for 96TET-2-N1 to N8)

Figure 72 shows good correlation is observed between the micro-structural data (number of growth centres per unit volume) and the XRD intensity data. This indicates that the two most intense peaks in the diffractogram are responsible for the resolved micro-structural features. However, because the lineal intercepts analysis did not differentiate between the contrasting crystalline phases, because of the limited contrast, no relative proportions are shown. However, the phases must be of similar origin as the characterising peaks are identical, i.e. the same peaks intensify and disappear together. This could be attributed to the purification of a phase through the process of exsolution, which is important in natural mineral intergrowth, or the transformation of a high temperature phase modification to a low temperature modification [24]. Thus, we have two active crystal growth mechanisms being promoted from whatever nuclei are present, as displayed by the two maxima in the growth-centre density curve. The conclusion of this stage of the work is that 650 °C is the optimum temperature for the nucleation process, due to the high number of nuclei, the small crystallite size of 4 μm and the high X-ray intensities. The nucleation process is very effective as it produces 1.6 x 10^{17} nuclei m^{-3} that are successful in growing crystals.

In contrast, the backscattered electron micrographs of 96TET2 – N1 and 96TET2 – N8, nucleated at 550 °C and 725 °C respectively, are shown in Figure 73. Here the larger crystallite size of 6.5 μm, and lower number of growth centres per unit volume of 2.5×10^{16} nuclei m^{-3} of the material can be observed in contrast to 95TET2 – N5, Figure 70.

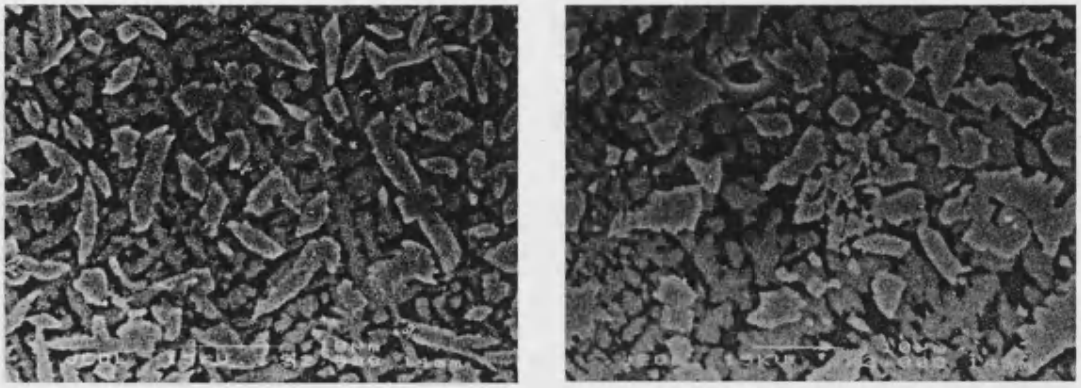

Figure 73: Backscattered electron micrograph of samples 96TET2 – N1, on the LHS, and 96TET2 – N8 on the RHS at (x 2,000)

8.2.2 Results of the Nucleation Time Study

For the nucleation time study, material samples were prepared and analysed in accordance with the laboratory work and the description in Section 8.2. As for the nucleation temperature study, SEM analysis indicated the presence of three phases, including the matrix phase. Backscattered electron micrographs for sample 96TET2-NT3, the sample treated at the optimum nucleation temperature and time, are presented in Figure 74.

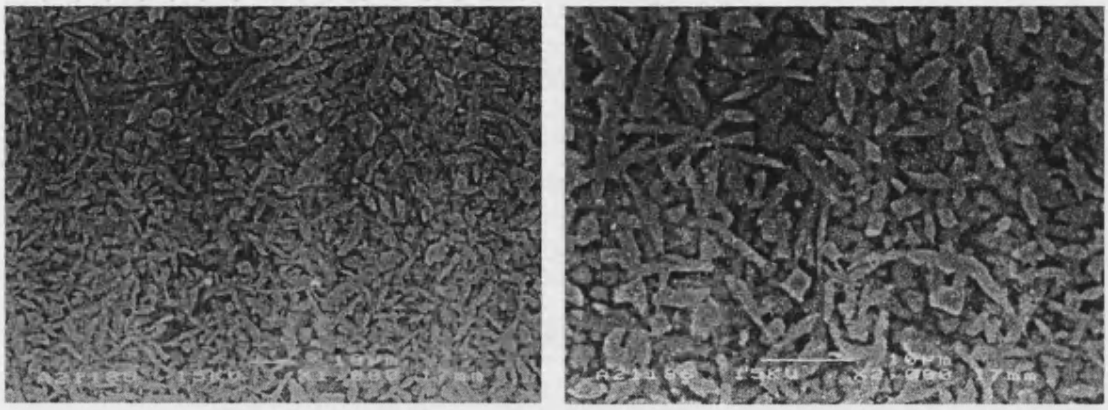

Figure 74: Backscattered electron micrograph of samples 96TET-2-NT3, on the LHS (x 1,000) and on the RHS (x 2,000)

The optimum nucleation time was defined by the low crystallite size and highest number of growth centres per unit volume, and was also associated with the avoidance of coarsening phenomena. Morphological similarities are evident between these micrographs and those acquired during the nucleating temperature research, and the average crystallite size '$D_{eff\ grain}$' has been retained at 4 μm. The material has been crystallised to a high degree, ~ 90 vol%, and the crystallites are frequent within the microstructure. All of the different nucleation times employed produced similar microstructures with two contrasting crystalline phases. EDX analysis indicated that the main qualitative atomic constituents of the crystalline phases were Al, Si and Ca with minor amounts of Mg, Fe and Ti, which are possibly attributed to a titanate phase. The XRD analysis of the samples is summarised in Figure 75.

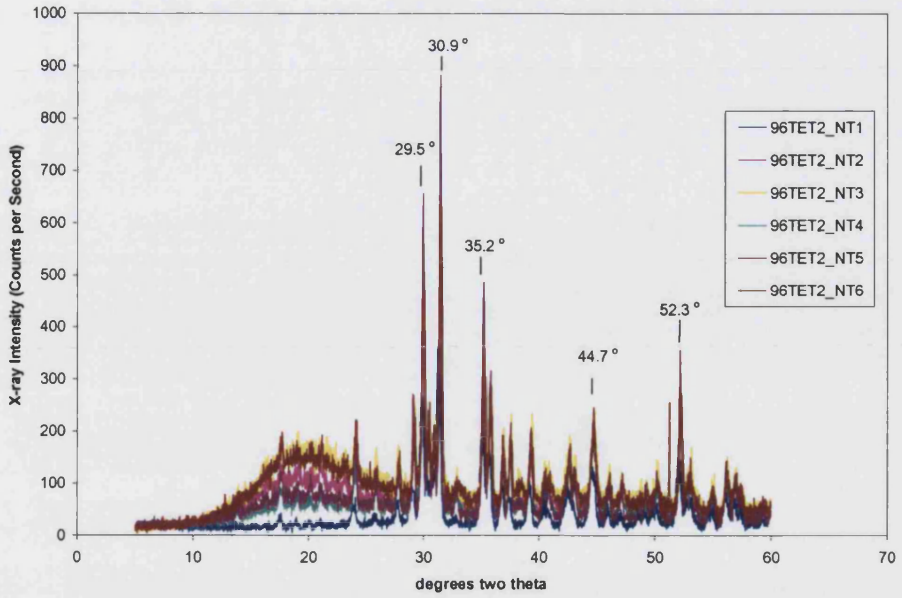

Figure 75: The X-ray diffractograms obtained in the assessment of nucleation time

The most intense peaks are those at 2θ values of 30.9° and 29.5°, these peaks are pronounced relative to the other spectral features and are similar in location to those observed in the nucleation temperature research. Hence the crystallite identity conclusion remains valid as a solid solution of albite with anorthite. The outcome of the visual and micro-structural analysis of the samples is summarised in Figure 76. The optimum nucleation time 0.3 hrs (18 minutes) as indicated by the lowest crystallite size of 3.9 μm and highest number of growth centres per unit volume of 8.0×10^{16} m^{-3}. With longer nucleation times the number of growth centres reduces and the intensity of the X-ray diffraction peaks increase. This indicates that the crystallites are being reduced in number density, but are becoming coarser. This phenomenon is to be avoided and its avoidance is an encouraging outcome.

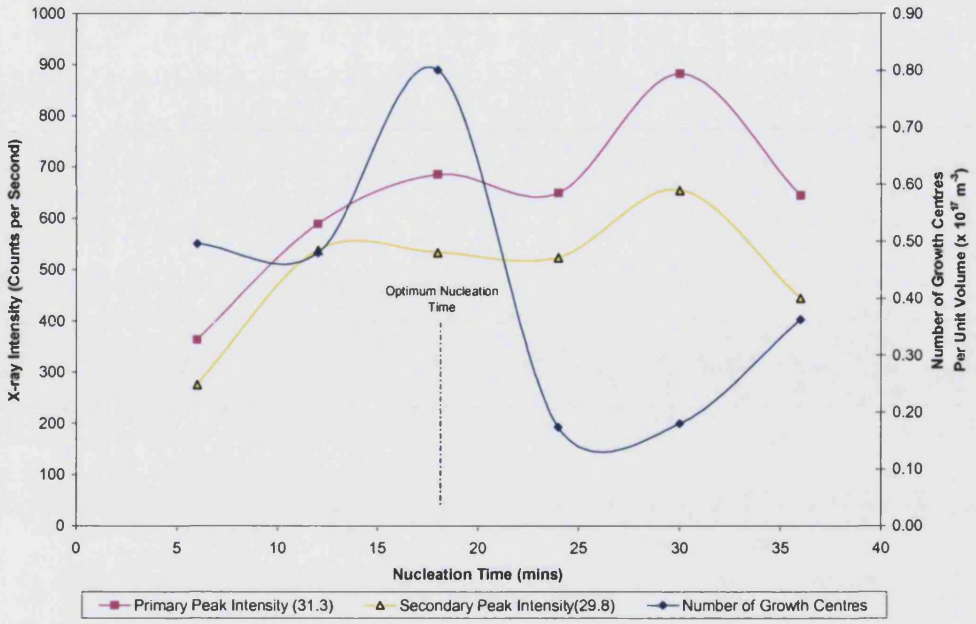

Figure 76: Micro-structural characteristics versus nucleation time obtained in the nucleation time assessment using the optimum nucleation temperature (for 96TET-2-NT1 to NT2)

Figure 76 shows that good correlation is observed between the micro-structural data (number of growth centres per unit volume) and the XRD intensity data. This indicates that the two most intense peaks in the diffractogram are responsible for the resolved micro-structural features. The data included in Figure 76 confirms that a traditional coarsening mechanism has operated; in the sense that longer holding times gave rise to fast growth rates giving a material system in which small crystal re-dissolve and larger crystals are enlarged. These changes work to reduce the overall free energy of the system, [20]. The conclusion is that 18 minutes is the optimum time for the nucleation process and that the nucleation process is very effective as it produces $8.0.x10^{16}$ nuclei m^{-3} that are successful in growing crystals. In contrast, the backscattered electron micrographs of 96TET2 – NT1 and 96TET2 – NT6, nucleated for 6 minutes and 36 minutes respectively at 650 °C, are shown in Figure 77. Here the larger crystallite size of 4.5 μm, and lower number of growth centres per unit volume of 40. x 10^{16} nuclei m^{-3} of the material can be observed in contrast with 95TET2 – NT3.

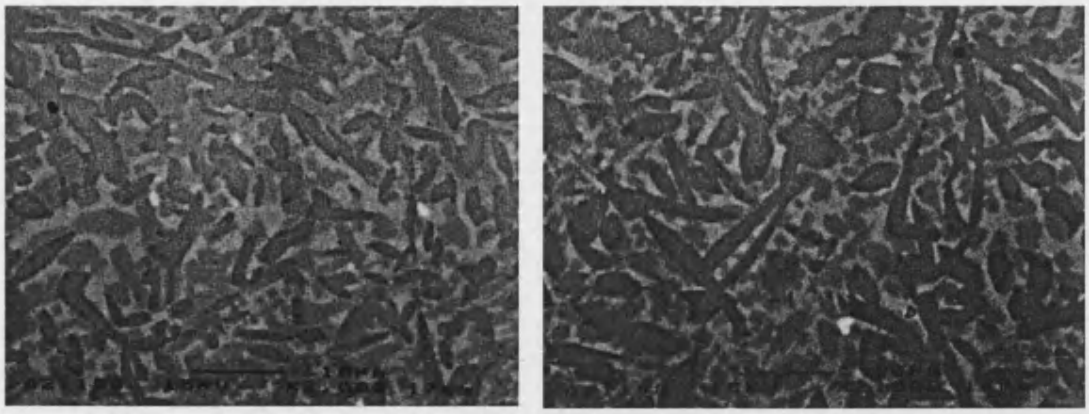

Figure 77: Backscattered electron micrograph of samples 96TET2 – NT1, on the LHS, and 96TET2 – NT6 on the RHS at (x 2,000)

8.2.3 Results of the Crystallisation Temperature Study

Material samples were prepared and analysed in accordance with Section 8.2. The experimentation considered temperatures close to the lower crystallisation temperatures, with an onset at 900 °C and a peak at 924 °C, as determined using DSC, presented in Section 5.2.2. Initial trials indicated that it was not feasible to work at the higher crystallisation temperature, with a peak at 1051 °C, because the samples deformed and sagged. SEM analysis indicated the presence of three phases including the matrix phase. Backscattered electron micrographs for sample 96TET2-C4, the sample treated at the optimum nucleation temperature and time with a crystallisation temperature of 930 °C, are presented in Figure 78.

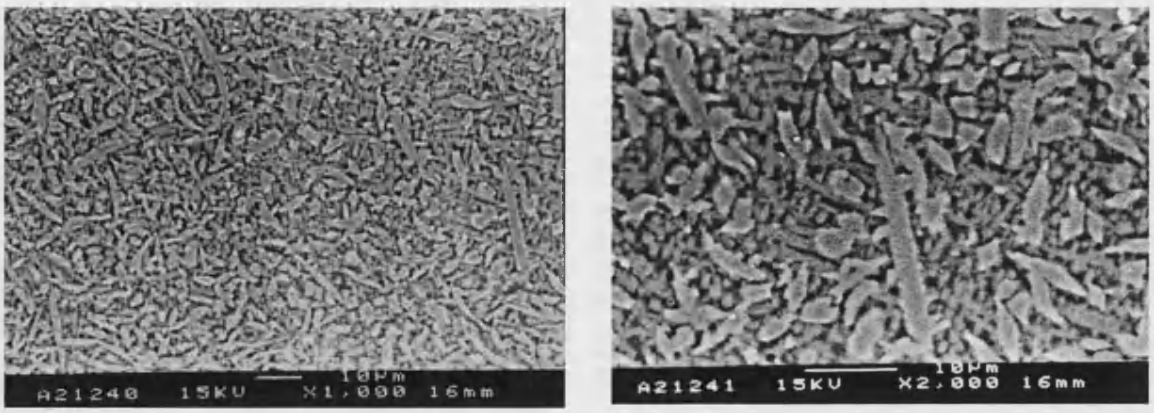

Figure 78: Backscattered electron micrograph of samples 96TET-2-C4, on the LHS (x 1,000) and on the RHS (x 2,000)

This was the optimum crystallisation temperature as it produced a uniform and fine microstructure. Morphological similarities are evident between these micrographs and those acquired during the investigation into nucleating temperature and time, and the average crystallite size '$D_{\text{eff grain}}$' has been retained at 4 μm. The material has been crystallised to a high degree, ~ 90 Vol%, determined using the lineal intercepts technique, Section 8.2. All of the different crystallisation temperatures employed produced similar microstructures with two contrasting crystalline phases, the microstructure coarsened and the level of porosity increased with temperature due to the reduced ability of the matrix to sustain the localised intensification of strain, attributed to phase density differences. The XRD analysis of the samples is summarised in Figure 79.

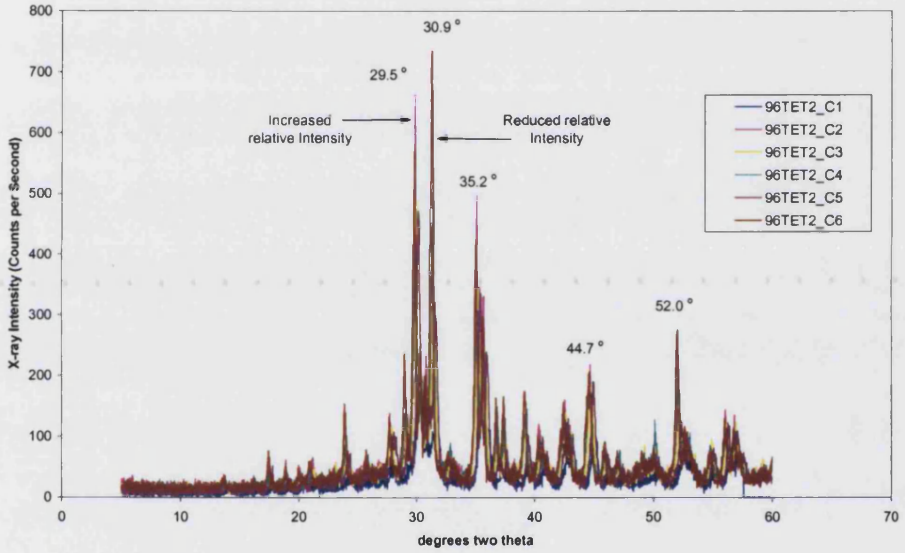

Figure 79: The X-ray diffractograms obtained in the assessment of crystallisation temperature

This is the first experimental stage in which crystallisation characteristics have been modified; the XRD analysis of the samples has identified two different crystalline phases. The lower temperature phase is replaced by the higher temperature phase or phase modification, as indicated by the relative shifts in the intensity of the characterising diffraction peaks [24]. It was not possible to distinguish between the two different phases.

All of the peaks become intense at high temperature indicating that all phases become stable. This is a waste material and therefore sample-to-sample variations must be expected. Similarly the occurrence of preferential orientation effects cannot be neglected. However, the large number of SEM micrographs acquired, show microstructures with random distributions of characteristic features. The EDX study indicates that there are subtle qualitative differences in the composition of the phases present. The outcome of the visual and micro-structural analysis of the samples is summarised in Figure 80.

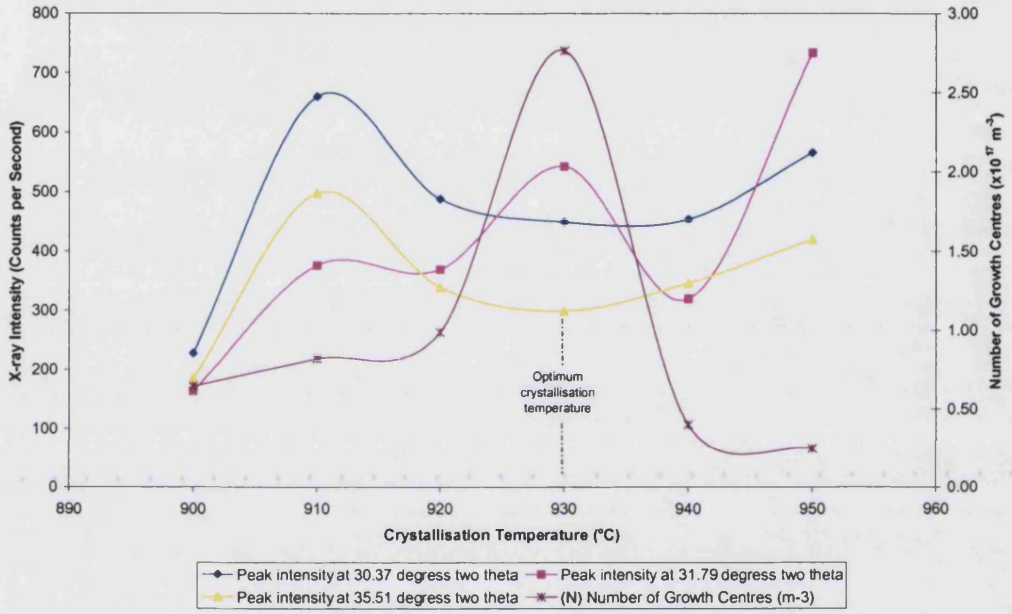

Figure 80: Micro-structural characteristics versus crystallisation temperature obtained in the crystallisation temperature assessment using the optimum nucleation conditions

The optimum crystallisation temperature was 930 °C, as indicated by the lowest crystallite size of 4 μm and highest number of growth centres per unit volume as acquired from the lineal intercepts technique. With higher crystallisation temperatures the number of growth centres reduced and the intensity of the X-ray diffraction peaks increased. This indicates that the crystallites were reduced in number density, and became coarser. Good correlation was obtained between the micro-structural data (number of growth centres per unit volume) and the XRD intensity data, and for the first time the relative intensity of the peaks changed. This indicated that phase transformation(s) were underway and the micro-structure was transforming as a function of temperature, phases being generated at the

sacrifice of others. The conclusion is that 930 °C is the optimum temperature for the crystallisation, as the microstructure is fine and uniform and should encourage improvements in mechanical properties. In essence, the transformation and temperature factor has been optimised leaving crystallisation time to be determined.

In contrast, the backscattered electron micrographs of 96TET2 – C6 nucleated at 650 °C for 18 minutes and crystallised at 950 °C, are shown in Figure 81. Here the larger crystallite size of 7.5 μm, and lower number of growth centres per unit volume of 2.5×10^{16} nuclei m^{-3} of the material can be observed in contrast to 95TET2 – N5, Figure 78.

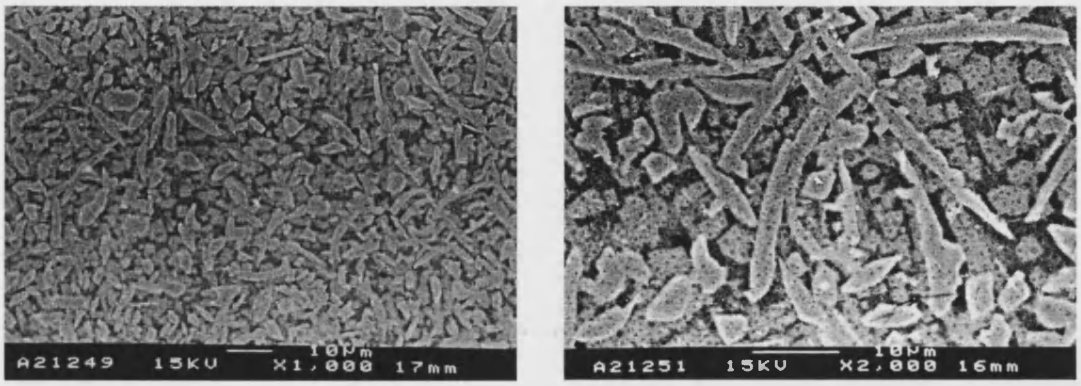

Figure 81: Backscattered electron micrograph of samples 96TET2-C6, on the LHS (x 1,000) and on the RHS (x 2,000)

8.2.4 Results of the Crystallisation Time Study

Samples were again prepared and analysed in accordance with Section 8.2. The experimentation considered times of economic practicality of between 30 minutes and 120 minutes. Certainty that 120 minutes delivered a desirable degree of crystallisation was acquired during the earlier stages of the experimentation, including the nucleation process assessment, Section 8.2.2. SEM analysis indicated the presence of three phases including the matrix phase. Backscattered electron micrographs for sample 96TET2-CT2, the sample treated using the optimum nucleation conditions and crystallisation temperature, are presented in Figure 82.

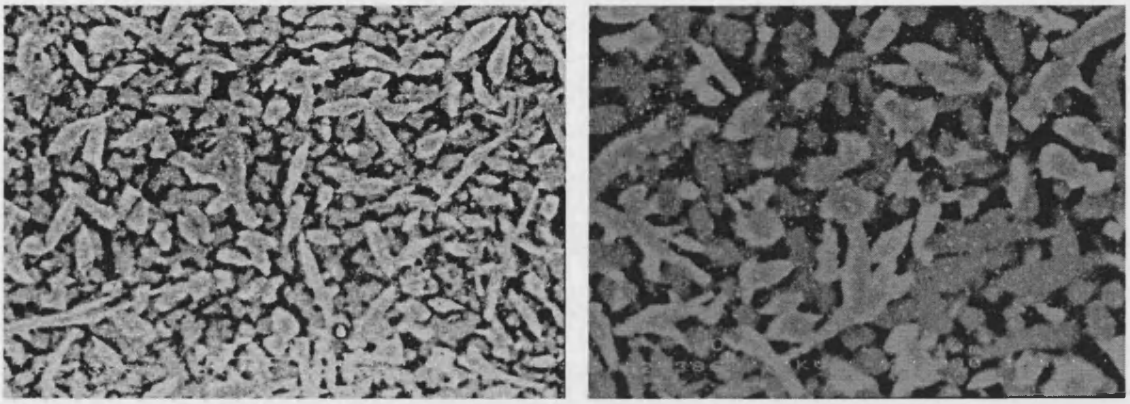

Figure 82: Backscattered electron micrograph of samples 96TET-2-CT2, on the LHS (x 2,000) and on the RHS (x 4,000)

Morphological similarities are evident between these micrographs and those acquired during the other stages of the experimentation. The material was crystallised to a high degree, ~ 80 vol%, determined using the lineal intercepts technique. All of the different crystallisation times employed produced similar microstructures that coarsened with increasing time. EDX analysis indicated that the main qualitative atomic constituents of the crystalline phases were aluminium, silicon and calcium with minor amounts of magnesium, iron and titanium. The primary (lighter) crystalline phase was slightly enriched in magnesium and titanium relative to the matrix and the secondary (darker) crystalline phase. The matrix and secondary crystalline phase appeared to be relatively enriched in potassium. However, light elements EDX responses can be deceiving due to limited fluorescent yield, the absorption of long wave characteristic X-rays and inter element absorption and fluorescence. The EDX spectra are shown in Figure 83.

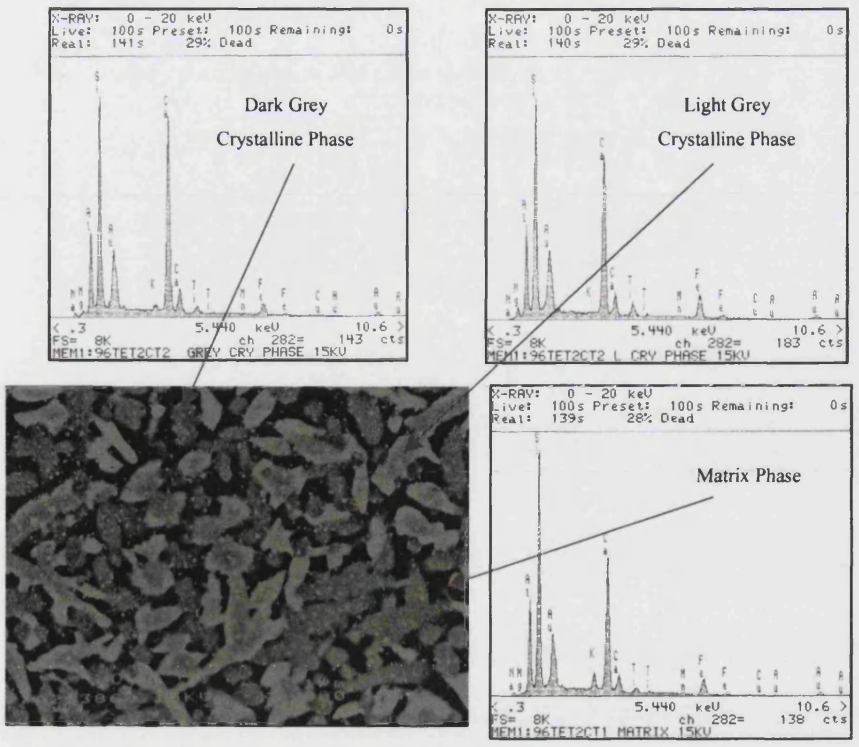

Figure 83: EDX spectra of the different microstructure regions of sample 96TET2-CT2, with annotated inset electron micrograph of 96TET2-CT2

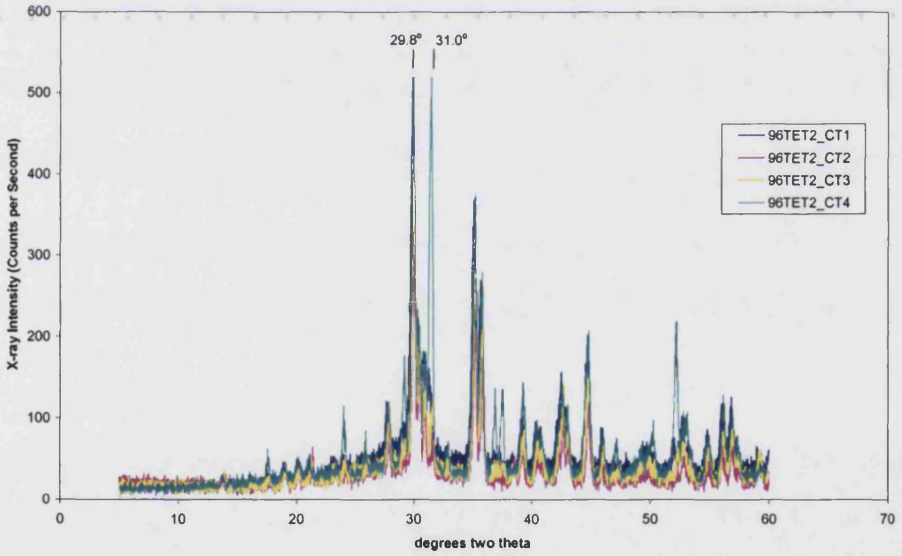

Figure 84: The X-ray diffractograms obtained in the assessment of crystallisation time

The XRD analysis of the samples is summarised in Figure 84, with brief peak annotation. Here the five most intense reflections show matched variations, indicating that the identity of the crystalline phases is not changing with time. The most intense peaks are located at 2θ values of 29° and 31°. These peaks are pronounced relative to the other spectral features and similar in location to those observed in the other stages of the experimentation. Hence, the crystalline phase identity conclusion remains valid as a solid solution of albite with anorthite. The outcome of the visual and micro-structural analysis of the samples is summarised in Figure 85.

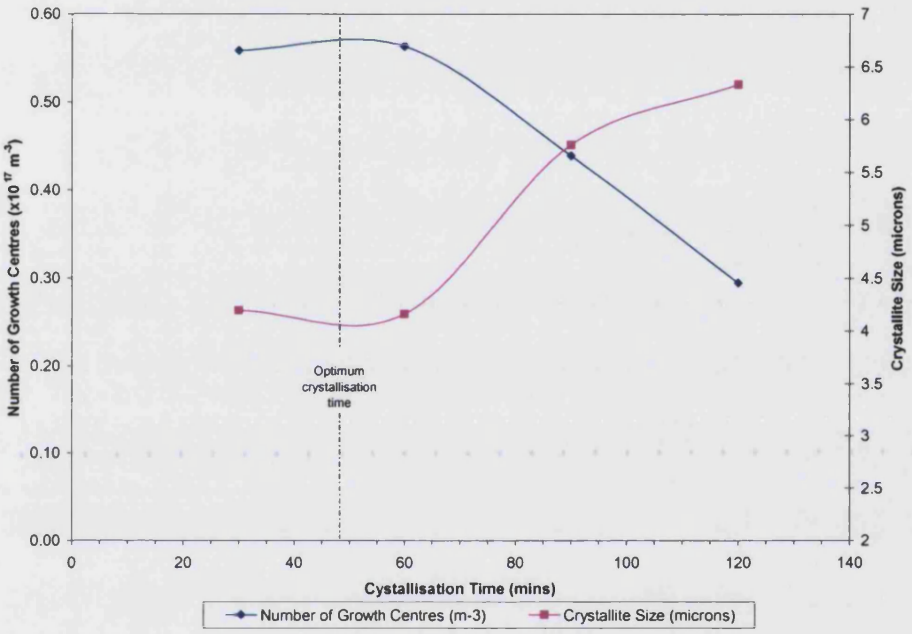

Figure 85: Micro-structural characteristics versus crystallisation time obtained in the crystallisation temperature assessment using the optimum nucleation conditions

The lowest crystallite size of < 4 μm and highest number of growth centres per unit volume defined the optimum crystallisation time of 48 minutes. Longer crystallisation times had a negative effect. Figure 85 indicates that the crystallites were reducing in number density, but becoming coarser with increasing holding times. This change was accompanied by a marked increase in the fraction transformed and higher levels of porosity, due to the reduced ability of the matrix to sustain the localised intensification of strain, which is attributed to phase density differences. To conclude, 48 minutes is the

optimum time for the crystal growth, as the product's microstructure was fine and uniform and should promote improvements in mechanical properties and applications performance.

8.3 Crystallisation Summary

Through a detailed and systematic examination of the nucleation and crystallisation temperature – time sensitivities, using XRD and SEM, an optimum heat treatment schedule was determined. This produced a semi-crystalline and fine-grained material. The optimum heat treatment cycle comprises of the following stages; nucleation at 650 °C for 18 minutes and crystallisation for 930 °C for 48 minutes, all intermediate temperature ramps were held constant at 6 °C min^{-1}.

A fine-grained crystalline microstructure should produce enhanced material properties, relative to the glassy material. This will be discussed in Section 10, however the ecological compatibility of the glassy material will be discussed now.

9 Ecological Compatibility Assessment

The aim of the ecological compatibility assessment was to demonstrate that plasma processed waste materials have low leaching characteristics, and that they do not compromise the quality of drinking water through direct physical contact, i.e. an extremely rigorous demonstration of the products' stability. This is of importance if the material is to be used in tile applications. The study aims to determine the inorganic leaching behaviour of the shaped cast monolithic ceramic tiles during their potential application as building materials. The tiles were cast from the cold skull plasma furnace, previously described in Section 7.0. The tiles were submerged in acidified water, at pH 4, with five times their own volume of leaching solution for each of the eight sampling stages, taken at increasing time. Therefore a total eluate volume of forty-five times the sample volume was employed. Diffusion test NEN 7345 was used for the determination of leaching behaviour, in which the eluant was periodically sampled, replaced and analysed over a period of 64 days. The test results are presented as 'cumulative releases' (in mg m^{-2}), from the interfacial area exposed for leaching, for each component analysed. The time dependency of the leaching of the materials was assessed under environmentally representative conditions. In the absence of UK limit values for the leaching characteristics of solidified waste products and waste acceptance criteria for disposal under the Landfill Directive (1999/31/EC), the results were compared with maximum acceptable concentrations (MACs) for the supply of drinking water. Emphasis is placed on the ability to re-use the cast product as a building material, as opposed to the treatment for disposal, and in ensuring ecological compatibility for potential applications and social acceptance.

9.1 Leaching Test Equipment and Methodology

Three different versions of cast plasma furnace vitreous tiles were analysed, all originating from different waste precursors including British China Clay (BCC) mining waste, Classified Municipal Solid Waste (C-MSW) grate ash and German Harbour Sediments (GHS), which were equivalent to 93TET, 95TET and 96TET, respectively, as described in Table 66. The samples were chosen to be representative of the plasma furnace product in terms of structure, homogeneity and composition. These tiles were not the best examples of the plasma furnace product in terms of appearance, but were typical examples containing surface imperfections and off-composition glass cords from the casting process, both of which were likely to increase leachability and were comparable in form and shape to natural

products. The samples were produced in the plasma furnace, and cooled in a controlled manner to avoid cracking upon solidification. The waste origins of the samples and their post-plasma compositions are presented in Table 66. In this table the trace element content of the tiles is compared to that of the earth's crust and with natural basalt. It is noted that there is similarity in the levels of metallic trace elements between the samples and the naturally occurring materials. This means that, in the long-term, the ecological impact of these materials will be no greater than that of tiles made from natural materials [67]. The high levels of chromium, lead and Fe_2O_3 in the glasses, was predicted to affect the leaching behaviour of the tile product. The magnitude of the effect will be determined by compositional homogeneity and the effectiveness of the matrix as a diffusion barrier.

Sample ID	93TET	95TET	96TET	Earth's Crust [72]	Basalt [72]
Waste Origin	**BCC***	**GHS***	**C-MSW***		
Bulk Oxide Species (% w/w)					
Na2O	0.19	0.85	3.01		
MgO	0.25	1.59	1.70		
Al2O3	22.3	26.2	19.8		
SiO2	42.7	36.8	39.8		
P2O5	<0.05	0.15	0.68		
SO3	<0.05	0.19	0.17		
K2O	2.06	0.77	0.85		
CaO	28.8	28.9	24.0		
TiO2	0.68	1.68	2.01		
Cr2O3	<0.05	<0.05	0.08		
Mn3O4	<0.05	0.10	0.13		
Fe2O3	0.79	2.96	8.67		
LOI @ 1025°C	0.29%	<0.02	<0.02		
Trace Elements ppm w/w					
As	94	<50	<50	1.8	2
Co	0.06%	79	73	22	48
Cr	<25	44	265	100	200
Cu	31	59	472	50	100
Mn	141	0.07 %	0.11%	0.1%	0.17%
Pb	34	47	43	12.5	3.5
Ti	0.42%	1.05%	1.31%	0.5%	0.9%
Zn	<25	<25	344	70	100
*BCC = British China Clay Waste, GHS = German Harbour Sediment, C-MSW = Classified Municipal Solid Waste incinerator bottom ash.					

Table 66: Comparison of blended plasma vitrified waste compositions with that of the earth's crust and basalt

The oxide species were analysed using wavelength dispersive X-ray Fluorescence Spectroscopy (XRF), a Philips pw 1400 instrument. Here, 1 gram of the material sample was fused with lithium tetraborate in a platinum gold alloy crucible. The trace elements

were analysed using inductively coupled plasma optical emission spectroscopy, (ICPOES) analysis, using a Spectro Analytical instrument, following sample digestion in acid under microwave radiation. Many of the components were analysed, but only those of interest in the context of the leaching characterization and regulatory standards are reported here.

The test pieces, supported on plastic legs, were placed in the sealable plastic containers and such that the test piece was surrounded by liquid on all sides with the upper surface of the test pieces covered by >2 cm depth of liquid. The eluant, was filtered (filter pore size <0.45 μm) and chemically preserved, to prevent precipitation or evaporation losses. The pH (± 0.05 pH) and ionic conductivity (± 1 μS cm^{-1}) of the eluant were also assessed.

The analysis was undertaken by considering the following:

(i). The quantity of eluate required for all component analysis within a given fraction, based on the methods of preservation and analysis was ~ 1.0 – 1.4 litres.

(ii). The availability of the components to be analysed in terms of mg kg^{-1} of dry matter, Table 66, was determined.

(iii). The samples were regular shaped, and the surface areas available for leaching, were determined using simple geometric measurements to within ± 1 mm.

(iv). Three inorganic components with clearly measurable leaching behaviour above the limit of detection (LOD) were selected.

The diffusion tests were carried out as follows:

(i). The plastic containers were rinsed with acidified water.

(ii). The container was filled with the required volume of leachant.

(iii). The test piece was located in the container on the supports and left for 6 hrs.

(iv). The stage 1 fraction of the eluant was drained off, without rinsing or drying of the sample. The eluate was filtered, the pH and conductivity measured and stored for analysis.

(v). Immediately after the drainage of stage 1 the container was filled with the same volume of leachant and the procedure was repeated a further seven times in accordance with Table 67.

(vi). The eluate for all required components was analysed as soon as possible after each stage, [68].

The eluate analysis was undertaken in a similar manner to the tile's trace element analysis, using inductively coupled plasma mass spectroscopy, (ICPMS), for the lower limits of detection.

Stage/Fraction Number 'n'	Time (in days, ± 10%)
1	0.25
2	1
3	2.25
4	4
5	9
6	16
7	36
8	64

Table 67: NEN 7345 leaching characterisation test replenishment times for leachant [68]

The analytical methodology employed is shown in Table 68. Table 69 gives a comprehensive presentation of all the analytical results; concentrations are quoted in both mg l^{-1} and μg l^{-1} units. The results are segregated in accordance with fraction number; 93TET T1 gives the eluate analysis from 93TET, at stage 1 (0.25 days interval). The results are ordered in accordance with the determinands listed at the top of the Table 69. The use of '<=' within Table 69 signifies that the LOD has been used in the position to the right of the marker, e.g. the concentration of Cl in 93TET T1 is less than or equal to 0.1 mg l^{-1}. Blank samples are required at all stages to quantify systematic baseline errors.

Method	Inductively Coupled Plasma - Mass Spectrometry
Sample Types	Potable, raw, surface and groundwaters. Acid digests of soils, sediments, sludges and biota.
Principle	All aqueous samples are collected in nitric acid. The sample is spiked with an internal standard (rhodium), and introduced in aerosol form into a argon plasma that is maintained at a temperature of ~7000 K. The plasma is produced and sustained by electromagnetic coupling through a coil in an RF circuit. Determinands in the sample are ionised in the plasma, and a small portion of these ions are sampled and introduced into the mass spectrometer. The ions are separated (and identified) by their mass:charge ratio and are detected using a dynode array detector.
Reference	SCA Publication "Inductively Coupled Plasma Spectrometry 1996", Methods for the Examination of Waters and Associated Materials, HMSO (ISBN 011 753244 4)

Table 68: Analytical protocol

Units		uS/cm		mg/l	mg/l		ug/l		ug/l		-		ug/l		ug/l		ug/l		ug/l		ug/l		ug/l		ug/l		ug/l		ug/l		ug/l		ug/l
Sample Code	pH	COND (K20)	**	Cl	SO4	**	Hg		Cr		Co		Fe		Ni		Cu		Zn		As		Se		Mo		Cd		Sb		Pb		Sn
		uS/cm		mg/l	mg/l		ug/l		ug/l		ug/l		ug/l		ug/l		ug/l		ug/l		ug/l		ug/l		ug/l		ug/l		ug/l		ug/l		ug/l
BLANK T1	3.19	304	<=	0.1	0.21	<=	0.1	<=	0.2	<=	1	<=	5		0.3		1.8	<=	0.7	<=	0.1	<=	0.2	<=	1		0.16	<=	2		0.25	<=	2
93 TET T1	3.34	217	<=	0.1	0.57	<=	0.1		0.5	<=	1		76	<=	0.2		35.3		10.1		0.12	<=	0.2	<=	1		0.32	<=	2		3.25	<=	2
95 TET T1	3.53	169	<=	0.1	0.79	<=	0.1		1	<=	1		268		0.6		34.3		19.5		0.15	<=	0.2	<=	1		0.21	<=	2		8.31	<=	2
96 TET T1	3.58	161	<=	0.1	1.28	<=	0.1		1.7	<=	1		55		0.4		79.4		35.4	<=	0.1	<=	0.2	<=	1		0.38	<=	2		7.06	<=	2
BLANK T2	2.38	2008	<=	0.1	0.3	<=	0.1	<=	0.2	<=	1	<=	5	<=	0.2		0.6	<=	0.7	<=	0.1	<=	0.2	<=	1	<=	0.02	<=	2		0.11	<=	2
93 TET T2	2.82	975		0.18	0.57	<=	0.1		8.8	<=	1		1020		1.1		95.1		50		0.47	<=	0.2	<=	1		1.1	<=	2		15.2		5.4
95 TET T2	3.07	777		0.59	2.11	<=	0.1		15.5	<=	1		4290		2.5		52.2		96.9		0.99	<=	0.2	<=	1		0.21	<=	2		10.8	<=	2
96 TET T2	2.74	1090		0.12	1.95	<=	0.1		40.6		1.2		5880		3		437		372		0.23	<=	0.2	<=	1		2.01	<=	2		208	<=	2
BLANK T3	2.45	1445		0.2	0.27	<=	0.1		0.3	<=	1		23	<=	0.2	<=	0.4	<=	0.7	<=	0.1	<=	0.2	<=	1	<=	0.02	<=	2		0.12	<=	2
93 TET T3	3.22	568		0.33	0.5	<=	0.1		6	<=	1		1400		1		43		24.6		0.24	<=	0.2	<=	1		0.33	<=	2		7.41	<=	2
95 TET T3	3.93	440		0.2	1.2	<=	0.1		35.6	<=	1		5370		2.8		83.7		184		0.13	<=	0.2	<=	1		0.34	<=	2		59.7	<=	2
96 TET T3	3.03	682		0.26	1.41	<=	0.1		10.9	<=	1		3150		2.3		20.4		55.9		0.24	<=	0.2	<=	1		0.08	<=	2		2.83	<=	2
BLANK T4	2.52	1230		0.42	0.65	<=	0.1	<=	0.2	<=	1	<=	5	<=	0.2		0.5	<=	0.7	<=	0.1	<=	0.2	<=	1	<=	0.02	<=	2	<=	0.1	<=	2
93 TET T4	3.51	431		0.45	3.08	<=	0.1		4.5	<=	1		603		1		39.4		17.8		0.18	<=	0.2	<=	1		0.21	<=	2		4.52	<=	2
95 TET T4	4.15	369		0.33	0.85	<=	0.1		9.9	<=	1		2010		1.9		14.8		43.7		0.2	<=	0.2	<=	1		0.04	<=	2		2.06	<=	2
96 TET T4	3.2	520	<=	0.1	0.82	<=	0.1		32.8	<=	1		4180		2.8		28.9		137	<=	0.1	<=	0.2	<=	1		0.14	<=	2		37.9	<=	2
BLANK T5	2.18	2710						<=	0.2			<=	5	<=	0.2	<=	0.4	<=	0.7											<=	0.1		
93 TET T5	3.81	777							8				3450		2		93.9		32												8.94		
95 TET T5	4.12	755							20.5				6430		4.5		27.8		83.4												3.53		
96 TET T5	3.54	811							96.6				11100		7.5		53.5		270												71.2		
Blank T6	2.14	3040							0.3			<=	20	<=	0.2		0.7	<=	0.7											<=	0.1		
93TET T6	3.91	850							10.5				1920		1.9		103		27.1												6.63		
95TET T6	4.09	838							24				6260		4.5		24.9		78.8												2.99		
96TET T6	3.85	857							107				16500		8.1		84.1		242												45.5		
Blank T7	2.4	1620						<=	0.2				13	<=	0.2		1		1.2												0.15		
93TET T7	4.02	470							4.3				2090		1		71.1		11.9												2.46		
95TET T7	4.17	465							9.5				4360		3.7		19.4		36.7												1.29		
96TET T7	4.12	464							31.9				9080		5.2		54.9		114												14		
BLANK T8	2.6	1210		1.96	3.73	<=	0.1	<=	0.3	<=	0.003	<=	0.02		0.02		0.6		4.6	<=	0.1	<=	0.9	<=	1	<=	0.01	<=	1	<=	0.1		3
93TET T8	4.1	363		0.64	0.99	<=	0.1		3.9		0.097		0.88		5.51		55.6		11.5		0.12	<=	0.9	<=	1		0.07	<=	1		1.86	<=	2
95TET T8	4.25	358		0.65	1.86	<=	0.1		5.7		1.44		3.32		3.3		19.9		31.4		0.21	<=	0.9	<=	1		0.02	<=	1		0.67	<=	2
96TET T8	4.13	362		0.79	2.25	<=	0.1		13.3		1.15		5.95		3.9		48.1		77.3	<=	0.1	<=	0.9	<=	1		0.05	<=	1		6.7	<=	2

Table 69: Eluate Analysis Results for the NEN 7345 test as applied to plasma furnace tiles

9.2 Calculations and Interpretations

The 'measured leaching of a component per fraction' was calculated for each component studied, [76]. If the concentration of the components was below the LOD, then the LOD value itself was used in the calculation, Equation 49, [68]. This is the most pessimistic view.

$$E^*_i = \frac{c_i \times V}{f' \times A'}$$

Equation 49

where:

E^*_i = measured leaching of a component in fraction i, in mg m^{-2}

c_i = concentration of component in fraction i, in µg l^{-1}

V = volume of the eluate in litres

A' = the surface area of the test piece in m^2

f' = a dimensionless factor: 1000 µg mg^{-1}

Secondly, the 'measured cumulative leaching of a component in successive fractions' was evaluated for n = 1 to 8, where n = 1 is the period from the start of the test to the first replenishment time, and n = 2 is the period from the start of the test to the second replenishment time, Equation 50. This includes the measured leaching of the previous periods, which means that any deviation in a given period affects subsequent periods. An example of such effects would be wash-off or depletion.

Measured cumulative leaching $\varepsilon^*_n = \sum_{i=1}^{n} E^*_i$ for n = 1 to N^*

Equation 50

where:

E^*_i = measured leaching of a component in fraction 'i', in mg m^{-2}

ε^*_n = measured cumulative leaching of a component for period n comprising fractions i = 1 to n, in mg m^{-2}

N^* = number of fractions which is equal to the number of specified replenishment times

Finally, the arithmetical cumulative leaching was calculated using Equation 51, [68].

Arithmetical cumulative leaching $\varepsilon_n = E^*_i \frac{\sqrt{t_i}}{\sqrt{t_i} - \sqrt{t_{i-1}}}$ for n = 1 to N*

Equation 51

where:

ε_n = arithmetical cumulative leaching of a component for period i = 1 to n, in mg m^{-2}

E^*_i = measured leaching of a component in fraction i, in mg m^{-2}

t_i = replenishment time of fraction i, in secs

t_{i-1} = replenishment time of fraction i-1, in secs

The arithmetical cumulative leaching ε_n determines only the cumulative leaching up to and including period i on the basis of the measured leaching in period i. Differences in the measured and cumulative leaching give insight into the wash-off effects, dissolution and also depletion of species. A wide spectrum of heavy metal and soluble anions were analysed, Table 69, but only those of leaching significance are discussed here. The selected species were those defined in the water regulations employed.

9.3 Tile Leaching Data and Characteristics

Until waste acceptance criteria (leaching limit values) for disposal of material as inert, non-hazardous or hazardous waste under the landfill directive are published and executed, it is appropriate to compare the eluate concentrations (μg l^{-1}) with the maximum acceptable concentrations (MACs) for drinking water supply. Of all the parameters determined those that approach the MAC thresholds, Table 70, have been considered to be most appropriate. Table 70 shows both the current and future water quality regulations, which were transposed into national regulation by the end of 2002 and will be report on by 2004, [70].

Parameter	Water Supply Regulations 1989, (μg l^{-1})	Directive 98/83/EC, (μg l^{-1})*
Antimony (Sb)	10	5
Arsenic (As)	50	10
Copper (Cu)	3000	2000
Lead (Pb)	50	10
Nickel (Ni)	50	20
Chlorine (Cl)	400,000	250,000
Iron (Fe)	200	Not regulated
Chromium	50	50
pH**	5.5 – 9.5	6.5 – 9.5
Conductivity***	1,500	2,500

*Implementation in 2002, **pH units apply, ***μS cm^{-1} units apply @ 20°C

Table 70: Comparison of current and future water quality regulations

9.3.1 93TET (British China Clay Waste)

For 93TET the actual measured leaching characteristics of four determinands show elevated values relative to other species. The concentration are below, but approaching the defined maximum acceptable concentrations (MAC's), Table 70. These are conductivity, chromium, iron and lead concentrations. Conductivity is a measure of the level of dissolved salts and is commonly found in water assessment protocol. Here the actual values are presented in a tabulated format, Table 71. Only iron actually exceeds the current MAC level, but additionally, the short-term release characteristics are more pronounced than the long-term release characteristics, and became de-regulated in 2002, [70]. The long-term release characteristics show a decreasing leaching trend directed towards and below the MAC value, which indicate long-term ecological stability and short-term adverse transient effects. The tabulated data are presented graphically in Figure 86. All leaching characteristics can be observed to arrest and to plateau within the time interval examined.

Times (days)	Conductivity ($\mu S\ cm^{-1}$)	Cr ($\mu g\ l^{-1}$)	Fe ($\mu g\ l^{-1}$)	Pb ($\mu g\ l^{-1}$)
0	217	1	76	3
1	975	9	1020	15
2	568	6	1400	7
4	431	5	603	5
9	777	8	3450	9
16	850	11	1920	7
36	470	4	2090	2
64	363	4	880	2

Table 71: Summarised leaching characteristics of 93TET

This information is also presented in a cumulative manner so that the rate of change, and significance of stages, can be examined as a function of time, Figure 87.

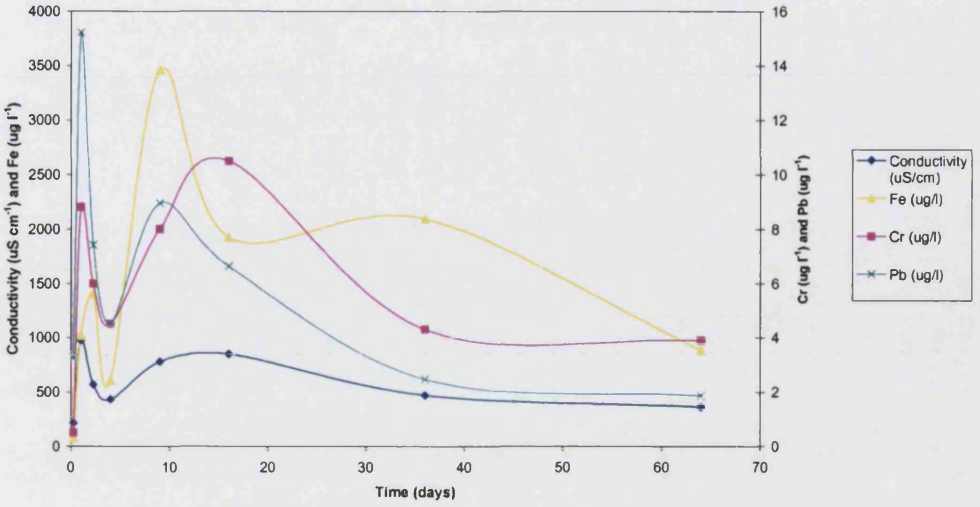

Figure 86: 93TET measured conductivity and leaching characteristics

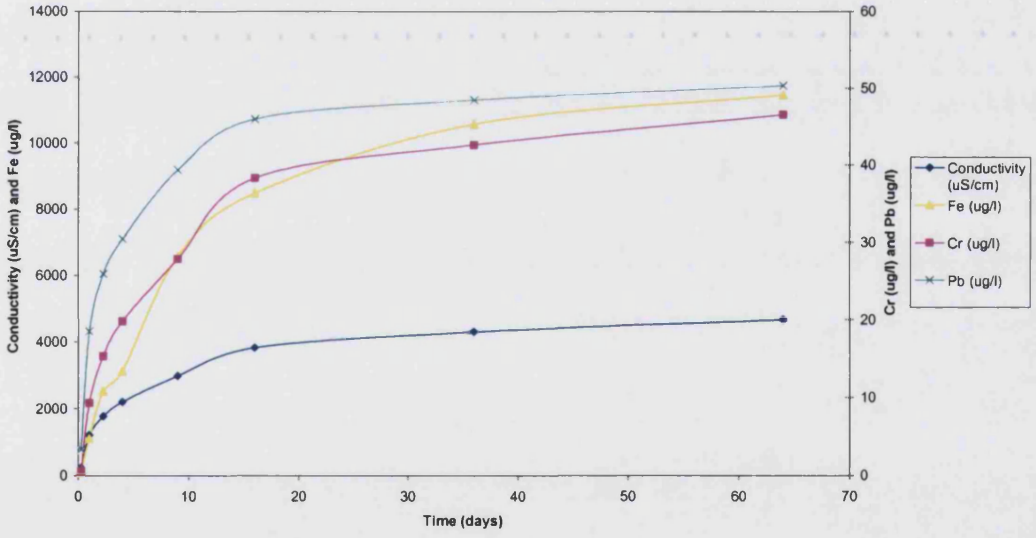

Figure 87: 93TET measured cumulative conductivity and leachate results

Finally, this can be compared with the actual surface specific measured cumulative leaching which allows the eluate analysis information to be related to sample dimensions, Figure 88.

This shows that the leaching characteristics of the heavy metal species were less than 2 mg m^{-2} over a period of 64 day, and that initial transient affects were dominant.

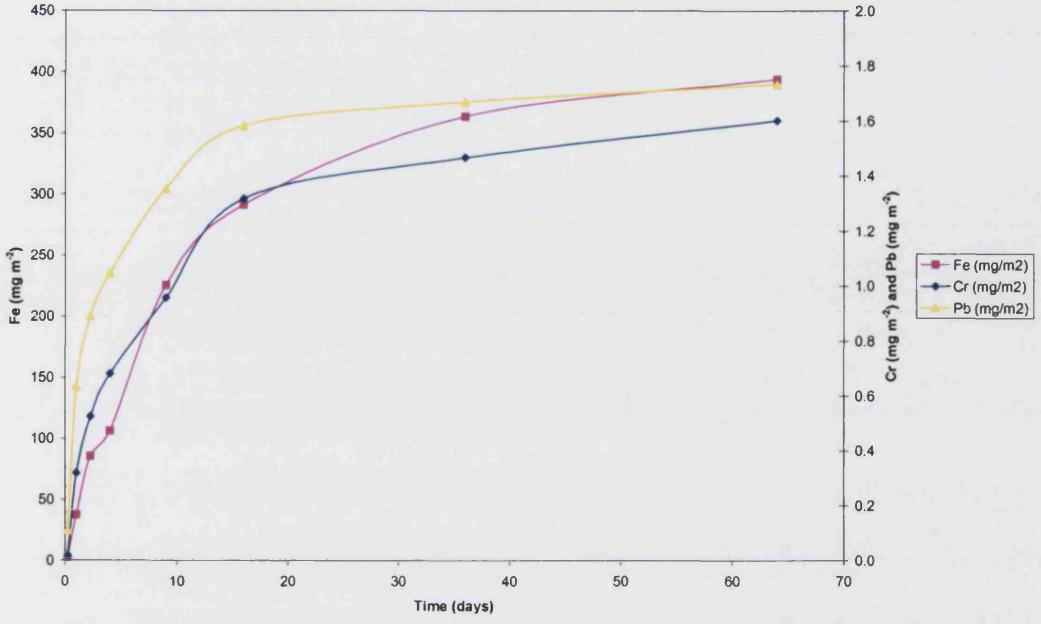

Figure 88: 93TET measured cumulative surface specific leaching

9.3.2 95TET (German Harbour Sediment)

As observed with the British China Clay (BCC) based tile, the 95TET system which is based on GHS shows leaching characteristics of conductivity, chromium, iron and lead concentrations that approach regulation defined MAC levels. The actual values are presented in Table 72.

Times (days)	Conductivity (µS cm^{-1})	Cr (µg l^{-1})	Fe (µg l^{-1})	Pb (µg l^{-1})
0	169	1	268	8
1	777	16	4290	11
2	440	36	5370	60
4	369	10	2010	2
9	755	21	6430	4
16	838	24	6260	3
36	465	10	4360	1
64	358	6	3320	1

Table 72: Summary leaching characteristics of 95TET

Significant differences between the leaching characteristics of 93TET and 95TET can be seen. The 95TET based material shows a greater release of iron and chromium, which can be explained through examination of the relative compositions and the tile material's origin, i.e. GHS contains a higher 'total' concentration of Fe_2O_3 and chromium and is associated with a heavily industrialised environment, Table 66. Again, through comparison with the drinking water regulations, only iron actually exceeds the current MAC level, and this will soon be de-regulated, leaving no environmental argument against exploitation. Additionally for iron, the short-term and long-term release characteristics show comparable magnitudes. The long-term release characteristics show a decreasing leaching trend, Figure 89.

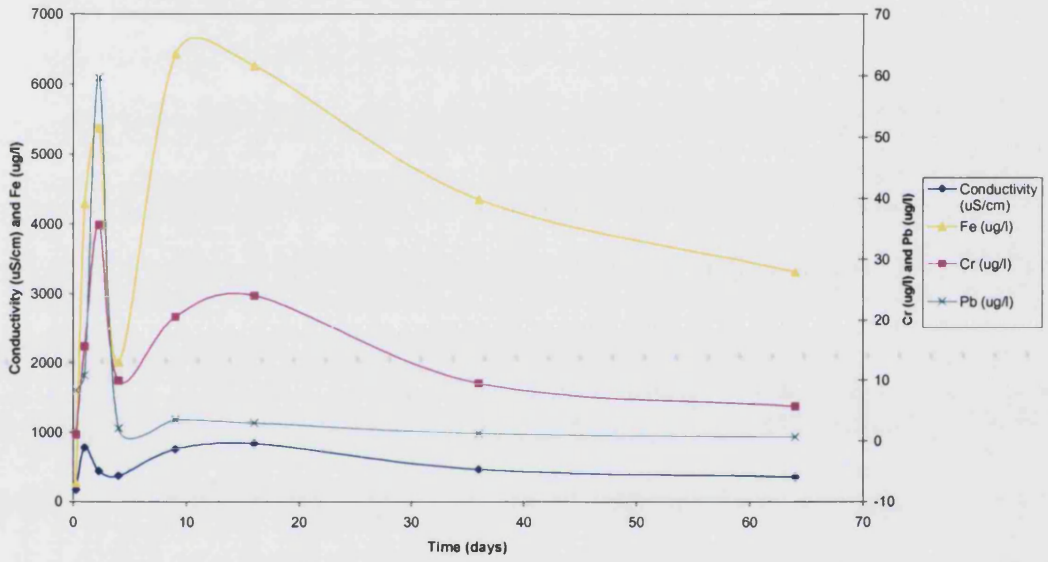

Figure 89: 95TET measured conductivity and leaching characteristics

The information is presented in a cumulative manner so that the rate of change, and significance of individual stages, can be examined as a function of time, Figure 90. Here there is an overall reduction in the rate of increase of the leaching characteristics as these approach a constant value. This plateau effect is less significant for iron.

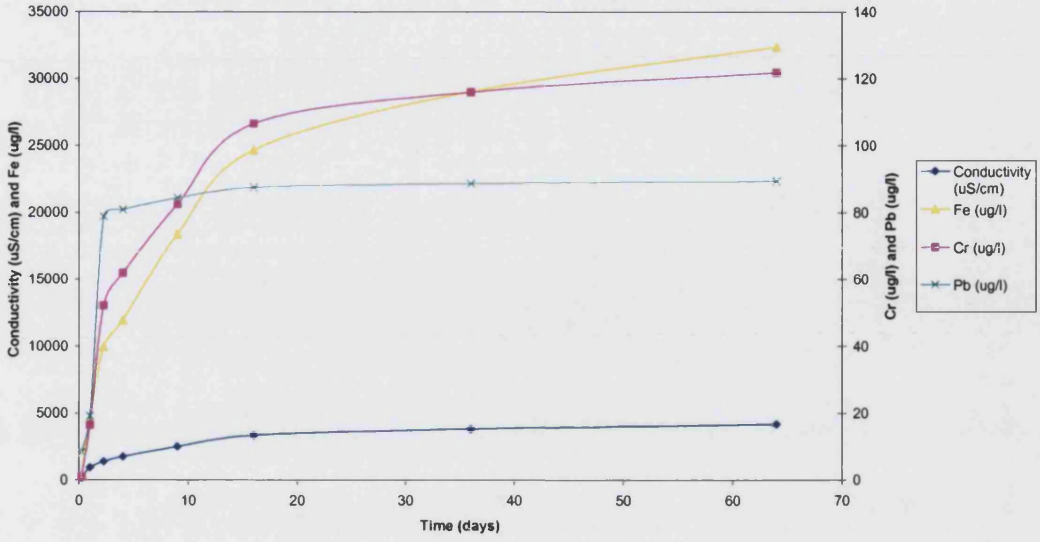

Figure 90: 95TET measured cumulative conductivity and leachate results

The overall release of iron, chromium and lead is dominated by the initial stages of the test, this can be compared with the actual surface specific measured cumulative leaching, which allows the data to be normalized for the samples' dimensions, Figure 91.

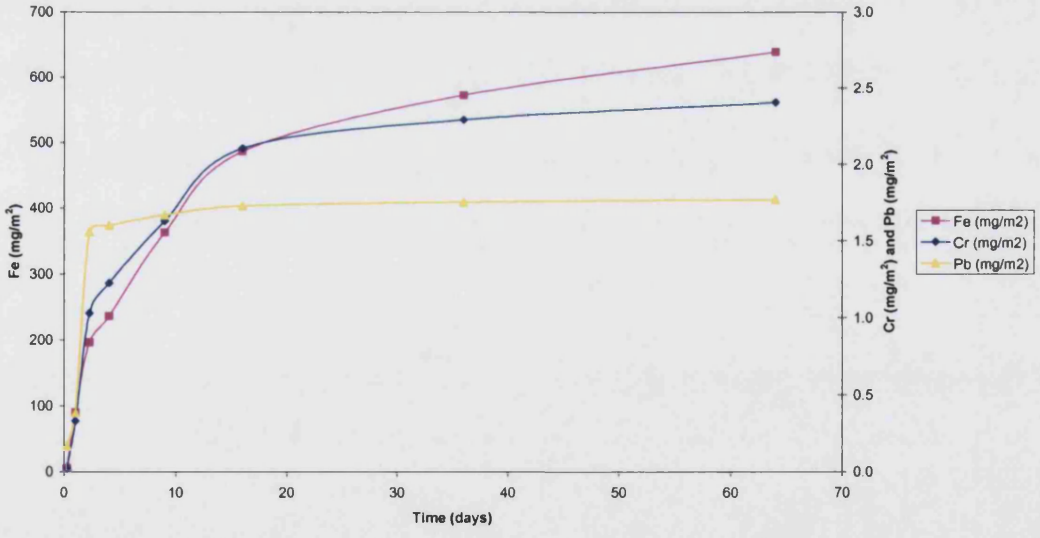

Figure 91: 95TET measured cumulative surface specific leaching

This shows that the leaching characteristics of the heavy metal species were less than 3 mg m^{-2} over a period of 64 day, and that initial transient affects were dominating.

9.3.3 96TET (Classified Municipal Solid Waste)

As for the BCC and GHS tiles, tiles of 96TET show leaching characteristics for only four determinands that approach the defined MAC levels. Again, these are conductivity, chromium, iron and lead concentrations, shown in tabulated format in Table 73. Significant contrast in the leaching characteristics of 96TET with the other samples can be noted. 96TET shows a greater release of iron, lead and chromium, which can be explained through examination of the blended post plasma tile compositions and the materials origin, Table 66. 96TET has high chromium, lead and Fe_2O_3 concentrations. Only iron exceeds the current MAC level and is to be de-regulated. Additionally for iron, the long-term release characteristics, after reaching a peak, present a depleting trend, similar to the release of chromium and lead, which have also plateaued and decayed abruptly. The tabulated data is presented graphically in Figure 92. The entire release of heavy metal species, determined as the overall sum of the products of multiplying the measured eluate analysis with the eluant volume, accounts for an extremely small fraction of the mass of heavy metals species present. Therefore, the plateau and decay of the leaching trends results from initial wash-off effects or surface depletion.

Times(days)	Conductivity ($\mu S\ cm^{-1}$)	Cr ($\mu g\ l^{-1}$)	Fe ($\mu g\ l^{-1}$)	Pb ($\mu g\ l^{-1}$)
0	161	2	55	7
1	1090	41	5880	208
2	682	11	3150	3
4	520	33	4180	38
9	811	97	11100	71
16	857	107	16500	46
36	464	32	9080	14
64	362	13	5950	7

Table 73: Summaried leaching characteristics of 96TET

This information is presented in a cumulative manner, and here the diminishing trends can be observed more clearly, i.e. the rate of change of slope is negative and increasing in magnitude, Figure 93.

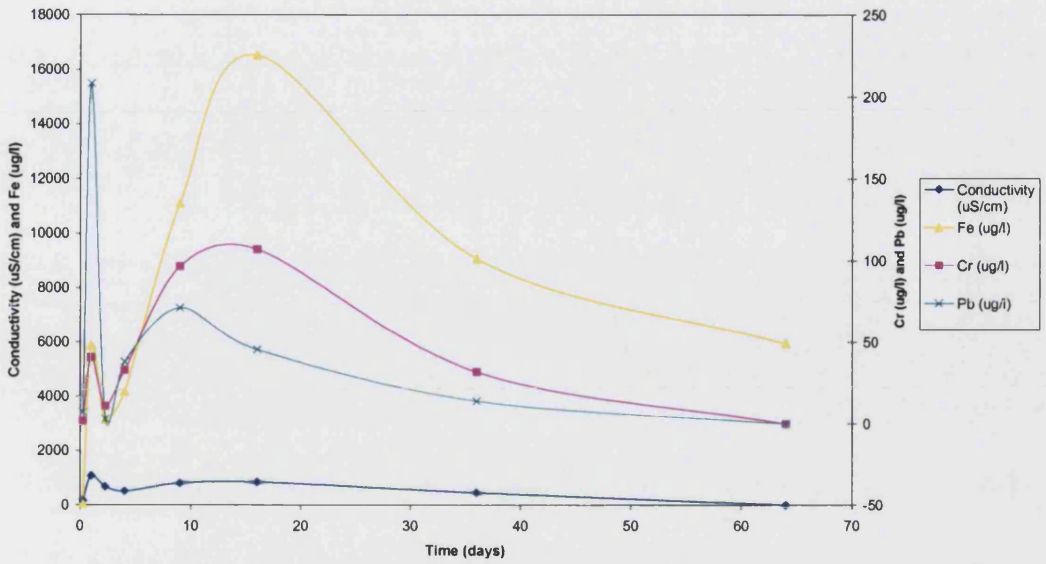

Figure 92: 96TET measured conductivity and leaching characteristics

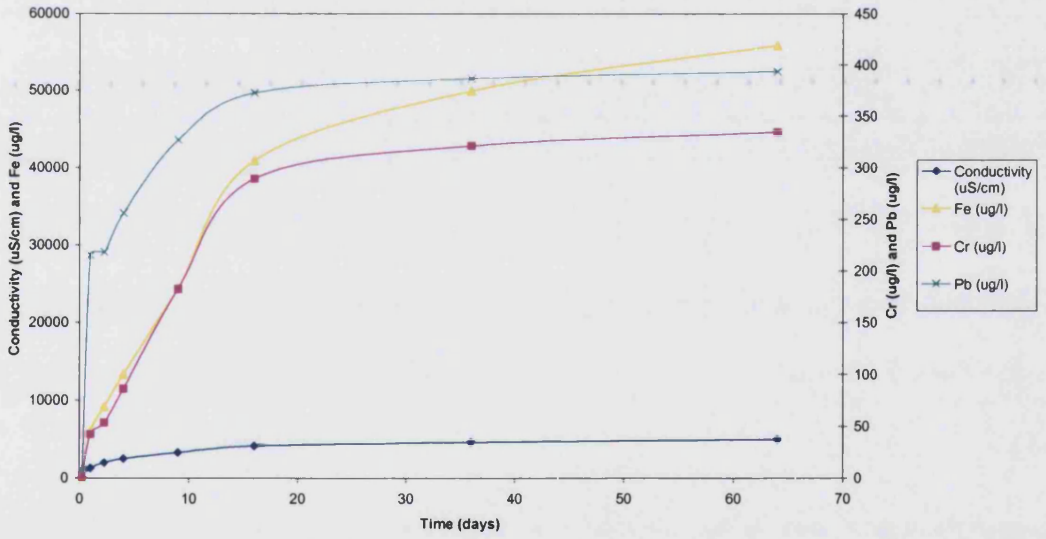

Figure 93: 96TET measured cumulative conductivity and leaching results

Finally, the cumulative leaching results can be compared with the surface specific cumulative leaching characteristics which allows the eluate information to be related to sample shape and size, Figure 94. This shows that the leaching of 96TET was a factor of four times greater that the other materials; the leaching characteristics of the heavy metal

species were less than 12 mg m^{-2} over a period of 64 day, and that initial transient affects were dominant

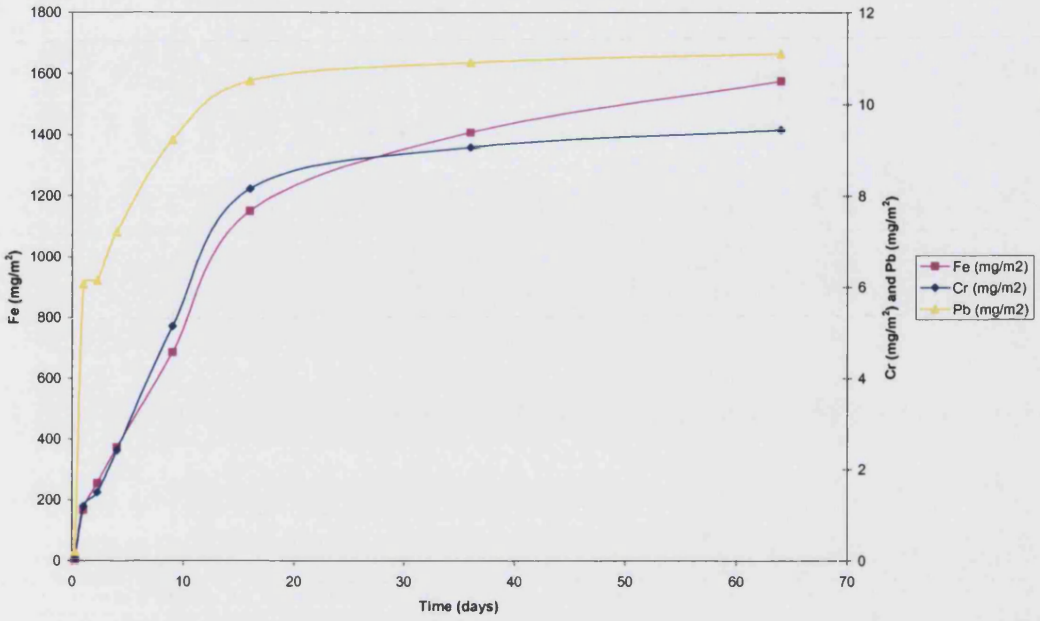

Figure 94: 96TET measured cumulative surface specific leaching

9.3.4 Commercially Available Granite

The same test was applied to a commercially available natural material, namely black Indian granite tiles, supplied by Odlings, code number KATTI/MA. The leaching characteristics were generally similar in order of magnitude to those of the waste materials examined, but were lower in eluate concentration value, in most cases. The four determinands of conductivity, chromium, iron and lead concentrations have been complemented by consideration of the nickel content. The values are presented in a tabulated format in Table 74. The test was terminated after 32 days, when it had been demonstrated that the data acquired, for the black Indian granite material, was similar to that acquired for the other waste based materials. Significant contrast in the leaching characteristics to the other waste samples was observed; although the conductivity and iron values are similar, the chromium and lead levels were up to two orders of magnitude lower. The eluate lead concentration as the 36 days interval was 1.10 μl^{-1} for the granite material and 2.00 μl^{-1}, 1.29 μl^{-1} and 14.00 μl^{-1} for 93TET, 95TET and 96TET respectively. Both iron and nickel, exceeded the current MAC levels, iron will be de-regulated, but the criteria for nickel will become more

stringent, Table 70. Both iron and nickel, exhibit long-term release characteristics, with an accelerating trend. In contrast chromium, conductivity and lead exhibit characteristics that have plateaued after a short period. The tabulated data is presented graphically in Figure 95.

Time (days)	Conductivity (μS cm^{-1})	Cr (μg l^{-1})	Fe (μg l^{-1})	Pb (μg l^{-1})	Ni (μg l^{-1})
0.25	592.00	1.7	836	5.74	3.5
1.00	598	1.8	1380	2.16	2.56
2.25	560	2.92	2590	1.5	4.03
4.00	548	3.8	3360	1.2	5.5
9.00	380	9.9	8.24	1.47	15.1
16.00	371	12.2	9.26	1.32	17.6
36.00	343	10.1	17700	1.05	54.8

Table 74: Summarised leaching characteristics of the granite tile

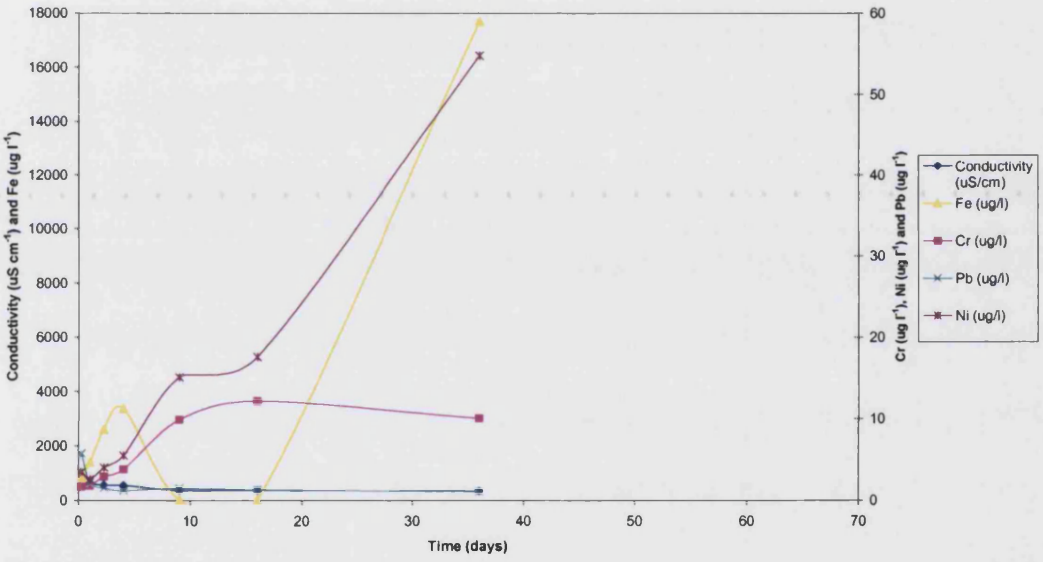

Figure 95: The conductivity and leaching data of the granite tiles

Again the information is presented in a cumulative manner where the diminishing trends of chromium, conductivity and lead can be observed more clearly. Additionally, the abrupt change in slope of the nickel and conductivity curves are evident, Figure 96.

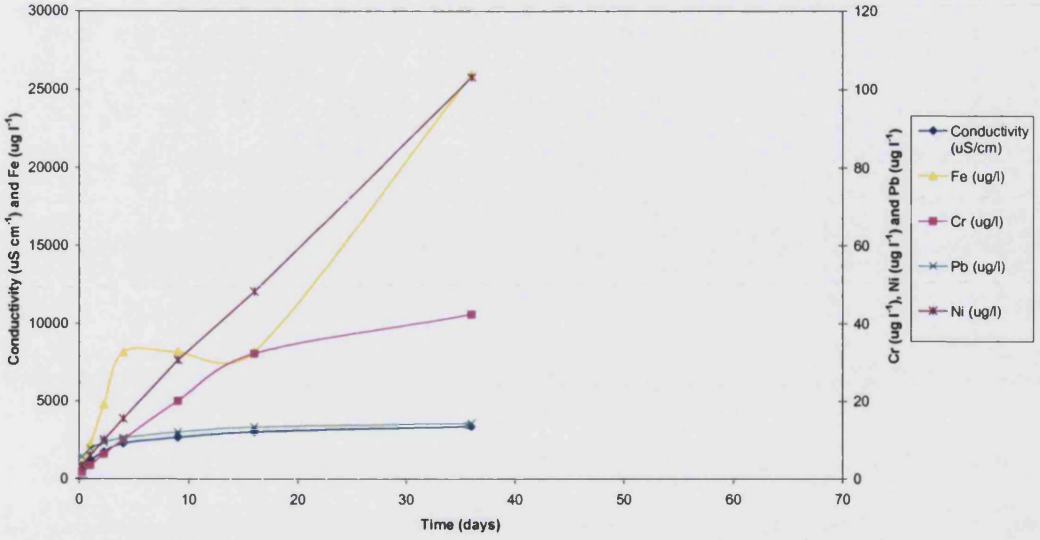

Figure 96: The cumulative conductivity and leachate data of the granite tiles

Finally these can be compared with the surface specific measured cumulative leaching data, which allows the eluate information to be related to sample shape and size, Figure 97.

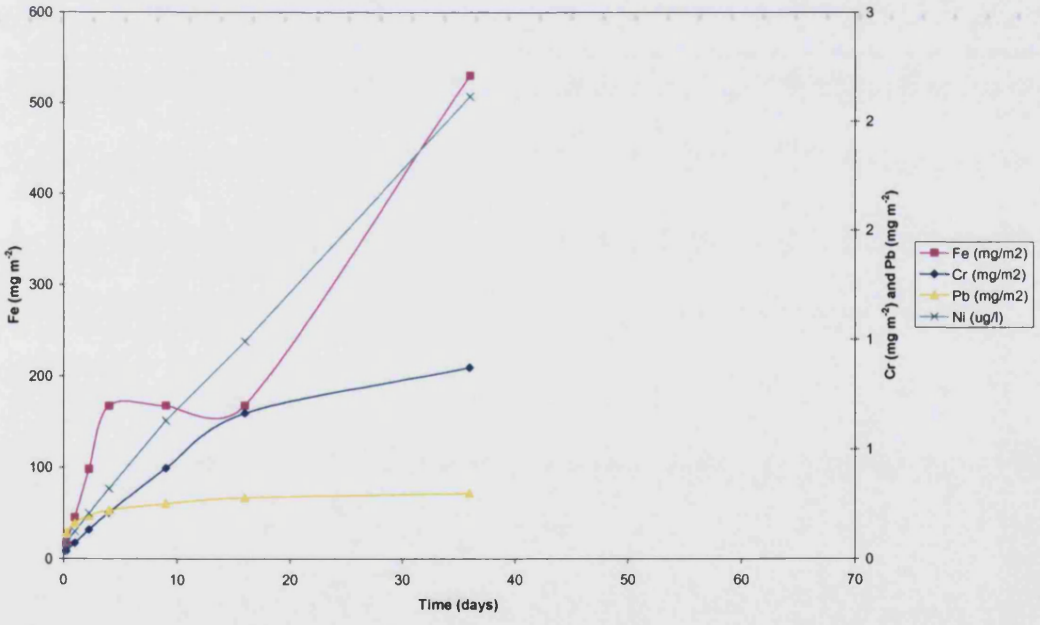

Figure 97: The cumulative surface specific leaching data of the granite tiles

In summary the surface specific leaching characteristics of the granite tile were comparable to those of 95TET and slightly greater than those of 93TET. The tile based on composition 96TET presents significantly higher surface specific leaching characteristics that correlate with the tiles' composition and waste materials origin.

9.4 Leaching Discussion

Comprehensive test data are presented that give a quantitative description of the leaching characteristics of cast plasma furnace tiles, generated from different materials, in comparision with a natural equivalent. The leaching test NEN 7345 supplied by Nederlands Normalisatie-Instituut (NNI), and recommended by the Water Research Council (WRC) is representative of the most pessimistic scenario, at pH 4, which accelerates the leaching processes. The materials were completely submerged in the acidified water and held in a total of 45 times their own volume of liquid, which is unlikely to occur naturally, and represented a total elapsed average rain fall period of approximately 0.6 years based on the foot print of the tiles analysed (130 x 130 mm) and an average annual UK rainfall of 850 mm yr^{-1}, [69].

The exact sample specific outcome of the calculation is given in Table 75. The difference in equivalent lapsed rainfall period arises from the different sample volumes employed, due to tile thickness variations arising from the manual casting, but identical sample cross-sectional areas for leaching. It is clear that the release of these materials is representative of a significant period of environmental field exposure, Table 75:

Sample Details	Eluant volume employed (cm^3)	Area of tile (cm^2)	Equivalent Rainfall (cm)	Equivalent exposure period (years)	Equivalent exposure period (months)
93 TET	12600	169	74.6	0.88	10.5
95 TET	6840	169	40.5	0.48	5.7
96 TET	11025	169	65.2	0.77	9.2

Table 75: Leaching test equivalent lapsed period of annual rainfall

The results are representative of a realistic tile product, based on the level of process control achieved within the scope of this project. This means that there is further room for improvements in terms of tile quality and product consistency, as it was difficult to address these issues further with the small demonstration reactor and the available operational time

windows. It is hoped that these improvements would give rise to further improvement in leaching characteristics. If the same tests had been undertaken in distilled water the degree of leaching would have been lower, as natural rainwater has a pH 6 – 7, [68, 70]. This is very encouraging as the waste tiles' leaching characteristics would be well within the current and future MACs thresholds, which have been used in this case as the basis for evaluating the eluate data, [70, 71].

The multiple eluate analyses have shown that the components that are more readily leached are Cl, SO_4, Cr, Fe, Ni, Cu, Zn and Pb. However, the large majority of these species are present at just above the LOD of the ICP-MS employed. The Water Supply (Water Quality) Regulations 1989, give prescribed concentrations/values for a total of 56 parameters, mainly as maximum acceptable concentrations (MAC's), [71]. Only four of the species / measurements; conductivity, chromium, iron and lead, show values approaching the MAC values, with iron having the most significant mass release. Additionally all of these elements show a correlation between bulk analysis and their leaching characteristics, so the overall elemental release will be limited as a function of time as the tiles' bulk compositional source will become exhausted. This is a favourable characteristic in the context of long-term ecological compatibility. The cationic release peaks of multiple species coincides with similar relative shifts in concentration and release probably occurs as a result of heterogeneity in the tiles, such as metallic inclusions, which have been observed. However, these results must be examined in light of the fact that the waste materials composition can vary significantly from that of natural materials, Table 66. The only cation that exceeds its MAC level is iron, however, this is not a significant problem because iron will shortly be de-regulated, Table 70. The performance of the waste tile materials has been demonstrated to match, and in some cases, exceed that of commercially available equivalents.

In December 1998 the Official Journal of the European Communities (OJ) presented Council Directive 98/83/EC [70] on the quality of water intended for human consumption, and this entered into European Law twenty days after publication. Member states have been given until 2002 for transposition into national law, and the first related official reports will cover the years 2002, 2003 and 2004. The objective of the directive is to 'protect human health from the adverse effects of any contamination of water intended for human consumption by ensuring that it is wholesome and clean'. The MAC levels assigned to

different parameters are set to change in specific instances, Table 70. Chromium will remain unchanged with a MAC level of 50 $\mu g\ l^{-1}$, whereas all of the other MAC levels have become more stringent, with the exception of conductivity and iron concentration. Iron is not regulated at all due to its ubiquitous occurrence within our environment. This means that in the majority of cases the tile leaching characteristics will be below all regulatory defined MAC levels and are therefore compatible with the material re-use requirements of the product. The conductivity (and pH) of poorly buffered water are very difficult to measure accurately due to the quality of atmospheric gases, e.g. SO_2 (g). High results are often seen without explanation; hence they should only be interpreted in an indicative manner.

The approach taken in analyzing the leaching characteristics of these materials has focused on treatment for re-use within the building industry, as opposed to treatment for disposal. This has led to comparison with maximum acceptable concentrations of the drinking water regulation [71] as opposed to the landfill directive [2]. In the context of this statement we can state the following:

(i). Comprehensive material leaching data has been acquired.

(ii). The leaching characteristics are accelerated due to the application of acidified water.

(iii). The leaching tests have simulated rainfall periods of months.

(iv). The tiles analysed have been representative of the plasma furnace product, however steps could be taken to improve product quality and hence leachability.

(v). The majority of leached species are below the MAC levels as defined by the water quality regulations. Only iron exceeds its current level over extended periods.

(vi). All species that exceed MAC levels (iron, lead and chromium) show long term trends that fall below the critical levels and/or these levels are set to change to permit the recorded release through the revision of regulations.

(vii). The tiles manufactured from the different waste materials exhibited similar leaching levels. Enhanced transient levels are noted for tiles made from municipal solid waste, which contain higher heavy metal concentrations. Figure 98 describes the relationship between material composition and leaching characteristics for all of the glass materials assessed. The leaching values for Cr and Pb were used in the construction of the graph.

(viii). Generally leaching characteristics are similar to those of commercially available equivalents.

The results show that plasma vitrification of waste material can produce shaped ceramic tiles that are ecologically viable, promoting reuse and safeguarding the environment at final disposal. The testing approach has been demonstrated to be sensitive enough to distinguish between the different material origins, through differences in leaching characteristics. This means that the plasma treated waste materials are suitable for re-use applications and processing constitutes a value added material treatment.

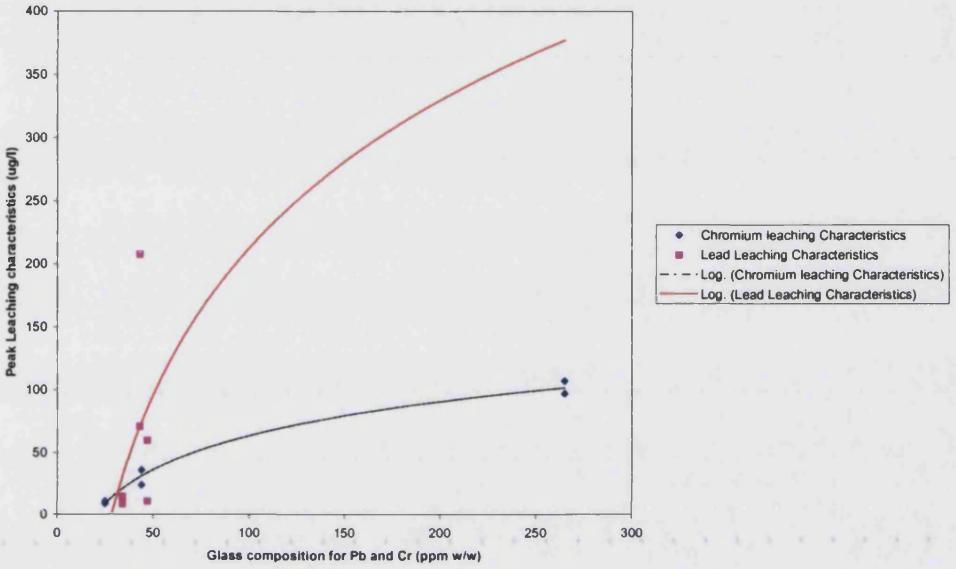

Figure 98: The relationship between tile composition and leaching characteristics, data for 93TET, 95TET and 96TET is included

These results also agree with the generic aims of the Landfill Directive 1999/31/EC as they under-pin the re-use of recovered materials as a means of potentially safeguarding valuable natural resources through a material treatment approach. The data supports a hierarchy of waste management approaches, leading firstly to re-use of different waste materials and secondly to both a reduction in waste volume and the stabilization of its chemical characteristics for ultimate disposal. The reported data fulfill the requirements of the Landfill Directives' Annex 2 and will allow the classification of the waste materials to be altered through processing without dilution, which will reduce costs, [3]. This reduces the requirement for landfill and will enable member states to meet their legislative commitments for the reduction of specific waste types going to landfill. The generic types of non-municipal wastes identified in the landfill directive are inert, non-hazardous and hazardous.

The leaching limits defined for the disposal of wastes, are orders of magnitude higher than those used for comparison within the context of the drinking water regulations. The Landfill Directives waste acceptance criteria are given in Table 76, based on a liquid to solids ratio of 10 l kg^{-1}. Note that there is both site and waste dependency.

Component	Inert Waste Landfill	Granulated Non-Hazardous Waste at Hazardous Waste Landfills***	Granulated Waste accepted at Hazardous Waste Landfills
As	0.5	2	25
Ba	20	100	300
Cd	0.04	1	5
Cr	0.5	10	70
Cu	2	50	100
Hg	0.01	0.2	2
Mo	0.5	10	30
Ni	0.4	10	40
Pb	0.5	10	50
Sb	0.06	0.7	5
Se	0.1	0.5	7
Zn	4	50	200
DOC*	500	800	320
TDS**	4000	60000	-

DOC = Dissolved Organic Carbon, **TDS = Total Dissolved Solids,
*** Also applies to Granulated Hazardous Waste at Non-Hazardous Waste Landfill

Table 76: Waste Acceptance Criteria Expressed as Leaching Limit Values in mg kg^{-1} [3]

The leaching data presented were acquired from the glassy materials. This was purposely undertaken to verify the adequacy of glassy matrix, as a barrier to leaching. It was considered to be the most important factor in quantifying the ecological performance of any glass-ceramic material produced from the plasma furnace glasses. The approach was considered to be a worst case evaluation, as the literature indicates that semi-crystalline materials have better leaching characteristics, which were accounted for as a result of their closer packed structures and the tendency for the contaminating cations to reside within the glassy matrix, [5, 26, 47, 72].

10 Tile Mechanical Properties

Ceramics are one of the major classes of engineering materials. Monolithic ceramic materials are used because they offer a highly attractive combination of properties including high compressive strength, stiffness and hardness, low density and resistance to oxidation, corrosion, wear and elevated temperature degradation. However, these desirable properties are frequently off-set, with respect to engineering applications, because of their inherent brittleness. Short-comings in the critical strength criteria (fracture toughness and flaw size) and large fluctuations in fracture strength lead to low service reliability and associated catastrophic failure due to the presence of flaws of a size not detectable by conventional non-destructive testing techniques. In summary the advantages of a ceramic are often displaced by their brittleness, in mechanical load bearing applications.

The strength and reliability of a ceramic may be increased in three ways. Firstly decreasing the size of intrinsic defects (flaws), an approach dependent on processing improvements and an essential part of this work. Secondly, it is possible to increase fracture toughness making the material less likely to fail in a brittle manner, leading to predictable and defined modes of failure. Large increases in strength, and moderate increases in toughness, can be achieved by modifications of micro-structural features such as porosity, grain shape and size. Here, crystallization has been used to improve material properties through the introduction of traditional toughening mechanisms. Finally it is possible to engineer compressive stresses during processing, these stresses must be overcome before tensile loading occurs.

In monolithic polycrystalline ceramics the main mechanisms of energy dissipation are friction sliding, crack deflection/blunting and grain pull out at the crack faces [60, 73]. All of these mechanisms result in energy absorption and dissipation, and improved fracture toughness. The effect on the fracture strength (σ_f) of increasing the fracture toughness (K_{IC}) and decreasing the critical flaw size (C_{crit}) can be seen from the relationship, [74]:

$$\sigma_f \propto \frac{K_{IC}}{\sqrt{C_{crit}}}$$

Equation 52

10.1 Mechanical Testing and Specimen Preparation Procedure

To define quantitatively the unique features of this ceramic system and the statistical variation of failure stress, Weibull analysis was used. This analysis is based on empirical reasoning and not theoretical hypothesis. It predicts the survival probabilities at a particular stress level, sample size and stress distribution. In using Weibull statistics it is assumed that the 'weakest link' model is valid for the system and that the flaws are non-interacting, [60].

Mechanical testing was done in accordance with ASTM C1161-94 in four-point bend testing mode using an Instron 1122. Here, the material was assumed to be isotropic and homogeneous, that the modulus of elasticity in tension and compression were the same and that the material was linear elastic. The testing was undertaken using a fully articulated four point loading fixture, to ensure that the parallelism requirements were met. The configuration used a 40 mm outer span and a 20 mm loading inner span. The specimens had the following average dimensions: 4.0 mm width, 3.0 mm depth and 45 mm length. The specimens were prepared and polished in the glassy state, they were then crystallized by heat treatment to round off any sharp micro-structural flaws. This approach was taken to give a realistic assessment of the 'as-fabricated' mechanical properties of the material. The testing fixtures can be seen in the following image, Figure 99.

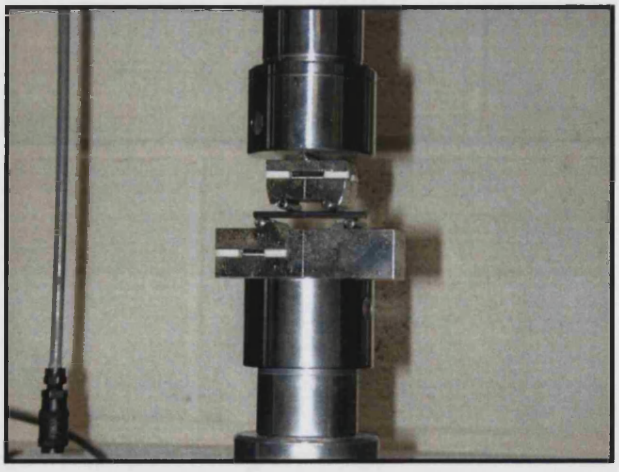

Figure 99: Fully articulated four point mechanical loading fixture in use

The specimens were mechanically prepared as follows. A glass tile, nominally 130 mm square by 10-15 mm thick, was selected from tile material 96TET2, Section 8. A Jones & Shipman surface grinder/slitting machine was used to prepare the specimens. Blanks (i.e.

bars larger than required) were prepared by cutting using a diamond impregnated wheel. These were then surface ground, using a water-cooled 400 grit diamond impregnated wheel with the bars fixed to a flat metal plate by means of a commercially available adhesive. Stock removal rate was approximately 0.01 mm per pass for grinding, and 0.005 mm per pass for final finishing. The long edges of the bars were chamfered using a diamond impregnated lapping wheel, the extent of chamfering employed removed the largest edge flaws. Polishing, restricted to the tensile face, was performed using a commercially available diamond polishing paste on a paper lap. The final polish used a 3 μm diamond paste, and was taken to the point of removing all machining marks. This left only the inherent porosity of the material visible on the surface. In total, 34 bars were prepared, which meets the minimum statistical requirement of 30 samples for the application of Weibull statistics with a singular flaw population [60]. The samples were crystallized in accordance with optimised outcome of the crystallisation study, Section 8. Mechanical testing was undertaken with the as-crystallised tensile surfaces.

The material surface characteristics were analysed using an optical microscope fitted with a JVC KY-F55BE high-resolution 3-CCD colour video camera. The microscope system was driven using the AcQuis Pro image acquisition system of Syncroscopy, allowing the capture of high resolution (1500 x 1100 pixel) images. To overcome the limitation of optical microscopy, namely limited depth of field and field of view, the Auto-Montage software system was used. Here a stepping motor controls the fine focus knob of the microscope capturing a large number of images at different focal depths. The high-resolution data from each image is combined, using pre-defined algorithms, giving a singular focused image. The calibrated motion of the stepping motor was also used to generate a three dimensional image of the material's surface, Figure 100.

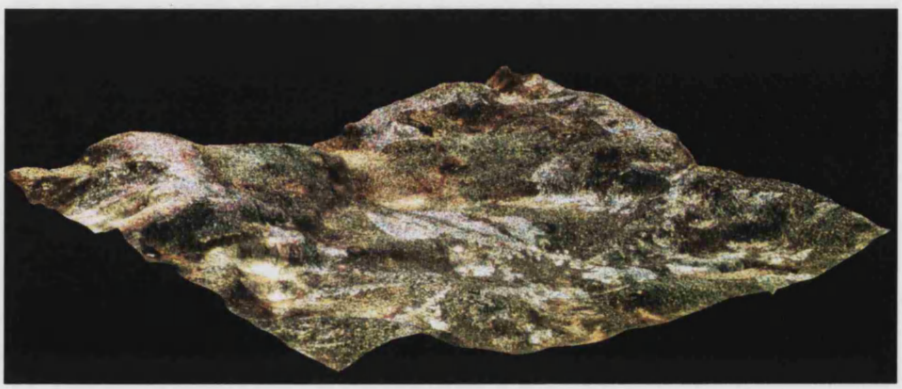

Figure 100: The tensile face surface topography of flexural test specimens (400 x 400 μm).

Here the z stepping motor was used to determine that the maximum vertical point-to-point displacement; it was determined to have an arithmetic average of 20.2 μm, based on four line scans, each of 400 μm in length. This defined the inherent feature of the tensile surface.

10.2 Mechanical Testing Results

The results of the flexural strength testing are presented in Table 77, which show the flexural strength of the specimens in order of increasing strength. The crosshead speed was 0.5 mm min^{-1}, with a chart speed of 20 mm min^{-1} and a full-scale load setting of 10 kgf (98 N). The load voltage was obtained directly from the testing machine and is relative to a 10 V full-scale deflection.

Weibull Sample Number (j)	Flexural Strength (MPa)	Small N Basis Probability of Survival $P_s(V_0)$
1	47.0	0.990
2	49.1	0.950
3	49.8	0.911
4	50.0	0.871
5	50.4	0.832
6	50.9	0.792
7	52.1	0.752
8	52.9	0.713
9	53.4	0.673
10	53.5	0.634
11	54.7	0.594
12	55.4	0.554
13	55.4	0.515
14	55.5	0.475
15	55.9	0.436
16	56.5	0.396
17	57.9	0.356
18	58.2	0.317
19	59.6	0.277
20	60.9	0.238
21	61.2	0.198
22	64.1	0.158
23	64.2	0.119
24	64.8	0.079
25	67.0	0.040

Table 77: Flexural test results for the glass-ceramic material samples

All the samples tested reacted in a similar manner; the rate of load increase increased with cross-head movement up to the point of failure which occurred in a catastrophic and brittle manner when the two halves of each sample physically separated. Figure 101 shows a typical stress – strain curve.

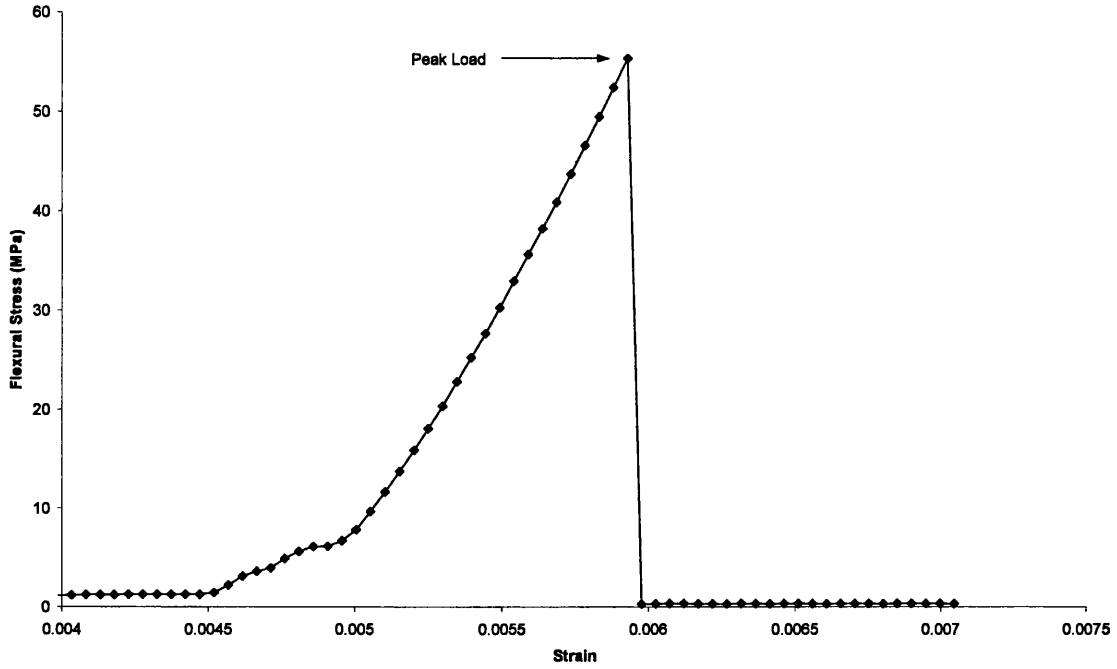

Figure 101: Applied flexural stress versus calculated strain for sample C26

The flexural strengths of the samples was determined using Equation 52 derived from simple beam theory, [60].

$$S = \frac{3PL'}{4bd'^2}$$

Equation 52

Where: P = Peak Load (N) b = Specimen width (m)

L' = Specimen inner span (m) d' = specimen thickness (m)

The samples were ranked in order of strength from the weakest to the strongest, Table 77. For small number of samples, each of volume 'V_o', the probability of survival is given by.

$$P_{sj}(V_o) = 1 - \left(\frac{j - \frac{3}{4}}{N_o + \frac{1}{4}} \right)$$

Equation 53

Where: j = rank number

N_o = total number of samples

To use Weibull analysis, similar flaw distributions must be present in all specimens. This has been assured through the use of a consistent means of material manufacture and sample preparation such that a consistent surface finish and bulk material properties should arise. The basis of the Weibull methodology is that the probability of a sample of volume V_o surviving a stress σ is $P_s(V_o)$:

$$P_s(V_o) = \exp\left(-\left(\frac{\sigma^* - \sigma_u}{\sigma_0}\right)^m\right)$$

Equation 54

Where: σ^* = externally applied engineering stress (Pa)

σ_u = the stress below which fracture is assumed to have zero probability for ceramics (Pa), this is 0 Pa.

σ_0 = a constant, the characteristic strength (Pa)

m = a constant, the Weibull modulus

Hence, for a ceramic system this expression reduces to Equation 55 as $\sigma_u = 0$:

$$P_s(V_o) = \exp\left(-\left(\frac{\sigma^*}{\sigma_0}\right)^m\right)$$

Equation 55

By taking natural logarithms of both side of the equation we get:

$$\ln\left(\frac{1}{P_s(V_o)}\right) = \left(\frac{\sigma^*}{\sigma_0}\right)^m$$

Equation 56

Next, a Weibull plot was produced to give the equation of a straight line by taking natural logarithms of both sides of the equation for a second time. This plot was used to determine the Weibull modulus 'm' and characteristic strength 'σ_0'.

$$\ln.\ln\left(\frac{1}{P_{sj}(V_o)}\right) = m\ln\sigma^* - m\ln\sigma_o$$

Equation 57

The characteristic strength has no physical significance, however the Weibull modulus is a measure of the degree of variability of the results, i.e. the higher the value of '*m*' the less variation in strength is observed. Ideally we would require a high 'σ_0' and a high 'm' indicating a high strength and a low distribution of strength. The Weibull plot is presented in Figure 102.

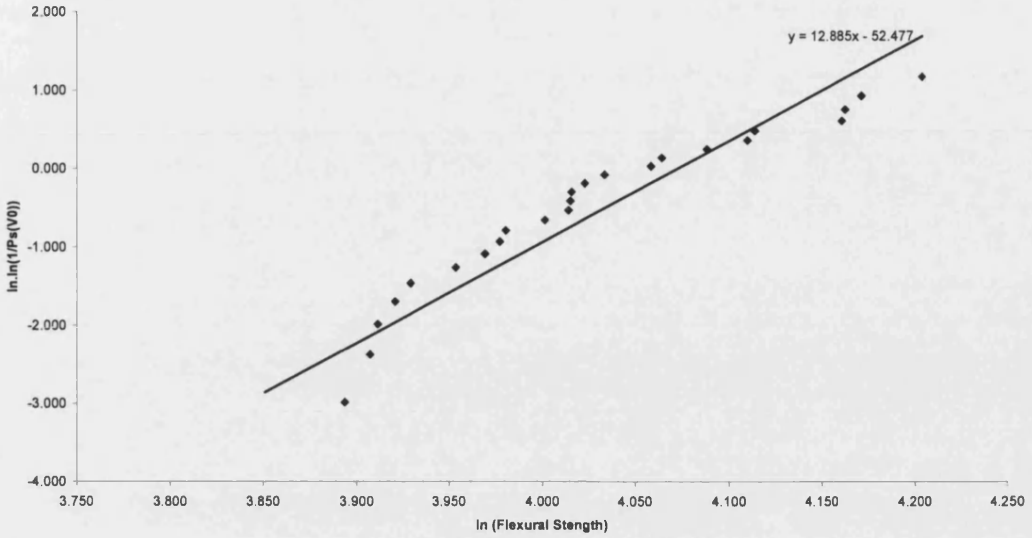

Figure 102: Weibull plot of the glass-ceramic samples' flexural test data

Linear regression determined the Weibull modulus of the material to be 12.9, and the characteristic strength, i.e. the strength at which $P_s(V_o) = 0.37$, was found to be 58.7 MPa. All of the data were used in the determination of these values. It is possible that there is a kink in the Weibull plot where there is a transition from surface to volume critical failure, [60], but this kink is not pronounced enough to justify segregated interpretation of the data. The data is presented more traditionally in Figure 103 as a probability of survival versus flexural strength graph.

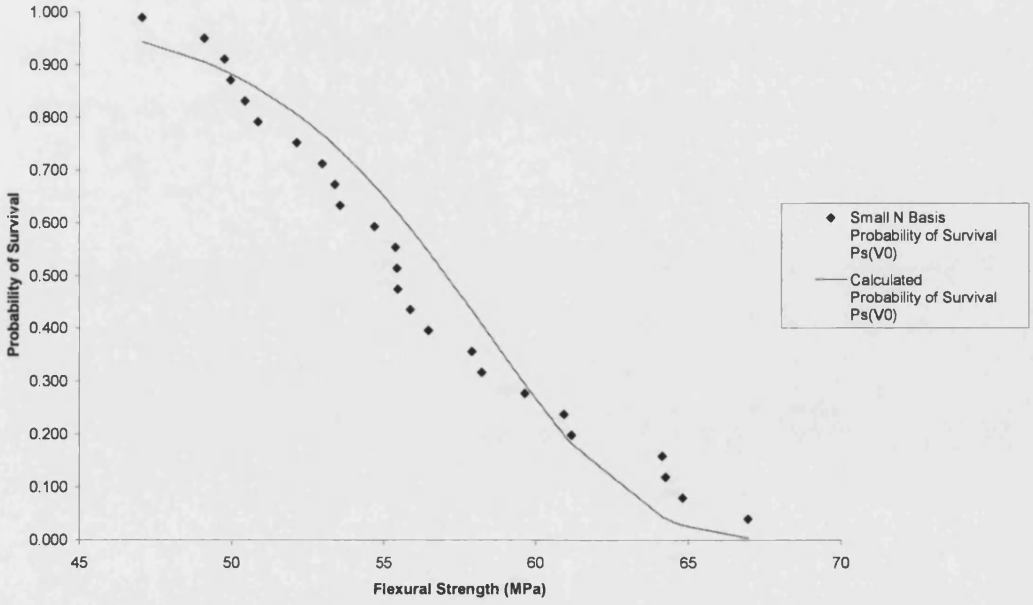

Figure 103: Traditional Weibull plot of flexural test data for the glass-ceramic

Typical values for the 'flexural strength' associated with a naturally occurring monolithic ceramic are 23 MPa for granite and 20 MPa for limestone. Similarly the Weibull modulus of borosilicate glass is typically 10 and the flexural strength is 55 MPa (the Weibull modulus was not available for granite or limestone) [60, 74]. This means that the results obtained are consistent with a reasonably small and uniform flaw size, or increased material fracture toughness. Of all the samples tested 55% had a flexural strength >55 MPa and 25% exceeded 60 MPa. The results are successful in the context of producing an engineering material, for construction applications, from a waste material. To indicate the rate of change of survival probability with applied stress the previous traditional graphical representation can be differentiated in accordance with Equation 58 and Figure 104.

$$\frac{d(P_s V_o)}{d\sigma} = -m\frac{\sigma^{m-1}}{\sigma_0^m}\exp\left(-\left(\frac{\sigma^*}{\sigma_0}\right)^m\right)$$

Equation 58

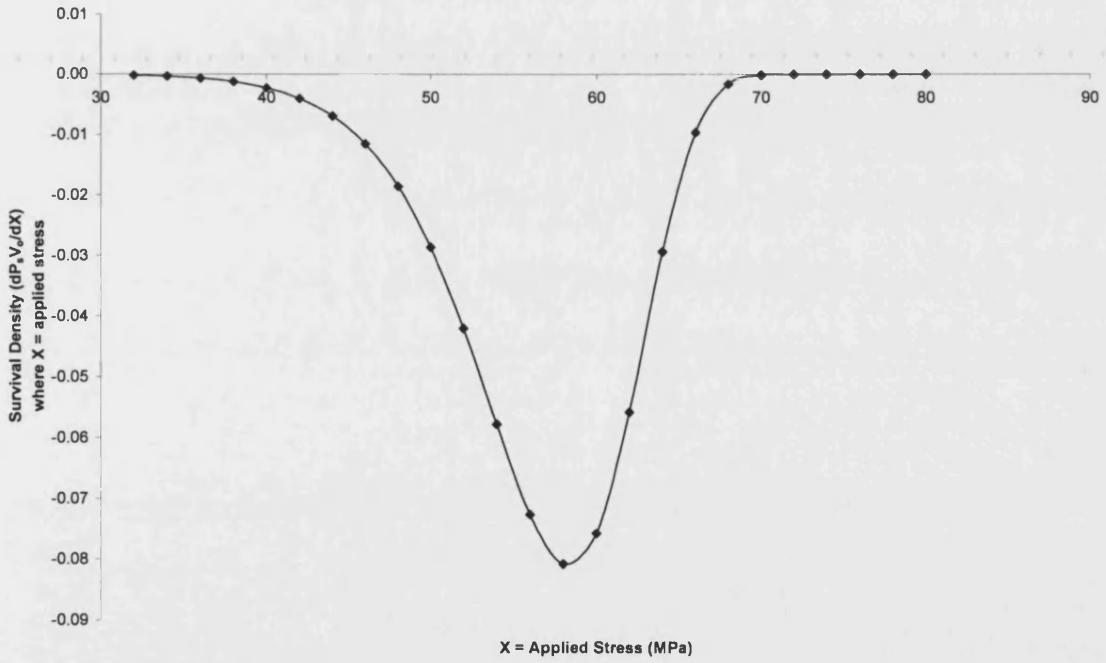

Figure 104: Survival density versus applied stress for the flexural strength testing

In addition to the statistical nature of the strength of the ceramic produced there is also a volume dependency. Consider a large volume 'V' that is sectioned into a number 'n' of smaller samples of volume 'V_0'. Hence $V = n\ V_0$. The probability of all n samples surviving a stress σ is equal to $[P_s(V_0)]^n$, [60].

Hence it follows that:

$$P_s(V) = P_s(nV_o) = [P(V_o)]^n$$

Equation 59

since $n = V/V_0$ we can write

$$P_s(V) = [P(V_o)]^{\frac{V}{V_o}}$$

Therefore

$$\ln[P_s(V)] = \frac{V}{V_o}\ln[P(V_o)]$$

$$P_s(V) = \exp\left(\frac{V}{V_o}\ln(P(V_o))\right)$$

Equation 60

Substituting in Equation 55 we can write.

$$P_s(V) = \exp\left\{-\frac{V}{V_0}\left(\frac{\sigma^*}{\sigma_o}\right)^m\right\}$$

Equation 61

Therefore for equal probabilities of survival.

$$\frac{V_1}{V_2} = \left(\frac{\sigma_2}{\sigma_1}\right)^m$$

Equation 62

Hence as the volume goes up the probability of survival at a defined stress level decreases, which is directly attributed to an increased probability of finding a flaw of critical dimension. This expression and the determined material constants can be used to evaluate survival probability as a function of stress level, loading conditions and component size.

As the arithmetical average volume of the 'as-manufactured' plasma furnace tiles are 211.25 cm^3 and the average volume of the flexural test samples are 0.54 cm^3 we can write the following.

$$391.2 = \left(\frac{\sigma_{flexural\ sample}}{\sigma_{tile}} \right)^{12.9}$$

Therefore as the four point flexural test samples, exposed to an applied stress of 58.7 MPa, exhibited a failure probability of 37% we can say that the same survival probability will be associated with an applied stress of 37.0 MPa for the as-cast and heat treated plasma furnace tiles.

In addition to testing the glass-ceramic, five glassy samples were tested in a similar manner for comparative purposes. Using linear regression, the Weibull modulus of the samples was calculated to be 8.23, and the corresponding characteristic strength was found to be <55 MPa, some very weak samples (flexural strength < 5MPa) were not included in this assessment. Very small sample numbers can lead to gross inaccuracies when using Weibull statistics through disproportionate representation. This indicates that heat treatment has given rise to an increase in flexural strength and a lowering of the distribution of flexural strength values for the glass-ceramic tile product. The Weibull plot is presented in Figure 105.

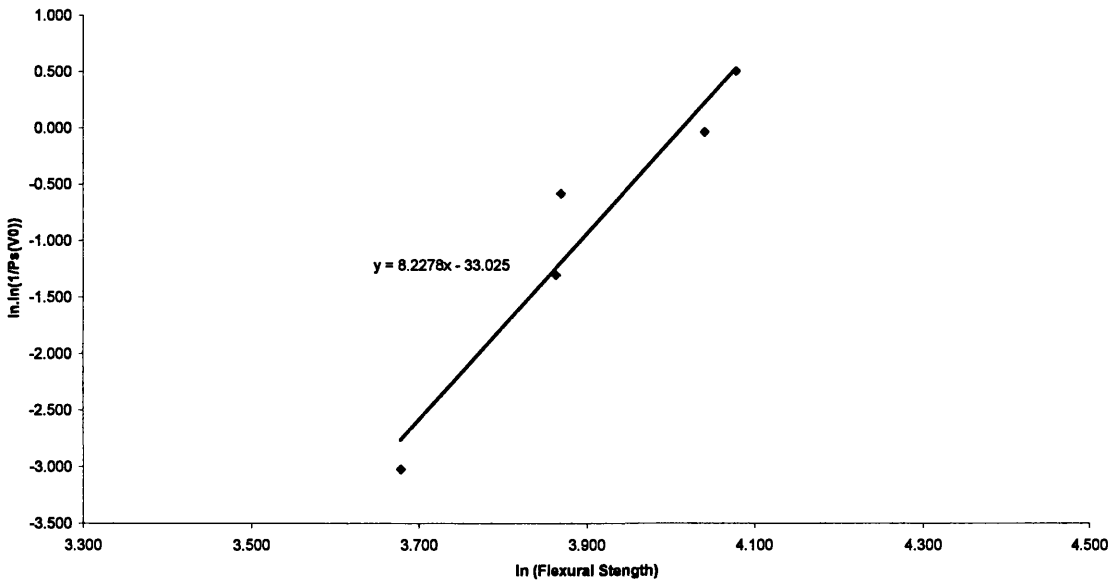

Figure 105: Weibull plot of flexural test data for the glass samples

The procedures used for the four-point flexural strength testing were designed to ensure reproducibility of the testing methods thereby ensuring that any variations in results were caused by variations in the material. The number of measurements used to assess the flexural strength of the glass and glass-ceramic materials were different because of the availability of the materials. To assess whether there was a difference between the flexural strength data sets, and its level of significance, the sample means were considered in relation to a function of the sample standard deviations using a "Students" t test, assuming that the data had a Gaussian distribution about a mean. A small value of t indicates considerable overlap of the distribution's data, and a larger t indicates considerable separation of the data. For the hypothetical data sets 'x' and 'w', t can be calculated using Equation 63, [91].

$$t = \left(\bar{w} - \bar{x}\right)\sqrt{\frac{n''_w\, n''_x \left(n''_w + n''_x - 2\right)}{\left(n''_w + n''_x\right)\left(n''_w\, s^{d2}_w + n''_x\, s^{d2}_x\right)}}$$

Equation 63

Where for data sets x or w:

n'' = the number of measurements in data set

s^d = the sample standard deviation of data set (using Bessel's correction)

$\bar{x}$ = the sample mean of data set

The derived value of t for the data in Table 78 equals 2.85 and indicates that there is a 'probable to significant' difference between the data sets, at a 95% confidence level (based on the degrees of freedom $n_x + n_w - 2 = 29$). So a definite improvement in flexural strength has been produced as a result of thermal processing.

Sample Statistical Data	Semi Crystalline Sample Population data	Glassy Sample Population data
Arithmetic Mean (MPa)	56.0	42.6
Standard deviation (MPa)	5.4	19.8
Number of measurement in the sample (n_x and n_w)	25.0	6.0
$n_x + n_w - 2$	29.0	29.0

Table 78: Statistical analysis of the flexural strength data

The conclusion drawn from the data is that the semi-crystalline material distribution is less dispersed, as indicated by the ± 5.4 MPa standard deviation of the sample. This is in contrast with the ±19.8 MPa standard deviation from the glassy samples.

To determine the elastic modulus values for both the glass and glass-ceramic material products, four-point-bend samples were fitted with strain gauges mounted longitudinally on the tensile face of the flexural test samples. The output voltage of the strain gauges, were acquired from the testing machine at a frequency of 2 Hz, and stored as comma separated variable files; the full-scale deflection of the device was 10 V. The output voltage of the strain gauges were converted to engineering strain data using Equation 64.

$$\varepsilon = \frac{2V_{output}}{G\left(500 - V_{output}\right)}$$

Equation 64

Where: ε = Strain

V_{out} = Output voltage

G = Gauge factor

The equation is only applicable for a gain of 200 and represents the structure and response a quarter Wheatstone bridge gauge. The gauge factor is dependent upon the materials of construction, mechanical construction and design of the strain gauge. During the experimentation a Measurements Group gauge, type EA-06-06-2AK-120, was employed with a gauge factor of 1.995 ± 0.5. The raw data were converted into engineering stress and strain and re-plotted to obtain an elastic modulus value of 80 GPa for the glass-ceramic material. The data is presented graphically, for Sample C25 (a glass-ceramic sample), in Figure 106.

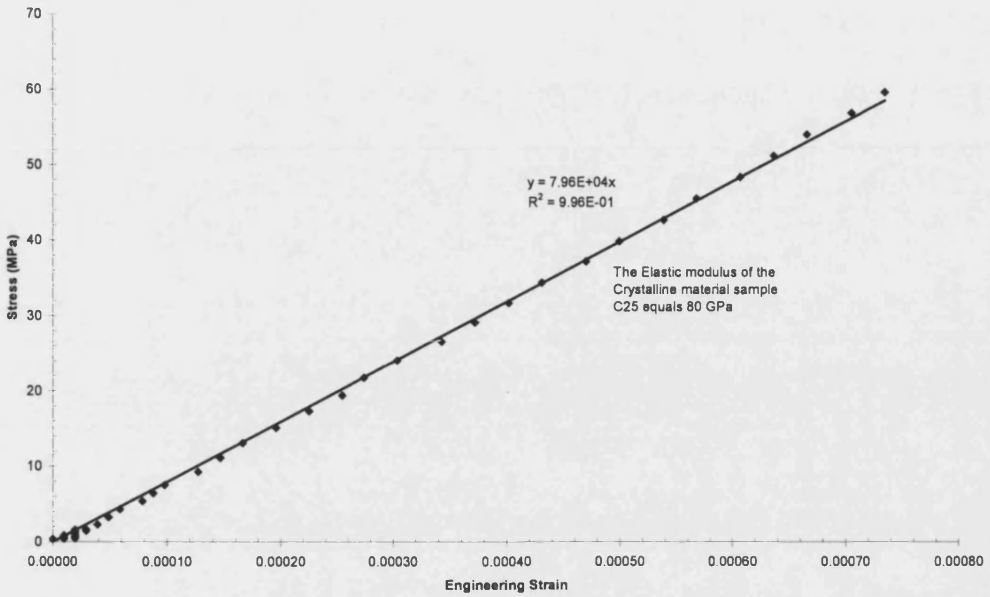

Figure 106: Flexural test stress versus strain characteristics of sample C25

The data are presented graphically, for Sample G7 (a glassy sample), in Figure 107. The results also show an elastic modulus value of 80 GPa for the glassy material product. These results are consistent with the conclusion and material property values quoted in the literature review [4, 15, 34].

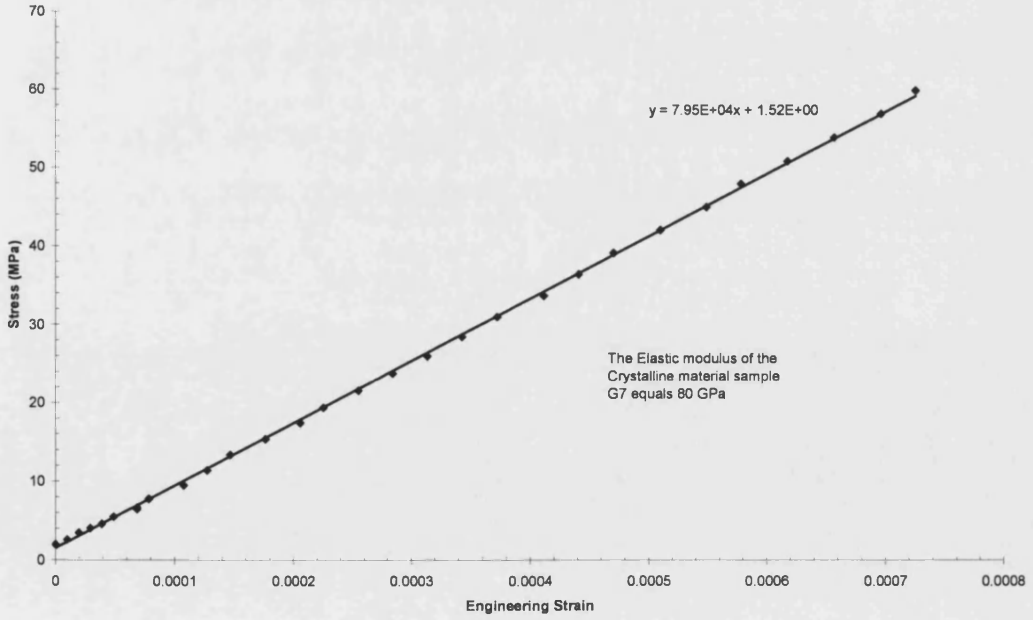

Figure 107: Flexural test stress versus strain characteristics of sample G7

The similarity of the elastic modulus values determined from both the glass and glass-ceramic materials, is expected and predicted, as the property is determined by the strength and directionality, of the atomic and molecular bonds and their frequency per unit volume. In contrast, strength properties and dependent on the microstructure and its processing route, points of high stress intensity and mechanisms of stress dissipation. Overall, the mechanical properties and micro-structural consistency of the product has been improved by the traditional two-stage glass-ceramic heat treatment methodology. The resulting properties equal those of similar virgin engineering materials such as borosilicate glasses.

11 Conclusions

The objective of this research, namely to process waste materials into economically viable, glass-ceramic tiles, with mechanical and ecological properties equivalent to those of commercial granite products has been achieved. It is hoped that this justifies the acceptance of processed wastes for use in tile applications.

(i). Overall, four-silicate mineral wastes were thermally processed in a plasma furnace, using cold skull containment, and successfully produced cast tiles.

(ii). Laboratory characterization of the prepared material confirmed that similar physico-mechanical properties could be obtained from different wastes, when processed similarly, in terms of normalized bulk oxide composition and phase diagram position.

(iii). The technology was capable of handling a wide range of waste materials in a similar manner and was verified as being robust and generic.

(iv). The outcome of the technological assessment determined that the cost of the waste products was significantly lower than that of existing commercial materials.

(v). Finally, the material processing costs offer economic advantage over current waste disposal routes when implemented on a large enough scale.

The scientific methodology adopted was different to that of the prior research as scientific principles were used to enable control within the boundaries imposed by the variability and complexity of the waste streams investigated. Process control and material characteristics were balanced to extend the scope of understanding within the subject area. During the laboratory trials, sample 96TET-2, produced from C-MSW, was chosen for the plasma experimentation due to its high density, hardness and fracture toughness and its low coefficient of linear thermal expansion. These properties made it the choice for the detailed crystallisation study.

Analytical ambiguities, such as inconsistent preparation and composition heterogeneities associated with the erosion of refractory containment materials were eliminated through the use of cold skull melting technology. This allowed a material baseline to be acquired and maintained throughout the different phases of the research. This manifested itself as similarities in the physical transition temperatures of high quality glasses produced from

the different wastes. This improved upon the techniques used in previous studies and was proven to be a valid technical solution.

Constant, non-volatile, bulk oxide compositions were retained across the plasma furnace. This was complemented by the use of an upper melt surface plasma heat source, which allowed the temperature of the molten glass to be varied quickly so that the required thermal profile, for glass production, was achieved. This minimized both material property and preparation uncertainties.

The bulk of the cited literature makes no reference to the shape or size of the materials under analysis, but here a uniform crystalline microstructure was obtained throughout the product's large cross-section. This was successfully addressed in the context of product formation and technological scale up. A nucleating agent, TiO_2, was used to give consistent microstructures on crystallisation and developed the basis of a robust and generic technology. Lineal intercept analysis of the microstructure showed that the optimum heat treatment cycle for the production of fine scale crystalline materials, for tiles based on C-MSW comprised of the following stages: nucleation at 650 °C for 18 minutes and crystallisation for 930 °C for 48 minutes, all intermediate temperature ramps were held constant at 6 °C min^{-1}.

Flexural strength test data indicate that there was an improvement of 22% in the flexural strength of the waste material produced from C-MSW upon crystallization with the optimum heat treatment cycle, to 67 MPa and a reduction in the variability of the material property, by a factor of 3.5. Statistical analysis of the same data determined that there was a probable distinction between the data distributions, which was consistent with the increase in Weibull modulus, from 8.2 to 12.9, seen for the semi-crystalline product, with respect to the glass precursor. The data for the semi-crystalline material distribution was less dispersed and the level of variation was equivalent to that associated with commercially available materials, e.g. borosilicate glass. This type of statistical analysis has not been applied to products of waste material systems in this manner before.

Ecological compatibility of these products, for all four wastes, was confirmed through the quantitative evaluation of their leaching characteristics. Whole tile products were tested

under acidic conditions and their toxic release characteristics related back to their physical dimensions. Indian granite was used to give a commercial basis for relative ecological performance characteristics. The waste tiles performed to an equivalent standard and the leaching experimentation confirmed that:

(i). The results showed that the plasma vitrification of wastes produced shaped ceramic tiles that were ecologically viable.

(ii). This advocates the re-use of recovered materials as a means of potentially safeguarding valuable natural resources through material treatment, reducing the waste's volume and stabilizing its chemical characteristics for ultimate disposal.

(iii). The leaching test was demonstrated to be sensitive enough to distinguish between the different material origins, through differences in leaching characteristics, which correlated with the bulk compositions of the glassy materials.

(iv). The adequacy of glassy matrix as a diffusion barrier for leaching was verified, which was considered to be the most important factor in quantifying the ecological performance of any glass-ceramic material produced from the plasma furnace glasses. The retained heavy metal species displayed low leachability, of the order of $\mu g\ l^{-1}$.

The glass-ceramic tiles (130 x 130 x 10 mm) produced from waste ashes were physically homogeneous and had flexural strengths of up to 70 MPa and Young's moduli of 80 GPa, a Weibull modulus of 12.9 and cost £11.8 m^{-2} to produce.

The tiles had an albite $Na(AlSi_3O_8)$ – anorthite $Ca(Al_2Si_2O_8)$ based microstructure. The waste materials were blended into the anorthite phase field, Figure 43, and the crystalline phase was successfully grown. The ternary feldspar system of albite-anorthite-orthoclase shows homogeneous solid solutions over vast compositional ranges at high temperatures, [63]. These solid solutions become unstable at lower temperatures and the combination of crystalline phases was expected and observed within the microstructure. This type of transformation occurs geologically, and was reproduced during the experimentation. The acicular crystallites morphology observed in the tiles' micro-structural is consistent with the 'exsolution' material transformation, resulting from an instability of solid solutions at lower temperatures. The micro-structural development of the material was systematically mapped and the result used to define a heat treatment that gave fine and uniform product

material microstructure. This was responsible for the improved material properties and verified the economic and technological viability of the process and product.

This work agrees with the majority of cited review papers in the field of plasma waste processing technology, but it superimposes the materials technology underpinning success; material composition, thermal and physical processing, microstructure and physical size have been controlled simultaneously to enhance material performance. The tiles' performance has been quantitatively defined.

12 Further Work

The plasma technology was reliable, and it is hoped that the growing voice of acceptance will mean that the research will be incorporated into further industrial waste management initiatives, [90].

The feed materials examined in this work were wastes and had obvious levels of variability. Appropriate sampling, milling, blending and process control were used to compensate for this uncertainty. However, this type of activity would need to occur continuously to ensure successfully commercialization of the industrial equivalent of the process. The first stage in addressing this issue is to quantify the variation observed in the waste materials. It is suggested that this should occur over the period of one year with the different seasons being examined separately, at different locations. This data would define the online analysis requirements, e.g. XRF, and the appropriate levels of blending and mixing pre-treatment required for the wastes.

Because of the broad scope of the waste treatment subject it is felt that the laboratory work should be extended, so that statistically meaningful sample numbers are prepared and analysed. To improve the relevance of the laboratory work cold skull melting should be incorporated into this phase of the work. Cold skull button melters have been configured to achieve this kind of result, but not in the context of a ceramic, and would simulate the conditions seen within the larger plasma furnace. Additionally, the material analysis techniques employed should be direct and give an accurate measure of the materials' mechanical and physical properties, as the homogeneity assumption associated with the indirect techniques are not always acquired, which leads to inaccuracy.

The larger-scale work produced encouraging results and the technology was determined to be scalable. However the defining assumptions used in the economic assessment produce inaccuracies. Therefore, the next stage of research should be to operate the furnace over longer campaign periods, possibly 48 hours in duration. This will necessitate the requirement for the level of ancillary equipment, before and after the plasma furnace, to be upgraded. Particular attention should be given to the casting process, as this determines the dimensional uniformity of the final product. The larger numbers of tiles produced from this scale of campaign should be employed in field trials as this will quickly highlight any of the product's inadequacies and change the public's perception of this kind of material. If these trials were successful the product's application could broaden into areas where the process could be used to encapsulate more hazardous materials.

Finally the semi-crystalline materials leaching characteristics should be examined in the same way that the glassy materials were in this research. This direct analysis will be required prior to commercial release of the material into the general environment. This should be accompanied by further mechanical testing to see if there are any variations in strength, modulus and property dispersion over longer furnace operating campaigns. At this stage it is felt that the product evaluation should become more application specific, this could take the form of a wear resistance or chemical durability study.

Moving beyond systematic extensions of the work presented, to meet both practical and economic performance requirements for the product, the following ideas should be pursued to extend technological understanding and application of waste streams:

1. The development of tiles with through body colours, produced by either transition oxide material additions or control of redox potential. This excludes the application of topographic colouring technologies that have already been exploited e.g. glazing. Here a fine balance of colour intensity and environmental performance will be required.
2. The same material systems should be processed using controlled cooling heat treatment methods. Here, both nucleation and growth should be achieved simultaneously, i.e. the petrurgic methodology. This will eliminate several process stages and positively influence the processing economics, as a number of energy intensive heating cycles will be eliminated.

3. The vitrified product glasses should be crushed and sintered to form glass-ceramic products. Here, the fine particles will be conventionally pressed and sintered to form a solid. The large surface area of the particulates will be used to promote heterogeneous nucleation and growth. The sintering temperatures employed will lie within the crystal growth temperature region, allowing nucleation and growth to occur. This will allow product dimensions, beyond the heat transfer limits identified here, to be achieved without the requirement for higher temperature processing and the addition of nucleating agents. However, the overall energy balance criteria, i.e. the saving of thermal processing energy at the expense of mechanical grinding energy should be quantified first.

13 References

1. Foster, M. (2000). *The Landfill Directive: How will the UK Meet the Challenge*, [www] http://www.environmental-expert.com, European Environmental Law Review, Jan 2000.
2. Council Directive 1999/31/EC, *On the Landfill of Waste*, Official Journal of the European Communities, 182, pp 1 - 18.
3. Commission of the European Communities, (2002). *Proposal for a Council Directive Establishing Criteria and Procedures for the Acceptance of the Waste at Landfills Pursuant to Article 16 and Annex II of Directive 1999/31/EC on the Landfill of Waste*. [www] http://www.defra web address, COM(2002 512 final).
4. Cortez, R. (1996). *Laboratory Scale Thermal Plasma Arc Vitrification Studies of Heavy Metal-Laden Waste*. University of lllnois, Urbana lllnois. Air & Waste Management Association. Journal of the Air & Waste Management Association, 46, p1075 – 1080.
5. TSK. (1995). *Melting and Crystallisation Technology*. Japan. Tsukishima Kikai Co., Ltd, Technical Reference.
6. Takeshi, Y. (1992). *Glass Crystallisation of Sludge Incinerated Ash*. Tsukishima Kikai Co., Ltd, Tokyo, Japan. Environmental & Sanitary Engineering Research. 6, No 3, p 62-67.
7. Sakai, S., Sawall, S.E., Chandler, A.J,. Eighmy, T.T., Kosson, D.S., Vehlow, J. (1996). *World Trends in Municipal Solid Waste Management*. Kyoto Research Park, Japan. Waste Management, 16, No 5/6, pp 341-350.
8. Gao, Z., Drummond, C. (1999). *Thermal Analysis of Nucleation and Growth of Crystalline Phases in Vitrified Industrial Wastes*. The Ohio State University, Columbus, Ohio. Journal of the American Ceramics Society. 82, No 3, pp561-565.
9. Davies, M.W., Kerrison, B., Gross, W.E., Robson, M.J., Wichall, D.F. (1970). *Slagceram: A Glass Ceramic from Blast-Furnace Slag*. Journal of the Iron and Steel Institute London, 208, pp 348 – 370.
10. Klug, H., Alexander, L. (1974). *X-ray Diffraction Procedures for Polycrystalline and Amorphous Materials*. Wiley Interscience Publication.
11. Bogatov, S.A., Souris, A.L. (1995). *Treatment of Low Level Radioactive Waste by Plasma Vitrification for Permanent Disposal*. Russian Research Centre

"Kurchatov Institute". Proceedings of the International Symposium on Environmental Technologies. Atlanta Georgia, pp 499 – 504.

12. Zaghloul, H., Cortez, R., Smith, E. (1995). *Plasma Waste Remediation Activities in the United States.* Atlanta, Georgia, USA. Proceedings of the International Symposium on Environmental Technologies: Plasma Systems and Applications. 1, pp 1-12.
13. Hoffelner W. Chrubasik A. Eschenbach R.C, Funfschilling M.R, Pellaud .P. (1992). *Plasma Technology for Rapid Oxidation, Melting and Vitrification of low/medium Radioactive Waste.* Nuclear Engineering International, Oct 1992, Vol 3, pp 15-16.
14. Barbieri, L., Corradi, B., Lancellotti, I., Siligardi, C. (1999). *The Production of Glass and Glass-Ceramic Materials from Municipal and Industrial Wastes.* Department of Chemistry, University of Madena and Reggio Emilia, Modena, Italy. The British Ceramics Society Proceeding No 60, Conference and Exhibition of the European Ceramics Society, extended abstracts. 1, pp177-178.
15. Scholes, S. (1974). *Utilisation of Industrial Wastes in the Production of Glass Ceramics.* Chicago. Advanced Material Consultancy. Proceeding 4th Mineral Waste Utilisation Symposium, pp 317 – 327.
16. Berezhnoi, A. Mersol, S. Pincus, A. (1970). *Glass-Ceramics and Photo-Sitalls.* Russia, Plenum Press.
17. Wang, M.C., Liaw, H.J., Wu, N.C., Hon, M.H. (1989). *Blast Furnace Slag as a raw material for glass melting.* Tiawan, Republic of China. Glass Technology. 30, part 1.
18. Matusita, K., Kinefuti, J., Koide, M. (1996). *Colour of Glasses Prepared from Sewage Sludge and Incinerator Ash.* Department of Environmental Engineering, Nagaoka University of Technology. The second international meeting of the Pacific Rim Ceramics Societies. Queens land Australia, Symposium 18, pp 28 – 37.
19. Davies, M.W., Hazeldean, G.S.F., Robson, M.J. (1970). *Nucleation and Crystallisation in Fe-S and Fe-Cr Containing Glass-Ceramics Based on Slag.* The Inter-Group Laboratories of the British Steel Corporation. Science of Ceramics, 5, pp 151-169.
20. McMillan, P. (1979). *Glass Ceramics.* 2nd ed. Warwick, England. Academic Press. Non-metallic Solids: A series of Monographs, Number 1.

21. Agarwal, G., Hong, K.S. (1991). *Crystallisation Behaviour of Cupola Slag Glass-Ceramics*. New York, Alfred University. Journal of Non-Crystalline Solids, 130, pp 187 – 197.
22. Agarwal, G., Speyer, R.F. (1992). *Devitrifying Cupola Slag for Use in Abrasive Products*. Journal of Minerals Metals and Materials Society, No 3, 46, pp 32 – 37.
23. Bikbau, M.Ya., Shcheglova, N.N. (1995). *Production of Stone Castings from Blast Furnace Slag from the Cherepovetsk Metallurgical Plant*. Moscow, Russia. Glass and Ceramics, 52, No 1 – 2.
24. Rawlings, R.D. (1997). *Production and Properties of Silceram Glass*. Glass-Ceramic Materials - Fundamentals and Applications. Mucchi Editore, Modena Italy, pp 115-133.
25. Marghussian, V. (1999). *Fabrication of Unglazed Floor Tiles Containing Iranian Copper Slag*. Department of Materials, Iran University of Science and Technology, Iran. Ceramics International, 25, pp 617-622.
26. Berzina, L., Cimdins, R., Rozenstrauha, I., Bossert, J., Cker, M.B. (1999). *Environment Friendly Glass Ceramic from Metallurgical Waste*. Biomaterials R & D Laboratory, Riga Technical University, Latvia. The British Ceramics Society Proceeding No 60, Conference and Exhibition of the European Ceramics Society, extended abstracts. 1, pp179-180.
27. Rozenstrauha, I., Cimdins, R., Berzina, L., Bajare, D., Bossert, J., Boccaccini, A. (2002). *Glass-ceramic Matrix Composites Made from Industrial Waste*. 7th Conference of the European Ceramics Society. Key Engineering Materials. 206-213, pp 867-870.
28. Tuan, C., Dass, W. (1996). Mechanical Properties of Vitrified Soils. Proceedings of the Materials Engineering Conference, pp 731 – 740.
29. Tzeng, C.C., Kuo, Y.Y., Hwang, I.J., Lang, D.L., Yu, Y.J. (1998). *Treatment of Radioactive Wastes by Plasma Incineration and Vitrification for Final Disposal*. Elsevier Scientific Publishing Company. Journal of Hazardous Materials 58, pp 207 – 220.
30. Hoffelner, W., Chrubasik, A. (1992). *Plasma Technology for Rapid Oxidation Melting and Vitrification of Low/Medium Radioactive Waste*. USA. Nuclear Engineering International. pp 14 – 16.
31. Bernard, S., Fauchais, P., Jarrige, J., Lecompte, J.P. (1999). *Transferred Arc Treatment of Flying Ashes from Domestic Wastes*. Limoges-France. The British

Ceramics Society Proceeding No 60, Conference and Exhibition of the European Ceramics Society, extended abstracts. 1, pp 175-176.

32. Geimer, R., Batdorf, J., Wolfe, P. (1993). *Test Results from the Demonstration of the Plasma Hearth Process.* Proceedings of the Incineration Conference. Science Applications International Corporation (SAIC). pp 301-305..
33. Hernandez, M. Rincon, J and Romero, M. (2002). *Modified porcelainized stoneware tiles obtained from recycling of granite and MSW incinerator fly ash.* 7th Conference of the European Ceramics Society. Key Engineering Materials, 206-213, pp 847-850.
34. Boccaccini, A. and Rawlings, R. (2002). *Waste Not – Producing Glass-Ceramics from Waste Materials.* Department of Materials, Imperial College London. Materials World, 10, No 5, pp 16 – 18.
35. Menzler, N., Mortel, H., Weibmann, R. (1999). *Examination of Two Glass Compositions for the Vitrification of Toxic Products from Waste Incineration.* University of Erlangen-Nuremberg, Department of Materials Science, Glass and Ceramics, Germany. Glass Technology, 40, No 2, pp 65-70.
36. Romero, M., Rawlings, R., Rincon, J. (1998). *Development of a New Glass-Ceramic by Means of Controlled Vitrification and Crystallisation of Inorganic Wastes from Urban Incineration.* Imperial College of Science, London, England. Journal of the European Ceramic Society, 19, No 12, pp 2049-2058.
37. Knowles, S.D., Brosnan, D.A. (1995). *Composition and Properties of Glass Cermaics Produced From Incinerator Residuals.* Clemson, USA. Jounal of the Canadian Glass Ceramic Society, No 4, pp 231 – 234.
38. Chapman, C.D., Williams, J.K. (1995). *Development of a Plasma Reactor for the Treatment of Incinerator Ashes.* Proceedings of the International Symposium on Environmental Systems, Plasma Systems, Atlanta Georgia, USA, October 1995.
39. Suzuki, S., Miyyano, K., Kaneko, T., Nagayoshi, Y. (1991). *Method for Converting Waste to Crystallised Glass.* United States Patent Number 809, 883. Tsukishima Kikai Co., Ltd, Tokyo Metropolitan Government, Japan.
40. Ekonomakou, A., Geralis, A., Stournaras, C.J. (2002). *The Utilisation of Water Industry Wastes in Ceramic Products.* 7th Conference of the European Ceramics Society. Key Engineering Materials, 206-213, pp 867-870.
41. Endo, H., Nagayoshi, Y., Suzuki, K. (1997). *Production of Glass Ceramics From Sewage Sludge. Japan,* Water Science and Technology, 36, No 11, pp 235-241.

42. Chu, J.P., Hwang, I.J., Tzeng, C.C., Kuo, Y.Y., Yu, Y.J. (1998). *Characterisation of Vitrified Slag from Mixed Medical Waste Surrogates Treated by a Thermal Plasma System.* Elsevier Scientific Publishing Company. Journal of Hazardous Materials 58, pp 207 – 220.

43. Chang, J. (2001). *Recent Developments of Plasma Pollution Control Technology: A Critical Review.* Science and Technology of Advanced Materials, 2, No 3 and 4, pp 571 – 576.

44. Tanaka, M., Suzuki, S. (1999). *β-Wollastonite Precipitated Glass-Ceramic Synthesised from Waste Granite.* The Tokyo Metropolitan Industrial Technology Research Institute, Tokyo, Japan. Journal of the Japanese Ceramic Society, 107, pp 627 – 632.

45. Omar, A.A., Salman, S.M., Khater, G.A. (1995). *Glass-Ceramics in the Cordierite-Spodumene System Based on Inexpensive Raw Materials.* Glass Research Dept, National Research Centre, Dokki, Clairo, Egypt. Fourth Euro Ceramics, 4, pp 501 – 506.

46. Diaz, C., Valle-Fuentes, F.J., Zayas, M.E., Avalos-Borja, M. (1999). *Corderite Glass-Ceramic from Geothermic Waste.* The American Ceramic Society Bulletin, 78, No 3, pp 62 - 64.

47. Eschenbach, R.C. (1996). *Plasma Arc Systems for Waste Treatment and Metal Recovery.* USA. JOM (International Conference), 48, pp 49 - 52.

48. Vursel, B.V. Camacho, S.B. (1995). *Plasma Activities in Russia and in the Newly Independent States.* Atlanta, Georgia, USA. Proceedings of the International Symposium on Environmental Technologies: Plasma Systems and Applications. 1, pp 35 - 44.

49. Mac Rae, D.R. (1988). *Plasma Arc Process Systems, Reactors and Applications.* Bethlehem Steel Corporation, Pennsylvania. Plasma Chemistry and Plasma Processing, 9, No 1, pp 85 - 118.

50. Wang, M.C., Hon, M.H. (1993). *Properties and Crystallisation of Li_2O-CaO-Al_2O_3 SiO_2-TiO_2 Glasses.* Pittsburgh. Journal of Materials Research, 8, No 4.

51. Paul, A. (1990). Chemistry of Glasses. 2nd ed. Indian Institute of Technology Kharagpur. Chapman and Hall, pp 1 – 50, 1990.

52. Turnbull, D. (1969). *Under What Conditions can a Glass be Formed?* Harvard University, Cambridge, Massachusetts, USA. Contemporary Physics, 10, No 5, pp 473 – 488.

53. Reece, R.J. (1995) Industrial Plasma Engineering. Institute of Physics. University of Tennessee. 1, pp 1 – 158 and 352 – 390.
54. Feinman, J., Editor. (1987). Plasma Technology in Metallurgical Processing. A Publication of the Iron and Steel Society, ppl – 49 and 125 – 130.
55. Brandes, E.A., Brook, G.B., Editor. (1998). *Smithells Metals Reference Book.* Reed Educational and Profesional Publishing Ltd, Edition 17, pp 18-1 to 18-10.
56. Nurnberg, K. (1981). *Slag Atlas*, Society of German Steel Makers, Germany.
57. Levin, E.M. (1964). *Phase Diagrams for Ceramists*, The American Ceramic Society Inc. Columbus, Ohio.
58. Clinton, D.J. (1987). *A Guide to Polishing and Etching of Technical and Engineering Caramics.* National Physical Laboratory, UK. The Institute of Ceramics, pp 17 – 54.
59. Antis, G.T., Chantikul, P., Lawn, B.R., Marshall, D.B. (1981). *Critical Evaluation of Indentation Techniques for Measuring Toughness 1.* University of New South Wales, Australia. Journal of the American Ceramic Society, 64, pp 533 – 538.
60. Davidge, R. (1979). *Mechanical Behaviour of Ceramics.* Ceramic Technology Group, AERE, Harwell. Cambridge University Press, Cambridge.
61. Turkdogan, E.T., Patricia, M.B. (1960). A Critical Review of Viscosity of CaO-MgO-Al_2O_3-SiO_2 Melts. British Iron and Steel Research Association, London, England. American Ceramic Society Bulletin, 39, pp 682 – 687.
62. Turkdogan. E.T. (1983). *Physicochemical Properties of Molten Slags and Glasses.* 1st ed. United States Steel Corporation Research Laboratory Monroeville, Pennsylvania. The Metals Society, London.
63. Hurlbut, C. (1959). *Dana's Manual of Mineralogy.* 18th ed, Great Britain: John Wiley & Sons, Inc.
64. Oberg, E., Franklin, D. (1995). *Machinery's Handbook 22nd Revised Edition.* Industrial Press Inc, New York.
65. William, L., Rainforth, W. (1995). *Ceramic Microstructures, Property Control by Processing.* Place. Chapman and Hall.
66. Wurst, J., Nelson, J. (1972). *Lineal Intercept Technique for Measuring Grain Size in Two-Phase Polycrystalline Ceramics.* Journal of the American Ceramic Society – Discussion and Notes, pp 109.
67. Krauskopf, K.B. (1973). *Introduction to Geochemistry.* Stanford University USA. McGraw-Hill Kogakusha, Ltd. Edition 2, pp 544 - 545.

68. NEN 7345 Draft Translation. (1995). *Leaching Characteristics of Soil and Stony Building and Waste Materials* – Leaching Tests – Determination of the Leaching of Inorganic Components from Building and Monolithic Waste Materials with the Diffusion Test, Revision April 1995.

69. Environment Agency. (2001). *Geography and Climate – Figure 4.* [www] http://www.environment-agency.gov.uk/index.htm (April 9 2001).

70. Prammer, B. *Council Directive 98/83/EC of the 3 Nov 1998 on the Quality of Water Intended for Human Consumption.* Official Journal of the European Communities, 330, pp 32 - 54.

71. Severn Trent Laboratories. (1989). *Standards for Drinking Water Quality* (as per The Water Supply (Water Quality) Regulations 1989).

72. Sakamoto, Y., Ueda, Y. (1992). *Sewage Sludge Melting System. Japan.* Tsukishima Kikai Co., Ltd, Tokyo, Japan. 2nd Water Environmental Federation Asia/Pacific rim Conference on Water Pollution Control.

73. Chantikul, P., Antis, G.T., Lawn, B.R., Marshall, D.B. (1981). *Critical Evaluation Indentation Techniques Measuring Fracture Toughness.* University of New South Wales, Australia. Journal of the American Ceramic Society, 64, pp 539 – 543.

74. Ashby, M. and Jones, D. (1986). *Engineering Materials 2, An Introduction to Microstructures Processing and Design.* Engineering Department, Cambridge University, England. Pergamon Press, 39, pp 147 - 177.

75. Barbieri, L., Ferrari, A.M., Leonelli, C., Manfredini, T., Pellacani, G.C. (1991). *MgO-CaO-Al_2O_3-SiO_2 Glassy and Glass Ceramic Systems: The Effect of Substitution of CoO or NiO in Place of MgO or CaO.* Italy. Physics and Chemistry of Glasses, Vol 36, No4.

76. Kajima Corp, Tsukishima Kikai Co Ltd, Ebara Corp, (1999). *Exterior Wall Tiles Made from Wastes Are Put to Practical Application.* Weekly Sewage Information, 42, No 1147.

77. Tsukishima Kikai Co., Ltd. *Commercial Plant Operation of Melting and Crystallisation Process Converts Sewage Sludge Ash into Stone Products.* Japan, IAWQ'99 Sludge Management for the 21st Century.

78. Lampman, S., Woods, M., Zorc, T. Editor. (1991). *Ceramics and Glasses.* 4th Vol, USA: ASM International. Engineering Materials Handbook.

79. Bramford, C. (1977). *Colour Generation and Control in Glass.* England. Elsevier Scientific Publishing Company. Glass Science and Technology 2.

80. Bamford, C. (1977). *Colour Generation and Control in Glass.* Pilkington Brothers Ltd Research and Development Laboratories, Lancs, Pilkington Brothers Limited, England. Scientific Publishing Company. Glass Science and Technology, Vol 2.
81. Charnock, H. (1970). *The Float Glass Process.* Pilkington Brothers Ltd Research and Development Laboratories, Lancs. Physics Bulletin, p153 – 156.
82. Taylor, R. (1985). *Chemical Engineering Problems of Radioactive Waste Fixation by Vitrification.* Great Britian. Pergamon Press Ltd. Chemical Engineering Science. 40, No 4. pp 541-569.
83. Thomas, A. (1974). *Utilisation of Waste Kiln Dust from the Cement Industry.* Birmingham, Alabama. Sponsored by the U.S. Bureau of Mines and IIT Research Institute. Proceeding of the Fourth Mineral Waste Utilisation Symposium.
84. Onyx.Aurora. (1998). *The Tyseley Energy- From-Waste Facility.* Tyseley Waste Disposal Ltd. Birmingham, England, pp 1 - 4.
85. BS 1902, Part 1C, pp14 -15, 1967. Determination of Porosity and Density.
86. Beall, G.H., Pinkney, L.R. (1999). *Nanophase Glass Ceramics.* Journal of the American Ceramics Society. Vol 82, No1, pp 5 –16.
87. Staley, L. (1992). *Site Demonstration of the Retech Plasma Centrifugal Furnace: The Use of Plasma to Vitrify Contaminated Soil.* U.S. Environmental Protection Agency, Ohio. Journal of Air Waste Management Association, 42, No 10, pp 1372 - 1376.
88. Doweidar, H. (1999). *Density-Structure Correlations in Silicate Glasses.* Mansoura Egypt. Jounral of Non-Crystalline Solids, No 249, pp 194 – 200.
89. Jones, D. (2002). *Proposal to Raise Landfill Tax Rate Opposed by Manufacturing Bodies. Professional Engineering*, 15, No 23, pp 7.
90. Cameron, R., Manik, J. (2002). *Waste Disposal, The Burning Issue.* Department of Trade and Industry, Eureka, Global Watch. 10, No1, pp 10 – 11.
91. Moroney, M.J. (1990). *Facts and Figures.* Penguin Books.